

Towards a massive directional dark matter detector: CYGNUS-TPC



Anthony C. Ezeribe

Department of Physics and Astronomy

The University of Sheffield

A thesis submitted in partial fulfilment for the degree of

Doctor of Philosophy

December 2016.

Dedicated to the Creator of the Universe and my wife.

Abstract

There is now overwhelming observational evidence to believe that only 15% of the matter content of the Universe is known. Hence, the prevailing 85% is composed of non-baryonic dark matter. The putative name for the most probable dark matter candidate is Weakly Interacting Massive Particles (WIMPs).

Theoretically, one powerful route to find WIMPs is through the detection of the expected directional galactic WIMP signatures using direction sensitive detectors. Recently, the DRIFT directional WIMP search collaboration identified the sources of background events in their detector and have taken positive measures to suppress or reject them. The sensitivity of the DRIFT experiment is now constrained mainly by target mass. This motivated the convergence of all the existing directional WIMP search experiments to form the CYGNUS-TPC collaboration to build a massive directional WIMP search detector with optimal sensitivity.

This thesis presents work on the possible use of signal multiplexers to reduce the number of front-end electronics required in the proposed CYGNUS-TPC detector project. Results from the analysis of simulated data obtained from the DRIFT-IIId detector in a simplified readout mode show prospects for an alternative readout technology with a lower cost of front-end electronics relative to the signal multiplexing scheme. Results from measurements of the head-tail and axial range components of the directional signatures suggest the possibility of directionality with events fiducialisation in the proposed CYGNUS-TPC detector. Also, results from analyses of a 54.7 live-time days of shielded WIMP search data obtained from the DRIFT-IIId directional detector with an improved fiducial volume are presented. In this, the detector reached best sensitivity to spin-dependent WIMP-proton cross section at 0.29 pb for a $\sim 100 \text{ GeV } c^{-2}$ WIMP.

Acknowledgements

I wish to sincerely thank my supervisor Prof. Neil Spooner for motivating my research with relevant science questions and for his guidance and criticisms. In fact, you have been a great source of inspiration for my research. Thanks for all the weekly research meetings, discussions, support and perhaps pains due to these tutelage for which I will ever remain grateful.

Many thanks to Dr. Steve Sadler and Prof. Dan Snowden-Ifft for helping me to understand the DRIFT-II data analyses procedures and for answering my analyses questions, especially during the early stages of this research. I am also very grateful for discussions and contributions from Prof. Dan Snowden-Ifft and Dr. Jean-Luc Gauvreau especially during my wire-winding operation visit to Occidental College Los Angeles. Also, thanks for all your educative and helpful e-mails during the construction phase of the DRIFT-IIe pro detector and my DRIFT-II data analyses. Special thanks to Prof. James Battat and Prof. John Harton of Wellesley College and Colorado State University, respectively, for your reviews and criticisms. I wish to thank every member of the DRIFT collaboration for your respective contributions especially, Prof. Dinesh Loomba and Prof. Alex Murphy of University of New Mexico and University of Edinburgh, respectively, for all your educative e-mails.

It is my pleasure to thank all the academic and non-academic staff of the department of Physics and Astronomy, University of Sheffield who contributed toward the successful completion of my studies. In a special way, I would like to thank Dr. John MacMillan for useful discussions, Dr. Matt Robinson, Dr. Leonid Yuriev and Dr. Dan Walker for their respective support and contributions during my work in the laboratory. Also, many thanks to Dr. Ed Daw, Dr. Susan Cartwright, Prof. Davide Costanzo, Prof. Daniel Tovey, Prof. Sean Paling and Dr. Chris Booth for their respective lectures in the early stages of this program. Special thanks to Laura Oliver, Rebecca Raynor and Angie Rollinson for administrative support.

I wish to say a big thanks to all my colleagues in room D35, especially Andrew Scarff, Mathew Thiesse, Calum Macdonald and Frederic Mouton for useful discussions. Sincere thanks to TETFund and Nnamdi Azikiwe University, Awka, Nigeria for

financial support. Finally, special thanks to my wife for all her support, my parents, family and friends for their prayers.

Author's Contributions

- In Chapter 3, the author built a high precision automated quad wire winder for making multiple one-plane multi-wire proportional chambers (MWPCs) with contributions from other members of the collaboration during his research visit to Occidental college Los Angeles. The design, construction and operation of a miniature one-plane MWPC based DRIFT-IIe pro detector and the field cage described in that chapter are sole work of the author. The author was also responsible for setting up the gas system, gas and power feed-throughs, calibration and adaptation of the pre-amplifiers and shaping amplifier front-end electronics, making the signal and power cables used in that work. Garfield, HEED and SRIM simulations performed in that chapter to determine the operational field and gas pressure for the DRIFT-IIe pro detector were also the work of the author. The design and construction of the multiplexing electronics discussed in Chapter 3 were done by the author with another member of the collaboration. The system optimisation work that allowed for testing of the multiplexer data acquisition system with real analogue signals were done by the author.
- The method used for the signal head-tail analyses using nuclear recoil events from ^{32}S , ^{19}F and ^{12}C nuclei as described in Chapter 4 were developed by the author for the new fiducialisation data for the DRIFT collaboration. Also the nuclear recoil axial directional range component measurements for these new data sets were also performed for the first time by the author. In these analyses, a new nuclear recoil selection algorithm was developed by the author to increase the analyses nuclear recoil identification and background rejection abilities. In that chapter, the author also presented results from his work towards separating each of the nuclear recoil candidates expected in the new fiducialisation data set. The author also performed all the SRIM simulations discussed in that chapter.
- The WIMP search analyses methods presented in Chapter 5 of this thesis leading to a 90% C. L. upper limit on SD WIMP-proton cross section sensitivity of the DRIFT-IIId detector for different WIMP masses are the work of the author. In

that chapter, the author developed a new analyses method that allows for events fiducialisation in the low- z region of the detector which improved the fiducial target mass of the DRIFT-IIId detector. The author also developed an analysis method as a simulation to test the viability of simplified one dimensional MWPC based readout technology which is capable of reducing the cost of signal read out electronics in massive MWPC based TPCs. This includes development of ^{55}Fe analysis algorithm for the signal sum-line needed for determination of ionization energies of events from neutron induced nuclear recoil or shielded WIMP search data analyses presented therein.

- The author also contributed to the DRIFT-IIId detector maintenance and operation control during the science runs that resulted in directed neutron, shielded WIMP search, neutron calibration and unshielded rock neutron measurement data sets which are used in the analyses presented in Chapters [4](#) and [5](#) of this thesis.

Contents

Contents	i
List of Tables	v
List of Figures	vii
1 Introduction	1
1.1 Introduction to dark matter	1
1.2 Evidence for existence of dark matter in the Universe	5
1.2.1 Velocity dispersion of galaxies in the Coma cluster	5
1.2.2 Rotation curves of Galaxies	6
1.2.3 Dark matter evidence through gravitational lensing	9
1.2.4 Bullet Cluster	11
1.2.5 Big Bang Nucleosynthesis	13
1.2.6 Cosmic microwave background (CMB)	15
1.2.7 Concluding remarks on the evidence for dark matter	18
1.3 Dark Matter candidates	19
1.4 Conclusion	23
2 WIMP Detection and experimental searches	24
2.1 WIMP detection	24
2.2 Direct WIMP detection	27
2.3 WIMP theoretical event rates in direct detection	27
2.3.1 Expected rate of WIMP events	28
2.3.2 Expected WIMP differential rate	29

2.3.3	WIMP velocity distribution	32
2.3.4	Nuclear form factor correction	33
2.4	WIMP-nucleon cross section	37
2.5	Reducing backgrounds in direct WIMP search detectors	41
2.6	Classification of direct WIMP search experiments	43
2.7	Non-directional WIMP search experiments	48
2.7.1	Large Underground Xenon (LUX) WIMP search detector	49
2.7.2	PICO WIMP search Experiment	52
2.7.3	Cryogenic Rare Event Search with Superconducting Thermometers II (CRESST-II) WIMP search experiment.	53
2.7.4	Cryogenic Dark Matter Search (CDMS) experiment	55
2.7.5	DM-Ice experiment and annual modulation searches	56
2.8	Directional WIMP search experiments	60
2.8.1	NEWAGE directional WIMP search experiment	60
2.8.2	DMTPC directional WIMP search experiment	62
2.8.3	MIMAC directional WIMP search experiment	64
2.8.4	DRIFT directional WIMP search experiment	65
2.9	R&D on directional WIMP search detectors	70
2.9.1	R&D on gas based directional WIMP search detectors	70
2.9.2	R&D on possible use of solids in directional WIMP searches	71
2.10	CYGNUS-TPC a future WIMP telescope	72
2.11	Conclusion	74
3	MUX readout for CYGNUS-TPC	75
3.1	Introduction	75
3.2	Design and construction of miniature TPC detector	77
3.2.1	EAGLE PCB design for the one-plane MWPC	78
3.2.2	Wire winding for construction of one-plane MWPC using Quad Wire Winding Robot (QWWR)	81
3.2.3	Design, construction and operation of a field cage for the DRIFT-IIe pro detector	86
3.3	Front-end electronics	91
3.4	Power and signal feedthrough	94

3.5	Commissioning the one-plane MWPC based miniature detector	95
3.6	Gain of the one-plane MWPC based miniature detector	100
3.7	LabVIEW based data acquisition system	104
3.8	Design and construction of a 20:1 signal multiplexer (MUX)	110
3.9	Operations of the MUX data acquisition system	116
3.10	Conclusion	125
4	Directionality measurements with the DRIFT-II detector	126
4.1	Introduction	126
4.2	Directed neutron exposures	127
4.3	Introduction to DRIFT data and analyses	130
4.4	Energy calibration	134
4.5	Fiducialisation of events z position in DRIFT-II detector	136
4.6	Measurement of nuclear recoil track vector sense	141
4.6.1	Nuclear recoil track vector sense results	145
4.7	Measurement of axial directional components of nuclear recoil tracks	153
4.7.1	Reconstruction of track Δx range	154
4.7.2	Reconstruction of track Δy range	154
4.7.3	Reconstruction of track Δz range	155
4.7.4	Other nuclear recoil axial parameters	156
4.7.5	Results from analysis of axial directional components of nuclear recoil tracks	158
4.8	Conclusion	168
5	WIMP search analyses and results from the DRIFT-II detector	170
5.1	Introduction	170
5.2	WIMP and background neutron data and analyses	172
5.2.1	Detector efficiency for nuclear recoil tracks	174
5.3	Unshielded background rock neutron measurements	180
5.3.1	WIMP search results from the normal fiducial volume	181
5.4	Simulated simplified readout configuration	186
5.4.1	Results from the simplified 1D readout analyses	192
5.5	Extending the fiducial volume to the low- z region of the detector	198

CONTENTS

5.5.1	WIMP results from the improved fiducial volume	204
5.6	Conclusion	210
6	Conclusions	212

List of Tables

1.1	Cosmological parameters measured by the <i>Planck</i> collaboration in 2015 [2].	3
4.1	Head-tail parameter obtained from high- z events in the $+z$, $-z$ runs. Only statistical uncertainties are quoted. The n is the number of events, other symbols used here are defined in the text.	150
4.2	Head-tail parameter obtained from mid- z events in the $+z$, $-z$ runs. Only statistical uncertainties are quoted. Symbols are defined in Table 4.1.	150
4.3	Head-tail parameter obtained from combined high- z and mid- z events in the $+z$, $-z$, $-x$, and $-y$ runs. Only statistical uncertainties are quoted. Symbols are defined in Table 4.1.	150
4.4	Axial range components of nuclear recoil tracks obtained from $+z$, $-z$, $-x$, and $-y$ directed neutron events. The mean neutron directions (MND) are shown in the first column, number of events n are in the second column while run live-time for each of the neutron exposures are in the third column. In columns four to six are the average Δx , Δy , and Δz parameters for each of the runs. The $\frac{\Delta z}{\Delta x}$ parameter obtained for each of these runs is shown in column seven. Only statistical uncertainties are quoted. Event energies are in the range of about $300 \leq \text{NIPs} \leq 6000$	159
5.1	Names of data files and total live times of events recorded during the WIMP search runs, nuclear recoil calibrations runs and rock neutron measurements. See text, for details of the row and column labels.	173

LIST OF TABLES

5.2	Expected background neutrons in the fiducial volume of the detector and RPR events during the 54.7 shielded data days, considering the detector efficiency.	183
5.3	Details of the parameters used for computation of the WIMP exclusion limit.	184

List of Figures

1.1	Major constituent of the Universe. The dark energy and dark matter content of the Universe are shaded in blue and red, respectively while that of the normal baryonic matter is shaded in green.	2
1.2	Particles of the standard model of particle physics [1].	4
1.3	Rotational velocity of H1 clouds in NGC 6503 dwarf spiral galaxy shown as a function of their radial distance. The circular points with error bars are the observed data, the dashed line is theoretical expectation from luminous matter, the dotted line is expectations from gas clouds while the dash-dotted line is the theoretical expectation from a dark matter halo. The solid line that agrees well with the observational data is the sum of the contributions from the gas cloud, stellar disk and the dark matter halo [19].	7
1.4	Four images of a gravitational lensed system in a galaxy scale structure. The massive celestial object acting as a lens is at the centre surrounded by four lensed images of a distant galaxy [27].	9
1.5	Einstein ring of a distant galaxy. The lensing galaxy can be seen in the middle surrounded by a ring of perturbed photons reaching the observer from a distant galaxy [28].	10
1.6	X-ray image of the Bullet Cluster. Luminous matter is in red while dark matter component is in blue. Credit: Chandra X-ray observatory.	12

LIST OF FIGURES

1.7	Standard model of BBN predictions for relative abundance of light elements shown as a function of present day baryon-to-photon ratio and compared to experimental measurements. The expected abundance of ${}^4\text{He}/{}^1\text{H}$, ${}^2\text{H}/{}^1\text{H}$, ${}^3\text{He}/{}^1\text{H}$ and ${}^7\text{Li}/{}^1\text{H}$ are shown with light green, blue, green and yellow lines, respectively. The red line that crosses each of the theoretical predictions shows the WMAP results. Points marked with red circle lines show agreement between the prediction and measurement. Credit: NASA/WMAP science team.	14
1.8	Temperature power spectrum (TT) data from <i>Planck</i> 2015 [2].	16
1.9	Theoretically favoured and leading dark matter candidates and their particle physics motivation.	20
1.10	Comoving number density of dark matter density shown as a function of temperature, time and density of the expanding Universe. The solid line predicts the correct present-day thermal relic dark matter abundance using $100 \text{ GeV } c^{-2}$ known as the WIMP miracle. Dotted line experienced no freeze-out, colours (from top to bottom) are results after the freeze-out mechanism as expected from weak to strong scale cross sections [1].	21
2.1	Possible search windows for WIMP dark matter particle.	25
2.2	WIMP-nucleon reduced mass μ obtained from various target nuclei shown as a function of WIMP mass and compared to contributions from one atomic proton. The black, pink, green, blue, red, tan and grey lines show results from ${}^{127}\text{I}$, ${}^{73}\text{G}$, ${}^{32}\text{S}$, ${}^{19}\text{F}$, ${}^{16}\text{O}$, ${}^{12}\text{C}$ nuclei and from one atomic proton, respectively.	31
2.3	Momentum dependent nuclear form factor parameter obtained for some of the target nuclei used in WIMP search experiments. The black, pink, grey, blue, red and tan lines show results from ${}^{127}\text{I}$, ${}^{73}\text{G}$, ${}^{32}\text{S}$, ${}^{19}\text{F}$, ${}^{16}\text{O}$ and ${}^{12}\text{C}$ nuclei, respectively.	34
2.4	Nuclear form factor obtained for different target nuclei used in WIMP search experiments shown as a function of WIMP recoil energies. The black, pink, grey, blue, red and tan lines show the nuclear form factor effect in ${}^{127}\text{I}$, ${}^{73}\text{G}$, ${}^{32}\text{S}$, ${}^{19}\text{F}$, ${}^{16}\text{O}$ and ${}^{12}\text{C}$ nuclei, respectively.	36

LIST OF FIGURES

2.5	Total muon flux in underground laboratories around the world shown as a function of their water equivalent depths. The blue points are observed data while the black line is the best fit for the effective laboratory depths [109].	42
2.6	WIMP search experiments and their search strategies.	44
2.7	Motion of the Earth around the sun as the solar system is rotating about the galactic centre. Credit: Sheffield Dark Matter Research Group. . .	45
2.8	Rotation of the Earth about its axis showing a change in the expected mean direction of WIMP wind signal reaching an Earth bound detector within a sidereal day.	46
2.9	Neutrino floor overlaid on typical sensitivities from direct detection experiments shown on WIMP-nucleon cross section-WIMP mass parameter space. The orange thick dashed line shows the upper limit for the neutrino floor. Each of the solid lines shows a parameter space excluded by the given experiment while the dotted lines are planned and projected sensitivities. The arrows show allowed parameter space for various theoretical models [132]. For up-to-date results from LUX, PICO, CDMS and DarkSide experiments, see Section 2.7.	47
2.10	Principles of operation of the Large Underground Xenon (LUX) dual-phased TPC detector [148].	49
2.11	Spin-dependent (SD) and spin-independent (SI) results from LUX compared to exclusion limits from other experiments as at 2016 [118, 150, 151].	51
2.12	Experimental setup of PICO-2L bubble chamber [157].	52
2.13	Schematic of the CREST-II detector [160].	54
2.14	Experimental set-up for one of the germanium crystals used in the CDMS. Arrays of these crystals make up the CDMS experiment [164]	55
2.15	Set-up of the DM-Ice17 NaI(Tl) detectors deployed in the South Pole [171].	57

LIST OF FIGURES

2.16	Spin independent WIMP-nucleon cross section limit obtained from the DM-Ice37 experiment shown as a function of WIMP masses marked with red line. This is compared to the DAMA/LIBRA allowed region marked with blue lines. The expected sensitivity from 500 kg-yr data from a future DM-Ice experiment is shown with black dashed line [172].	58
2.17	WIMP annual modulation results from the DAMA/LIBRA experiment [142].	59
2.18	Comparison of annual modulation signal from neutron events produced by muon and neutrino backgrounds to the WIMP results from the DAMA/LIBRA experiment [129].	59
2.19	Schematic of a NEWAGE μ -PIC detector. The left panel shows an image of the detector in a vacuum vessel while the right panel shows the details of the GEM based μ -PIC readout system [176].	61
2.20	Sky map of background nuclear recoil events observed in the NEWAGE-0.3b μ -PIC detector during WIMP search operations [144].	62
2.21	Schematic of the DMTPC detector [182].	63
2.22	Principle of operation of the MIMAC directional WIMP search μ -TPC detector [190].	64
2.23	Pictorial view of the DRIFT-II detector when it is partly removed from the stainless steel vacuum vessel.	66
2.24	Wire configuration in each of the MWPCs in the DRIFT-II detector.	67
2.25	Automated gas mixing and flow control for DRIFT-II detector.	68
2.26	Peltier cooling systems used to maintain the temperature of the DRIFT-II detector below the intrinsic underground laboratory temperature. In (a) is the four Peltier units marked 1 to 4 in black while (b) shows the four Peltier cooling system after installation marked 1 to 4 in red.	70
3.1	Sketch of possible cylindrical and modular design for a 100 m ³ CYGNUS-TPC. The number of signal channels from each of the constituent one-plane MWPC readout are shown without considering the veto signal channels. All dimensions are in mm.	76

LIST OF FIGURES

3.2	Configuration of anode and grid wires in the DRIFT-IIe pro detector to be operated with an anode-grid field of 850 V mm^{-1} . Dimensions are in mm.	78
3.3	EAGLE PCB design layout editor.	79
3.4	Board layout of the miniature one-plane MWPC used in the DRIFT-IIe pro detector.	80
3.5	Pictorial view of the Juggernaut used for positioning the wires on the QWWR wire frame during the winding process.	82
3.6	Simplified schematic of the major components of the QWWR.	83
3.7	Snapshot of the user interface of the wire winding control system.	84
3.8	Tensioned wires wound on the QWWR wire winding frame and secured with transparent DP-100 epoxy.	85
3.9	Pictorial view of an anode wire sandwiched between two grid wires in the miniature one-plane MWPC as recorded with a microscope.	86
3.10	Field cage of the miniature detector with one-plane MWPC readout. Typically, a drift field of 350 V cm^{-1} can be achieved at -3.5 kV cathode voltage applied through about $750 \text{ M}\Omega$ resistors.	87
3.11	Current drawn by the grid channels at different grid bias voltages.	88
3.12	Variation of drift field as a function of the cathode bias voltage.	89
3.13	Illustration of the field strength variation between the anode and grid wires as determined with Garfield and HEED Monte Carlo. Regions with 0 and 850 V potentials are shown in red and blue, respectively while the regions with potentials >0 and $<850 \text{ V}$ are shown in green.	90
3.14	Electric circuit diagram showing the FDH-300 protection diode, other major electronic components and the operational potential biases of the grid and anode wires.	91
3.15	Pictorial view of the Cremat CR-111 chip and its simplified circuit diagram showing the major components [202].	92
3.16	Electric circuit diagram of CR-150-R5 evaluation board used in driving the CR-111 charge sensitive preamplifier chip [232].	93
3.17	Signal feedthrough used to route signals out from the vacuum vessel and in, to power the amplifiers.	95

LIST OF FIGURES

3.18	Some of the major constituents of the experimental set-up used in commissioning the DRIFT-IIe pro detector. This comprises of a stainless steel vacuum vessel, high voltage power supply in NIM crate, CF ₄ gas cylinder, DC power supply and pressure gauge.	96
3.19	Miniature one-plane MWPC based DRIFT-IIe pro detector.	97
3.20	3D alpha range in various pressures of CF ₄ gas determined using SRIM Monte carlo.	98
3.21	Oscillogram of signal pulse obtained from a single anode channel of the DRIFT-IIe pro detector	99
3.22	Signal pulse height recorded on a single anode wire due to an alpha track shown as a function of grid voltage.	100
3.23	Experimental set-up used to calibrate the gain of the front-end electronics.	102
3.24	Simple illustration showing a possible configuration for GEM+MWPC readout technology. All dimensions are in mm.	104
3.25	Constituents of the FPGA FlexRIO module from National Instrument [247].	105
3.26	National Instrument chassis used to power and interface the digitizer and FPGA FlexRIO.	106
3.27	Block diagram of the LabVIEW based data acquisition system for the DRIFT-IIe pro detector.	107
3.28	Front panel of the data acquisition system showing a sample of the detector response when exposed to an alpha source.	108
3.29	Average event pulse height on anode wires as obtained from 10 alpha induced signal tracks detected with the miniature one-plane MWPC based DRIFT-IIe pro detector showing a Bragg curve effect. Note that larger Source-Wire distances are closer to the tail of the observed alpha tracks.	110
3.30	Principles of operation of a 4:1 analogue multiplexer.	111
3.31	Pin layout of a single LMH6574, 4:1 analogue signal multiplexer [224].	112
3.32	Principles of operation of the LMH6574 MUX chips in the expanded mode [224].	114

LIST OF FIGURES

- 3.33 EAGLE board layout for the 20:1 signal multiplexing PCB. Positions of four connectors used for routing power to the chips, analogue signal output, analogue signal input and digital signal input are marked as C-1, C-2, C-3 and C-4, respectively. Positions of the five LMH6574 MUX chips are labelled M-1, M-2 . . . , M-5. 116
- 3.34 Pictorial view of the 20:1 printed multiplexer device in a shielding box, ready for operation. The grey ribbon cable carries the analogue signal from the detector and the blue connector carries digital signals from the FPGA device to the multiplexer. The 3 electric cables (blue, red, grey) are used to power the chips while the black BNC cable carries the analogue output signal. 117
- 3.35 Cartoon illustration of signal multiplexing and demultiplexing of 20 analogue input channels at a total frequency of 20 MHz. The point in time where the input signals are multiplexed is marked as MUX while the point where they are demultiplexed is marked as DeMUX. Signal channels are marked such that ch. 1 stands for channel 1, ch. 2 stands for channel 2, etc. 118
- 3.36 Block diagram of the experimental set-up used for the signal multiplexing and demultiplexing. 119
- 3.37 LabVIEW virtual instrument used as the signal multiplexer and demultiplexer data acquisition system. 120
- 3.38 Sample of demultiplexed signals (multiplexed at 625 kHz) showing signal channels of the DRIFT-IIe pro detector when exposed to an alpha source. 121
- 3.39 Samples of demultiplexed signal pulses obtained from different channels of the one-plane MWPC based DRIFT-IIe pro detector when exposed to an ^{241}Am alpha source. 123
- 3.40 Average event pulse heights on anode signal wires obtained from 1000 demultiplexed alpha induced signal tracks detected with the miniature one-plane MWPC based DRIFT-IIe pro detector showing a Bragg curve effect. 124

LIST OF FIGURES

4.1	DRIFT-II detector showing different directions of neutron exposures, central cathode, veto, field direction and stainless steel vacuum vessel. Positions of the ^{252}Cf neutron source during the $+z$, $-x$, $-z$ and $-y$ runs are shown with small cylinders, which represent the lead canister used as the source container. The dotted double-headed arrows show the separation distance between the neutron source and the vacuum vessel during the runs. There is a separation of 250 mm (150 mm) between the detector and the vacuum vessel from the $+z$ and $-z$ ($-y$ and $-x$) directions. Dimensions in mm.	128
4.2	Sample of raw nuclear recoil event recorded by the DRIFT-II detector.	131
4.3	Block diagram showing the major analyses steps.	133
4.4	Energy calibration constant E_C obtained during the optimal directed neutron exposures shown as a function of time. The circle grey points are the E_C values for the left detector while the down pointing triangles in black are for the right detector.	135
4.5	Signal pulses from neutron-induced recoils at different z -positions within the active volume of the detector. The S specie charge carriers can change to other species of anions during drift, which reduces amplitude of the S peak (see (a)). Distinct D, P, S, and I peaks are shown for a mid- z event in (b). Typical behaviour of these peaks as they merge in the low- z region is shown in (c). The worst case in the very low- z region (closer to MWPC) is shown in (d). Events in the low- z region were rejected during analysis since their minority carriers become concealed under the main charge cloud. NIPs here stands for number of ion pairs.	138
4.6	Event distribution in the z -NIPs space obtained from neutron exposure using a ^{252}Cf source. This is before the z cuts described in the text. The dashed red lines at 0 and 50 cm mark the locations of the readout plane and central cathode respectively. The colour scale represents the density of the events.	139

4.7	Energy spectra of neutron-induced nuclear recoils with the source in the optimal direction. (a) Experimental data before the z cuts (described in the text) from a $+z$ run. (b) Results of a GEANT4 Monte Carlo simulation. Red line is a density fit. The exposure live time of the experimental data is about a factor 4 less than that of the simulated data set.	140
4.8	Spectrum of minority peak ratio (mp.ratio) for neutron induced nuclear recoil events obtained in all the directions of exposure before Q_r cuts.	143
4.9	Event waveform from a single wire showing the analysed I peak with η_1 (integral charge in the first half of region of interest) shaded dark grey and η_2 (integral charge in the second half of the region of interest) shaded light grey. The two blue lines mark the region where the signal exceeds 25% of the peak amplitude. The green line is the mid-point time (half of signal duration above analysis threshold) between the first and second halves of the signal and the red line shows the 25% of the I peak used as the analysis threshold.	144
4.10	Percentage difference δ parameter for different recoil energies represented by NIPs equivalent. Results from this analysis (obtained with ^{12}C , ^{19}F and ^{32}S tracks) are shown with blue circle points for the optimal runs and red asterisk points for the anti-optimal runs. The black triangle points are 2009 results obtained with only ^{32}S tracks in pure CS_2 (see Ref. [253]). Colour online.	146
4.11	Experimental data overlaid with the maximal Δz predictions for ^{32}S recoils in 30:10:1 Torr of $\text{CS}_2:\text{CF}_4:\text{O}_2$ gas mix obtained using SRIM. The heat map is the experimental data while the black line is the maximum Δz predictions for ^{32}S recoils. The colour scale represents the density of the events.	148
4.12	Spectrum of α parameter in the left and right detector obtained from optimal runs. The top panels are $-z$ events while the bottom panels are $+z$ events.	149

LIST OF FIGURES

- 4.13 Event waveform showing the analysed I peak and the determined full width half maximum (FWHM) parameter. The red line marks 50% of charge amplitude in the I peak, the two blue lines are the lower and upper temporal bounds of the FWHM while the shaded region is the area under the determined FWHM. 156
- 4.14 Distribution of Δx , Δy and Δz axial nuclear recoil range components obtained from different directions of neutron exposure. The top panels show the Δx parameters, the middle panels are the Δy parameters while the bottom panels are the Δz parameters obtained from $+z$, $-z$, $-x$, and $-y$, respectively. 161
- 4.15 Average difference of the axial range components obtained from the average results in each of the two perpendicular directions shown for neutron events from $-x$, $-y$ and $+z$ directions. Results from $-x$ neutrons are shown in red square points, the circular blue points are results from $-y$ directed neutron exposure while results from the $+z$ neutrons are shown in black triangular points. Only statistical uncertainty are shown. 162
- 4.16 Magnitude of oscillation as the neutron source is moved from $+z$ to $-x$ and from $-z$ to $-x$ ($A_{o_{zx}}$) expressed in percent and shown as a function of nuclear recoil NIPs equivalent energy. Data from this analysis which are average values from bins of 200 NIPs interval are shown with blue square points for $+z$ to $-x$ oscillation. Pink triangular points show results from $-z$ to $-x$ oscillation and red circle points are results obtained with only ^{32}S recoil tracks in Ref. [254]. 164
- 4.17 Axial range component ratio ($\Delta z/\Delta x$) obtained from the optimal neutron events shown as a function of NIPs recoil energy equivalent. The colour scale represents the density of the events. 165

LIST OF FIGURES

4.18	Axial range component ratio ($\Delta z/\Delta x$) obtained from optimal neutron events shown as a function of distance of the event vertex from the MWPC readout plane. Events from the low- z region of the detector were added to demonstrate how diffusion smears the separation between these recoil candidates at the high- z region. The two dotted red lines on 0 and 50 cm represent the MWPC and central cathode, respectively. The colour scale represents the density of the events.	166
4.19	Spectrum of $\frac{\Delta z}{\Delta x}$ parameter showing populations of distinct nuclear recoil data clusters.	167
5.1	Pictorial view of the GEANT4 simulated DRIFT-II detector in the underground laboratory cavern. Blue and red lines are simulated wood that marks the underground laboratory cavern, the rectangular green box is underfloor polypropylene pellet shielding. The cubic volume above the green box is the simulated DRIFT-II detector.	175
5.2	Distribution of neutron induced nuclear recoil events obtained from a 0.803 live-time days of nuclear recoil calibration data shown in z -NIPs space. The red lines show the region where background contaminations are expected from Radon Progeny Recoils (RPRs) emanating from the central cathode while the blue lines mark the fiducial volume used in this analysis. The bottom boundary of the RPR region and the top boundary of the fiducial volume are bounded with a red line on $z = 48$ cm.	177
5.3	Nuclear recoil detection efficiency for the DRIFT-II detector. This is without considering events from low- z regions of the detector with $z < 11$ cm. In (a) is the efficiency map for different z and NIPs bins while (b) shows the average efficiency in a given energy bin. The colour scale in (a) is the bin efficiencies presented in percent.	179

LIST OF FIGURES

5.4	Distribution of nuclear recoil events as obtained from the rock neutron measurement data. The fiducial volume and the region where RPR events were expected are marked with blue and red lines, respectively. The red lines on $z=48$ cm separates the fiducial volume and the RPR region. The black dashed lines on $z = 0$ and $z = 50$ cm represent the readout MWPC and central cathode, respectively.	180
5.5	Distribution of background events recorded during the 54.7 days of WIMP search runs. The RPR regions are marked with red lines and the fiducial volume is bounded by the blue lines. The black dashed lines on $z = 0$ and $z = 50$ cm represent the readout MWPC and central cathode, respectively.	182
5.6	Spin-dependent WIMP-proton cross section limit at 90% confidence level shown as a function of WIMP masses. The results from this analyses obtained with the DRIFT-II _d directional detector is shown in blue, cyan line is the latest result from DMTPC [177], light green line is that from NEWAGE [144], grey line is 2015 DRIFT-II _d result obtained with a higher hardware threshold [113] while red line is the latest PICO (non-directional detector) result [157].	185
5.7	Sample of a ^{55}Fe events obtained from the DRIFT-II _d detector when set to the simplified readout mode. In (a) is a signal pulse from ^{55}Fe event as observed from the sum-line while in (b) is a typical energy spectrum of these ^{55}Fe events from a set of calibration.	189
5.8	Sample of ^{55}Fe event showing merged charge pulses on the sum-line after energy calibration operations on the left detector. The anode sum-line is labelled as LAS. Black circular lines show merged ^{55}Fe charge pulses.	190
5.9	Spectra of up and down-veto parameters obtained from events in the detector, without any Q_r cut. In (a) is spectrum of up-veto parameter while (b) is that of the down-veto. All events beyond the red lines (to the right) were rejected in this analysis.	191

LIST OF FIGURES

- 5.10 Distribution of neutron induced nuclear recoil events obtained from the 0.803 live-time days of neutron calibration data. The normal detector fiducial volume is marked with blue lines while red lines show the RPR region. The boundary between this RPR region and the fiducial volume is shown with a red line. The black dashed lines on $z = 0$ and $z = 50$ cm represent the readout MWPC and central cathode, respectively. 193
- 5.11 Nuclear recoil detection efficiency of the detector obtained from the simulated simplified 1D readout mode analyses. In (a) is efficiency map for different z and NIPs bins while (b) is the average efficiency in a given energy bin. The colour scale in (a) is the bin efficiencies presented in percent. 195
- 5.12 Background events that passed the simplified 1D readout nuclear recoil selection cuts obtained from the 54.7 live-time days of WIMP search data. The normal detector fiducial volume is marked with blue lines while red lines show the RPR region. The boundary between this RPR region and the fiducial volume is shown with a red line. The black dashed lines on $z = 0$ and $z = 50$ cm represent the readout MWPC and central cathode, respectively. 196
- 5.13 Spin-dependent WIMP-proton cross section limit set at 90% confidence level obtained from the simplified 1D readout mode analyses shown as a function of WIMP masses. The results obtained from this simplified 1D readout analyses is shown with a blue line, cyan line is the latest result from DMTPC [177], light green line is that from NEWAGE [144], grey line is 2015 DRIFT-IIId result obtained with a higher hardware threshold [113], red line is the result obtained with the normal fiducial volume analyses shown in Figure 5.6 while black line is the latest non-directional result from PICO [157]. 197
- 5.14 Minority charge carrier species (D, P and S charge carrier species) after arriving to the read out plane ahead of the main charge cloud (I charge carrier specie) obtained from a nuclear recoil event in the DRIFT-IIId detector. 199

LIST OF FIGURES

- 5.15 Behaviour of integral charges in the D, P, S and I charge carrier species shown as a function of event z positions. The integral charge in D (green downward triangular points), P (red upward triangular points) and S (blue circular points) charge carrier species were normalized to the integral charges in the I charge carrier species in (a) while integral charges in each of the D (grey downward triangular points), P (green square points), S (blue circular points) and I (red upward triangular points) charge carrier species were normalized to the overall integral charge obtained from each of the events in (b). The integral charge between the beginning of the ROI and the start boundary of the D charge carrier is shown with purple square point in (a) and (b) while the integral charge between the end of the I charge carrier boundary and the end of the ROI is shown with black asterisk points in (a) and (b). 200
- 5.16 Temporal separation Δt between the arrival times of two different charge carrier species at the readout plane. The upward triangular points are the Δt between the arrival times of I and S charge carrier species while the downward triangular points are Δt between the S and P charge carrier species. The lines are fitted linear models. No Q_r cuts were applied to this dataset. 201
- 5.17 Signal pulse duration $\Delta\tau$ shown for a neutron induced nuclear recoil event obtained from the DRIFT-IIId detector. The boundaries of the $\Delta\tau$ parameter are marked with blue lines. 203
- 5.18 Distribution of neutron induced nuclear recoil events recorded during the 0.803 days of neutron calibration operations. The RPR regions are marked with red lines while the fiducial volume of the detector is bounded in the left and right with blue lines and with red lines from the top and bottom sides. The black dashed lines on $z = 0$ and $z = 50$ cm represent the readout MWPC and central cathode, respectively. 205
- 5.19 Nuclear recoil detection efficiency of the detector obtained from data in the extended fiducial volume mode. This is considering all events including the low- z events. In (a) is efficiency map for different z and NIPs bins while (b) is the average efficiency in a given energy bin. The colour scale in (a) is the bin efficiencies presented in percent. 207

5.20 Distribution of nuclear recoil events shown in z -NIPs space as obtained from the 54.7 live-time days of shielded WIMP search data using the new extended fiducial volume z reconstruction algorithm. The regions where RPRs are expected from the cathode and MWPC readouts are marked with red lines while the fiducial volume of the detector is bounded in the left and right with blue lines and with red lines from the top and bottom sides. The black dashed lines on $z = 0$ and $z = 50$ cm represent the readout MWPC and central cathode, respectively. 208

5.21 Spin-dependent WIMP-proton cross section exclusion limit set at 90% confidence level shown as a function of WIMP masses obtained from the extended fiducial volume analyses. The results obtained from the improved fiducial volume analyses is shown in blue, cyan line is the latest result from DMTPC [177], light green line is that from NEWAGE [144], grey line is 2015 DRIFT-IIId result obtained with a higher hardware threshold [113], red line is the result obtained with the normal fiducial volume analyses shown in Figure 5.6 while black line is the latest non-directional result from PICO [157]. 209

5.22 Comparison of the spin-dependent WIMP-proton cross section sensitivity of the DRIFT-IIId detector obtained using the simplified 1D readout, normal and the improved fiducial volume analyses at at 90% confidence level. Results from the simplified 1D readout analysis is shown with a green line while that from the normal and improved fiducial volume analyses are shown with red and blue lines, respectively. 210

Chapter 1

Introduction

1.1 Introduction to dark matter

One of the longest lasting tasks in current physics is to identify the nature of the non-baryonic dark matter (DM) known to constitute 26 % of total energy density of the Universe. This is about six times larger than baryonic matter [1, 2]. DM is expected to form halos around all the stars, galaxies and clusters in the observable Universe. The most recent results on the energy density of DM, baryonic matter and dark energy in the observable Universe obtained from the *Planck* measurements [2] is compared in Figure 1.1. The dark energy, dark matter and baryonic (normal) matter contents of the Universe are shown in blue, red and green, respectively. The dominance of the dark sector (dark energy and dark matter) of the Universe can be eminently seen in this figure.

The properties of the Universe are constrained using the cosmological parameters obtained from the most recent *Planck* temperature and lensing low-multipole or angular likelihood data analyses in Table 1.1 [2]. These results in that table indicate that our ~ 14 Gyr old observable Universe is flat and expanding. This is consistent with theoretical predictions and results from previous measurements performed by the Wilkinson Microwave Anisotropy Probe (WMAP) and other independent measurements [3, 4]. The age t_0 of the observable Universe can be determined using the Hubble constant H_0 given by [5, 6, 7]:

$$H_0 = \frac{1}{t_0}. \quad (1.1)$$

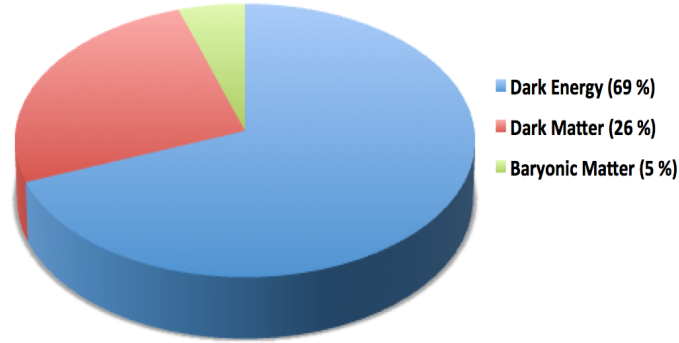


Figure 1.1: Major constituent of the Universe. The dark energy and dark matter content of the Universe are shaded in blue and red, respectively while that of the normal baryonic matter is shaded in green.

Results from this computation of the age of the Universe is shown in Table 1.1. Also, using the results in this table the energy density of matter Ω_M in the Universe can be constrained via:

$$\Omega_M = \Omega_B + \Omega_{DM}, \quad (1.2)$$

where Ω_B and Ω_{DM} are the energy densities of the baryonic and non baryonic matter, respectively. Considering, the energy density Ω_{rel} of relativistic particles (photons and neutrinos) and the energy density Ω_Λ of the vacuum, then, the overall energy density Ω of the Universe can be defined as [7, 6]:

$$\Omega = \frac{\rho}{\rho_c} = \Omega_M + \Omega_\Lambda + \Omega_{rel}, \quad (1.3)$$

where ρ is the observed density and ρ_c is the critical density of the Universe. There are four possible implications of Equation 1.3, an empty Universe would have a zero Ω parameter and if $0 < \Omega < 1$, then the expansion of the Universe will continue forever. The Ω parameter for a collapsing Universe should be greater than unity but if there is enough mass in the Universe to stop the expansion of the Universe, one would expect the Ω parameter to be equal to unity. The results shown in Table 1.1 indicate that $\Omega = 1$. This implies that the dominant influence of the vacuum energy content results in the accelerated expansion rate of the Universe. The *Planck* results on dark energy

Table 1.1: Cosmological parameters measured by the *Planck* collaboration in 2015 [2].

Parameter	Value	Description
H_0	67.81 ± 0.92	Hubble constant in $\text{km s}^{-1} \text{Mpc}^{-1}$
Ω_Λ	0.692 ± 0.012	Dark energy density parameter
Ω_{DM}	0.258 ± 0.012	Dark matter density parameter
Ω_B	0.049 ± 0.002	Baryonic matter density parameter
$ \Omega_K $	< 0.005	Spatial curvature parameter
t_0	13.799 ± 0.038	Age of the Universe in Gyr

and the accelerated expansion of the Universe which is consistent with data from type Ia supernovae events are evidences for the existence of dark energy [8]. However, this thesis will focus on dark matter, hence, see Ref. [8] and references therein for more discussions on dark energy. It can be seen from Table 1.1 that the absolute spatial curvature $|\Omega_K|$ parameter of the Universe is approximately zero indicating that our Universe today is flat.

Different theoretical models have proposed various dark matter candidates in the last eight decades. But, leading dark matter candidates are thermal relics which were in thermal equilibrium with baryonic matter in the early Universe before their freeze-out [1, 9]. These thermal relics candidates are known as Weakly Interacting Massive Particles (WIMPs) which are not constituent of the Standard Model (SM) [1, 9, 10, 11].

The SM of particle physics (built on the gauge symmetry $SU(3) \times SU(2) \times U(1)$) has explained many concepts of nature but has failed to decipher the nature of the dark matter [1, 9, 12]. The summary of SM particles are shown in Figure 1.2. In that figure, u is used to represent the up quark, d is the down, c is the charm, s is the strange, t is the top while b is the bottom quark. Quarks are one of the two categories of fermions which are major constituents of baryonic matter. The second classification of fermions are leptons. These are shown as ν_e for electron neutrino, ν_μ is the muon neutrino, ν_τ is the tau neutrino, e is the electron, μ is the muon while τ is the tau particles in Fig-

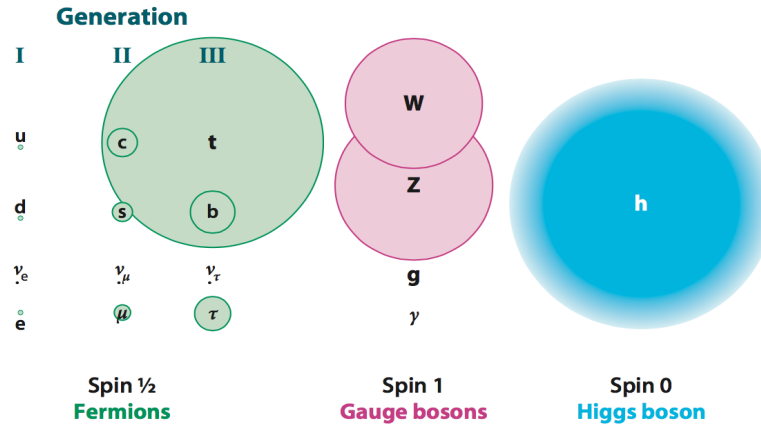


Figure 1.2: Particles of the standard model of particle physics [1].

Figure 1.2. Fermions have half-integer $(+\frac{1}{2}, -\frac{1}{2}, +\frac{3}{2}, -\frac{3}{2}, \dots)$ spin values and interact via four known mechanisms: strong, weak, electromagnetic and gravitational interactions. These interactions are mediated by integer $(0, 1, 2, \dots)$ spin particles known as gauge bosons. These gauge bosons are represented in Figure 1.2 as g for gluons which mediate strong interactions, W and Z for W^\pm and Z_0 bosons which mediate the weak interactions and γ for photons which mediate the electromagnetic interactions. The massive Higgs boson is shown as h in Figure 1.2. The mass of fermions, W^\pm and Z_0 bosons are generated due to their interactions with the Higgs boson [12, 13]. Higgs bosons induce these masses by slowing these particles down. There are also theoretical gravitons which are predicted as mediators of gravitational interaction. However, the gravitons are yet to be discovered and hence were not shown in Figure 1.2. None of these SM particles or theories can explain the dark matter problem. Hence, the need for a new physics beyond the SM.

Supersymmetry (SUSY) is a framework for new physics theories beyond the SM that has proffered solutions to the DM problem. SUSY models allow every SM particle to have a super-partner [1, 14]. These particle pairings in SUSY are done such that boson super-partners are assigned to fermions while fermion super-partners are assigned to bosons. The lightest SUSY particle known as the neutralino is a good WIMP candidate. For more on WIMPs and other dark matter candidates, see Section 1.3 while in the following section, various evidence for the existence of dark matter are

discussed.

1.2 Evidence for existence of dark matter in the Universe

There is now overwhelming evidence that a large fraction of the Universe is made up of non-baryonic dark matter. The main evidence for this is the topic of discussion in this section.

1.2.1 Velocity dispersion of galaxies in the Coma cluster

In 1933, Fritz Zwicky a Swiss observational astrophysicist attached to the California Institute of Technology observed that the mass of all the luminous matter in the constituent galaxies of the Coma cluster was too small to be consistent with their respective observed average velocities [13, 15]. This result was deduced using the virial theorem which states that the absolute potential energy GM^2/r of isotropically distributed matter in a gravitating galaxy cluster should be twofold greater than the observable kinetic energy $2M\langle v^2 \rangle$ of the cluster. The implication of this theorem is that the mass M of the given cluster of radius r can be defined as:

$$M = \frac{2r\langle v^2 \rangle}{G}, \quad (1.4)$$

where $\langle v^2 \rangle$ is the mean square velocity of the constituent matter in the cluster while G is the gravitational constant given by $6.67 \times 10^{-11} \text{ m}^3 \text{ kg}^{-1} \text{ s}^{-2}$. Substituting the observed values of $\langle v^2 \rangle$ and r in that equation for the Coma cluster, Zwicky discovered that more than 400 times the observed luminous mass were required to account for the observed gravitational effects. Then, he concluded that these missing mass are due to “dunkle materie” (German name for “dark matter”) in the Coma cluster. This was the first compelling evidence for the existence of gravitationally active non-luminous so-called DM [9, 15, 16].

1.2.2 Rotation curves of Galaxies

Further evidence for DM was found by Rubin and Ford in 1970 when they observed the rotational velocity of a satellite H1 cloud in Andromeda M31 galaxy [16]. H1 clouds are interstellar media made up of atomic hydrogen that emits radio radiations of 21 cm wavelengths at 1.42 GHz frequency with no other visible emissions. These radio radiations in the H1 clouds are due to relative effect of electron and nuclear spins on the 1s ground energy state of the abundant atomic hydrogen. The H1 clouds can only be detected by their unique 21cm radiation lines. The result from Rubin and Ford was achieved by measuring the doppler shift in the H1 clouds at various distances from the galactic centre [9, 16, 17, 18]. Andromeda is a spiral galaxy, the nearest galaxy to our own milky way galaxy. In a galaxy, a gas cloud of mass m can be related to the integral mass $M(r)$ of the galaxy within radial distance r using the Newtonian law of universal gravitation given by:

$$F_G = \frac{GmM(r)}{r^2}, \quad (1.5)$$

here $M(r)$ comes from the integral $4\pi \int_0^r \rho(r)r^2 dr$, where $\rho(r)$ is the mass density profile from the centre of the galaxy to the radial distance [9]. The F_G and G parameters in Equations 1.5 are the gravitational force of attraction between the galaxy and H1 cloud and the universal gravitational constant, respectively. To keep the H1 cloud of mass m in rotational motion about the galactic centre with velocity $v_{rot.}$, physical law requires the presence of a centripetal force F_c given by:

$$F_c = \frac{mv_{rot.}^2}{r}. \quad (1.6)$$

The magnitude of the centripetal force is expected to be about the same as the gravitational force existing between the H1 cloud and the galactic centre. Hence, equating Equations 1.5 and 1.6, the $v_{rot.}$ can be deduced as:

$$v_{rot.} = \sqrt{\frac{GM(r)}{r}}, \quad (1.7)$$

It can be seen from Equation 1.7 that the rotational velocity of the H1 cloud should decrease as $1/\sqrt{r}$. However, Rubin and Ford found that rotational velocity of the

galaxy approaches a constant at high r [9]. This result implies that $M(r) \propto r$ and $\rho \propto 1/r^2$ showing that there are populations of non-luminous matter at these high r regions of the galaxy. An example of this rotation curve is shown in Figure 1.3 for NGC 6503 dwarf spiral galaxy [19, 20]. In that figure, it can be seen that the

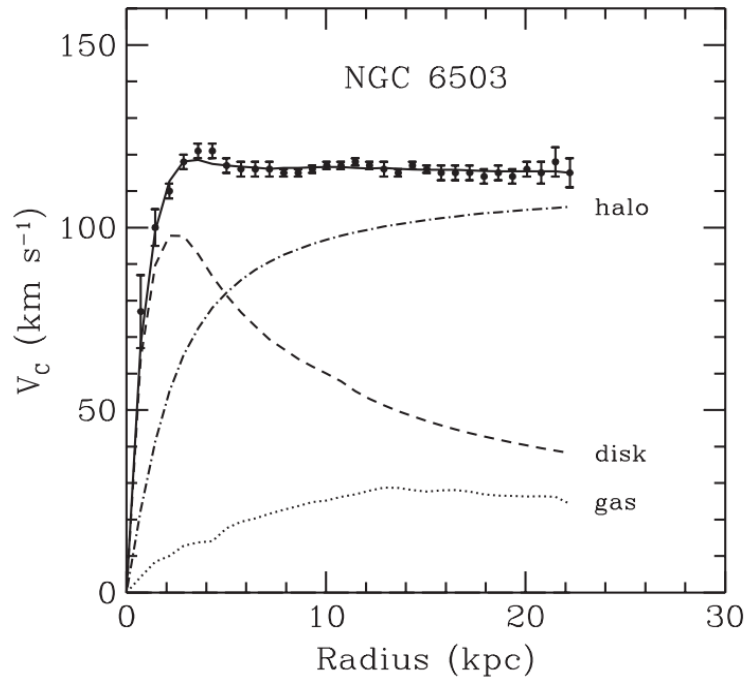


Figure 1.3: Rotational velocity of H1 clouds in NGC 6503 dwarf spiral galaxy shown as a function of their radial distance. The circular points with error bars are the observed data, the dashed line is theoretical expectation from luminous matter, the dotted line is expectations from gas clouds while the dash-dotted line is the theoretical expectation from a dark matter halo. The solid line that agrees well with the observational data is the sum of the contributions from the gas cloud, stellar disk and the dark matter halo [19].

measured rotational velocity (circular points with error bars) of H1 clouds at different radial distances of the galaxy deviated from theoretical expectations for only luminous matter (dashed line and marked as disk) especially at high r regions. The observed data shows that the H1 clouds at these high r regions were moving so rapidly contrary to theoretical predictions. It is also clear from this figure that individual contributions from only the gas component (dotted line) of the galaxy or contributions from only the theoretical dark matter halo (dash-dotted line) cannot explain the observed data. The

most consistent explanation of the observed data was determined by combining the expectations from each of these components of the galaxy. These results indicate the presence of a dark matter halo in galaxies. In Figure 1.3, the combined contribution from the gas, stellar disk and dark matter halo of the galaxy is shown with a solid line. Similar evidence for the existence of dark matter halo in the Universe was recently confirmed in the core of our own galaxy by Fabio Iocco and his group [21]. They were able to employ almost all available data from different compilations of the rotation curve measurements for the Milky Way galaxy.

Successful efforts have been made to explain these flat rotation curves observed at high r regions of galaxies without the assumption of a dark matter halo. One of these phenomenological theories is called the Modified Newtonian Dynamics (MOND) model proposed by an Israeli Physicist Mordehai Milgrom in 1983 [22]. The MOND model hypothesized that the acceleration a of objects orbiting galaxies are smaller than the threshold that can be accurately measured by an Earth bound observer thereby leading to violation of Newton's second law of motion. This violation was accounted for using:

$$F_N = ma\mu(a), \quad (1.8)$$

where F_N is the Newtonian force, m is the mass of the objects, $\mu = a/a_0$ and a_0 is a constant determined from observed rotation curves as $1.2 \times 10^{-10} \text{ m m}^{-2}$. Combining Equations 1.5 and 1.8, it can be determined that the acceleration a is given by:

$$a = \frac{\sqrt{GMa_0}}{r}. \quad (1.9)$$

When this is equivalent to the centripetal acceleration $a = v^2/r$, then the rotational velocity $v_{rot.}$ previously shown in Equation 1.7 can be defined in terms of MOND assumptions as:

$$v_{rot.} = (GMa_0)^{\frac{1}{4}}. \quad (1.10)$$

These predictions of MOND for $v_{rot.}$ explained the observed constant velocities for galactic objects at sufficiently large values of r . However, the MOND model was not generally accepted because it fails to explain all the details of the rotation curve and other galactic evidence for dark matter. For some of these observed concepts that the MOND model could not explain, see gravitational lensing and bullet clusters in

Sections 1.2.3 and 1.2.4, respectively.

1.2.3 Dark matter evidence through gravitational lensing

The laws of general relativity suggest that the presence of matter at any point in the Universe causes curvature of spacetime [23, 24]. This curvature can induce bends in the local paths of photons toward the lensing massive celestial object. For instance, a distant star can be a source of photons while the lensing object could be a dark matter halo in the local galaxy. These bent photons can converge on an Earth bound telescope to form false images of the distant star or elongated arc of the images [25, 26]. The observed images are formed by extending the path trace of these perturbed photons along their respective incident directions in a straight line. Depending on the number of photons that reach the telescope, many images of the star can be reconstructed. This is illustrated in Figure 1.4 with a massive celestial object acting as a gravitational lens surrounded by four lensed false images of a distant galaxy. In that figure the celestial



Figure 1.4: Four images of a gravitational lensed system in a galaxy scale structure. The massive celestial object acting as a lens is at the centre surrounded by four lensed images of a distant galaxy [27].

massive object can be seen surrounded by four lensed images of a distant galaxy.

In a rare case where the galaxy is perfectly aligned with the massive celestial object and with an Earth bound telescope such that photons can reach the observer from every direction, this results in a ring of images of the distant galaxy around the lensing object. This ring of images is known as Einstein ring [13, 25], see an example in Figure 1.5. For an Einstein ring to occur, the spacetime around the lensing object should be so



Figure 1.5: Einstein ring of a distant galaxy. The lensing galaxy can be seen in the middle surrounded by a ring of perturbed photons reaching the observer from a distant galaxy [28].

warped that photons can travel around it through multiple paths [27, 29]. The radius of the Einstein ring scales with the square root of the mass of the constituent matter in the lensing object. In practice, there are three types of gravitational lensing: strong, weak and micro lensing. The distinctions between these lensing methods depend on the size of the massive celestial object and positions of the lensing object relative to the source of photons and the observer. Massive concentrated celestial lensing objects and perfect alignment between the three components (source, lensing object and observer) are required in strong gravitational lensing leading to either multiple images of the source of photons or an Einstein ring [27, 29, 30]. In weak lensing, the general light

perturbation due to the presence of the massive celestial object can be observed without multiple images of the source of photons. This is because of poor alignment between the lensing components and small mass concentration of the celestial object. For micro lensing, the luminosity of the source and the mass concentration of the celestial objects are required to be smaller than the amount needed for strong and weak lensing to occur.

These gravitational lensing methods can be used to estimate the mass of objects in a galaxy cluster including the mass of dark matter [29]. The presence of dark matter in the halo of galaxy clusters have been affirmed using the observed perturbation on photons travelling through them [29, 30]. For instance, weak lensing has been used by the Sloan Lens ACS (SLACS) Survey collaboration [30] to determine the average mass density profile ($\rho(r) \propto 1/r^2$) of 22 galaxies covering a total distance of about 300 h^{-1} kpc. The SLACS result is consistent with presence of isothermal dark matter halo in the galaxies.

1.2.4 Bullet Cluster

The Chandra X-ray observatory found other compelling evidence for the existence of dark matter in the Bullet Cluster formed by the merger of two massive clusters known as IE 0657-56 [31, 32, 33]. During this energetic collision of the galaxy clusters, there was a temporary boost in their overall temperature and X-ray luminosity by more than a factor of 2 [33, 34, 35]. The boost in the X-ray luminosity of the Bullet Cluster made it an attractive site for X-ray astronomy. X-ray information from luminous baryonic matter in the Bullet Cluster shows high matter concentration in the cluster centre which is consistent with existence of dark matter. Overlaying the X-ray image on the projected mass obtained from strong gravitational lensing, revealed the presence of dark matter outside the central region as can be seen in Figure 1.6.

The X-ray data, which correlates to contributions from luminous matter is shown in red while the data from gravitational lensing, made up of all the matter in the cluster is shown in blue. It can be seen in Figure 1.6 that there is more luminous baryonic matter (shown in red) near the centre of the Bullet Cluster and more non-luminous dark matter (shown in blue) around the outer region. This is because the luminous baryonic matter from the two colliding clusters was slowed down as they interact while the non baryonic dark matter passes the centre of the cluster nearly unhindered, ahead of the

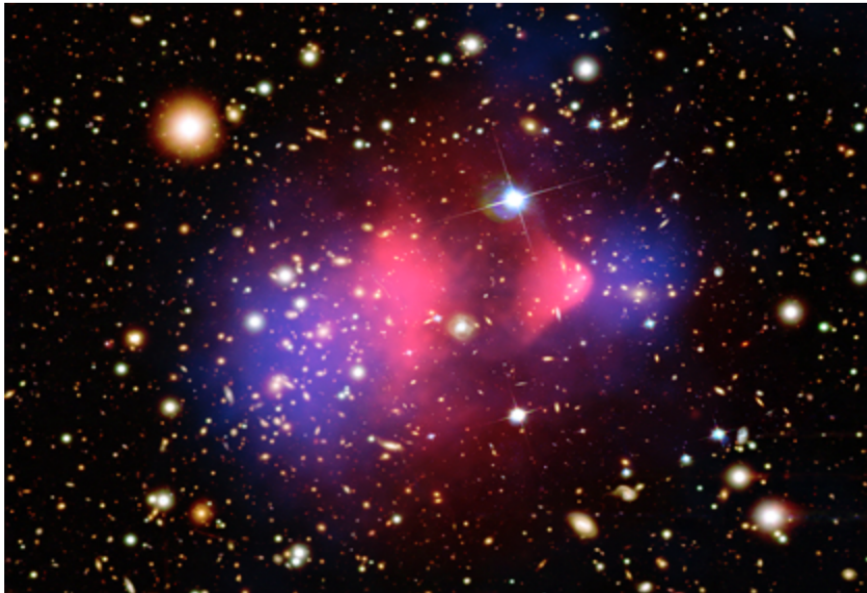


Figure 1.6: X-ray image of the Bullet Cluster. Luminous matter is in red while dark matter component is in blue. Credit: Chandra X-ray observatory.

baryonic matter subcluster. These results suggest the existence of non-luminous dark matter in the Bullet Cluster. This type of cluster merger with evidence of dark matter has also been found recently in smaller clusters, for instance in Abell 562, Abell 754, Abell 2146, Abell 2256, Abell 3888 etc [36].

Further results obtained from the Bullet Cluster show that about 30% of the dark matter content in the central part of the merged clusters vanished after the collision via self-interaction [37]. The mass-to-light ratio data obtained from the blue and red subclusters in Figure 1.6 with that of the main cluster have been used to set the most stringent constraint on the dark matter self-interaction cross section to mass ratio σ_{DM}/M_{DM} of $1 \text{ cm}^2 \text{ g}^{-1}$, equivalent to 1.8 b GeV^{-1} [34, 35]. Hence, the Bullet Cluster motivates a self-interacting particle dark matter with cross section and particle mass of σ_{DM} and M_{DM} , respectively. This produces a cross section that is consistent with weak scale interaction when M_{DM} is in GeV c^{-2} .

1.2.5 Big Bang Nucleosynthesis

Another fascinating evidence for the existence of dark matter can be seen by comparing the theoretical predictions of the Big Bang model for formation of light nuclei in the early Universe to the actual measurements [13, 38]. This study of formation of nuclei in the early Universe is known as Big Bang Nucleosynthesis (BBN). Free neutrons and protons (baryons) dominated the early Universe especially between 0.1 s to 10^4 s after the Big Bang [38, 39, 40]. The expansion mechanism of the Universe made the Universe cool, until the temperature was low enough to allow neutrons to combine with protons to yield deuterium (^2H or D). Deuterium combined with neutrons and fused with each other to form isotopes of Helium ^3He and more stable ^4He nuclei, respectively [38, 41]. Further combinations of the light elements then produced Lithium (^7Li), though in smaller abundances. These nuclear fusion processes were quenched about 20 minutes after the Big Bang due to temperature reduction as the Universe continued to expand [10, 41, 42]. The standard model of BBN predictions for abundance of different light elements in the Universe is shown as a function of baryon-to-photon ratio η (density of ordinary matter relative to photons) in Figure 1.7.

The expected abundance of $^4\text{He}/^1\text{H}$ is shown with a light green line while that of $^2\text{H}/^1\text{H}$ is shown with a blue line. The theoretical predictions for $^3\text{He}/^1\text{H}$ and $^7\text{Li}/^1\text{H}$ are overlaid in that plot with green and yellow lines, respectively. The points where the theoretical predictions agree with the WMAP measurements are shown with red circle lines. It can be seen there that the measured relative abundance for each of the considered elements has a common baryon-to-photon ratio η equivalent to the present day η value.

The present day baryon-to-photon density can be determined by considering the number density of photons η_γ . This η_γ parameter for a black body radiation is related to the temperature of the Universe as:

$$\eta_\gamma = 0.244 \times \left(\frac{KT}{\hbar c} \right)^3, \quad (1.11)$$

where $\hbar = h/2\pi$, h is the Planck constant given by 6.626×10^{-34} J s, c is the speed of light given by 2.998×10^8 m s $^{-1}$, then we take T to be equal to the present day temperature of the cosmic microwave background radiation given by $T_{CMBR} = 2.73^\circ\text{C}$ [2].

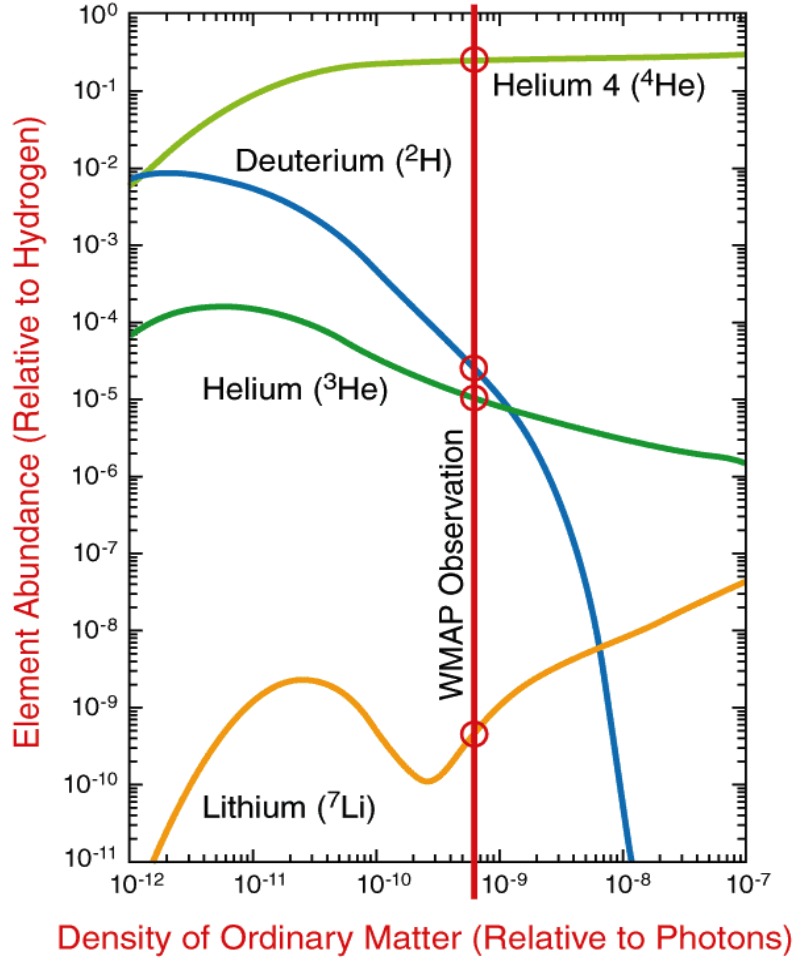


Figure 1.7: Standard model of BBN predictions for relative abundance of light elements shown as a function of present day baryon-to-photon ratio and compared to experimental measurements. The expected abundance of $^4\text{He}/^1\text{H}$, $^2\text{H}/^1\text{H}$, $^3\text{He}/^1\text{H}$ and $^7\text{Li}/^1\text{H}$ are shown with light green, blue, green and yellow lines, respectively. The red line that crosses each of the theoretical predictions shows the WMAP results. Points marked with red circle lines show agreement between the prediction and measurement. Credit: NASA/WMAP science team.

Then, the dimensionless baryon-to-photon ratio η can be determined using:

$$\eta = \frac{\eta_B}{\eta_\gamma} = 5.4 \times 10^{-10} \left(\frac{\Omega_B h_0^2}{0.02} \right) = 0.601 \times 10^{-9}, \quad (1.12)$$

where h_0 is the Hubble parameter given by:

$$h_0 = \frac{H_0}{100 \text{km s}^{-1} \text{Mpc}^{-1}}. \quad (1.13)$$

Here H_0 refers to the Hubble constant (see Equation 1.1) with its most recent value shown in Table 1.1 as obtained from Ref. [2]. The η_B parameter in Equation 1.12 is the number density of baryonic matter in the Universe while Ω_B , the baryon density parameter is defined as:

$$\Omega_B = \frac{\rho_B}{\rho_c}, \quad (1.14)$$

where ρ_B is the density of baryon in the Universe and ρ_c is the critical density (see Equation 1.3) of the Universe given by:

$$\rho_c = \frac{3H_0^2}{8\pi G}. \quad (1.15)$$

Using the 2015 data for $\Omega_B h_0^2$ obtained from Ref. [2], the η value today is about 6.01×10^{-10} , see Equation 1.12 for details. This is consistent with the results obtained by WMAP shown in Figure 1.7. Hence, from Equation 1.12, the number density Ω_B of baryonic matter in the Universe can be determined with the observed η value shown in Figure 1.7. This shows that the density parameter of normal baryonic matter in the Universe today is about 15% of the total matter content of the Universe. It is expected that the Ω_B in a Universe with only baryonic matter should be equal to Ω_M . However, results from these measurements show that about 95% of the total energy density of the Universe is made up of non baryonic dark matter and dark energy.

1.2.6 Cosmic microwave background (CMB)

The power spectrum of the 2.7K relics radiation known as the Cosmic Microwave Background (CMB) radiation can be used to constrain different cosmological parameters including the baryonic mass density Ω_B parameter of the Universe. This can be obtained from the measurement of temperature power spectrum of the relics radiation as it cools from the recombination epoch of the Universe which is $\sim 379,000$ years after the Big Bang. Observations of these CMB radiations are anisotropic or direction dependent mainly because of interaction of photons with surrounding hot gases

[2]. The structure of the cosmic microwave background anisotropy depends on the effect of acoustic oscillations due to non-unity of photon-to-baryon ratio and diffusion damping (i.e. collisionless damping) in the early Universe. This follows that the pressure from cosmic radiations do not support anisotropy but it is countered by gravitational effects from baryonic matter. The interplay between these two phases creates the acoustic oscillation that defines the resonance peak structure of the CMB. For example, these resonance peaks can be seen in the temperature power spectrum of the cosmic microwave background measured by the *Planck* mission [2] in Figure 1.8.

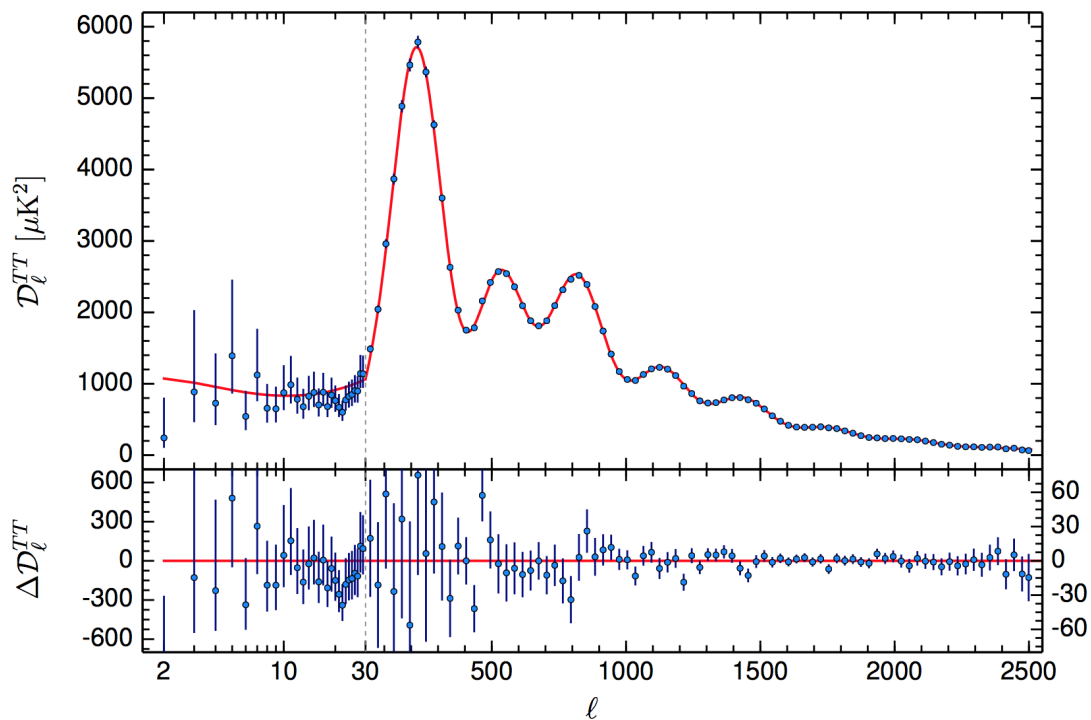


Figure 1.8: Temperature power spectrum (TT) data from *Planck* 2015 [2].

The upper panel of the figure shows the data obtained from the *Planck* (blue points) compared to the best fit from the theoretical predictions of Λ CDM model (red line) while the lower panel is the residual after the model fit. The Λ CDM model, also known as the standard cosmological model, describes an expanding flat Universe dominated by dark matter and cosmological constant Λ , that obeys the general relativity theory [43].

To make these measurements, the *Planck* collaboration divided the visible sky into

angular sizes such that the angle between the horizon and overhead of the telescope is 90° . These angular sizes are shown in terms of multipole moments ℓ in Figure 1.8. The angular size is inversely proportional to the multipole moment given by π/ℓ and expressed in degrees [44]. Then, the two-dimensional temperature fluctuation $T(\theta, \phi)$ in a given direction of the sky can be determined using [44]:

$$T(\theta, \phi) = \sum_{\ell=0}^{\infty} \sum_{\kappa=-\ell}^{\ell} a_{\ell\kappa} Y_{\ell\kappa}(\theta, \phi), \quad (1.16)$$

where θ and ϕ are elevation and azimuthal angles of the measurement directions, respectively. The $Y_{\ell\kappa}(\theta, \phi)$ parameter is the spherical harmonic of the visible sky in 2D defined as:

$$Y_{\ell\kappa}(\theta, \phi) = \sqrt{\frac{2\ell+1}{4\pi} \frac{(\ell-\kappa)!}{(\ell+\kappa)!}} P_{\ell}^{\kappa}(\cos\theta) e^{i\kappa\phi}, \quad (1.17)$$

where $\ell = 0, \dots, \infty$, $-\ell \leq \kappa \leq \ell$ and κ is the measurement mode parameter. Then, P_{ℓ}^{κ} and $e^{i\kappa\phi}$ are the associated Legendre Polynomials for expansion of the 2D spherical harmonics of the temperature fluctuation and the azimuthal parameter, respectively. The coefficient $a_{\ell\kappa}$ in Equation 1.16 is defined as:

$$a_{\ell\kappa}(\theta, \phi) = \int_{\theta=-\pi}^{\pi} \int_{\phi=0}^{2\pi} T(\theta, \phi) Y_{\ell\kappa}(\theta, \phi) d\Omega. \quad (1.18)$$

Then the power spectrum \mathcal{D}_{ℓ}^{TT} of the temperature fluctuations is given by:

$$\mathcal{D}_{\ell}^{TT} = \frac{\ell(\ell+1)C_{\ell}}{2\pi}, \quad (1.19)$$

measured in μK^2 (see observed data in Figure 1.8) where:

$$C_{\ell} = \frac{1}{2\ell+1} \sum_{\kappa=-\ell}^{\ell} \langle |a_{\ell\kappa}|^2 \rangle. \quad (1.20)$$

The position of the peaks in the temperature spectrum can be used to study primordial adiabatic perturbations and most importantly encodes information about different cosmological parameters. The first peak while moving from left to right in Figure 1.8 can be used to determine the curvature parameter of the Universe, the ratio of the second

peak to the odd peaks and that to the even peaks are used to determine the baryon density parameter while the third peak shows the abundance of dark matter in the Universe. Also, the information about density variations in the early universe (primordial density perturbation) is encoded in the positions of all the peaks. These results extracted from the plot in Figure 1.8 are shown in Table 1.1 which show that only 4.9% of the energy density of the Universe is baryonic matter while 25.8 % are made up of dark matter. It can be seen from Figure 1.8, that the plot in the lower panel is consistent with zero suggesting that the main result (shown in the upper panel) has good agreement with the theoretical predictions. This is yet another irresistible evidence that supports the existence of dark matter.

Similarly, future results from cosmic neutrino backgrounds (CνBs) measurements can be used to study the very early Universe, before the recombination epoch [45]. This is because CνBs decoupled at about one second after the Big Bang with a present-day temperature of $\sim 1.95\text{K}$. Efforts are underway to confirm the existence and measure these CνBs using electron neutrino captures in Tritium based detectors as in the proposed PTOLEMY [46] and KATRIN [45] experiments. The expected interaction rate of these events should result in about 56 electron-neutrinos per cm^3 . Successful observation of CνBs in the future will reveal more details about the dark matter content, nature and evolution of the expanding Universe.

1.2.7 Concluding remarks on the evidence for dark matter

So far, we have seen that there is compelling evidence to suggest that most of the matter content of the Universe is made up of non-baryonic DM. The results discussed in Sections 1.2.1 and 1.2.2 show that the mass of these DM in galaxies and galaxy clusters grow with radial distance suggesting the existence of a DM halo in galaxies and galaxy clusters. The gravitational effects of these DM masses were discussed in Section 1.2.3 which shows how they cause perturbation to the intrinsic paths of photons passing through them, thereby acting as lenses for the photon source. The Bullet Cluster discussed in Section 1.2.4 show the first clue on the physical nature of DM which motivates a self-interacting DM particles with a constraint on its possible cross section. The results from the measurements shown in Sections 1.2.5 and 1.2.6 further affirms the existence of DM with constraint on its abundance in the Universe. The

aim of the following section is to review the most likely dark matter candidates with characteristics that are consistent with the predictions and measurements in Section 1.2.

1.3 Dark Matter candidates

Non-successful dark matter candidates have been proposed in the past. These are Massive Compact Halo Objects (MACHOs) which are made up of planets, neutron stars, white dwarfs, black holes, primordial black holes etc [13, 47]. Progress made by different dark matter search groups in the past few decades with results from studies performed with data from the Bullet Cluster discussed in Section 1.2.4 and several theoretical studies have led to a consensus that dark matter should be in form of self-interacting particles. Different theoretically motivated dark matter candidate particles have been considered. They are grouped into hot, warm and cold dark matter candidates depending on their velocities when matter decoupled from radiation in the early Universe. Starting from the most viable candidates, these are Weakly Interacting Massive Particles (WIMPs), Lightest Supersymmetric Particles (LSP), Lightest Kaluza-Klein Particle (LKP), Axions, Gravitinos, Neutrinos, Sterile neutrinos, Heavy leptons, Non-topological solitons and Q-balls, QCD nuggets, Mirror matter and WIMPzillas [1, 13, 47, 48, 49, 50]. For details of the top two leading particle dark matter candidates, see Figure 1.9.

Relativistic particles such as neutrinos and sterile neutrinos are hot candidates while non-relativistic particles such as WIMPs, LSPs, LKPs, Axions etc are cold dark matter candidates. Hot dark matter candidates have been ruled-out because they do not support small scale gravitational clustering and formations in the Universe and hence, predicted the so-called “top-down” formation scheme [13, 47, 49]. In this hypothetical scheme, super clusters should have formed first and later break-up to form galaxies and other smaller objects in the Universe which is not consistent with expectations from the Large Scale Structure (LSS) formation [51] and the Big Bang theory. In the LSS studies, primordial density fluctuations determined from the CMB measurements were used to model how large structures formed in the Universe. Results from these simulations are consistent with predictions of the Big Bang theory which favour a “down-top” formation scheme [47, 51, 52, 53]. Also, hot dark matter candidates are not massive

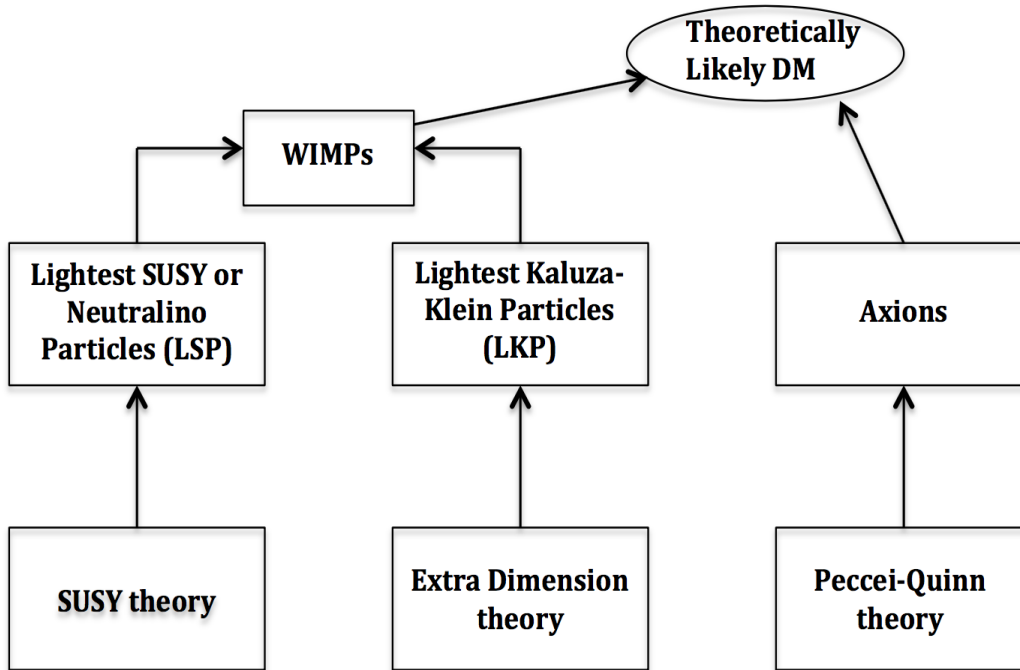


Figure 1.9: Theoretically favoured and leading dark matter candidates and their particle physics motivation.

enough to produce the gravitational effects that are observed from non-baryonic dark matter in the Universe [1, 13, 47, 49]. The rare case where particle candidates are neither hot nor cold in terms of their decoupling velocities in the early Universe, are referred to as warm candidates.

Thermal relic particles are most studied cold dark matter candidates because of their contributions in structure formation in the early Universe [1, 54, 47, 55, 56]. These particles were in thermal equilibrium with SM particles at very high temperatures in the early Universe via their annihilation to SM particles and vice versa. This equilibrium continued until the temperature T of the expanding Universe cooled and became less than M_{DM} . This caused an exponential increase in the dark matter annihilation process resulting in their decreased number density until when the rate of the dark matter annihilation dropped below the expansion rate of the Universe causing a freeze-out, see illustration in Figure 1.10. The rate of dark matter annihilation approached a constant after the freeze-out (see Figure 1.10). At this point, the thermal relic dark matter particles were isolated by the expanding Universe resulting in a re-

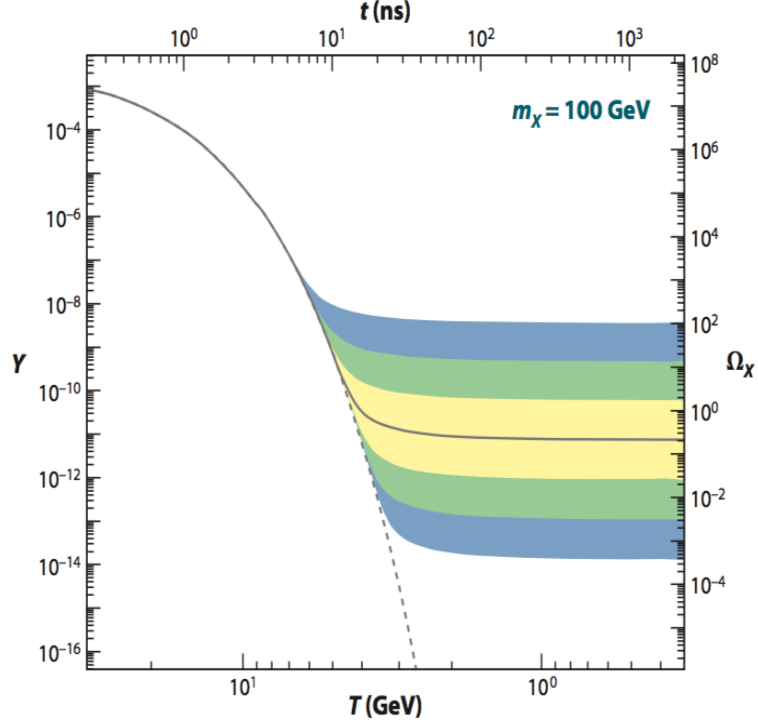


Figure 1.10: Comoving number density of dark matter density shown as a function of temperature, time and density of the expanding Universe. The solid line predicts the correct present-day thermal relic dark matter abundance using 100 GeV c^{-2} known as the WIMP miracle. Dotted line experienced no freeze-out, colours (from top to bottom) are results after the freeze-out mechanism as expected from weak to strong scale cross sections [1].

duced number density n_{DM} , hence, they can hardly interact with each other. Using the fact that the expected annihilation cross section σ_{av} of the thermal relics dark matter at freeze-out is inversely proportional to the dark matter abundance given by [54]:

$$\Omega_{DM} h_0^2 = \frac{n_{DM} M_{DM}}{\rho_c} \approx \frac{3 \times 10^{-27} \text{ cm}^3 \text{ s}^{-1}}{\langle \sigma_{av} \rangle}, \quad (1.21)$$

then, the observed $\Omega_{DM} h_0^2$ value of 0.119 ± 0.002 [2] can be used to constrain the mass and $\langle \sigma_{av} \rangle$ parameter, where v is the relative velocity of the particles. It was found that implementing Equation 1.21 for Weakly Interacting Massive Particles (WIMPs) motivated by supersymmetry reproduced the observed dark matter abundance in the

Universe. This dark matter abundance is shown for a 100 GeV c^{-2} WIMP with a solid line in Figure 1.10. Hence, WIMPs are the leading particle dark matter candidate as shown in Figure 1.9. They are predicted to be non-baryonic, neutral, colourless, stable, long-lived with appropriate thermal relic density of the Universe, negligible or no electromagnetic coupling and possible mass range of 10 GeV c^{-2} to 1 TeV c^{-2} [57, 58]. Also, they can interact weakly in pairs with standard model particles, for instance, via the Higgs boson as discussed in Refs. [59, 14].

It can be seen in Figure 1.9 that LSPs (also known as neutralinos) and LKPs are good WIMP dark matter candidates. They are motivated by the gauge hierarchy problems of the standard model of particle physics [1, 14, 60]. The gauge hierarchy problem deals with why the standard model of particle physics requires quantum corrections or fine tuning beyond the Planck scale [61, 62]. A typical example of the problem is why $m_h \sim 125 \pm 0.32 \text{ GeV c}^{-2}$, the physical mass of the Higgs boson is very small compared to the expected mass of $\sim \sqrt{\hbar c/G} \simeq 1.2 \times 10^{19} \text{ GeV c}^{-2}$. The supersymmetric theory (SUSY) solved this problem and on the process predicted the LSPs while extra dimension theory in the quest to solve this problem predicted the LKPs [14].

Axions comprise of other weakly interacting particles that do not match the WIMP framework. They were predicted by charge conjugation (C) and parity inversion (P) violation (CP violation) problems which are observed in strong interactions [1, 48]. Strong CP violation problems arise due to some complex relative phases of coupling constants in physical theories (for instance in Quantum Chromodynamics simply known as QCD). For example, CP-violation can occur in decay processes where two amplitudes that contribute to the decay rates tend to possess different coupling constant coefficients that are out of phase [42, 48]. The Peccei-Quinn symmetry [63] solved this problem and predicted light neutral particles called Axions which are now seen as a possible dark matter candidate [50]. Axions can couple to quarks using weak scale interaction mechanism. The strength of this interaction scales with the Axion mass. The known mass range of Axions is about $1 \mu\text{eV c}^{-2}$ to $1000 \mu\text{eV c}^{-2}$. It is expected that good Axion dark matter candidates should have a few $\mu\text{eV c}^{-2}$ mass and as a result, massive Axions emanating from the sun are not good dark matter candidates. Hence, these massive solar Axions with stronger coupling to quarks may be a major source of backgrounds in Axion dark matter search experiments. Also, the mass range of Axions in $\mu\text{eV c}^{-2}$ is small (depending on their abundance) to account for the observed energy

density of the non-baryonic matter in the Universe.

Another group of particles that have been considered as dark matter candidates are hypothetical Gravitinos which are super-partners of gravitons. These Gravitino dark matter candidates are problematic because they are required to be sufficiently heavy beyond $30 \text{ TeV } c^{-2}$, else theoretical predictions suggest that they would have decayed during or after the Big Bang Nucleosynthesis. This results in what is known as the Gravitino problem [9, 48, 64]. Also imposing the characteristics of the Lightest Supersymmetric Particles (LSP) on Gravitinos requires that their life-time should be stretched beyond the age of the Universe [64], which is not feasible thereby strengthening the Gravitino problems further. For details on other non-viable particle dark matter candidates see Refs. [1, 13, 14, 47, 48, 49, 50, 65].

The focus of the following chapters of this thesis will be on efforts toward detecting this most viable putative WIMP dark matter candidates.

1.4 Conclusion

In this chapter, the concept of non-baryonic dark matter was introduced, through a review of the matter content of the Universe using recent results from the *Planck* mission. In this review, the nature of the Universe was discussed in the context of measured energy density. More discussions were made using many observational results as prime evidence to support the existence of dark matter in the Universe. The failure of the standard model of particle physics in explaining the dark matter problem was discussed with some possible theoretical solutions motivated by SUSY and extra dimension models. Non-successful dark matter candidates that were predicted in the past decades were also discussed after which the most viable dark matter candidates known as the Weakly Interacting Massive Particles (WIMPs) were introduced. These WIMP candidates are most favoured because their mass and most of their physical properties are consistent with predictions from gravitational effects observed from non-baryonic dark matter in the Universe. In fact, expectations from WIMPs are consistent with the present-day thermal relic abundance and large scale structure formation. Hence, the following chapters of this thesis will focus on strategies and efforts toward detecting these putative WIMP dark matter particles.

Chapter 2

WIMP Detection and experimental searches

The first section in this chapter discusses different channels to WIMP detection which include direct detection, indirect detection and WIMP production in collider experiments. Theoretical formulations used in the direct detection WIMP search method are discussed in the following sections. These theoretical formulations are essential because other chapters of this thesis will focus on the direct detection method. Different methods used to reduce backgrounds in WIMP-search experiments are also presented. The last two sections of this chapter are dedicated to a review of progress and prospects of some experimental searches for the WIMP dark matter particle from around the world.

2.1 WIMP detection

In theory, there are three main methods through which an experimental physicist can search for WIMP (χ) dark matter particles. These methods include: direct detection, indirect detection and through χ production in collider experiments. Different experimental groups have built detectors to exploit each of these WIMP detection methods. The pictorial representation of these WIMP search windows are shown in Figure 2.1.

Direct WIMP detection experiments hope to detect nuclear recoil products due to a weak interaction between a standard model particle (for instance, within an atomic

2. WIMP Detection and experimental searches

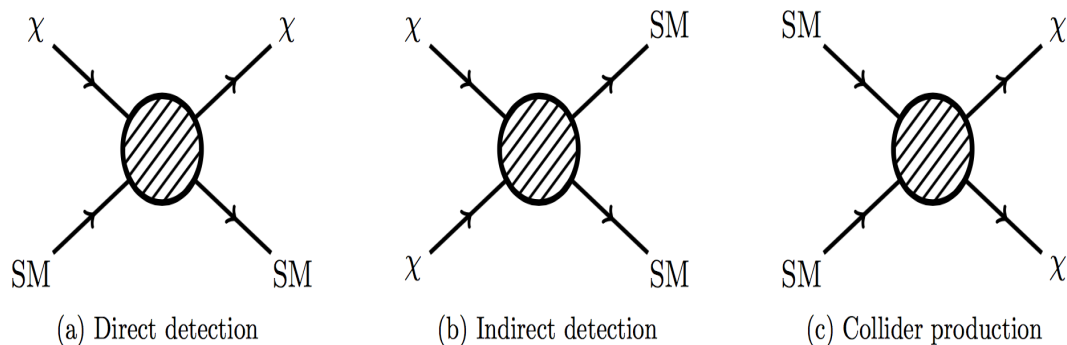


Figure 2.1: Possible search windows for WIMP dark matter particle.

nuclei used as target material in a detector) and the χ particle resulting in an elastic scattering process. In the interaction channels shown in Figures 2.1(a) to 2.1(c), the standard model particles are marked as SM while χ represents the WIMP particle. The shaded region in the illustrations shown in Figure 2.1 indicate that the interaction mechanisms of χ and SM particles are not fully understood. Many particle detectors designed to search for these type of interactions using the direct WIMP search method are located in different underground laboratories around the globe, see Section 2.2 for more details.

Indirect WIMP search groups utilise the theoretical prediction that the WIMP dark matter particle is a Majorana particle (super partner of itself), hence can annihilate at rest into mono-energetic (narrow range of energies) standard model particles [66, 67, 68, 69] which can be observed in conventional detectors. This method of searching for products of WIMP annihilation is regarded as indirect WIMP detection. This is illustrated in Figure 2.1(b). Typical examples of the expected mono-energetic SM particles from χ annihilation are neutrinos, gamma rays, protons and antiprotons, electrons and positrons and antideuterons [70, 71, 72, 73]. The first two WIMP annihilation signatures are widely favoured by indirect WIMP searches because they are stable and neutrally charged. For instance, the IceCube experiment [74, 75] has employed this method by searching for neutrinos generated by possible WIMP annihilation activities in the centre of the sun without major success. Also, no signature of WIMP annihilations were found in a joint analyses using gamma ray data from Fermi-LAT and MAGIC experiments for WIMPs of masses $10 \text{ GeV } c^{-2}$ to $100 \text{ TeV } c^{-2}$ [73]. The result

2. WIMP Detection and experimental searches

obtained from this analysis was used to set an upper limit of $3.4 \times 10^{-25} \text{ cm}^3 \text{ s}^{-1}$ on the expected average WIMP annihilation cross section at 95% confidence level in the relevant energy range [73]. This is the current most stringent global WIMP annihilation limit set by any gamma ray data analysis in the given mass range. In the lower mass range $< 100 \text{ GeV c}^{-2}$, the analysis excluded the thermal relic cross section for WIMP annihilation with $b\bar{b}$ and $\tau\bar{\tau}$ final states.

There are efforts aimed toward the production of WIMP dark matter particles in the Large Hadron Collider (LHC) which can be achieved by forcing two SM particles to interact [76, 77, 78, 79]. New particles are created in this type of process that follows $pp \rightarrow \bar{p}\bar{p}$ where pp represent two SM particles, accelerated with high energy such as in the LHC while $\bar{p}\bar{p}$ are products of the interaction. This is known as WIMP production hence, the collider experiment can be regarded as a WIMP factory if it ever succeeds in this quest. This is illustrated for the hypothetical WIMP dark matter production in the LHC in Figure 2.1(c). It is expected that any associated WIMP particle in these interactions should elude the detector leaving a missing transverse momentum P_T and energy E_T^{miss} signatures. In addition to these signatures, corresponding recoiling SM photons and jets of quarks, gluons, W^+ , W^- and Higgs boson oriented in the opposite direction of the WIMP signature can be observed as part of the final state [76, 80, 81]. Mainly, s and t -channel interactions with spin 0 or 1 mediators are used in LHC based WIMP search analyses [81]. However, at the time of writing this thesis, the LHC has not succeeded in detecting the supersymmetric neutralino or any other particle predicted by supersymmetry [76, 79]. In 2015, the ATLAS collaboration of the LHC analysed data [82] generated with 20.3 fb^{-1} of integrated luminosity at 8 TeV centre of mass energy for s -channel interaction commonly known as the \sqrt{s} parameter. In the analyses, simplified Effective Field Theory (EFT) assumptions were adopted resulting in higher detector sensitivity to lower WIMP mass of $< 10 \text{ GeV c}^{-2}$. The results show the detector sensitivity for the spin-dependent and spin-independent WIMP-nucleon cross sections of 2.12 ab and 7.13 zb, respectively, for WIMPs of 1 GeV c^{-2} mass at 90% confidence level. This is assuming that the WIMP dark matter particle is a Dirac fermion (Majorana particle) that can be produced in qq interactions with tensor (scalar) couplings to quarks in the spin-dependent (spin-independent) analyses [82].

The following sections of this thesis discusses theoretical formulations, experimental methods and global efforts toward the detection of the WIMP dark matter particles

from the direct WIMP search channel.

2.2 Direct WIMP detection

Direct WIMP search experiments run in subterranean laboratories in order to shield detectors from cosmic backgrounds. These experiments aim to detect nuclear recoils induced by WIMPs that are elastically scattering off target nuclei. It is customary for direct WIMP search experiments to exclude a range of WIMP cross section and WIMP mass in the allowed parameter space after searching for WIMPs for a given period without recording a positive signal. In the following section we will discuss how such exclusion limits are determined in a WIMP search experiment.

2.3 WIMP theoretical event rates in direct detection

There is enough evidence to believe that the WIMP dark matter particles can interact with conventional matter through either gravitational interaction or weak-scale cross section [83]. Direct WIMP search experiments share similar basic theoretical frameworks toward detecting WIMP-induced nuclear recoils. The expected differential event rate for WIMP-induced nuclear recoils is formulated based on existing WIMP models [84, 85]. Due to variations in target materials, threshold, sensitivity etc used/achieved by different detectors, a WIMP search window is defined for every detector. This is with a range of detectable WIMP masses M_W and corresponding WIMP-nucleon cross sections σ_{WA} . The scalar case of this cross section σ_{WA}^{SI} is spin-independent (SI) while the axial vector case σ_{WA}^{SD} is spin-dependent (SD) depending on the target material used in the experiment. Target nuclei with odd proton numbers (for instance ^{19}F) are known to have non-zero spin J values and are used in the SD WIMP search experiments. These theoretical parameters needed for setting WIMP detection limits are subject of the following section. The parameters derived in this chapter will be employed in Chapter 5 to set a detection limit using data from a direct WIMP search experiment.

2.3.1 Expected rate of WIMP events

If a WIMP dark matter particle travelling with velocity v enters a detector of volume L^3 which contains N number of uniformly distributed target nucleons. It will take this WIMP particle a total of L/v seconds to traverse the length L of the detector. Taking σ to be the individual nucleon cross section, the total nucleon cross section in the detector is given by $N\sigma$. Therefore, the expected number of WIMP interactions N_i in the detector is the ratio of the total nucleon cross section per unit area given by $N_i = N\sigma/L^2$. The rate R_s at which a single WIMP interacts in the detector is the N_i per unit time, given by [86]:

$$R_s = \frac{N\sigma}{L^2} \times \frac{v}{L} = \frac{Nv\sigma}{L^3}. \quad (2.1)$$

Assuming that the density of the WIMP dark matter halo is $\rho_W = 0.3 \text{ GeV c}^{-2} \text{ cm}^{-3}$ [84] for a WIMP of mass M_W in GeV c^{-2} . The dimensionless number of nucleons N in Equation 2.1 can be expressed in terms of the Avagadro's number N_A (in atoms kg^{-1}) and the total detector mass M_D using $N = 10^3 M_D(\text{kg})N_A$. Substituting this into Equation 2.1, the rate for a single WIMP interaction in the detector can be written as:

$$R_s = \frac{10^3 M_D N_A v \sigma}{L^3}. \quad (2.2)$$

Then, the expected number of WIMP dark matter particles per cm^3 becomes ρ_W/M_W or $10^6 \rho_W/M_W$ per m^3 . Hence, the expected number of WIMPs N_W in a detector of volume L^3 as in the detector used in the work presented in Chapter 5 becomes:

$$N_W = \frac{10^6 L^3 \rho_W}{M_W}. \quad (2.3)$$

Therefore the total classical WIMP interaction rate R_r (rate of WIMP induced nuclear recoils) in the detector, assuming no nucleon binding and that all the WIMPs have a uniform velocity, R_r can be expressed by combining Equations 2.2 and 2.3 as shown below:

$$R_r = R_s \times N_W = \frac{10^9 M_D N_A \rho_W v \sigma}{M_W}. \quad (2.4)$$

2. WIMP Detection and experimental searches

However, experiments can measure the rate R at which WIMPs of different energies interact with target nucleon which can be determined by integrating R_r over the allowed recoil energy window using:

$$R = \int_{E_r=E_{min}}^{E_r=E_{max}} \frac{dR_r}{dE_r} dE_r, \quad (2.5)$$

where E_r is the detectable recoil energy in a given detector with values ranging from a minimum value E_{min} to a maximum recoil energy E_{max} and dR_r/dE_r is the differential event rate of the WIMP-nucleon interaction. Since the rate R scales with the differential event rate as shown in Equation 2.5, Section 2.3.2 is used to determine the corrected dR_r/dE_r parameter, considering contributions from the WIMP halo velocity distribution, the nuclear spin and form factor of target materials.

2.3.2 Expected WIMP differential rate

The differential interaction rate dR_r/dE_r can be defined in terms of the probability density $p(E_r)$ that a WIMP in the detector can induce a recoil of energy E_r , this is following discussions in Ref. [84] and references therein. The definition is given by:

$$\frac{dR_r}{dE_r} = R_r p(E_r). \quad (2.6)$$

For a WIMP particle interacting with a target nuclei of mass M_A in the centre of mass frame by inducing a recoil of energy E_r which can be defined as [86]:

$$E_r = \frac{\mu^2 v^2}{M_A} (1 - \cos \theta). \quad (2.7)$$

This is assuming that the WIMP scatters with a scattering angle of θ after its interaction with the target nucleus in the centre of mass frame. From Equation 2.7, E_r becomes equal to E_{min} when θ is 0. Then, the maximum recoil energy E_{max} will be observed when the WIMP particle collides head-on with the target, then θ becomes equal to

2. WIMP Detection and experimental searches

180°. In that context, Equation 2.7 reduces to

$$E_{max} = \frac{2\mu^2 v^2}{M_A}, \quad (2.8)$$

where M_W is equal to M_A , Equation 2.8 becomes $M_W v^2/2$ which is the best case for E_{max} . The μ parameter is the WIMP-nucleon reduced mass given by:

$$\mu = \frac{M_W M_A}{M_W + M_A}. \quad (2.9)$$

A typical WIMP-nucleon reduced mass μ is 15.04 GeV c^{-2} for a 100 GeV c^{-2} WIMP traveling with a speed of 230 km s^{-1} ($7.667 \times 10^{-4} \text{ c}$). This WIMP particle can scatter off from a target fluorine (^{19}F) nuclei of mass $0.932 \times A$ (17.71 GeV c^{-2}) in a given detector, inducing a nuclear recoil with maximum energy E_{max} of $\sim 15.03 \text{ keV}$ to the target. The factor 0.932 GeV c^{-2} in the atomic mass conversion to GeV c^{-2} units is equivalent to the proton mass. The WIMP-nucleon reduced mass for different target nuclei used in WIMP search experiments are shown as a function of WIMP masses in Figure 2.2. These results are compared to contributions from one atomic proton in a target nuclei. It can be seen in that figure that the reduced mass reaches a constant at high WIMP masses for each of the nuclei. The reduced mass effect increases with target mass as predicted by Equation 2.9 resulting in the observed minimum reduced mass effect for the WIMP-proton interactions. Assuming that the probability density $p(E_r)$ for these WIMP interactions in a given detector can be defined as:

$$p(E_r) = \frac{M_A}{2\mu^2 v^2}. \quad (2.10)$$

See Refs. [84, 86, 87, 88] for more discussions on the probability density parameter. It can be seen in equation 2.10 that the probability density $p(E_r)$ is independent of the recoil energy of the target nucleus which implies that there exist equal probability for an interaction to produce a recoil energy in the range of E_{min} and E_{max} . Hence, the differential rate can be re-written in terms of measurable quantities by substituting

2. WIMP Detection and experimental searches

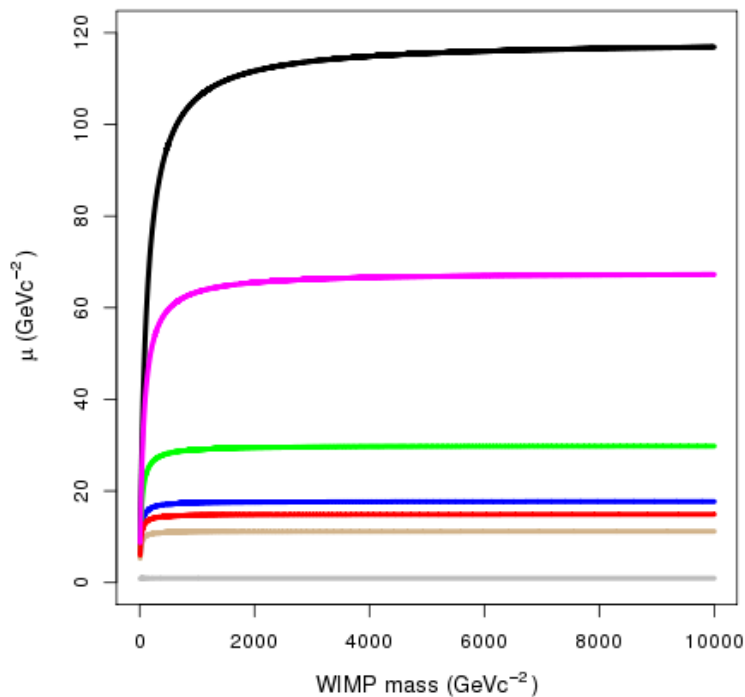


Figure 2.2: WIMP-nucleon reduced mass μ obtained from various target nuclei shown as a function of WIMP mass and compared to contributions from one atomic proton. The black, pink, green, blue, red, tan and grey lines show results from ^{127}I , ^{73}G , ^{32}S , ^{19}F , ^{16}O , ^{12}C nuclei and from one atomic proton, respectively.

Equations 2.4 and 2.10 in 2.6 to obtain:

$$\frac{dR_r}{dE_r} = \frac{10^9 M_D N_A \rho_W \sigma M_A}{2\mu^2 v M_W}. \quad (2.11)$$

It can be seen that Equation 2.11 does not consider contributions from the velocity distribution of the WIMP halo and contributions from nuclear physics of the target nuclei. The following few sections will be used to determine the velocity distribution and nuclear physics contributions which are used to determine the effective differential rate in an ideal WIMP search detector.

2. WIMP Detection and experimental searches

2.3.3 WIMP velocity distribution

Assuming that the velocity distribution $f(v)$ of the WIMP dark matter halo is Maxwellian (obeys Maxwell-Boltzmann distribution) [86], the $1/v$ parameter in Equation 2.11 can be defined as:

$$\frac{1}{v} \approx \int_{v_{min}}^{v_{esc}} \frac{f(v)}{v} dv, \quad (2.12)$$

where v is expected to take any value between v_{min} and v_{esc} . The Maxwell-Boltzmann velocity distribution $f(v)$ is thus defined as:

$$f(v) = \frac{4\pi v^2}{\left(\frac{2\pi}{3}\right)^{\frac{3}{2}} v_{rms}^3} e^{-\frac{3v^2}{2v_{rms}^2}}, \quad (2.13)$$

where $v_{rms} = v_0 \sqrt{\frac{3}{2}}$ and v_0 is the average circular velocity of galactic objects in the WIMP halo. This can be taken as $243 \pm 7 \text{ km s}^{-1}$, equivalent to $0.81 \pm 0.02 \text{ mc}$ [86, 87] (where $1 \text{ mc} = 10^{-3} \text{ c}$), then in terms of v_0 , Equation 2.13 becomes:

$$f(v) = \frac{4\pi v^2}{\pi^{\frac{3}{2}} v_0^3} e^{-\frac{v^2}{v_0^2}}. \quad (2.14)$$

Substituting Equation 2.14 in 2.12, the resultant equation obtained can be simplified by taking $v_{min} = \sqrt{\frac{M_A E_r}{2\mu^2}}$ which can be evaluated to obtain $7.667 \times 10^{-4} \text{ c}$. Then, the v_{esc} parameter is the escape velocity of the halo assumed to be $544_{-46}^{+64} \text{ km s}^{-1}$ ($1.813_{-0.15}^{+0.21} \text{ mc}$) to ∞ [84, 86, 87, 89, 90]. Therefore the integral in the right hand side of Equation 2.12 can be evaluated to obtain:

$$\frac{1}{v} \approx \int_{v_{min}}^{\infty} \frac{f(v) dv}{v} = \frac{2}{v_0 \sqrt{\pi}} e^{-\left(\frac{v_{min}}{v_0}\right)^2}. \quad (2.15)$$

Hence, the differential event rate can then be presented in terms of Equation 2.15 as:

$$\frac{dR_r}{dE_r} = \frac{10^9 M_D N_A \rho_W \sigma M_A}{2\mu^2 M_W} \times \frac{2}{v_0 \sqrt{\pi}} e^{-\left(\frac{v_{min}}{v_0}\right)^2} \quad (2.16)$$

2. WIMP Detection and experimental searches

The above definition of the differential event rate can be simplified by substituting Equation 2.4 in 2.16 to obtain:

$$\frac{dR_r}{dE_r} = R_r \frac{M_A}{\mu^2 v_0^2 \sqrt{\pi}} e^{\left(\frac{-v_{min}}{v_0}\right)^2} \quad (2.17)$$

Equations 2.17 and 2.16 are definitions for the theoretical differential rate for an isothermal WIMP halo being probed by stationary Earth bound detectors (i.e. stationary relative to the galactic frame) as the galactic escape velocity v_{esc} approaches ∞ .

2.3.4 Nuclear form factor correction

The nuclear form factor measures the expected momentum-dependent response of the target nuclei after interacting with the WIMP dark matter particle. For fluorine (^{19}F) target nucleus interacting with a 100 GeVc^{-2} WIMP, it is expected that the total momentum q transferred to the target nucleus is given by [84]:

$$q = \sqrt{2M_A E_r} = 23 \text{ MeV c}^{-1}. \quad (2.18)$$

This transferred momentum can be represented in terms of the de Broglie wavelength λ of the WIMP dark matter particle, defined by:

$$\lambda = \frac{2\pi\hbar}{q}, \quad (2.19)$$

where \hbar is $h/2\pi$ and h is the the Planck constant given by $4.136 \times 10^{-15} \text{ eV s}$. Substituting Equation 2.18 in 2.19, we obtain a de Broglie wavelength of 54 fm for a 100 GeVc^{-2} WIMP, travelling with a velocity of 230 km s^{-1} after scattering off from a ^{19}F nucleus target. This λ parameter is expected to be far greater than the nuclear radius of the ^{19}F nucleus, given by:

$$r_n \approx a_n A^{\frac{1}{3}} \approx 3.2 \text{ fm}, \quad (2.20)$$

2. WIMP Detection and experimental searches

where a_n is 1.2 fm and A is 19 for the ^{19}F nucleus. Figure 2.3 shows a dimensionless $qr_n/\hbar c$ parameter for different target nuclei used in various WIMP search experiments as a function of recoil energies. The $\hbar c$ parameter is given by 197.3 MeV fm as shown

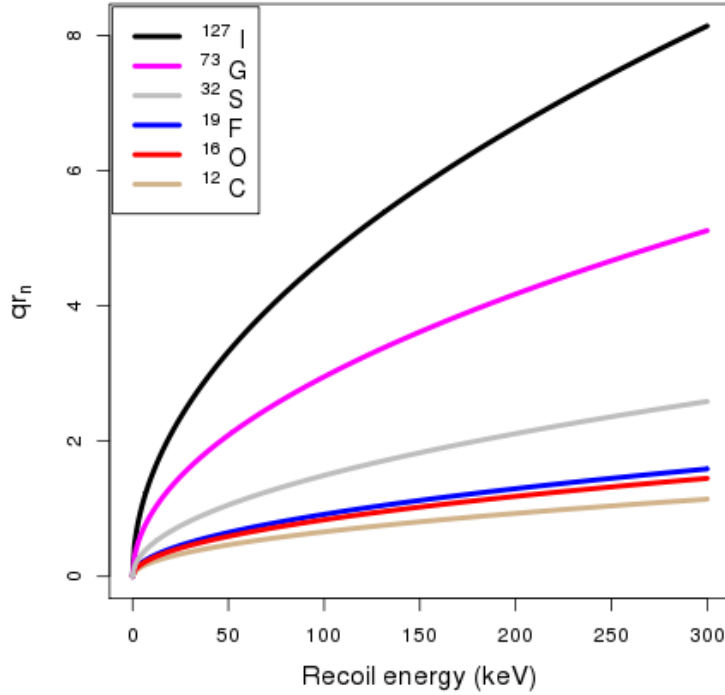


Figure 2.3: Momentum dependent nuclear form factor parameter obtained for some of the target nuclei used in WIMP search experiments. The black, pink, grey, blue, red and tan lines show results from ^{127}I , ^{73}G , ^{32}S , ^{19}F , ^{16}O and ^{12}C nuclei, respectively.

in Ref. [84]. It can be seen in Figure 2.3 that the dimensionless qr_n parameter increases with the atomic mass of the target nuclei. Hence, in that figure, the maximum values of the dimensionless qr_n parameter was obtained for ^{127}I nucleus while the minimum values were obtained for ^{12}C nucleus as predicted in Equation 2.18. Comparing Equations 2.20 and 2.19, it can be seen that the value of r_n is about only an order of magnitude less than the λ parameter obtained in Equation 2.19 for ^{19}F nuclei. This indicates that more corrections are needed on the hard sphere approximation (assuming no nucleon binding) done so far to be able to validate the differential event rate of the WIMP-

2. WIMP Detection and experimental searches

nucleon interaction mechanism. Hence, the nuclear form factor $F^2(qr_n)$ correction can be added to Equation 2.17, by substituting σ with a fraction of its corresponding zero momentum transfer cross section σ_0 , given by [84, 91, 92]:

$$\sigma = F^2(qr_n)\sigma_0 \quad (2.21)$$

In particular, the nuclear form factor $F^2(qr_n)$ can be studied in terms of WIMPs coupling with nuclear spin J of a target nuclei, for instance, the J value for the ^{19}F nucleus is $1/2$. This nuclear spin correction is essential because some theoretically motivated WIMP candidates do not have a scalar coupling in the neutralino-neutron lagrangian [91]. The DRIFT-II detector described in Section 2.8.4 uses ^{19}F targets to probe this important spin-dependent (unpaired nucleon case: for ^{19}F , a single unpaired proton) WIMP interaction. For details on the SD WIMP-nucleon interaction with ^{19}F target, see Section 2.4. Considering that a WIMP particle can scatter off a ^{19}F nucleus as a plane wave, we adopt the first Born approximation and define the $F^2(qr_n)$ parameter as a Fourier transform of the scattering distribution density, given by [84, 91]:

$$F^2(qr_n) = j_0^2(qr_n), \quad (2.22)$$

where j_0 is a Bessel function of the first kind, defined as:

$$j_0(\theta) = \frac{\sin(\theta)}{\theta}. \quad (2.23)$$

Though, a commonly used and more detailed approximation of Equation 2.22 has been proposed for the experimental useful range of $0 < qr_n \leq 4.5$ in the SD WIMP-nucleon interactions as described in Ref. [91, 93]. This is using the so-called *odd-group* model, defined as:

$$F^2(qr_n) = \begin{cases} j_0^2(qr_n) & (\text{if: } qr_n < 2.55 \text{ and } qr_n > 4.5), \\ a \text{ constant } \approx 0.047 & (\text{if: } 2.55 \leq qr_n \leq 4.5). \end{cases} \quad (2.24)$$

2. WIMP Detection and experimental searches

This nuclear form factor effect is expected to be stronger for heavy WIMPs or heavy target nucleus as shown in Figure 2.4. In this figure, the nuclear form factor parameter

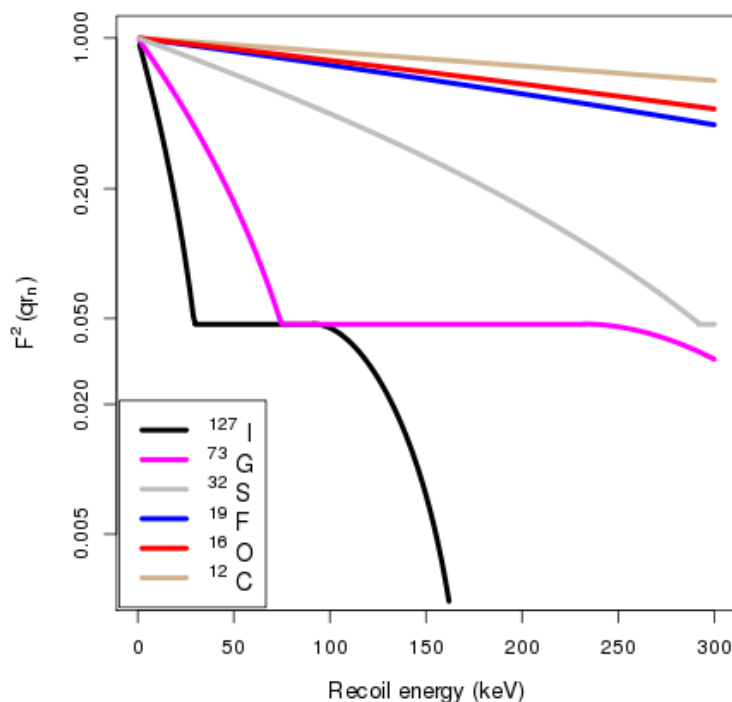


Figure 2.4: Nuclear form factor obtained for different target nuclei used in WIMP search experiments shown as a function of WIMP recoil energies. The black, pink, grey, blue, red and tan lines show the nuclear form factor effect in ^{127}I , ^{73}G , ^{32}S , ^{19}F , ^{16}O and ^{12}C nuclei, respectively.

is shown as a function of WIMP recoil energies obtained for various target materials used in WIMP search experiments. It can be seen in Figure 2.4 that the maximum and minimum nuclear form effects were observed for the ^{127}I and ^{12}C nuclei, respectively. This shows that indeed the nuclear form factor effects decrease with the mass of the target material. There are many other methods in the literature which can be used to estimate the $F^2(qr_n)$ parameter, these methods can be found in Refs. [91, 92, 94, 95, 96] but the difference between results that are obtained from each of these methods is small [97]. Empirically, it is more convenient to write the $F^2(qr_n)$ parameter as a function of nuclear recoil energy using $F^2(E_r)$. This is because the nuclear form factor

effects are reconstructed using Equation 2.18 [98].

2.4 WIMP-nucleon cross section

To be able to compare results on the WIMP-nucleon cross section σ_{WA} as obtained from different direct WIMP search experiments using different target materials, it is useful to represent σ (see equation 2.17) in terms of free target nucleons (proton or neutron). This can be achieved using the model-independent technique discussed in Ref. [85], provided there is an odd number of protons and an even number of neutrons in the target nuclei (e.g. excess proton in fluorine nucleus) or vice versa. One assumption of this technique is that the WIMP-proton cross section σ_{WP} is expected to be approximately equal to the WIMP-nucleon cross section σ_{WA} , assuming that the proton dominates the ^{19}F nucleus. Then the total WIMP-nucleon cross section is defined by [85, 99]:

$$\sigma_{WA} = \left(\sqrt{\sigma_{WP}} + \sqrt{\sigma_{WN}} \right)^2, \quad (2.25)$$

where σ_{WP} and σ_{WN} , the WIMP-proton and WIMP-neutron cross sections are defined in Refs. [85, 99, 54] as:

$$\sigma_{WP} = 4G_F^2 \mu_P^2 C_{WP}, \quad (2.26)$$

and

$$\sigma_{WN} = 4G_F^2 \mu_N^2 C_{WN}, \quad (2.27)$$

respectively, where G_F is the Fermi coupling constant given by $1.16637 \times 10^{-5} \text{ GeV}^{-2}$ [100], μ_P (μ_N) is the proton (neutron) reduced mass which can be defined by setting $A = P$ ($A = N$) in Equation 2.9 for the WIMP-proton (WIMP-neutron) interaction. The C_{WP} and C_{WN} parameters are the contributions of proton and neutrons to the total enhancement factor C_{WA} of a given target nucleus, which are defined by:

$$C_{WA} = \frac{8}{\pi} \left(|a_p \langle S_p \rangle| \pm |a_n \langle S_n \rangle| \right)^2 \frac{J+1}{J}, \quad (2.28)$$

where

$$C_{WP} = \frac{8}{\pi} \left(|a_p \langle S_p \rangle| \right)^2 \frac{J+1}{J}, \quad (2.29)$$

2. WIMP Detection and experimental searches

and

$$C_{WN} = \frac{8}{\pi} (|a_n \langle S_n \rangle|)^2 \frac{J+1}{J}. \quad (2.30)$$

These relationships hold where a_p and a_n are the effective WIMP-proton and WIMP-neutron couplings predicted theoretically by the WIMP model under consideration. The S_p and S_n are expectation values of the proton and neutron spins respectively. But σ_{WP} and σ_{WN} are not measured cross sections, they are theoretical quantities that are used to identify the proton and neutron contributions to the total WIMP-nucleon cross section σ_{WA} . These can be related to the effective WIMP-proton $\sigma_{WP}^{eff.}$ and WIMP-neutron $\sigma_{WN}^{eff.}$ cross sections with an assumption that the WIMP-nucleon cross section is dominated by σ_{WP} (i.e. when $\sigma_{WP} \approx \sigma_{WA}$) using:

$$\frac{\sigma_{WP}^{eff.}}{\sigma_{WA}} = \frac{4G_F^2 \mu_P^2 C_P}{4G_F^2 \mu^2 C_{WA}}. \quad (2.31)$$

After factorisation, we obtain from Equation 2.31 that:

$$\sigma_{WP}^{eff.} = \sigma_{WA} \frac{\mu_P^2 C_P}{\mu^2 C_{WA}}. \quad (2.32)$$

where $C_P = 6a_p^2/\pi$ and similarly, $C_N = 6a_n^2/\pi$. Then, for the WIMP-proton interaction, the ratio C_{WA}/C_P can be obtained using Equation 2.28, when $C_{WP} \approx C_{WA}$, we write:

$$\frac{C_{WA}}{C_P} = \frac{8}{\pi} (a_p^2 \langle S_p \rangle^2) \times \frac{J+1}{J} \times \frac{\pi}{6a_p^2}. \quad (2.33)$$

This can be simplified by factorisation to obtain:

$$\frac{C_{WA}}{C_P} = \frac{4}{3} \langle S_p \rangle^2 \frac{J+1}{J}. \quad (2.34)$$

Substituting Equation 2.34 in 2.32, then the effective SD WIMP-proton cross section becomes:

$$\sigma_{WP}^{eff.} = \sigma_{WA} \frac{\mu_P^2}{\mu^2} \left(\frac{4}{3} \langle S_p \rangle^2 \frac{J+1}{J} \right)^{-1}. \quad (2.35)$$

2. WIMP Detection and experimental searches

Combining Equations 2.21 and 2.35, the σ_{WA} can be written in terms of the nuclear form factor as:

$$\sigma_{WA} = \sigma_{WP}^{eff} F^2(E_r) \frac{4\mu^2}{3\mu_p^2} \langle S_p \rangle^2 \frac{J+1}{J}. \quad (2.36)$$

Hence, assuming that $\sigma_{WA} \approx \sigma$, then, Equation 2.36 can be substituted in Equation 2.17 to obtain the effective theoretical differential event rate in terms of measurable quantities. This is given by:

$$\frac{dR_r^{SD}}{dE_r} = 10^9 N_A M_D M_A \cdot \frac{4}{3} \langle S_p \rangle^2 \frac{J+1}{J} \cdot \frac{F^2(E_r) \sigma_{WP}^{eff}}{M_W \mu_p^2} \cdot \frac{\rho_W}{v_0 \sqrt{\pi}} e^{\left(\frac{-v_{min}}{v_0}\right)^2}. \quad (2.37)$$

The dR_r^{SD}/dE_r parameter is measured in $s^{-1} \text{ GeV}^{-1}$. It can be seen that there are four bulk factors in Equation 2.37, separated with multiplication dots. There are at least contributions from four different aspects of physics to this equation. The first and second terms consist of information about the detector, and macroscopic and microscopic parameters from the target nuclei (nuclear physics). In the third term is information about the WIMP interaction which include the WIMP mass and its interaction cross section (particle physics). The last term contains the properties of the WIMP halo which consist of the velocity distribution of the WIMP halo (astrophysics) and the halo density (cosmology). In practice, Equation 2.37 can be presented in a more generalized form using Equation 2.4, a recoil energy parameter E_0 and dimensionless s_0 parameter. This is done using the event rate R_0 expected in a detector per unit mass, given by:

$$R_0 = \frac{2R_r}{\sqrt{\pi}} = \frac{2 \times 10^9 N_A M_D \sigma_{WP}^{eff} \rho_W v_0}{M_W \sqrt{\pi}}. \quad (2.38)$$

The unit of the R_0 parameter is s^{-1} , note that the product $N_A M_D$ is dimensionless. Then, we introduce the $E_0 s_0$ parameter, given by:

$$E_0 s_0 = \frac{2\mu_p^2 v_0^2}{M_A}. \quad (2.39)$$

2. WIMP Detection and experimental searches

The dimensions of Equation 2.39 are the same as that of the nuclear recoil energy. This is where the s_0 parameter is defined by:

$$s_0 = \frac{4\mu_p^2}{M_A M_W}. \quad (2.40)$$

Note that the s_0 parameter is unity when $M_W = M_A$. It can be obtained by computing the ratio of Equation 2.8 to Equation 2.39 that:

$$\frac{E_r}{E_0 s_0} = \left(\frac{v_{min}}{v_0} \right)^2. \quad (2.41)$$

Then, using this and other definitions shown in Equations 2.38, 2.39 and 2.41, we obtain:

$$\frac{dR_r^{SD}}{dE_r} = \frac{R_0}{E_0 s_0} e^{\left(\frac{-E_r}{E_0 s_0}\right)} F^2(E_r). \quad (2.42)$$

Then, the correction due to the detector efficiency ϵ can also be included to Equation 2.42 to obtain the observable differential rate in a given detector defined by:

$$\frac{dR_r^{SD}}{dE_r} = \frac{R_0}{E_0 s_0} e^{\left(\frac{-E_r}{E_0 s_0}\right)} F^2(E_r) \epsilon. \quad (2.43)$$

Therefore, the overall expected spin-dependent WIMP-proton interaction rate in a detector can be determined by combining Equations 2.5 and 2.43 as:

$$R = \int_{E_{min}}^{E_{max}} \frac{dR_r^{SD}}{dE_r} dE_r = \int_{E_{min}}^{E_{max}} \frac{R_0}{E_0 s_0} e^{\left(\frac{-E_r}{E_0 s_0}\right)} F^2(E_r) \epsilon dE_r. \quad (2.44)$$

Equation 2.44 can be used to compute the WIMP event rates in detectors that are sensitive to the SD WIMP-proton interactions. In particular, this equation will be used in Chapter 5 of this thesis to determine the expected WIMP interaction event rates in the DRIFT-II detector which can be compared to the observed event rates in the detector to set an upper limit to the spin-dependent WIMP-proton cross section. The DRIFT-II detector is a directional WIMP search Time Projection Chamber (TPC) [101, 102] currently recording data in the Boulby underground laboratory, England. For further discussions on the DRIFT-II detector and other directional and non-directional WIMP search experiments see Section 2.6. Steps taken to reduce backgrounds in these WIMP

search experiments are discussed in Section 2.5.

2.5 Reducing backgrounds in direct WIMP search detectors

Detectors used for WIMP search experiments are deployed in underground laboratories around the globe. This is to ensure that the intrinsic environment where these detectors are installed are quiet, at reduced muon flux with low rate of other cosmic backgrounds reaching the detector [103, 104, 105]. Cosmic radiations are high energetic particles that reach the Earth atmosphere from outside the solar system. They are made up of 99% light nuclei (protons from ^1H and alphas ^4He) and 1% heavier nuclei. They interact with other particles in the upper atmosphere to form different particles, which are mainly charged pions (π^+ and π^-) [106, 107, 108]. These pions then decay to more stable muons (μ) and muon neutrinos (ν_μ). Muons are stable because they do not undergo strong interactions with other particles and hence can penetrate the lower atmosphere and the ground. Figure 2.5 shows the total muon flux as a function of vertical water equivalent depth, for a flat overburden, in some typical underground laboratories around the world.

The kilometre water equivalent (km w. e.) depth is used to enable comparison of results from various underground sites. This is because variations in material overburden in these laboratories affect the observed muon flux. Three of the laboratories shown in Figure 2.5: WIPP (Waste Isolation Pilot Plant), Soudan (Soudan Underground Laboratory), and SURF (Sanford Underground Research Facility) are located in USA while SNOLAB (SNO Laboratory) is located in Canada [109]. The LSBB (Laboratoire Souterrain a Bras Bruit) and LSM (Laboratoire Souterrain de Modane) are located in France. The Y2L (Yang Yang Underground Laboratory), Kamioka observatory and Jin-Ping (Jin-Ping Laboratory) are located in Korea, Japan and China, respectively. The Boulby (Boulby Underground Laboratory), and LNGS (Laboratori Nazionali del Gran Sasso) are located in England and Italy, respectively [103, 104, 105, 109]. In that figure, the minimum muon flux was observed in the Jin-Ping laboratory which is the deepest underground laboratory in the world. This is because the muon flux in a given laboratory is inversely proportional to its water equivalent depth

2. WIMP Detection and experimental searches

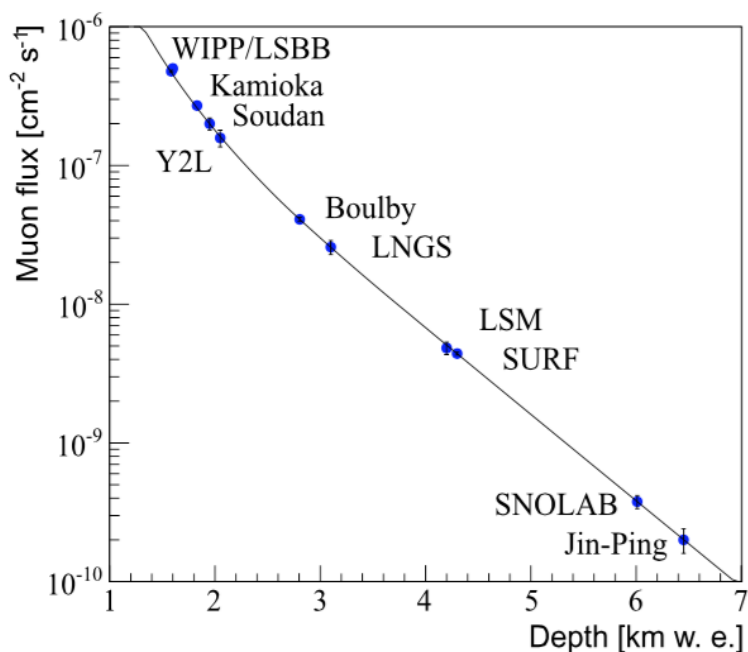


Figure 2.5: Total muon flux in underground laboratories around the world shown as a function of their water equivalent depths. The blue points are observed data while the black line is the best fit for the effective laboratory depths [109].

[103].

Observed background events in WIMP search experiments situated in these underground laboratories are mainly due to neutrons from alpha-neutron reactions as a result of alpha decays in materials used in building the detectors [104, 110]. This is because these materials can be contaminated by radioactive substances such as Uranium (^{238}U), Thorium (^{232}Th), Radium (^{223}Ra) which can decay via background emitting processes as in α -n reactions. There are also neutrons from spallation reactions from radioactive decays in the surrounding rocks [110, 111, 112]. Detectors are actively shielded with hydrogen abundant materials such as water and polypropylene pellets to stop fast neutrons from these rocks from reaching the detector thereby reducing the overall event rate of these rock neutrons [113]. After the installation of the active shielding, the edge of the active volume of the detector can be monitored and used to veto events that may pass the shielding materials. Material assay are conducted to select only high radioactive materials during detector construction to reduce radioactive decays in the active

volume of WIMP search detectors [110, 111]. The detector can also be fiducialised if the distances of event vertex from the readout plane are known [113]. Then, data which are used for WIMP search analyses can be selected from only the central region of the detector in order not to include possible background events due to radioactive decays emanating from the wall of the detector. For examples of these direct WIMP search experiments, see Section 2.6.

2.6 Classification of direct WIMP search experiments

Generally, it is expected that energy transferred to target nuclei by incident WIMP signals in fiducial volumes of detectors can induce ionization, phonon heat or generate scintillation light depending on the target material used in an experiment. For instance, the DRIFT experiment [113] use Multi-Wire Proportional Chambers (MWPCs) to record ionization charge signals in a Time Projection Chamber (TPC), the CRESST-I experiment [114] used sapphire (Al_2O_3) cryogenic calorimeters operating at intrinsic temperature of about 15 mK in a thermal radiation shielding to record variations in temperature (phonon heat) due to interactions in the detector. Other experiments like DM-Ice [115] and DAMA/LIBRA [116] use photomultiplier tubes to detect scintillation photons induced by these interactions in NaI(Tl) crystals. Figure 2.6 shows more experiments that utilise each of these WIMP search strategies with example of target materials that have been used in some of these experiment.

In Figure 2.6, ionization based experiments are shown in blue. These ionization based experiments are marked as “Directional” because they can reconstruct directions of events in the detector. The experiments marked as “Bubble Nucleation” use induced bubbles in super heated liquids to reconstruct energy of an interaction. Experiments that are sensitive to phonon heat signals generated from interaction of particles are shown in red while those that are scintillation based are shown in green. Also, it can be seen from Figure 2.6 that some of the experiments can combine two of these methods to enhance the detector ability to reject backgrounds and sometimes aid signal fiducialisation in the active volume of the detector and event discrimination. For instance, the CDMS experiment [117] combines phonon and ionization signals, LUX WIMP search experiment [118] combines ionization and scintillation while CRESST-II experiment [119] combines phonon heat and scintillation signals.

2. WIMP Detection and experimental searches

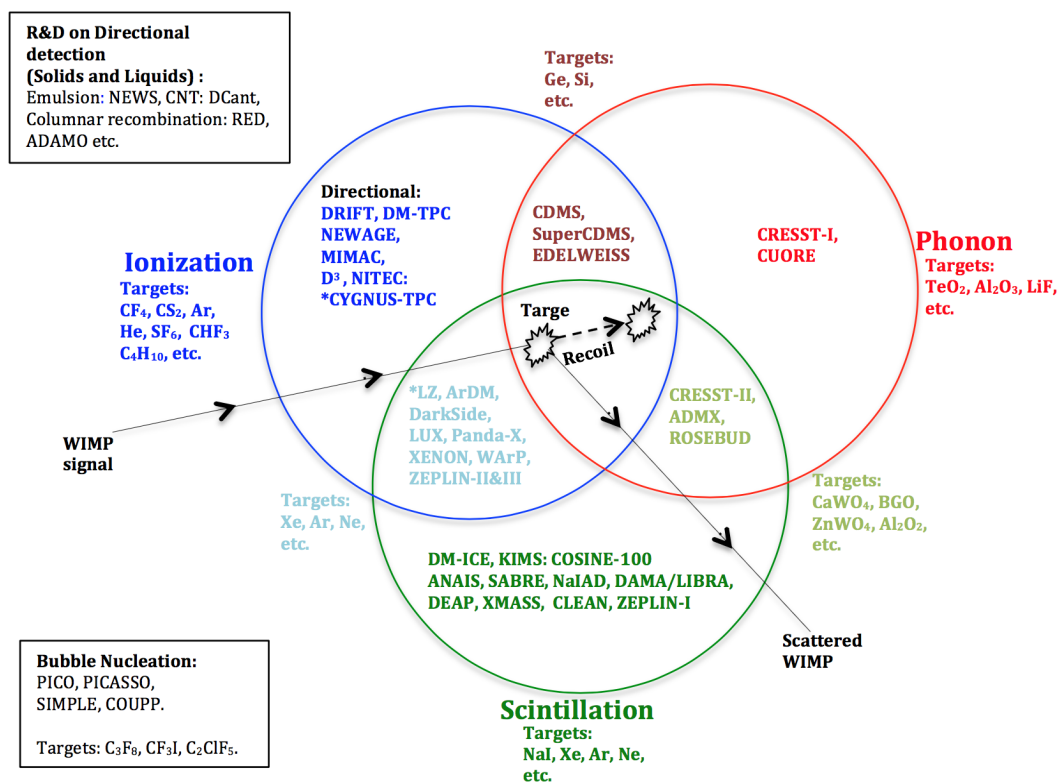


Figure 2.6: WIMP search experiments and their search strategies.

After an incident particle scatters off a target nucleus in each of these experiments, the energy of that particle can be reconstructed using the magnitude of the observed signal. Most of these direct WIMP search experiments use the observed Bethe-Bloch energy loss per unit nuclear recoil distance (dE_r/dR_3) [120, 121] of events in the detector to identify and reject charged particles which are potential backgrounds. This dE_r/dR_3 parameter is equivalent to the amount of ionization lost per unit recoil distance in gas TPCs. This information is used in gas TPC detectors to differentiate the beginning (tail) of a nuclear recoil track where high charge density is expected from the end (head) of the track with lower charge density. This charge density asymmetry along nuclear recoil tracks are measured and termed the head-tail effect. See later part of this section (Chapter 4) for more details on the head-tail effect (head-tail measurements using data from a gas TPC based WIMP search experiment).

Apart from energy measurements and particle identifications, there are two galactic WIMP signatures which some direct WIMP search experiments can detect. Due to the

2. WIMP Detection and experimental searches

motion of the Earth around the sun and motion of the solar system around the galactic centre, an Earth bound detector should be passing through the WIMP halo. The motion of the Earth around the sun is illustrated in Figure 2.7.

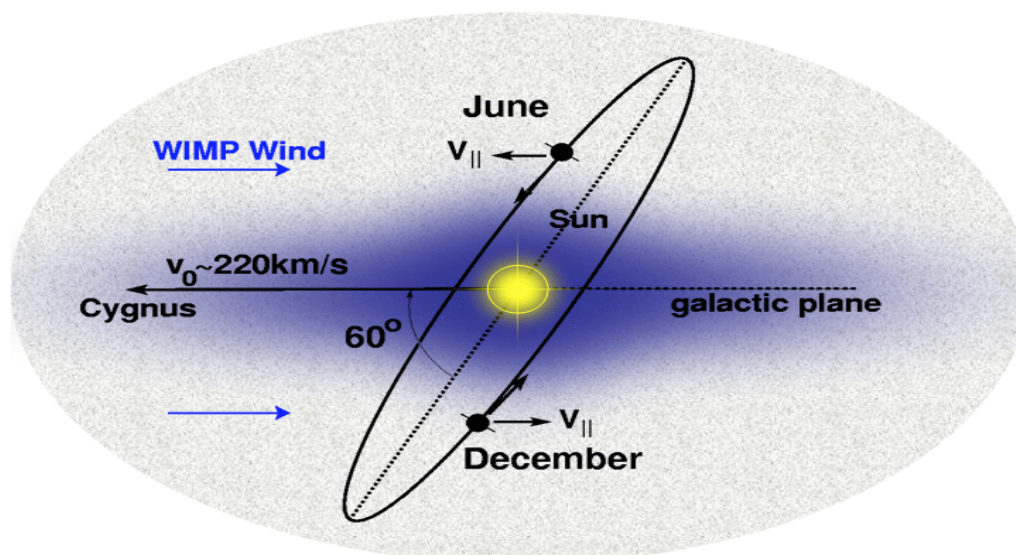


Figure 2.7: Motion of the Earth around the sun as the solar system is rotating about the galactic centre. Credit: Sheffield Dark Matter Research Group.

The expectation is that this should create a WIMP wind oriented in the opposite direction of the Earth travel, such that WIMPs can scatter off detector target nuclei [122]. Hence, Earth bound detectors should observe an annual modulation in the WIMP event rate with maximum in June and minimum in December [123]. These two periods correspond to the time the Earth changes its rotation phase as it rotates around the centre of the sun. The black shaded circles in Figure 2.7 represent different locations of the Earth along its axis in different seasons of the year as it orbits the sun with velocity $v_{||}$. Arrows near the Earth show the direction of the Earth motion in June and December. The arrow passing through the centre of the sun (yellow blob) shows the direction of the solar system as it moves with velocity v_0 . In this present epoch, the direction of motion of the solar system is oriented toward the Cygnus constellation [122]. This annual modulation strategy is currently used by some WIMP search experiments. For instance, the DAMA/LIBRA experiment has been claiming the detection of $0.0112 \pm 0.0012 \text{ cpd kg}^{-1} \text{ keV}^{-1}$ annual modulation signal for over a decade [124]. However, the technique remains controversial [117, 125, 126, 127] and the signal can

2. WIMP Detection and experimental searches

be mimicked by background events [126, 128, 129, 130].

A robust and potentially more powerful galactic signature is encoded in the direction of the WIMP-induced nuclear recoils [122]. The angular distribution of WIMP-induced recoils is highly anisotropic in galactic coordinates, with the average direction oriented away from our direction of travel towards the constellation Cygnus. In contrast, the distribution of any terrestrial background would be expected to be uncorrelated with this direction. In laboratory coordinates, due to the Earth's rotation, a sidereal oscillation in WIMP-induced recoil directions would be expected [60, 122, 130] as illustrated in Figure 2.8.

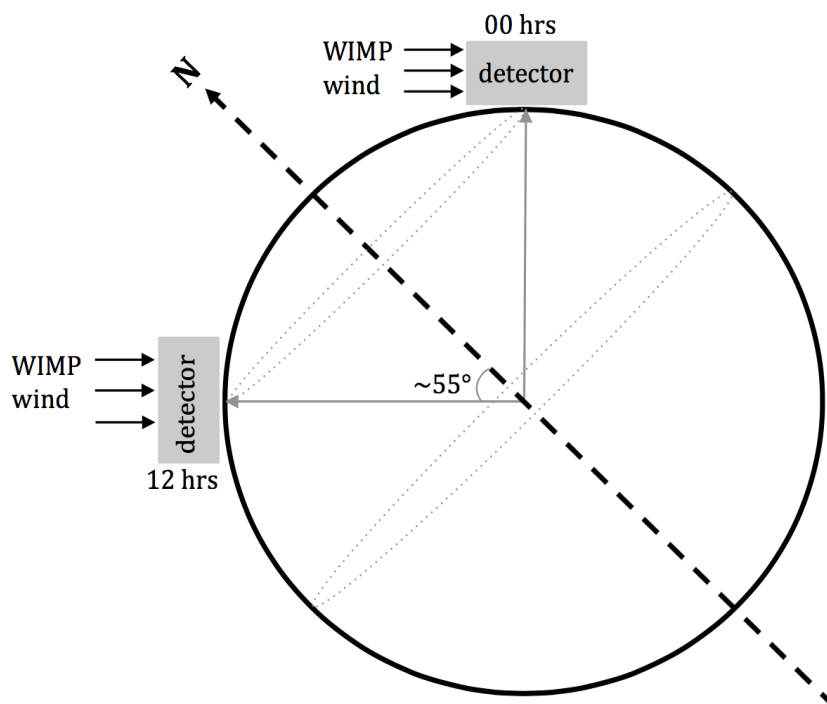


Figure 2.8: Rotation of the Earth about its axis showing a change in the expected mean direction of WIMP wind signal reaching an Earth bound detector within a sidereal day.

The WIMP signal in Figure 2.8 arrives at the detector (located for instance on 55°N latitude as in Boulby) from the mean direction of the Cygnus constellation. Hence, an Earth bound detector is expected to have a 90° axes offset relative to Cygnus in a period of about 12 hours of a sidereal day. As a result, a twofold modulation amplitude relative to the annual modulation signature can be obtained from this sidereal case

2. WIMP Detection and experimental searches

[122]. Also, this WIMP sidereal modulation signals should be statistically distinguishable from anisotropic (isotropic) background events induced by solar (atmospheric and diffused supernova) neutrinos [130, 131, 132]. Solar neutrinos [133] are produced in the sun while atmospheric [134] and diffused supernova [135] neutrinos are produced by cosmic ray interactions in the atmosphere and from supernova explosions, respectively. In principle, these neutrinos can scatter off target nuclei in ton-scale WIMP search detectors with enough sensitivity to reach the neutrino floor. Nuclear recoil signatures from these coherent neutrino background events should be similar to expectations from WIMPs [136, 137]. The parameter spaces beyond which, these coherent neutrino events are expected is known as the neutrino floor as illustrated in Figure 2.9.

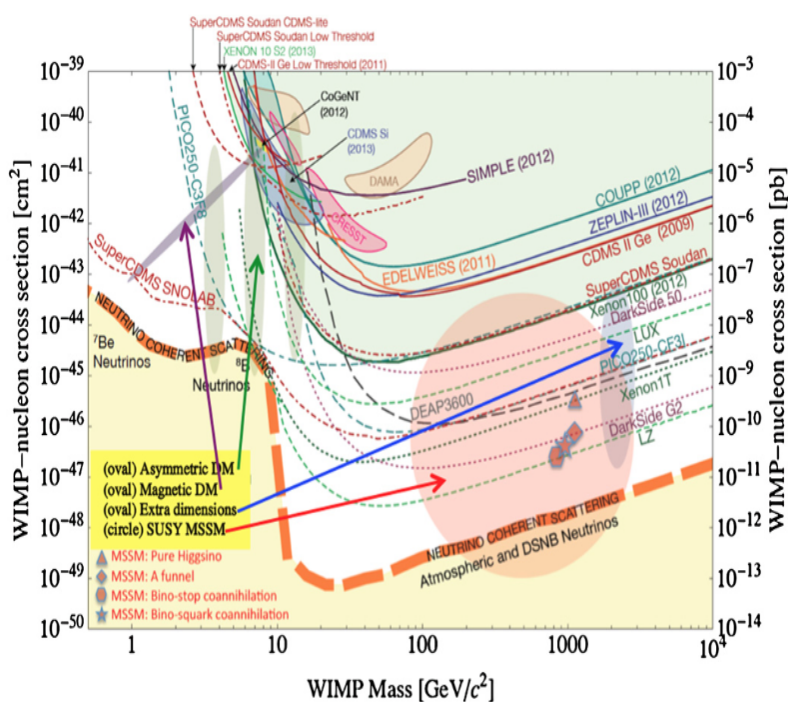


Figure 2.9: Neutrino floor overlaid on typical sensitivities from direct detection experiments shown on WIMP-nucleon cross section-WIMP mass parameter space. The orange thick dashed line shows the upper limit for the neutrino floor. Each of the solid lines shows a parameter space excluded by the given experiment while the dotted lines are planned and projected sensitivities. The arrows show allowed parameter space for various theoretical models [132]. For up-to-date results from LUX, PICO, CDMS and DarkSide experiments, see Section 2.7.

2. WIMP Detection and experimental searches

The orange thick dashed line in Figure 2.9 marks the upper bound below which coherent neutrinos scattering off target nuclei are expected as backgrounds in WIMP search experiments. It can be seen that in few more years, some WIMP search detectors may have enough sensitivity to reach the background-rich neutrino floor.

An idealised directional detector sensitive to the nuclear recoil track axis only (not the vector direction), would need a few hundred events to confirm a galactic WIMP signal [138]. If, however, the recoil track vector (head-tail effect) is measured, then only tens of events are required [139, 140]. This head-tail capability is of great importance in development of directional WIMP search technologies because detector volumes cannot be infinite. For instance, there is significant cost and engineering implications of large volume scale TPC detectors. Hence, small number of WIMP induced events are expected in fiducial volumes of existing detectors per live-time year [97, 141]. Chapter 4 covers the nuclear recoil head-tail effect in more detail.

WIMP search experiments, for instance CDMS [117], DAMA/LIBRA [142], LUX [118] etc. use non-directional detectors and hence, are insensitive to nuclear recoil track directions and the head-tail effect. As such, these non-directional detectors will find it difficult if not impossible to discriminate background events from positive signals especially for WIMPs whose cross sections are below the neutrino floor. However, this can be potentially improved statistically with larger non-directional detectors and target complementarity [143]. Directional WIMP search experiments, for instance, the DRIFT-IIId [113], NEWAGE [144], D³ [145] etc. can reconstruct and point back to the source of observed events in their fiducial volumes, hence, are sensitive to the sidereal modulation signal, described in Figure 2.8. These track orientation sense properties of directional WIMP search experiments can be used to distinguish neutrino backgrounds from real WIMP events, if detected [146, 147]. To achieve this, a ton-scale directional detector with <10 keV_r energy threshold will be required.

2.7 Non-directional WIMP search experiments

In this section, world leading non directional WIMP search experiments are discussed. This brief review will be done such that at least one experiment out of several others in each of the respective WIMP search strategies shown earlier in Figure 2.6 is discussed. The review will aim to outline the major principle of detector operations, recent results

and future prospects of the selected experiments.

2.7.1 Large Underground Xenon (LUX) WIMP search detector

The Large Underground Xenon (LUX) dark matter experiment combines the ionization and scintillation WIMP search strategies (see Figure 2.6). It is located in Sanford Underground Research facility (SURF) in the Black Hills of South Dakota. The detector comprises a 250 kg liquid xenon target, operated as a dual-phased TPC as illustrated in Figure 2.10.

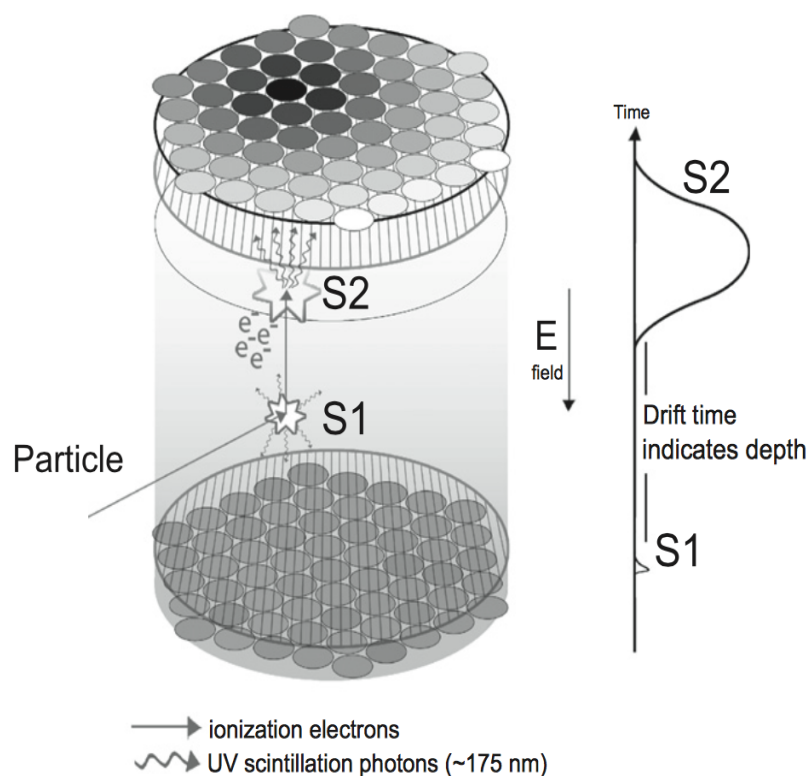


Figure 2.10: Principles of operation of the Large Underground Xenon (LUX) dual-phased TPC detector [148].

When a particle deposits energy in the LUX TPC, two signals called S_1 and S_2 are generated and acquired through arrays of photomultiplier tubes (PMTs) located above and below the active volume of the detector [118, 148, 149]. The signals include a primary scintillation signal S_1 in the liquid phase and an electroluminescence signal

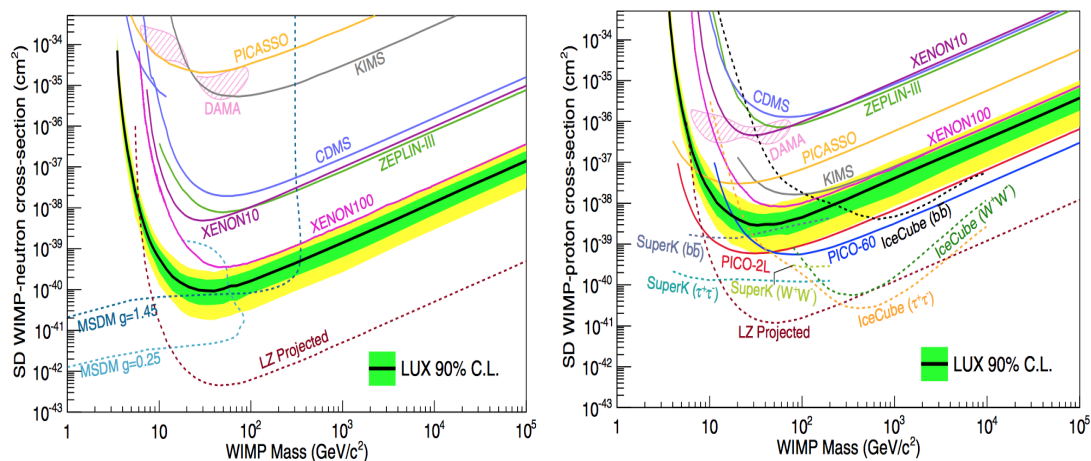
2. WIMP Detection and experimental searches

S_2 (signal due to voltage induced photon emission), generated in the gas phase after ionization electrons are drifted through a uniform field to the surface of the liquid xenon where they are extracted into the gas phase. The bottom and top PMT arrays are used to image the S_1 and S_2 signals, respectively. It is the difference in the arrival times of the S_1 and S_2 signals that are used to infer the depth of an event vertex within the fiducial volume of the detector.

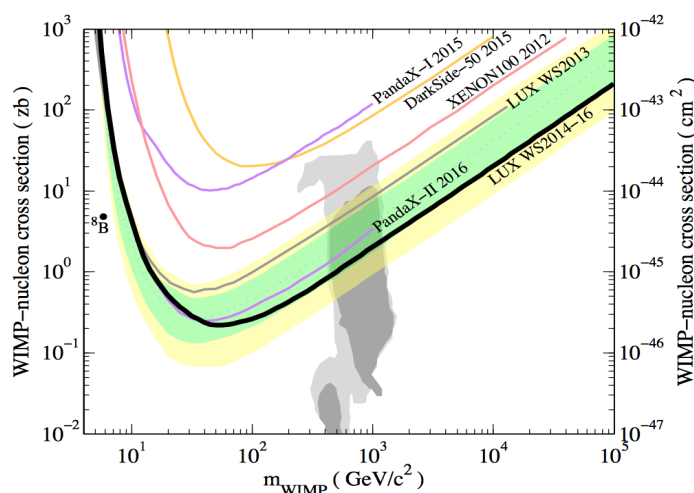
The main source of backgrounds in LUX and most WIMP search experiments are due to electron recoils from gamma interactions and nuclear recoils induced by rock neutrons [150, 151]. But the LUX experiment has the capacity to reject up to 99.7% of all the electron recoils in analysis. The most recent spin-dependent WIMP-proton and WIMP-neutron cross section exclusion limits and spin-independent WIMP-nucleon results from the LUX experiment are shown in Figures 2.11(a) to 2.11(c), respectively.

In these figures, a black line with green and yellow bands corresponds to $\pm 1\sigma$ and $\pm 2\sigma$ exclusion limits from LUX, respectively. This is compared to various results from other experiments in each of the plots for the spin-dependent WIMP-neutron, spin-dependent WIMP-proton and spin-independent WIMP-nucleon sensitivities in Figures 2.11(a), 2.11(b) and 2.11(b), respectively. The spin-dependent WIMP-proton and WIMP-neutron results were obtained at 90% confidence level using 1.4×10^4 kg-days of data. The analysis of these data led to the exclusion of all parameter spaces above 0.094 fb and 2.9 fb for the WIMP-proton and WIMP-neutron cross sections, respectively, each at $33 \text{ GeV } c^{-2}$ WIMP mass by the LUX experiment in April 2016 [150]. It can be seen that the spin-dependent WIMP-neutron and WIMP-proton results in Figure 2.11 are compared to model dependent results from the WIMP production and indirect WIMP search experiments. The minimal simplified dark matter (MSDM) [152, 153] results were obtained from analyses of LHC data while the $b\bar{b}$, $\tau^+\tau^-$ and W^+W^- WIMP annihilation final state constraints are from indirect searches. In the spin-independent WIMP-nucleon analysis, a 90% confidence limit result was obtained using a total of 3.35×10^4 kg-days of WIMP search data. The result from that analysis was released in August 2016 where all WIMP-nucleon cross sections greater than 0.22 zb for $50 \text{ GeV } c^{-2}$ WIMP mass were excluded [118, 151]. This result is overlaid on $\pm 1\sigma$ (dark grey region) and $\pm 2\sigma$ (light grey region) theoretical parameter spaces allowed by the constrained minimal SUSY models (CMSSM) [154] in Figure 2.11(c).

2. WIMP Detection and experimental searches



(a) LUX SD WIMP-neutron limit: 2.9 fb at 33 GeV c^{-2} (b) LUX SD WIMP-proton limit: 0.094 fb at 33 GeV c^{-2}



(c) LUX SI WIMP-nucleon limit: 0.22 zb at 50 GeV c^{-2}

Figure 2.11: Spin-dependent (SD) and spin-independent (SI) results from LUX compared to exclusion limits from other experiments as at 2016 [118, 150, 151].

As can be seen in Figure 2.11, the present LUX result on the spin-independent WIMP-nucleon cross section is the most stringent limit set so far by any direct detection WIMP search experiment in the spin-independent parameter space. Also the LUX experiment is leading direct searches in the spin-dependent WIMP-neutron parameter space but falls behind PICO results in the spin-dependent WIMP-proton parameter space.

2. WIMP Detection and experimental searches

The LUX and previous ZEPLIN WIMP search collaborations are now working together toward a 10 tonne target mass of liquid xenon WIMP search experiment called LZ, which is also planned to be installed at the Sanford Underground Research Facility in South Dakota by 2020 for a 5 year WIMP search operation [155].

2.7.2 PICO WIMP search Experiment

The PICO experiment was formed as a merger of former PICASSO [156] and COUPP WIMP search experiments [157]. It is located at the SNOLAB underground laboratory in the Vale Creighton nickel Mine near Sudbury Ontario, Canada. The PICO experiment is made up of a bubble chamber based WIMP search detector filled with 2.90 kg of octafluoropropane (C_3F_8) gas used as the WIMP target material. Details of the experimental setup used in one of the PICO experiment is shown in Figure 2.12.

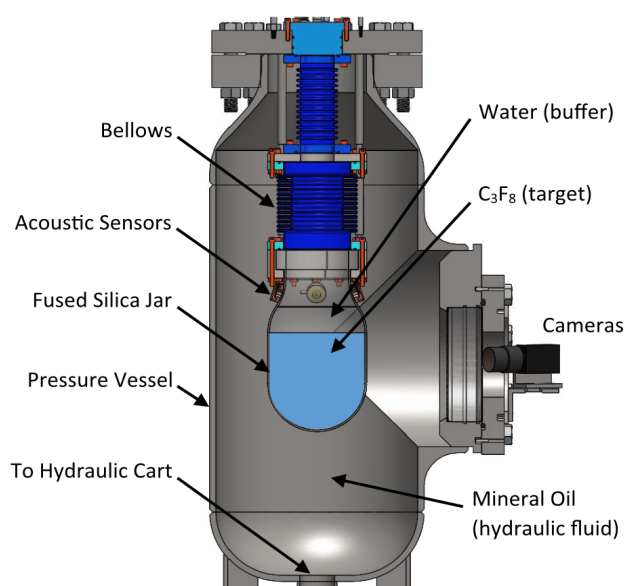


Figure 2.12: Experimental setup of PICO-2L bubble chamber [157].

The bubble chamber consists of 150 mm diameter synthetic fused silica bell jar coupled to flexible stainless steel bellows which are immersed in propylene glycol hydraulic fluid contained in a stainless steel pressure vessel [158]. The hydraulic fluid maintains the inner pressure of the stainless steel vessel especially that of the silica bell jar, suspended from the flexible bellows. The bell jar containing the C_3F_8 target is

2. WIMP Detection and experimental searches

topped with water which serves as buffer to ensure that the target does not have any contact with the surface of the stainless steel vessel, rather, it maintains contact with only the smooth silica gel. Lead based acoustic transducers that are epoxied to the exterior of the bell jar are used to readout acoustic emissions from bubble nucleations induced by ionization signals after particle interaction in the active volume of the detector [159]. Pictures of these bubble nucleation signals are read out using CMOS cameras attached to the pressure vessel.

In 2015, the PICO collaboration used 211.5 kg-days of data from the detector to set the world leading (as at the time of writing) spin-dependent WIMP-proton exclusion limit (see Figure 2.11(b)) from a direct WIMP search experiment [157]. The results from that analysis show strongest sensitivity at about 1.81 fb WIMP-proton cross-section for 35 GeVc⁻² WIMP, making the detector the first among its kind to probe the supersymmetric parameter space from the spin-dependent WIMP-proton cross section channel [157]. These PICO-2L results are shown with a red line in Figure 2.11(b). The PICO results shown with a blue line was obtained with a bigger version of the PICO-2L detector known as PICO-60.

2.7.3 Cryogenic Rare Event Search with Superconducting Thermometers II (CRESST-II) WIMP search experiment.

The Cryogenic Rare Event Search with Superconducting Thermometers phase-II otherwise known as CRESST-II comprises of an array of cryogenic detectors situated at the Gran Sasso National Laboratory, Italy. The CRESST-II experiment combines phonon heat and scintillation strategies (see Figure 2.6). For details of the set-up used in the CRESST-II WIMP dark matter search experiment see Figure 2.13.

The CRESST-II detector uses a scintillating calorimeter made up of 18 modules of cylindrical calcium tungstate (CaWO₄) crystals, yielding a total target mass of 5 kg. These crystals are operated in millikelvin temperature scale [119, 161, 162]. Each of the detector modules is coupled to two readout channels, one for phonon heat and the other for coincidence scintillation light. It is expected that particle interactions in each of the target crystals will deposit energy enough to generate phonon heat and a coincidence scintillation light signal. The phonon heat signals are read out with Transition Edge Sensors (TES) and are used to reconstruct the energies deposited in

2. WIMP Detection and experimental searches

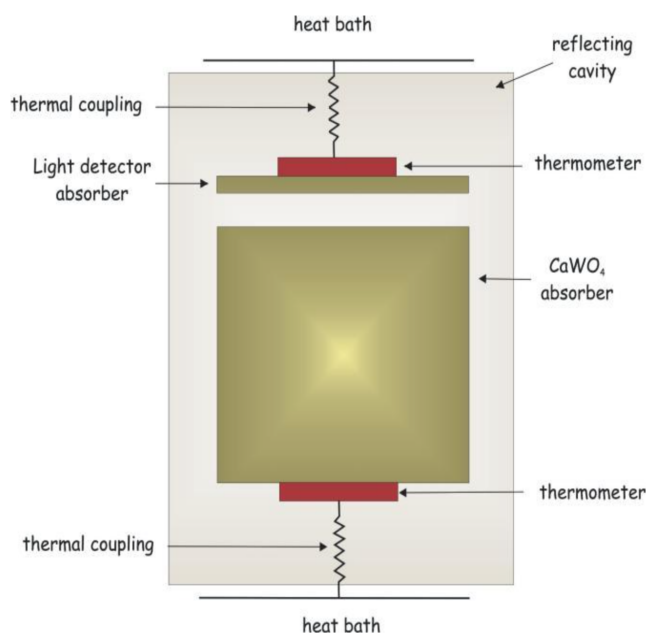


Figure 2.13: Schematic of the CREST-II detector [160].

the crystal by the interacting particles. The coincidence scintillation light signals are read out with silicon on sapphire based light absorbers [119, 161]. Then the light yield given by the ratio of the nuclear recoil energy obtained with the coincidence light signal to that obtained with the coincidence phonon signal is used to discriminate different types of signals in the detector. Hence, common background events (alpha events for instance) can be rejected in analyses of WIMP search data obtained with the CREST-II detector.

In 2012, the CREST-II experiment claimed detection of the WIMP dark matter signal at 4σ statistical significance [127] but subsequent analyses with data from the same detector failed to confirm this claim [161]. Recently, the collaboration analysed a 52 kg-days of WIMP search data with an energy threshold of 0.31 keV to obtain an exclusion limit of 1.1 pb spin-independent WIMP-nucleon cross section for a $0.5 \text{ GeV } c^{-2}$ WIMP mass [119]. This result posits the CREST-II experiment as the first direct detection WIMP search experiment to explore the sub-GeV c^{-2} parameter space. The experimental group are currently focusing on improving the detector sensitivity (developing a new version called CREST-III) and reducing backgrounds for possible scale up to a new phase of the experiment called EURECA (European Underground

Rare Event Calorimeter Array) [160] detector in collaboration with EDELWEISS.

2.7.4 Cryogenic Dark Matter Search (CDMS) experiment

The Cryogenic Dark Matter Search (CDMS) experiment combines both the ionization and phonon heat strategies (see Figure 2.6) to search for the WIMP dark matter. The experiment uses arrays of silicon and germanium based detectors located in Soudan underground laboratory, Minnesota [117, 163]. The principle of operation of the CDMS detector is shown in Figure 2.14.

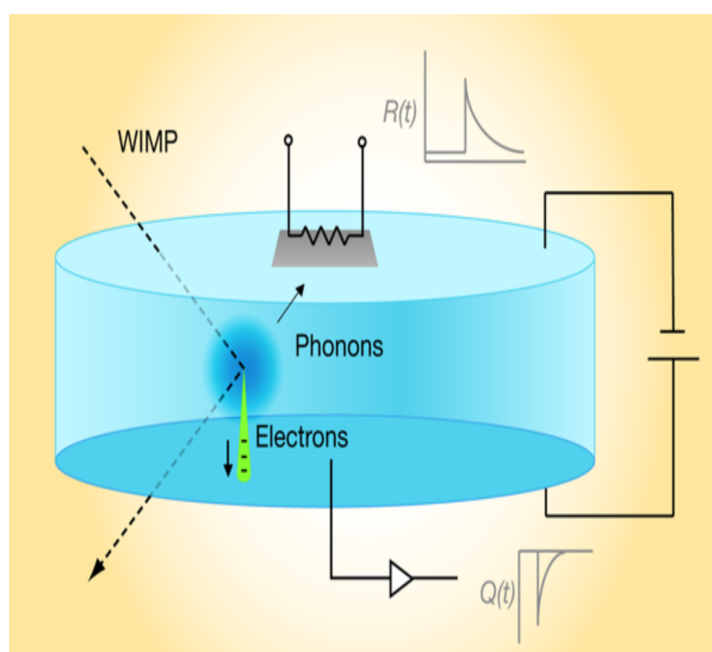


Figure 2.14: Experimental set-up for one of the germanium crystals used in the CDMS. Arrays of these crystals make up the CDMS experiment [164]

It is expected that WIMP-induced recoils in one of the germanium crystals in the detector can produce ionization and phonon signals [117, 163, 164, 165]. The phonon signals are collected in the opposite face of the germanium crystal, bonded to a thin superconducting aluminium layer to enhance Cooper pair breaking [166, 167] due to electron-phonon interactions. Hence, the resulting momentary change in resistance $R(t)$ of a transition edge sensor coupled to the superconducting layer are measured [164]. The faces of the crystal are biased in voltage to allow for the coincidence ioniza-

2. WIMP Detection and experimental searches

tion signals to drift to the more positive terminal in the opposite face of the germanium crystal where they are readout using charge $Q(t)$ sensitive amplifiers, see Figure 2.14 for illustration. Then the temporal difference in arrival times of the $Q(t)$ and $R(t)$ signals and their ratio are used to reconstruct the position of event vertex in the detector and for background discrimination, respectively.

In October 2015, the collaboration set 90% and 60% confidence limits on WIMP-nucleon spin-independent scattering cross sections of $1.80 \times 10^{-44} \text{ cm}^2$ and $1.18 \times 10^{-41} \text{ cm}^2$ respectively, for a WIMP of $8.6 \text{ GeV } c^{-2}$ mass [163]. These results were obtained from a two-fold analysis (using 10 keV and 5 keV thresholds) on 612 kg-days of data from arrays of germanium crystals in the CDMS-II detector. The new results have now excluded the parameter space where the CDMS experiment initially claimed to have detected three WIMP candidate signals in their 2013 analysis reported in Ref. [117]. The collaboration are working towards a larger germanium detector with a better sensitivity called SuperCDMS, planned to be deployed in a deeper, SNOLAB underground laboratory located in Sudbury.

2.7.5 DM-Ice experiment and annual modulation searches

The DM-Ice experiment is based on the scintillation search strategy (see Figure 2.6) with the aim of testing the highly controversial claim of DAMA/LIBRA experiment [123, 142, 168, 169, 124] for detection of the WIMP annual modulation signal. This is using the same target material (NaI(Tl)) at lower background and higher radiopurity. The annual modulation signal is due to the variation in WIMP interaction rate due to the motion of the Earth around the sun as discussed earlier in Section 2.6. In the quest for this, the DM-Ice collaboration have published results on the detector characterisation and backgrounds from operation of two cylindrical 8.47 kg NaI(Tl) scintillation crystals of 15 cm height and 14 cm diameter, known as DM-Ice17 detector [115, 170, 171, 172]. This DM-Ice17 detector shown in Figure 2.15 was deployed 2457 m below surface of the Antarctic ice in the South Pole from 2011 [115, 171]. The detectors are located 7 m below the bottom of the IceCube neutrino observatory. It is expected that the glacial ice surrounding the detector will provide higher intrinsic radio-pure laboratory and low temperature for stable science operations [171]. Photomultiplier tubes (PMTs) coupled to either end of the crystals as shown in Figure 2.15 are used to

2. WIMP Detection and experimental searches

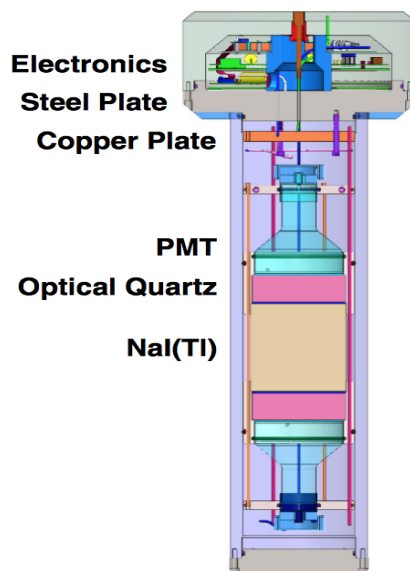


Figure 2.15: Set-up of the DM-Ice17 NaI(Tl) detectors deployed in the South Pole [171]

read out scintillation photon signals which are in coincidence after interactions in the detector.

The DM-Ice collaboration published null result for the annual modulation signal using a 60.8 kg-years WIMP search data obtained with the DM-Ice17 detectors [172]. The spin-independent WIMP-nucleon exclusion limit determined from that analysis at 90% confidence level is compared to DAMA/LIBRA allowed region in Figure 2.16. It can be seen that the DM-Ice17 data does not have enough sensitivity to reach the DAMA/LIBRA annual modulation parameter space. But it is expected that the DM-Ice experiment can reach these parameter spaces with more 500 kg-years of data. Since that work at the South Pole, the collaboration has been operating a pair of NaI(Tl) based detectors in the STFC underground science facility in Boulby, England to be able to understand the modulation of muons and other backgrounds in the Northern Hemisphere for possible future multi-site (North-South) operations.

The next generation of the DM-Ice detector, planned to be made up of 250 kg scintillating NaI(Tl) crystals can reach the required sensitivity to investigate the DAMA/LIBRA claims in two data years [170]. Recently, the DM-Ice and KIMS [173] collaborations agreed to work together as COSINE-100 experiment. This new collaboration

2. WIMP Detection and experimental searches

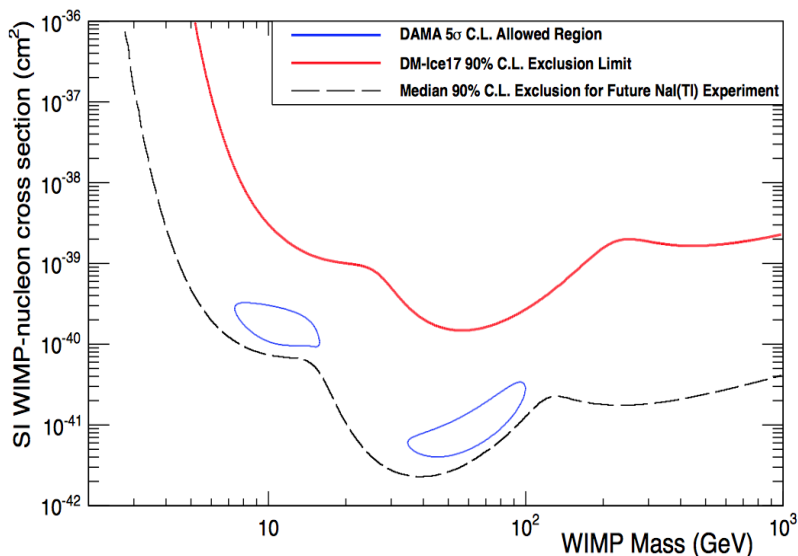


Figure 2.16: Spin independent WIMP-nucleon cross section limit obtained from the DM-Ice37 experiment shown as a function of WIMP masses marked with red line. This is compared to the DAMA/LIBRA allowed region marked with blue lines. The expected sensitivity from 500 kg-yr data from a future DM-Ice experiment is shown with black dashed line [172].

was formed to enhance their ability to obtain the amount of data required to reach the DAMA/LIBRA sensitivity in few data years. In fact, the COSINE-100 collaboration is currently taking science data in the Yang Yang laboratory located in South Korea with a 106 kg NaI(Tl) based detector. There are also efforts from other NaI(Tl) based experiments, for instance, ANAIS [174] and SABRE [175] experiments toward achieving this ultimate goal of testing these DAMA/LIBRA results. For more on the DAMA/LIBRA experiment, see discussions below.

The DAMA experiment, located in the LNGS (Laboratori Nazionali del Gran Sasso), published a claim for detection of WIMP dark matter annual modulation signal in 1998 [168, 124]. The most recent version of this result is shown in Figure 2.17. Since then, the collaboration has reached a cumulative exposure of 1.33 ton-year after the detector upgrade to DAMA/LIBRA [142]. Analysis of 1.04 ton-year of the DAMA/LIBRA data has allowed them to consolidate their initial claim of detection of the galactic WIMP annual modulation signature using NaI(Tl) scintillation signals at 2-6 keV threshold with statistical significance of 9.3σ . The reported annual modulation signal reaches

2. WIMP Detection and experimental searches

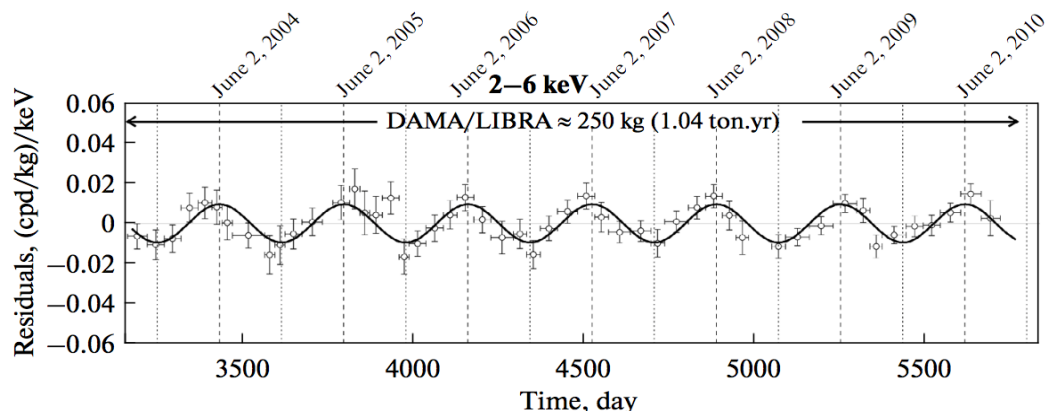


Figure 2.17: WIMP annual modulation results from the DAMA/LIBRA experiment [142].

maximum rate in June 2nd as shown in Figure 2.17. Though, many other experiments have excluded the WIMP-nucleon cross sections (10^{-2} pb to 10^{-6} pb) for given WIMP masses (~ 10 GeV c^{-2} to 100 GeV c^{-2}) where DAMA/LIBRA claimed to have detected the WIMP annual modulation signals [118]. Efforts have been made towards explaining the DAMA/LIBRA results with background muon induced neutron events [126, 129]. For instance, it can be seen from Figure 2.18 that the annual modulation signal detected by the DAMA/LIBRA experiment can fit to background neutron events in the LNGS laboratory [129]. Hence, the DAMA/LIBRA results remain very contro-

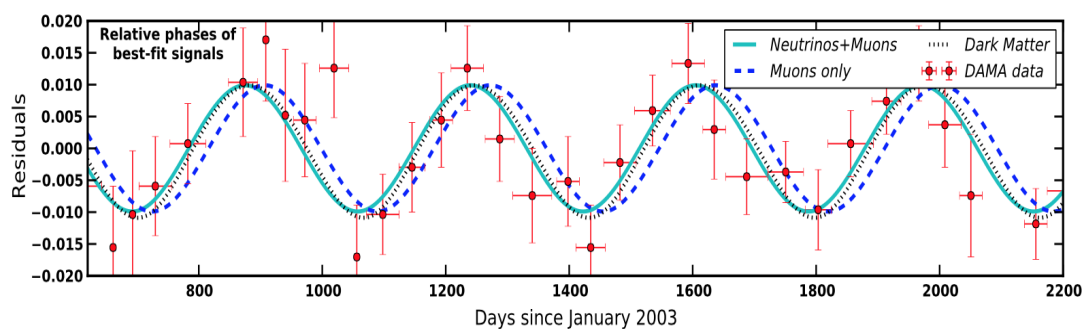


Figure 2.18: Comparison of annual modulation signal from neutron events produced by muon and neutrino backgrounds to the WIMP results from the DAMA/LIBRA experiment [129].

versial as at the time of writing this thesis. The expectation is that, in the next few

years, future results from the DM-Ice experiment will help to make a stronger case toward strengthening or invalidating the DAMA/LIBRA results.

2.8 Directional WIMP search experiments

World leading directional WIMP search experiments use the ionization strategy as earlier shown in Figure 2.6. There are four directional WIMP search time projection chambers that have been taken to an underground laboratory to record WIMP interaction data [97]. Various directional technologies are also in different stages of R&D in surface laboratories around the globe. The directional WIMP search experiments which are currently operating in underground laboratories are DRIFT [113], NEWAGE [176], DMTPC [177] and MIMAC [178]. All these groups are currently working together to form a larger directional WIMP search collaboration called CYGNUS-TPC. The principle of operation and update on the status of these directional WIMP search detectors are discussed below.

2.8.1 NEWAGE directional WIMP search experiment

The current generation of the detectors in the NEWAGE series known as the NEWAGE-0.3b is located in the Kamioka underground laboratory [144]. The NEWAGE-0.3b is a 0.3 m³ time projection chamber filled with 76 Torr of CF₄ gas. Figure 2.19 shows the experimental set-up and dimensions of the main constituents of a typical NEWAGE detector.

Particles scattering off a ¹⁹F or ¹²C nucleus in the active volume of the detector creates ionization electrons. These ionization electrons are drifted through a uniform field toward a Gaseous Electron Multiplier (GEM) [179] which with appropriate potential bias creates electron avalanches which serve as a first amplification stage [176, 180, 181]. The ionization electrons then move from the GEM to readout strips, where they undergo a secondary and final avalanche on the more positive anode strips of a micro-pixel chamber (μ -PIC). This μ -PIC is a 2-d imaging detector consisting of orthogonal anode and cathode strips, with a pitch of 400 μ m, biased at +510 V and 0 V (for NEWAGE-0.3b detector), respectively [144]. This is enough to create a typical gas gain of 2500. The separation between the GEM and the μ -PIC read out is 4 mm but

2. WIMP Detection and experimental searches

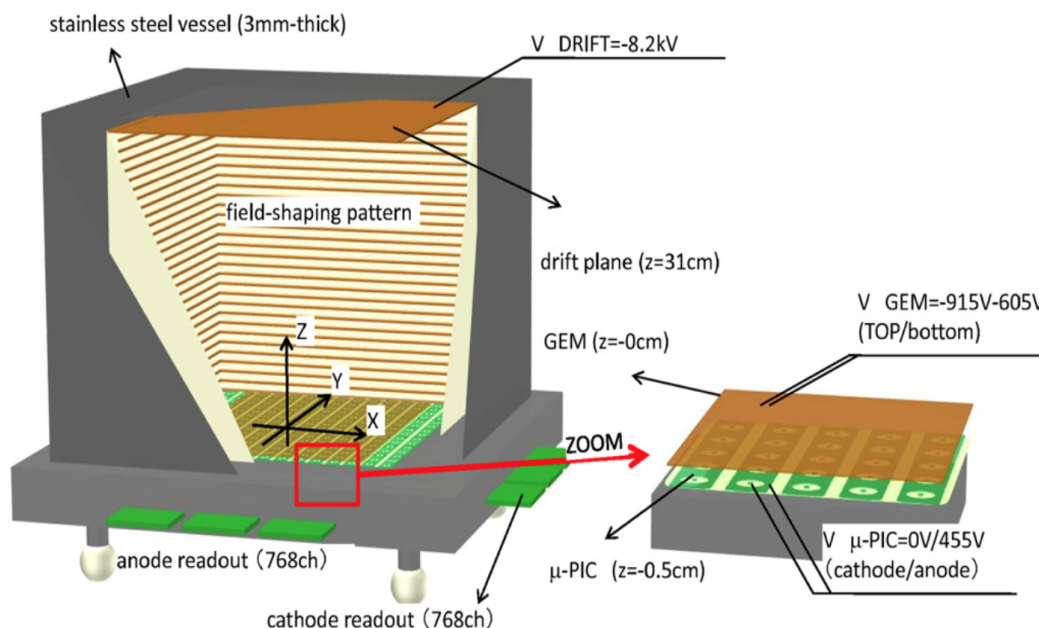


Figure 2.19: Schematic of a NEWAGE μ -PIC detector. The left panel shows an image of the detector in a vacuum vessel while the right panel shows the details of the GEM based μ -PIC readout system [176].

the maximum drift distance of the detector is 31 cm for the previous NEWAGE-0.3a (see Figure 2.19) and 41 cm for the current NEWAGE-0.3b μ -PIC detectors. Since both the anode and cathode strips are read out, event localisation in the 2-d plane can be achieved.

The detector achieved a nuclear recoil threshold of 50keV_r in 2015 with efficiency of 40% for 60keV_r recoils and reached 100% for 350keV_r events [144]. Despite the high threshold and small size of the NEWAGE detector, the collaboration is the first directional WIMP search experiment to project the reconstructed direction of observed background events on a sky map as shown in Figure 2.20. These results were obtained after analysing 31.6 days of their WIMP search data. In that figure, the expected nuclear recoil directions for WIMPs arriving from the direction of travel of the solar system (toward the Cygnus constellation) is compared to the actual observed background events. The red points in Figure 2.20 are observed background events while blue points are the expected WIMP induced nuclear recoils which should be oriented in the direction of the Cygnus constellation. It can be seen that the observed nuclear recoil events (red points) are not consistent with the expected WIMP induced

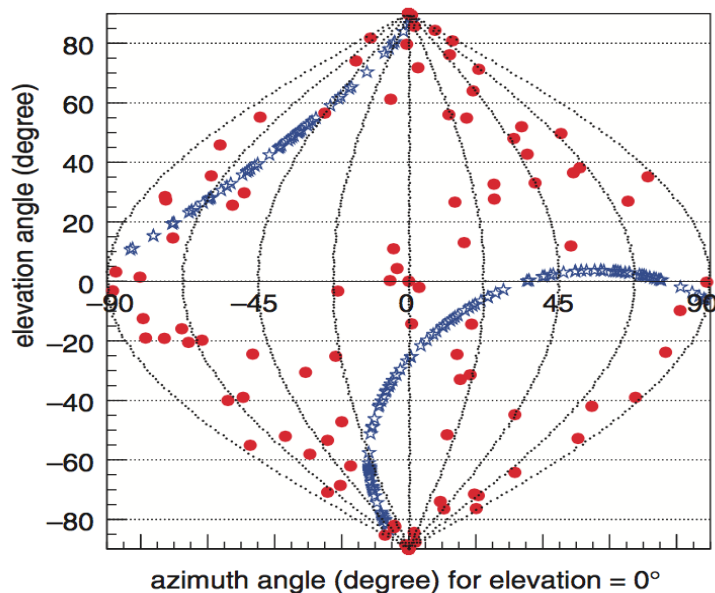


Figure 2.20: Sky map of background nuclear recoil events observed in the NEWAGE-0.3b μ -PIC detector during WIMP search operations [144].

event distribution (blue points). Hence, using these results, an upper spin-dependent WIMP-proton cross section limit of 557 pb was obtained for $200 \text{ GeV } c^{-2}$ WIMPs. This result is a factor of 10 better than their first ever direction sensitive WIMP search result presented in Ref. [176]. The results in Figure 2.20 show that the NEWAGE-0.3b μ -PIC is highly dominated by background events. The NEWAGE collaboration are working towards reducing this background level and have recently attracted funding to build a 1 m^3 directional WIMP search detector with similar readout configuration to be operated in the Kamioka underground laboratory, as part of the CYGNUS-TPC project.

2.8.2 DMTPC directional WIMP search experiment

The Dark Matter Time Projection Chamber (DMTPC) is a 10 litre electron-drift directional WIMP search detector located in the Waste Isolated Pilot Plant (WIPP), New Mexico, USA [177]. Figure 2.21 shows the basic components in the DMTPC detector. The detector consists of two optically isolated back-to-back TPCs with drift length of 10 cm [177, 183]. For a typical operation, it is filled with 75 Torr of pure CF_4 gas. The

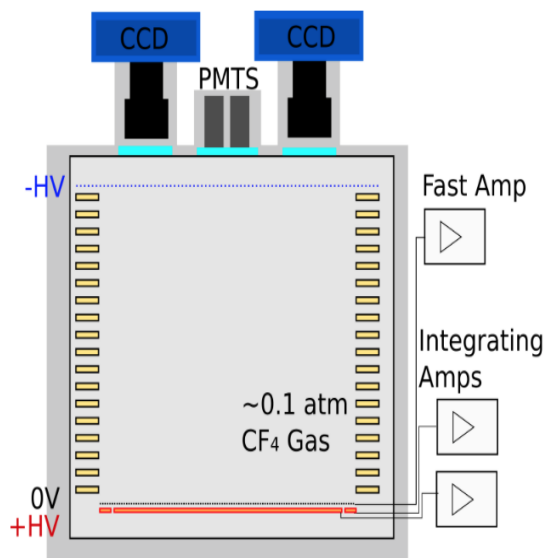


Figure 2.21: Schematic of the DMTPC detector [182].

field cage is made up of copper rings with 27 cm inner diameter.

When a particle scatters off a target nuclei within the active volume of the detector, ionization electrons due to the resultant nuclear recoils are drifted in a uniform field of 0.25 kV cm^{-1} toward a mesh based amplification region where electron avalanche is created with gas gain of about 50×10^4 [182]. In a typical operation, the amplification mesh and the anode can be biased to 0 V and 680 V, respectively. The mesh to anode separation is $440 \text{ }\mu\text{m}$ [183]. The scintillation light produced from this avalanche is recorded with two CCD cameras and a photomultiplier tube (PMT) while the charge signals are readout through charge sensitive amplifiers.

In 2011, the collaboration analysed 35.7 g-days of WIMP search data and obtained an upper limit of $<2000 \text{ pb}$ spin-dependent WIMP-proton cross section for WIMP of 115 GeV c^{-2} mass [177]. The results from that analyses demonstrated directional sensitivity for nuclear recoils with a threshold of 80 keV at 40° recoil angle resolution. Since that work, the DMTPC collaboration has developed a new 1 m^3 TPC [184]. During the commissioning science runs with the new DMTPC detector operated in a surface laboratory, an improved threshold of about 20 keV was achieved when operated with 23 Torr of pure CF_4 gas [184, 185]. In the future, the collaboration aims to optimise the directional sensitivity of the optical imaging read out, gas gain and

improve background level of the cubic meter scale detector.

2.8.3 MIMAC directional WIMP search experiment

The MIMAC directional WIMP search detector is a bi-chamber TPC installed in the Modane underground laboratory, France [178, 186, 187]. Both chambers are back-to-back, hence, they share a common central cathode. The total volume of the MIMAC detector is $10\text{ cm} \times 10\text{ cm} \times 25\text{ cm}$. For a typical operation, the detector is filled with 38 Torr of 70% CF_4 + 28% CHF_3 + 2% C_4H_{10} gas mixture running in automatic circulation mode [186]. The CF_4 gas is used for the spin-dependent WIMP-proton sensitivity while the CHF_3 + C_4H_{10} admixture is used to reduce electron drift velocities in the active volume of the detector to enhance track reconstruction [187].

When a particle scatters off a target nuclei in the MIMAC detector, ionization electrons are drifted toward a bulk metallic micro-mesh for charge amplification through electron avalanche. The amplified signals are passed through a $256\text{ }\mu\text{m}$ amplification region to reach a pixellized ($424\text{ }\mu\text{m}$ resolution) anode strips [178]. This readout technology where micro-mesh is coupled to an anode strip is known as MicroMegas [188, 189]. In Figure 2.22, the micro-mesh is marked as grid while the anode strips are marked as anode.

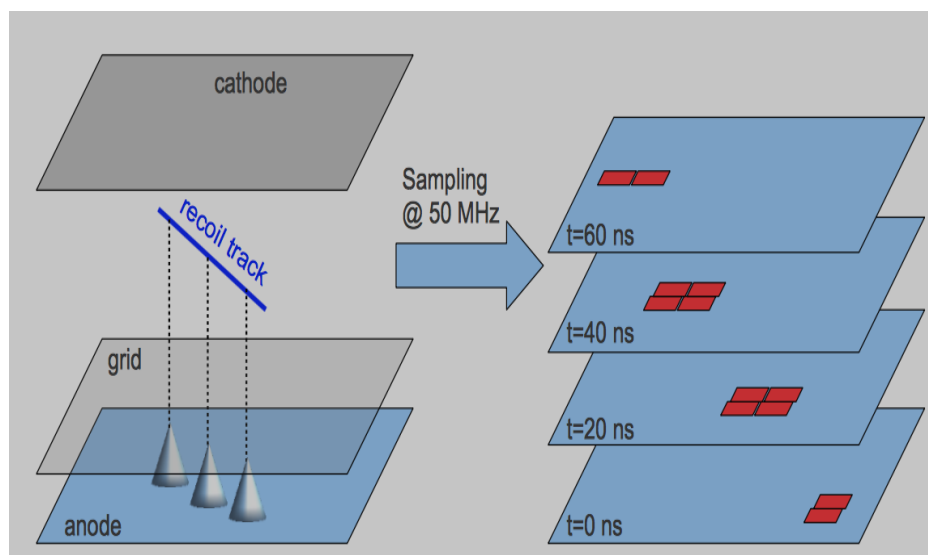


Figure 2.22: Principle of operation of the MIMAC directional WIMP search μ -TPC detector [190].

2. WIMP Detection and experimental searches

Finally, the signals on the anode strips are read out every 20 ns using fast electronics as shown in Figure 2.22. The MIMAC collaboration has not released any WIMP search data at the time of compiling this thesis, rather their studies have been mainly on optimization of three dimensional track reconstruction with directional sensitivity at low recoil energies. In this, they have achieved a threshold of 2 keV_r being the first directional experiment to develop the capability to probe this lower energy window [186, 190]. Currently the MIMAC group are developing a 1 m^3 time projection chamber (TPC) detector with readout configurations and electronics similar to their prototypes. The aim is to test the low-energy 3-d track reconstruction in larger directional WIMP search experiment proposed to run in China Jinping Underground Laboratory (CJPL) located in Yalongjiang Jinping Hydropower Station, Sichuan, China as part of the CYGNUS-TPC project.

2.8.4 DRIFT directional WIMP search experiment

The Directional Recoil Identification From Tracks (DRIFT) experiment is the world's most sensitive directional WIMP search experiment in the spin-dependent WIMP-proton and WIMP-neutron parameter cross sections parameter spaces. The experiment has been in operation for over a decade in the STFC underground science facility in Boulby mine [191, 192], England. During these years, the DRIFT collaboration has operated different versions of gas based TPCs as directional WIMP search detectors. These include DRIFT-IIa, DRIFT-IIb, DRIFT-IIc to the present version of the detector known as DRIFT-IIId. See Figure 2.23 for a pictorial view of the DRIFT-IIId detector.

The detector comprises two back-to-back negative ion TPCs of 1 m^3 total volume instrumented with multi-wire proportional chamber (MWPC) readouts [192]. In this device, the two 50 cm long TPCs are separated by an aluminized-mylar thin-film central cathode biased at -31.9 kV to create a drift field of 580 V cm^{-1} for anions drifting towards the two MWPCs [112, 113, 193]. The target gas used in the DRIFT-IIId detector comprise of 30:10:1 Torr mix of CS_2 : CF_4 : O_2 gases. The CS_2 gas is a highly electronegative gas added to capture free electrons in the gas for reduced diffusion effects on the signal tracks along the drift axes. Fluorine component in the CF_4 gas is used for spin-dependent WIMP-proton interaction searches [98] while the 1 % of O_2 creates different species of anions. This observation of different species of anions is consistent

2. WIMP Detection and experimental searches



Figure 2.23: Pictorial view of the DRIFT-II detector when it is partly removed from the stainless steel vacuum vessel.

with expectations from three-body electron attachments to gas molecules in presence of oxygen via Block-Bradbury mechanisms [194, 195, 196, 197, 198]. The attachment of electrons to neutral molecules through this mechanism in oxygen gas mixtures can result in formation of different species of anions with disparate mobilities [196, 198]. Each of the resulting anion species observed in the DRIFT experiment drifts at slightly different speed [199]. The difference in the arrival times of these species of anions to the MWPC readouts are used to determine the distance of event vertex relative to the readout plane. This has aided the full fiducialisation of the DRIFT-II detector resulting in background free operations at relevant sensitivities [113].

Each MWPC comprises parallel stainless steel anode wires of 20 μm diameter placed between and orthogonal to two grid wire planes made from parallel 100 μm

2. WIMP Detection and experimental searches

diameter stainless steel wires at 1 cm anode-grid distance as illustrated in Figure 2.24.

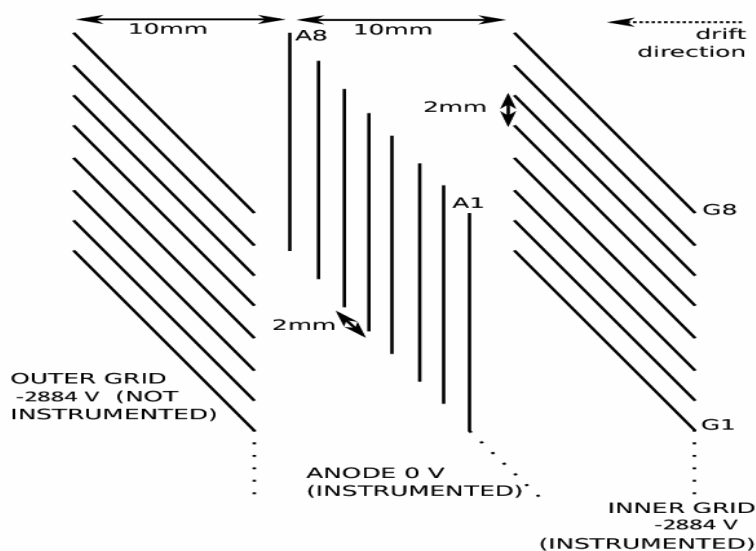


Figure 2.24: Wire configuration in each of the MWPCs in the DRIFT-II detector.

For more on operational principles of MWPCs, see Refs. [200, 201]. The grid potential is set at -2.884 kV, which is enough to strip off electrons from the drifting anions and induce electron avalanches near the grounded anode wires. Each of the wire planes consist of 552 wires with 2 mm spacing. In the anode plane, 22 edge wires are grouped as guard wires, while the subsequent 82 wires are grouped as an anode veto. For the grid plane, 104 edge wires are grouped as a veto against side events. The remaining 448 wires each in the anode and grid planes are grouped down to 8 channels such that every 8th wire in each of the readout planes is read out by the same electronics channel. Each of the 8 channels is then read out with a Cremat CR-111 charge sensitive pre-amplifier [202], followed by a Cremat CR-200-4 μ s shaping amplifier [203]. Signals from the shaping amplifiers are passed through high-pass filters with a time constant of 110 μ s. Each of the high-pass filters consist of 2.2 μ F capacitor and 50 Ω resistor. Signals below the cut-off frequency of ~ 10 kHz are then digitised and recorded to disk for analyses using NI PXI-6133 data acquisition system at 1 MHz sampling speed per channel. These data are recorded with a trigger threshold of 15 mV corresponding to about 20 keV_r. Two inbuilt ^{55}Fe and an external ^{252}Cf

2. WIMP Detection and experimental searches

sources are used to calibrate event energies and the nuclear recoil detection efficiency of the detector as discussed in Chapters 4 and 5.

In any given WIMP search or calibration source operation, the CS_2 and $\text{CF}_4 + \text{O}_2$ gases are mixed in a mixing cylinder. This mixing cylinder is marked as Mixing Chamber in Figure 2.25. The resulting mixture is then stored in the supply cylinder (marked

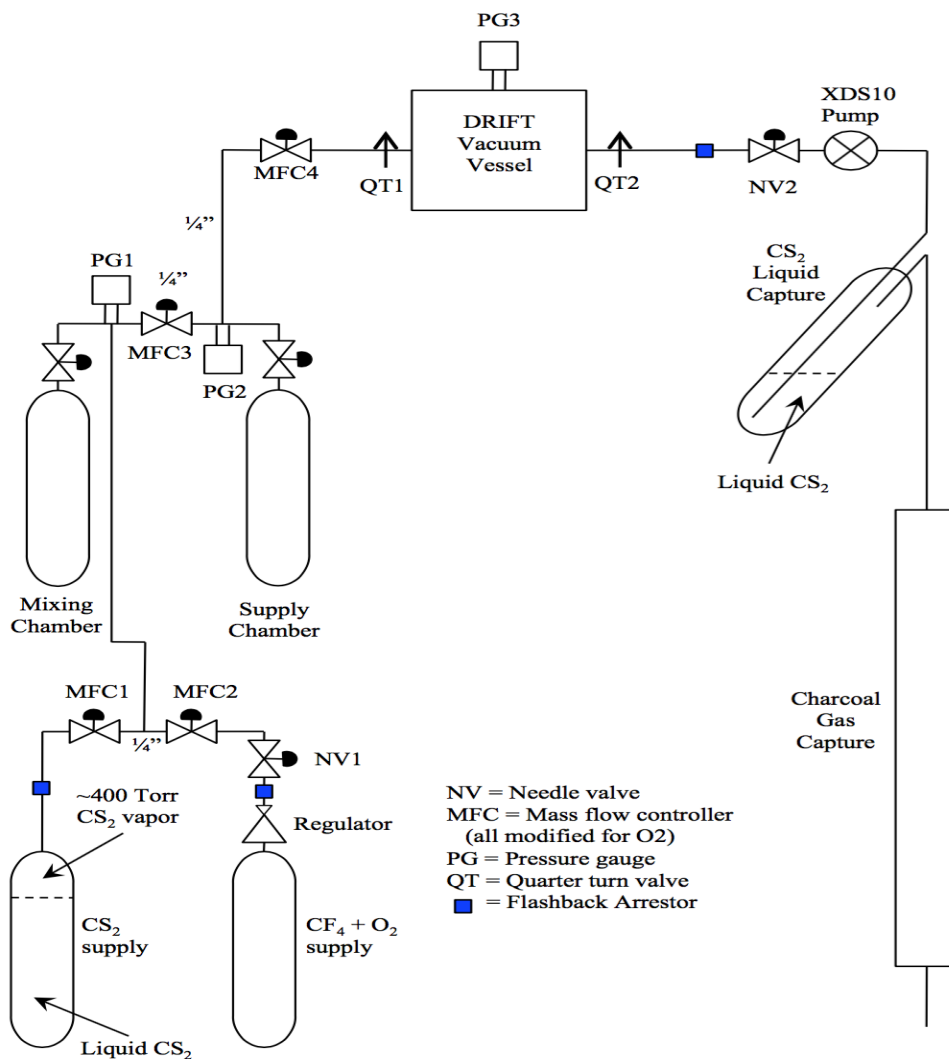


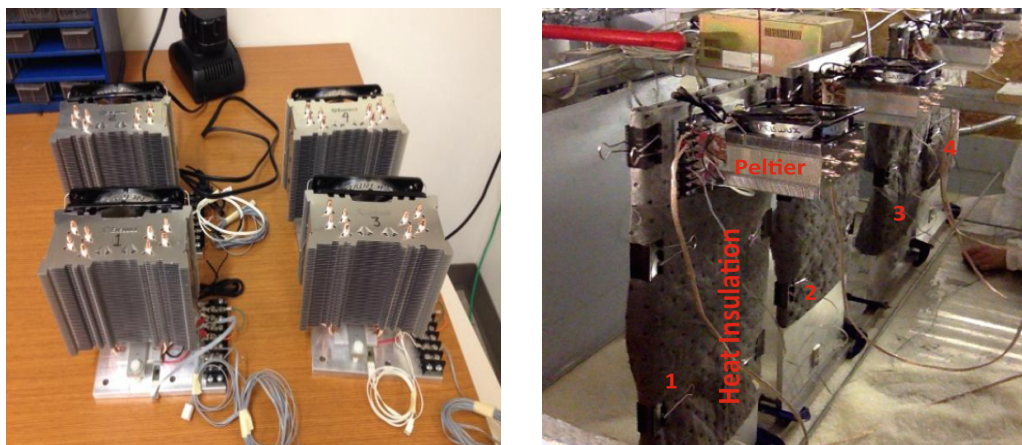
Figure 2.25: Automated gas mixing and flow control for DRIFT-II detector.

as Supply Chamber in Figure 2.25) and used to maintain the gas pressure of the stainless steel vacuum vessel. In the output of the vacuum vessel, the used CS_2 gas are collected with a liquid capture mechanism while the CF_4 and O_2 gases are diluted with

2. WIMP Detection and experimental searches

nitrogen gas and then passed to the mine cavern through a charcoal tube to capture any residual CS_2 as shown in Figure 2.25. The CS_2 extraction is necessary because of its toxicity and fetid odour, hence, requires careful and regulated handling. The pressures in the Mixing Chamber, Supply Chamber and the stainless steel vacuum vessel are measured with pressure gauges, marked as PG1, PG2 and PG3, respectively in Figure 2.25. The quarter turn valves (QT1 and QT2) are always open when the detector is operated in the automated gas flow mode. The needle valves (NV1 and NV2) are used to control the overall gas flow rate in the detector. The four mass flow controllers (MFC1 to MFC4) in Figure 2.25 ensure that appropriate gas pressures are maintained at all stages of the gas mixing procedure while the flashback arrestors (shown as blue square boxes in Figure 2.25) are used to avoid any gas back-flow. This is because uncontrolled forward and backward gas flow in the presence of the O_2 admixture can result in a fire burst incident. A typical gas mixing frequency during an automated gas flow run is ~ 16 mixing cycles per day corresponding to a rate of about 140 h^{-1} which is equivalent to about one detector volume change per day.

The temperature of the $1500 \text{ mm} \times 1500 \text{ mm} \times 1500 \text{ mm}$ stainless steel vacuum vessel which holds the detector under pressure is regulated using four Peltier cooling units shown in Figure 2.26. To achieve temperature of 6° below the intrinsic temperature of the laboratory, each of the Peltier cooling units was coupled to the stainless steel vacuum vessel ribs through an aluminium plate and powered with a 12 V desktop computer (PC) power supply. The aluminium plates are insulated as shown in Figure 2.26(b) to minimize heat radiation from the laboratory to the vessel. In 2015, the DRIFT collaboration analysed 46.3 live time days of background free WIMP search data and obtained an upper limit of 1.1 pb on spin-dependent WIMP-proton cross section for a $100 \text{ GeV } c^{-2}$ WIMP [113]. This result is the most stringent limit from a direction sensitive WIMP search detector. In fact, this new DRIFT-II d result is better than results from other directional WIMP search experiments by at least a factor of 700. For more details on the detector fiducialisation, status and recent results, see Chapters 4 and 5 of this thesis.



(a) Peltier cooling units before installation.

(b) Cooling system installed on DRIFT-II detector.

Figure 2.26: Peltier cooling systems used to maintain the temperature of the DRIFT-II detector below the intrinsic underground laboratory temperature. In (a) is the four Peltier units marked 1 to 4 in black while (b) shows the four Peltier cooling system after installation marked 1 to 4 in red.

2.9 R&D on directional WIMP search detectors

There are many R&D projects in different universities around the world aimed at developing new improved technologies for directional WIMP search experiments. These developmental projects can be divided into gas based studies and other states (solid and liquid) projects.

2.9.1 R&D on gas based directional WIMP search detectors

There are many directional WIMP search time projection chambers used for optimization of the readout technologies and other general R&D purposes. Some of such project that need a mention include the D^3 experiment [145, 204] located in the University of Hawaii and NITEC detector based in Italy [205]. The principle of operation of the D^3 and NITEC detectors is based on ionization electron multiplication through electron avalanches using gaseous electron multipliers (GEMs). There is double GEM amplification stages in the D^3 detector. After signal amplification via electron avalanches, the final signals from the detector are read out using ATLAS FE-13 pixel chips [206]. The

2. WIMP Detection and experimental searches

detector achieved a threshold of 1 keV_r with 3-d track reconstruction in 2015 when measurements were performed with 760 Torr of Ar:CO₂ mixed in a 70%:30% ratio [145].

The NITEC detector use triple GEMs separated by mm scale distance with an appropriate potential bias to create the required ionization electron avalanche [205]. Typically, the detector operates with 760 Torr of CF₄, CS₂ mixture. The directional aim of the NITEC experiment is to investigate the viability of other alternative methods that can be used to localise an event vertex in the fiducial volume of a directional detector using mixtures of negative ion gas.

Computational results indicate that columnar recombination in dense Xenon gas TPCs may be used to extract directional information from WIMP induced nuclear recoil tracks [207, 208, 209]. This follows the argument that electron-ion pair recombination in gas TPCs depend mainly on the existing angle between the nuclear recoil track and the electric field, after ionization [208]. This can be applied by comparing scintillation signals recorded with photomultiplier tubes (PMTs) before columnar recombination occur to surviving ionization electrons to determine the required recoil angle [208]. However, there are no existing empirical measurements to support these claims at the time of writing this thesis. There are also efforts to test this potential directional signatures in Liquid Argon based experiments as described in Refs. [210, 211]. The use of spin 1/2 polarized high pressure ³He targets for discrimination of events directions in WIMP search experiments has also been motivated in Ref. [212] but requires empirical measurements.

2.9.2 R&D on possible use of solids in directional WIMP searches

The NEWS collaboration has made some progress in the use of nuclear emulsions for directional WIMP searches [213, 214, 215]. The experiment consists of gel immersed AgBr crystal. When a particle scatters off a Ag nucleus in the crystal, the recoiling nucleus causes ionization along its track thereby leaving a latent image of the track which is recorded using a fine grained X-ray microscope [214]. Typical track length of a keV_r nuclear recoil in nuclear emulsions is in nm scale. In the NEWS detector, these tracks are recorded with μm scale spatial resolution readout [215] with no resolution in time [213]. This resolution needs more improvement for optimal performance of the

2. WIMP Detection and experimental searches

detector technology in directional WIMP search experiment.

In 2015, the DCant collaboration suggested the use of arrays of aligned carbon nanotubes (CNTs) for applications in directional WIMP search experiments [216]. The principle of operation of the detector follows that a particle can scatter off target carbon nuclei in a layer of one of the CNTs. Then the ejected carbon nuclei recoils into the hollow of the tubes or could be stopped in the bulk of the array depending on the energy and the direction of the particle that initiated the interaction [216]. The ionization signal due to the recoil is channeled to a triple GEM setup for signal amplification and read out. Studies of the directions of nuclear recoils in the hollow of the CNTs could then be used in WIMP search experiments to discriminate backgrounds from WIMP events coming from the direction of constellation Cygnus.

The ADAMO collaboration has proposed and made some theoretical efforts toward using zinc tungstate (ZnWO_4) anisotropic crystal scintillator to develop a solid state directional WIMP search detector [217, 218]. This could be achieved by utilising the anisotropic nature of the ZnWO_4 crystal which makes its response and resulting pulse shape to depend mostly on the direction of the incident particle relative to the crystal axes. There are R&D works [219] toward building a prototype of the ADAMO project.

However, since the observable nuclear recoil track lengths in solid crystals are relatively small (in nm to μm) and hence, will be very hard for charge distribution along nuclear recoil tracks to be resolved compared to events of the same energy range in TPCs (tracks in mm). The later remains the best technology for directional WIMP search experiments.

2.10 CYGNUS-TPC a future WIMP telescope

The CYGNUS-TPC is a world wide initiative to build a ton-scale directional WIMP observatory with enough sensitivity to probe for WIMPs beyond the neutrino floor (see Section 2.6). In this region of the WIMP-nucleon cross section, it is expected that non-directional experiments will be dominated by coherent neutrino backgrounds, hence, the need for a massive directional detector. This is because the sensitivity of a WIMP search detector scales with mass of the target material as shown in Equation 2.37.

There is current effort by all the TPC based directional experiments earlier discussed in Sections 2.8 and 2.9, toward building this modular detector. The current plan

2. WIMP Detection and experimental searches

is to build 6 independent 100 m³ volume TPC detector modules which can be installed in 6 different participating countries: UK, USA, Japan, Italy, China and Australia and operated with 200 Torr of SF₆ target gas. Thus, WIMP search data obtained from this current design can be combined in the CYGNUS-TPC analyses framework to reach the solar neutrino bounds in about 6 data years.

However, there are some technical issues to be considered before the detector can be built. One of the key issues is the readout technology to be used. The MicroMegas, the Gaseous Electron Multipliers (GEMs) or the Thick Gaseous Electron Multipliers (ThGEMs) can be used, if there are future experimental evidence that can show that these readout technologies can work as large area read outs for gas TPCs. For more details on the experimental reach of each of these readout technologies in the context of directional WIMP searches, see Ref [220]. The configuration of the conventional MWPCs discussed in Refs [200, 201] (which works for large area TPCs) does not allow that one MWPC can be used as a common readout for two back-to-back TPCs, hence, the need for an alternative design. The so-called one-plane MWPC may be a viable alternative. In the one-plane MWPC, the anode and grid wires are sandwiched on the same wire plane, reducing the number of wire planes from usual 3 (in conventional design) to 1 (one-plane design). Thereby reducing the overall cost of front-end electronics for signal read out. For more on the one-plane MWPC, see Chapter 3. The cost of the signal readout can be further reduced if the MWPC readouts can be grouped without compromising the detector directional sensitivity.

To address these issues, a multiplexing scheme is developed in Chapter 3 of this thesis with the aim of reducing the cost of readout by a factor 20 relative to a situation where each of the signal channels is readout. To understand the possibility of one dimensional readout in the CYGNUS-TPC detector, data from each of the MWPCs in the DRIFT-IIId detector were grouped in a simplified mode as a simulation of this operational mode. Results from the analysis of the simplified 1-D data is shown in Chapter 5 of this thesis.

The CYGNUS-TPC detector can also be fiducialised using the existing technology through the addition of 1% of O₂ in mixtures of CS₂+CF₄ gas, as done in the DRIFT-IIId detector. Another possible operational gas is SF₆ (electronegative) gas which has been shown to produce a kind of fiducialisation minority carrier peaks at very high drift voltages [221, 222]. Electronegative gas mixtures with ¹⁹F component are most

2. WIMP Detection and experimental searches

favoured for low signal diffusion and WIMP-proton spin-dependent sensitivity. The possible operational threshold of the detector ranges from 1 keV_r to 20 keV_r depending on the adopted readout technology as discussed in Section 2.8.

In the future, it is expected that current directional experiments will continue operations as R&D projects for the CYGNUS program. Presently all the directional WIMP search TPC-based experiments are sourcing for funding to build this gigantic modular WIMP search telescope using existing technologies.

2.11 Conclusion

This chapter presented and discussed the three main channels that are presently used in WIMP search experiments. These include, the concept of direct detection, indirect detection and WIMP production in the large hadron collider experiment. Theoretical backgrounds needed to compute WIMP induced nuclear recoil rates in direct WIMP search detectors were also discussed, especially for spin-dependent WIMP-proton and WIMP-neutron interactions. Typically, this calculation was performed for a detector with fluorine target as needed for the analysis presented in Chapter 5 of this thesis.

The expected signals from WIMP induced nuclear recoils in direct WIMP search detectors were presented. These signals are ionization charges, scintillation lights and phonon heats. The chapter also discussed the two main galactic signatures that can be observed in some WIMP search experiments. These galactic signatures include the directional and non-directional components due to motion of the Earth relative to the WIMP wind. These were discussed in the context of existing detectors. Current status and results obtained from leading experimental WIMP search efforts were also presented.

Finally, the plan and motivations for a massive directional WIMP search detector known as CYGNUS-TPC was discussed. The summary of efforts toward building this massive directional WIMP search detector was presented. It is essential to build a massive directional WIMP search detector especially now that many experiments have excluded almost all the parameter spaces above the neutrino floor, beyond which coherent neutrino backgrounds are expected. Hence, leading non-directional WIMP search detectors will soon be dominated by these neutrino backgrounds.

Chapter 3

MUX readout for CYGNUS-TPC

3.1 Introduction

CYGNUS-TPC is a proposed massive gas-based time projection chamber to be operated as the first directional WIMP search telescope, see section 2.10 in Chapter 2 for more details on the CYGNUS-TPC concept. The need to scale-up directional WIMP search time projection chambers with low energy threshold has been building [97, 141]. A massive directional WIMP search detector is essential to be able to obtain the required sensitivity to probe for WIMPs beyond the neutrino floor. In that parameter space, non-directional WIMP search detectors searching for low mass WIMPs will be dominated by solar neutrino backgrounds coherently scattering off target nuclei in few more years [146]. A directional WIMP telescope will also be needed to confirm the origin and anisotropic nature of WIMP-induced nuclear recoils detected by non-directional detectors especially when there is a hint for WIMP discovery [223].

There are many issues to be considered before deciding on the best technology to be adopted in the design of this type of massive directional WIMP search detector. One of these issues is optimisation of the TPC design and construction so as to minimize cost. Since the readout electronics are likely to be situated inside the vacuum vessel (to minimize signal loss), minimum power dissipation from the front-end electronics is desirable in order to maintain a low ambient temperature in the vessel. The physical size of the front-end electronics should also be reasonably small.

One method that offers solutions to these issues is signal multiplexing, provided

3. MUX readout for CYGNUS-TPC

this can be achieved without significantly compromising sensitivity to the x-y position information of the recorded interactions. The choice of the multiplexer (MUX) design and electronics needs to be carefully made to avoid introduction of unnecessary delays and noise which can smear the signal.

For instance, consider a 100 m^3 volume of CYGNUS-TPC directional WIMP search detector with a maximum drift distance of 500 mm, as illustrated in Figure 3.1 with one-plane multiwire proportional chamber (MWPC) readout. In the one-plane

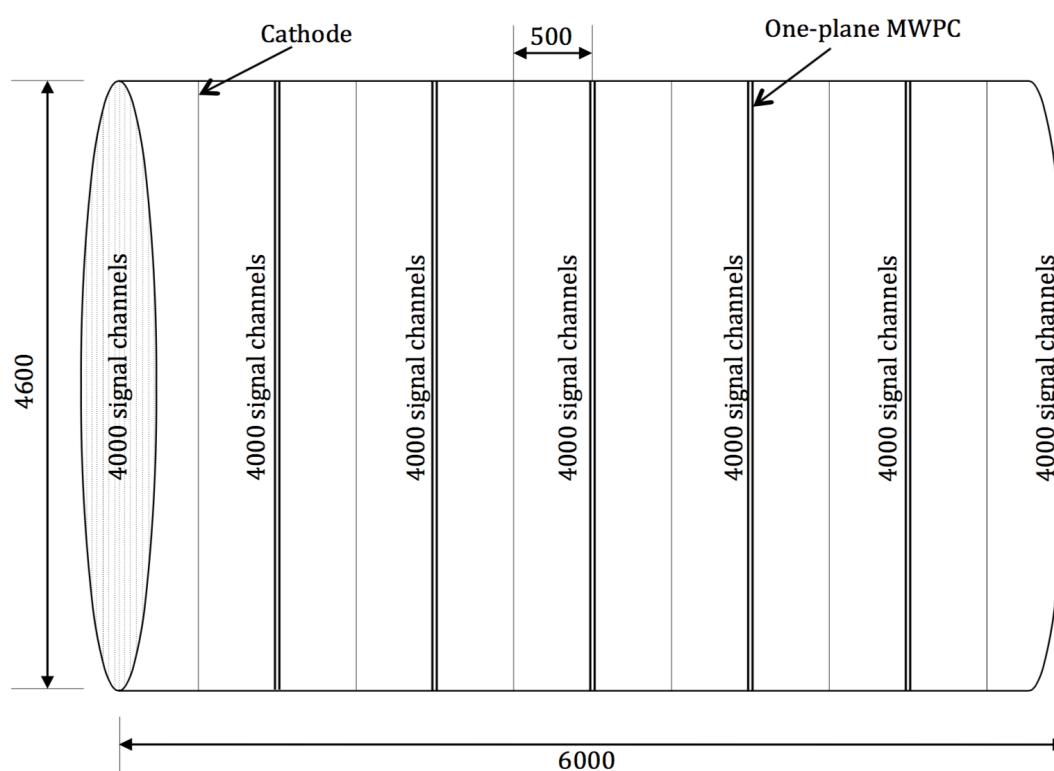


Figure 3.1: Sketch of possible cylindrical and modular design for a 100 m^3 CYGNUS-TPC. The number of signal channels from each of the constituent one-plane MWPC readout are shown without considering the veto signal channels. All dimensions are in mm.

MWPC configuration, grounded anode wires are sandwiched between two parallel grid wires which are biased with the appropriate voltage to create signal amplification through electron avalanche. But conventionally for directional WIMP searches as in the DRIFT-II experiment (see Section 2.8.4 and Ref. [192]), an MWPC consists

of three wire planes: one anode and two grid wire planes. In this conventional MWPC set-up, the grounded anode wire plane is placed in the orthogonal orientation between the two grid wire planes.

For a one-plane MWPC with 2 mm anode-to-anode wire spacing, the detector in Figure 3.1 will produce 14000 anode signal readout channels and 2100 anode veto channels resulting in a total target mass of about 1 ton when filled with 200 Torr of SF₆ gas. This is because a single one-plane MWPC can be used to readout two back-to-back TPCs separated by a common cathode as shown in Figure 3.1 thereby reducing the cost of the front-end electronics relative to the conventional design. But if every 20 signal channels can be multiplexed with a 20:1 multiplexer board, then the overall cost of the detector readout can be further reduced by a factor of 20.

Hence, this chapter will focus on R&D work done to investigate the feasibility of the signal multiplexing in the CYGNUS-TPC design using a 20:1 multiplexer board, designed with 5 pieces of low noise, low cost and low power dissipating 4:1, LMH6574 [224] chips from Texas Instruments. To do this, a miniature prototype of the one-plane MWPC based detector was designed and constructed for use in testing the performance of the multiplexing electronics. The details of the design and construction of the miniature time projection chamber with the one-plane MWPC readout used in testing the multiplexing electronics and that of the multiplexing electronics are discussed below.

3.2 Design and construction of miniature TPC detector

The miniature time projection chamber is a 2.6 cm × 2.6 cm × 10 cm (known as DRIFT-IIe pro) detector with one-plane MWPC readout and a copper plate cathode. In the one-plane MWPC, each of the anode wires are sandwiched between two parallel grid wires with anode-grid separation of 1 mm as illustrated in Figure 3.2. In that figure, the bigger circular black dots represent the grid wires while the smaller ones are the anode wires. This wire configuration was chosen to enhance the chance of using one MWPC to read out two back-to-back TPCs and to minimise the risk of sparks due to anode and grid wire frame sag when subjected to the required tensions at these large areas. The anode and grid channels were made up of 20 μm and 50 μm diameter stainless steel wires, respectively. These anode and grid wires were placed into position

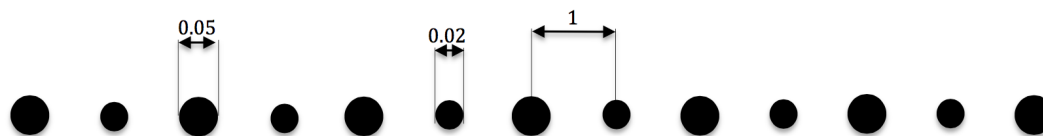


Figure 3.2: Configuration of anode and grid wires in the DRIFT-IIe pro detector to be operated with an anode-grid field of 850 V mm^{-1} . Dimensions are in mm.

on a customized printed circuited board (PCB) using a Quad Wire Winding Robot (QWWR). The QWWR was designed and setup by the author, with other members of the collaboration in Occidental College, Los Angeles, between May and June 2014. The design details of the one-plane MWPC PCB and processes used to wind the wires using QWWR are discussed in Sections 3.2.1 and 3.2.2, respectively.

3.2.1 EAGLE PCB design for the one-plane MWPC

The CadSoft Easily Applicable Graphical Layout Editor (EAGLE) printed circuit board (PCB) design software, version 6.5.0 [225] was used to design the 20 channels miniature MWPC board. The layout editor of the EAGLE PCB design software is shown in Figure 3.3.

In EAGLE, the *Tool Box* located at the left side of the panel in Figure 3.3 comprises of major design tools which can be used to add and edit components in the EAGLE design *workspace* during circuit design. The *workspace* is the region of the layout editor used for viewing design progress. For instance, the *Add* key in the *Tool Box* or *Command line* can be used to import design packages, surface mount devices (SMDs) and solder pads from one of the EAGLE libraries to the *workspace*. In this work, the more complete and free-available *adafruit.lbr* library was used. The design packages in the EAGLE library were used to set up the circuit schematic diagram developed in the EAGLE schematic layout editor. The area of each of the SMDs, included on the board design for soldering signal wires to the board is $3.532 \text{ in} \times 0.254 \text{ in}$. These are marked as "Soldering pads" in Figure 3.4. During the board design, R2512W and C1808 SMDs were added in each grid channel to aid installation of $100 \text{ M}\Omega$ power resistor and 10 nF decoupling capacitor, respectively. The power resistors were used to minimize the amount of current (μA) that can be drawn by the grid wires, while

3. MUX readout for CYGNUS-TPC

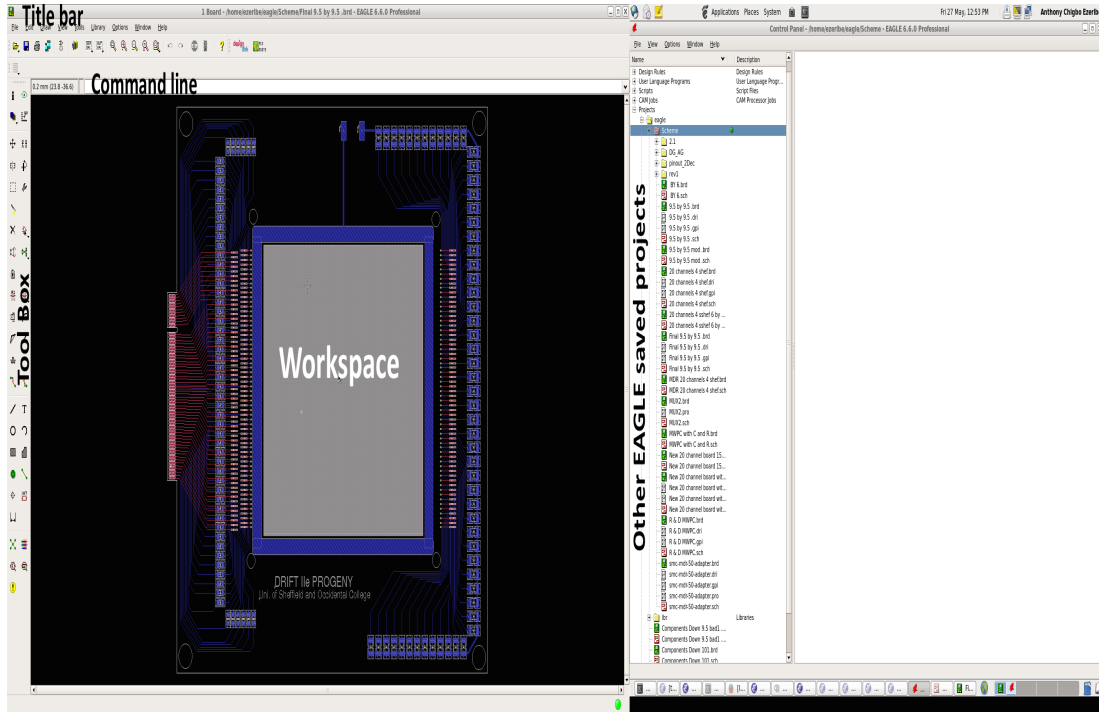


Figure 3.3: EAGLE PCB design layout editor.

the decoupling capacitors allow only a.c. signals to pass through it, thereby serving as an active veto line for unwanted d.c. signals. They also help to prevent the preamplifiers connected on the the signal line after the capacitors from discharging the grid wire. Hence, in this mode, signals from the anodes and the grids can all be recorded to disk for analyses.

In Figure 3.4, the $2.6 \text{ cm} \times 2.6 \text{ cm}$ sensitive aperture is the active area of the one-plane MWPC used for building the DRIFT-IIe pro detector. This is surrounded by a blue 4 mm thick copper field ring, biased to enhance signal avalanche on grounded anode wires. In that figure, electrical components which are located at the bottom layer of the board are shown in blue while components on the top layer of the board are shown in red. It can be seen that there are two arrays of wire soldering pads for the anode and grid wires in the left side (signal side) of the sensitive aperture while in the right side (power side), only one array for the grid wire channels can be seen. This is because the anode signal wires can be held in position with epoxy on the power side of the board since they are not biased.

3. MUX readout for CYGNUS-TPC

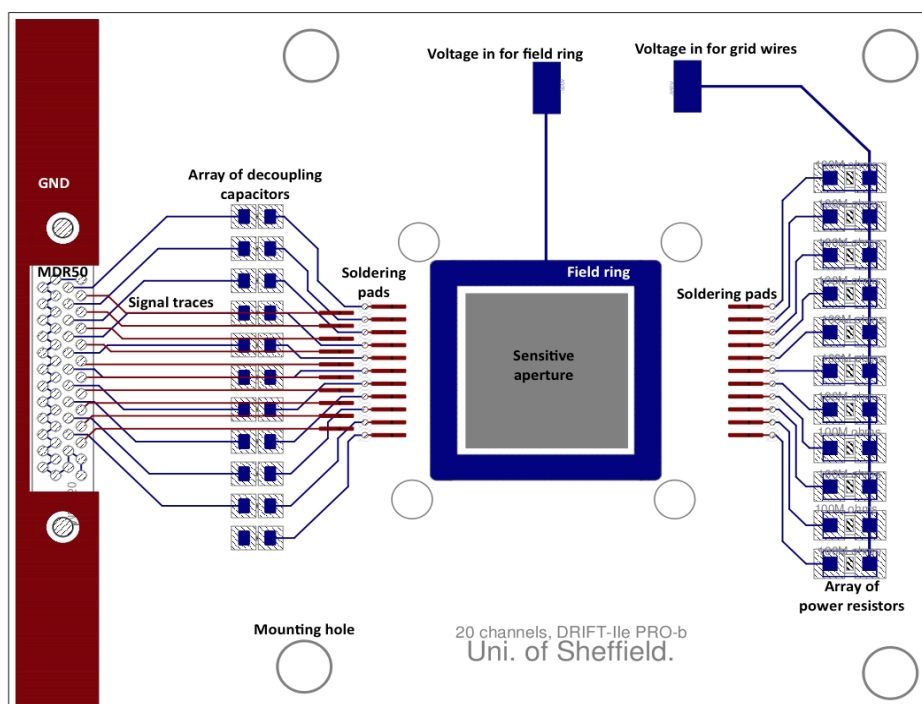


Figure 3.4: Board layout of the miniature one-plane MWPC used in the DRIFT-IIe pro detector.

The final version of the EAGLE PCB schematic was then loaded into the EAGLE board layout editor, this is after proper signal routing, placement of circuit packages such as the surface mount devices, connector pads, grounding points etc, have been completed for more advanced finishing processes in the board design. This is to set the actual board dimension, arrange the SMDs, soldering pads, connector pads and signal traces in the right position on the board depending on specific design requirements. A snapshot of the EAGLE designed PCB for the miniature one-plane MWPC in the board layout format is shown in Figure 3.4.

After the design process in the board layout editor, identical board components were selected and exported in a gerber file format [226] using the *CAM processor* function in EAGLE. In total, eight gerber files with extensions *.GTL*, *.GBL*, *.GTS*, *.GBS*, *.GTO*, *.LOX*, *.CNC* and *.TXT* were generated and submitted to Newbury Electronics limited for manufacture. In this gerber file formats, information about signal ground (GND) copper pour for the top and bottom layers of the board are exported as *.GTL* and *.GBL* files, respectively. The soldermask (thin insulator over the signal

traces) in the top layer of the board are exported as *.GTS* file while that in the bottom layer were saved as *.GBS* file. The files with *.CNC* and *.TXT* extensions were generated with the EXCELLON device in the *EAGLE CAM processor*. These files consist of the board drill data (vias and mounting holes). The *.GTO* file consists of SMD components and board labels. The two layer board of 0.16 cm thickness and 13.8 cm × 10.9 cm surface area was printed on FR4 material. After printing the two layer board, the QWWR was used to place the wires into positions on the MWPC board before the wires were soldered. The details of this method of wire winding is the subject of Section 3.2.2, below.

3.2.2 Wire winding for construction of one-plane MWPC using Quad Wire Winding Robot (QWWR)

One of the main issues in building MWPCs is wire placement on the readout frames. This is because the wires used are very fragile when subjected to the required tensions due to their thin diameters. Hence, using an automated wire winding system reduces the risk of wire breakage while winding and also helps to ensure that uniform tensions are applied to the wires. For the purpose of the work reported here, an automated wire winding robot known as QWWR was developed to produce four 30 cm × 30 cm wire frames in one wire winding session. This wire winding system consists of two major workstations which include the control and wire winding terminals. The control terminal comprise of mainly electronics used in driving the Juggernaut and the winding frame. A pictorial view of the Juggernaut is shown in Figure 3.5.

It can be seen in that figure that the Juggernaut is a motorised pulley system used for sandwiching two wires of different diameters at a given pitch with high precision. It consists of two wire spools, two single grooved pulleys and one double grooved pulley. The wire spools installed in the Juggernaut are represented with shaded triangle headed arrows in Figure 3.6.

Each of the wire spools was mounted on a SPH-54AB-094 stepping motor for unspooling the wires before they are placed on the winding frame. Each of the two single grooved pulleys was used to channel one of the wires (anode and grid) to the double grooved pulley with groove pitch of 1 mm. The anode and the grid wires were then channeled from the double grooved pulley to the winding frame as shown in

3. MUX readout for CYGNUS-TPC

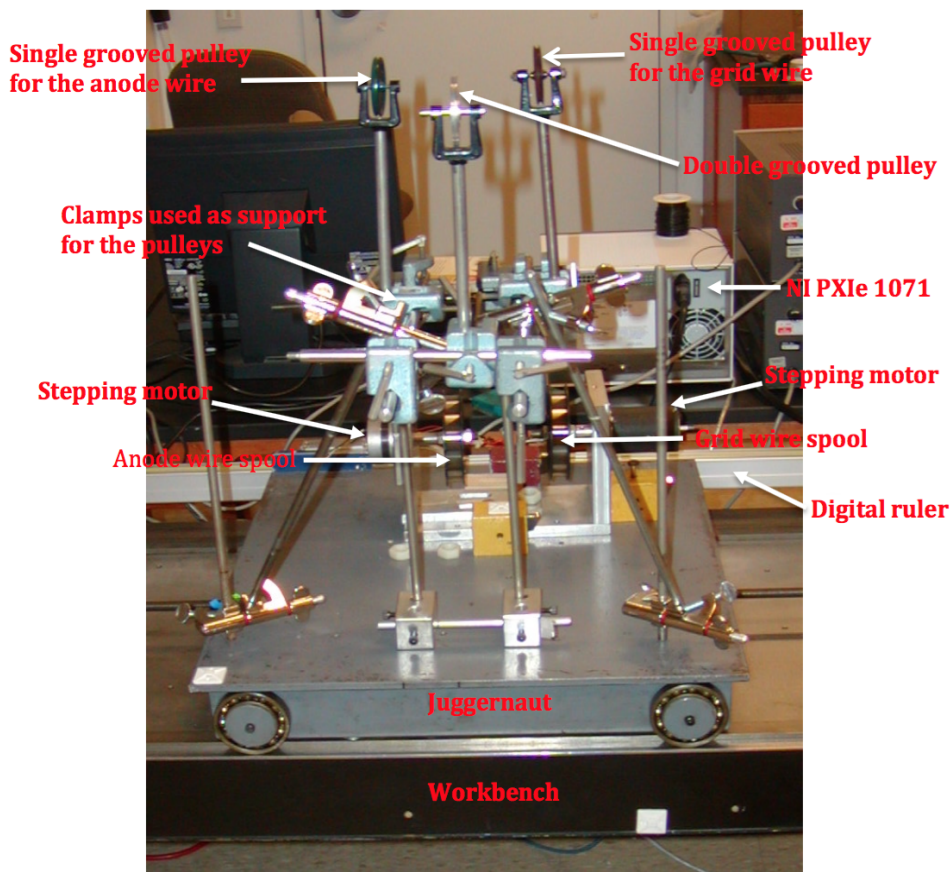


Figure 3.5: Pictorial view of the Juggernaut used for positioning the wires on the QWWR wire frame during the winding process.

Figure 3.6.

A set of tensioning masses M_a and M_g for the anode and the grid wires were applied on the wires, halfway between the double and single grooved pulleys. This is with one end of each of the wires fixed and secured to the wire spool while the other end was secured on the winding frame. The appropriate mass for tensioning the anode and grid wires can be determined using $M_g = \left(\frac{d_g}{d_a}\right)^2 \times M_a$, where d_a and d_g are the diameters of the anode and grid wires, respectively. This mathematical relation was used to ensure that particles of the same energy can induce about the same magnitude of signal pulse (gain) on each of the wires. For this work, the M_a and M_g values used are about 20 g and 130 g, respectively, which scales with the applied tension. The extent and

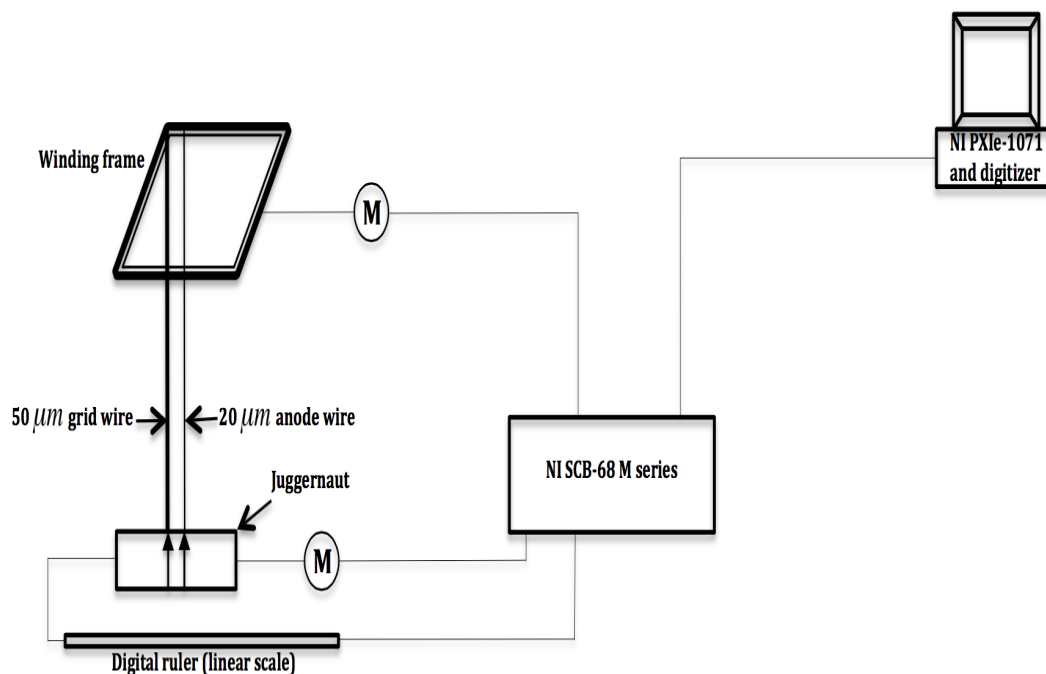


Figure 3.6: Simplified schematic of the major components of the QWWR.

length of the wires that are released from the spool was regulated with a double beam intrusion detector. This stopped the unspooling process when triggered. The intrusion detector was set to trigger when the tensioning masses obstructs the detector beam from reaching the focus. This was useful in preventing the tensioning masses from hitting the laboratory floor while unspooling.

On the winding frame, a Pasco scientific photo-gate 514-06266 was used to stop the winding process when triggered, which also served as a trigger required to unspool the wires after the winding frame completes a quarter turn. A quarter turn occurs when the cubic wire frame completes a 90° turn thereby placing each of the wires at position on one of the four winding frames. The use of the photo-gate to break the winding process, in this form was necessary to ensure that the length of unspooled wires are enough for the next quarter wire wind turn. Apart from the four sides of the winding frame used for positioning the wires the remaining two opposite sides of the cubic wire winding frame were used to keep the frame fixed on a U-shaped base. The wire winding frame and the Juggernaut were driven with SS150-1129 synchronous motors

3. MUX readout for CYGNUS-TPC

while the position of the Juggernaut was tracked with a digital ruler to ensure more accurate control of the position of the wires. The uncertainty in the position of the wires as determined with the digital ruler is about ± 0.005 mm.

The winding process was automated using a C++ based code. The user interface of the QWWR control system is shown in Figure 3.7. It can be seen from that figure that

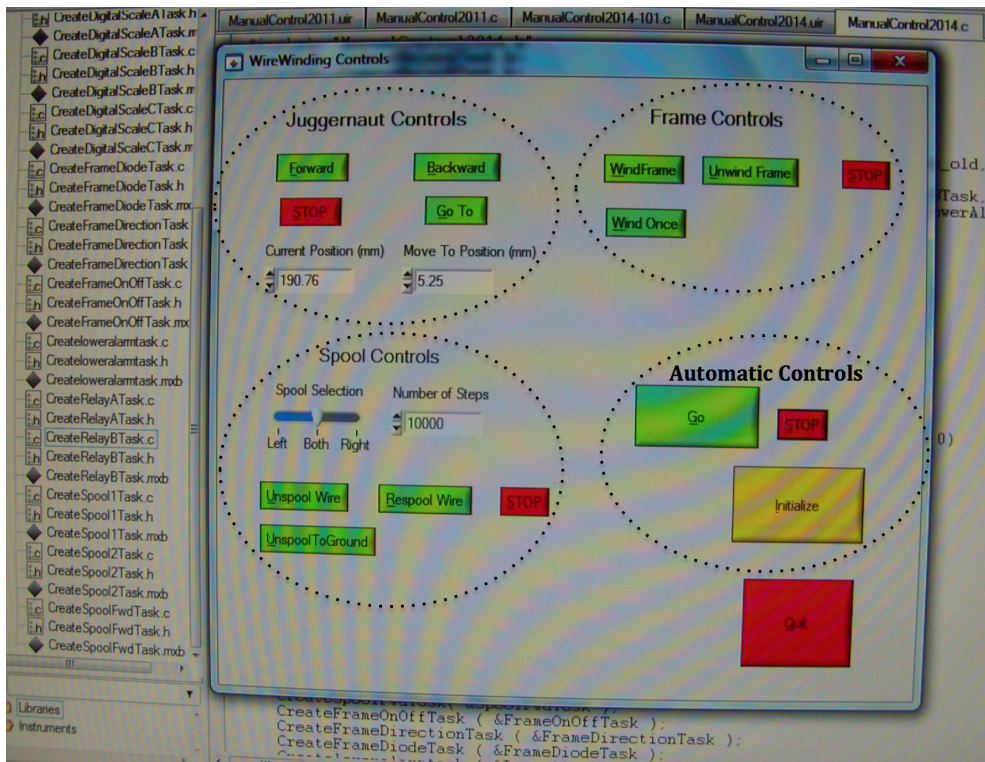


Figure 3.7: Snapshot of the user interface of the wire winding control system.

the user interface is divided into four control sections which include the Juggernaut, winding frame, wire spool and full automated operation control sections. The winding system can be set to an automated wire winding mode by clicking the “Go” button in the automated control section. The automated operation runs the wire spool, Juggernaut, and the wire frame control commands in a loop until the process is killed with a click on the “STOP” button in the automated control section. The “Initialize” button returns the Juggernaut to the beginning of the wire frame. This is normally done once before a new winding process begins. Figure 3.8 shows the wire winding frame with tensioned anode and grid wires secured to the frame with transparent DP-100 epoxy.



Figure 3.8: Tensioned wires wound on the QWWR wire winding frame and secured with transparent DP-100 epoxy.

After the wire winding process, the tensioned wires were then systematically transferred and secured with new set of DP-100 epoxy on the printed MWPC board. This is after the power resistors and decoupling capacitors have been soldered on the MWPC board. It is necessary to solder the components on the MWPC board before the tensioned wires are transferred from the winding frame to the board to avoid the risk of wire breakage while soldering the components. After the wire transfer process, good contacts were maintained along each signal channels by soldering the wires to the pads and ensuring channel continuity. The soldered pads were covered with DP-100 epoxy to reduce sparks. This is after the one-plane MWPC behaved within expectation when ramped to -1200 V in 1 atm (760 Torr) of air.

To determine the accuracy of the anode-grid wire pitch obtained with the QWWR, a BS-6020TRF microscope with $\sim 2\text{ }\mu\text{m}$ spatial resolution was used to analyse the wire separation. To do this, pictorial samples of the wires were recorded and analysed after their pixel separations were calibrated. For instance, a pictorial view of one anode wire sandwiched between two grid wires is shown in Figure 3.9 as obtained with the microscope.

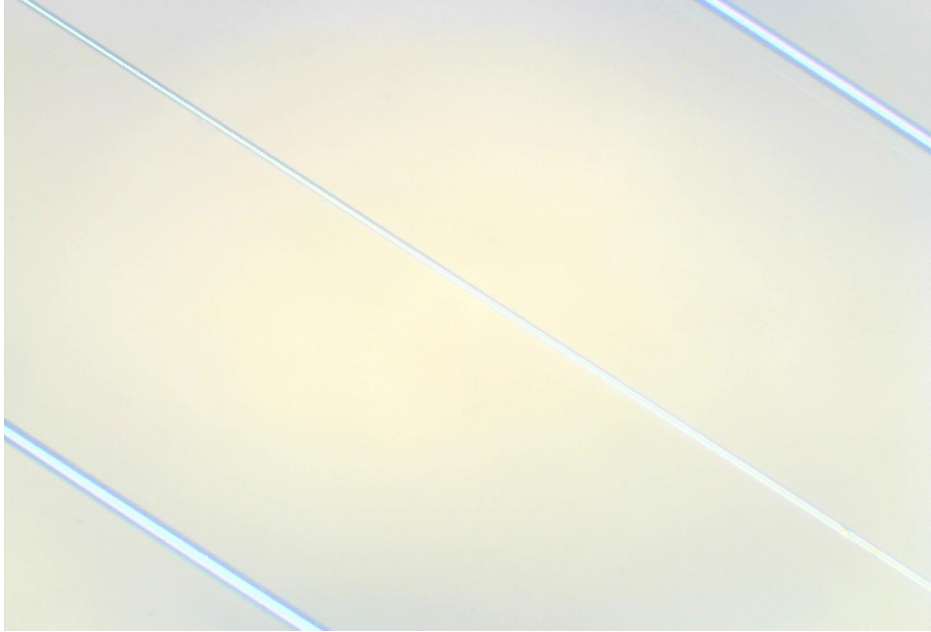


Figure 3.9: Pictorial view of an anode wire sandwiched between two grid wires in the miniature one-plane MWPC as recorded with a microscope.

Results show that the mean pitch between the grid and the anode wires is 0.9984 ± 0.0148 mm. The accuracy of 0.0016 mm and precision of 0.0148 obtained in this measurement is indeed consistent with the values reported in Ref. [227, 228] as requirements for optimal performance in MWPCs. See Section 3.2.3 for details on design, construction and operation of a field cage used for commissioning and operation of the MWPC.

3.2.3 Design, construction and operation of a field cage for the DRIFT-IIe pro detector

To be able to operate the miniature one-plane MWPC as a gas TPC, a drift cage was needed. This is to ensure that charge signals within the active volume of the detector were drifted in a uniform field to avoid signal track smearing. To achieve this, a simple drift cage illustrated in Figure 3.10 was designed and constructed to provide the required uniform field and to mark the active volume of the DRIFT-IIe pro detector.

The field cage consists of eight field rings made with copper wires of 0.6 mm diam-

3. MUX readout for CYGNUS-TPC

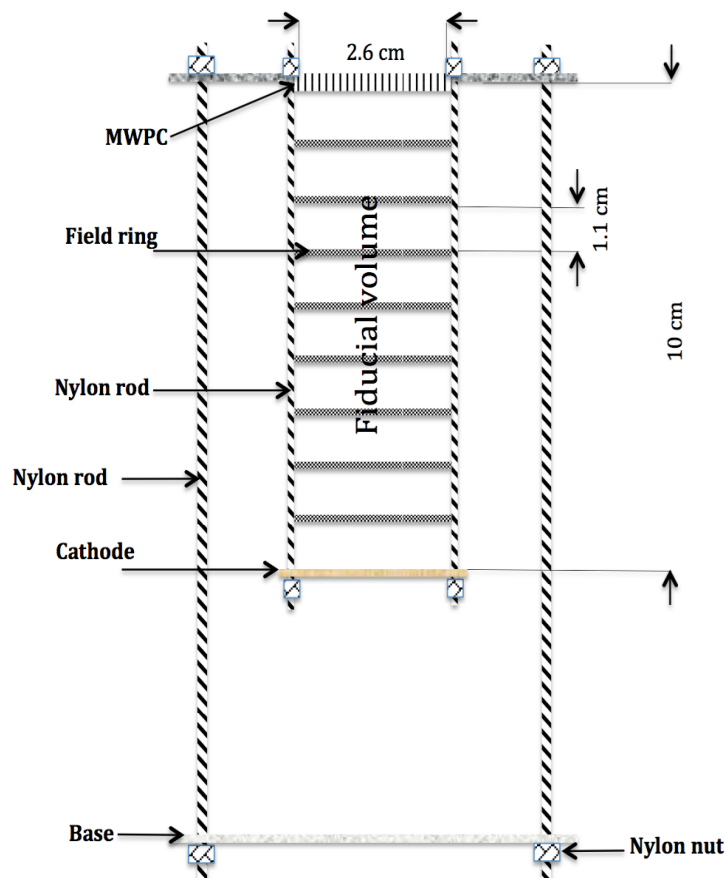


Figure 3.10: Field cage of the miniature detector with one-plane MWPC readout. Typically, a drift field of 350 V cm^{-1} can be achieved at -3.5 kV cathode voltage applied through about $750 \text{ M}\Omega$ resistors.

eter and separated by a distance of 1.1 cm resulting in nine drift spaces. This field ring separation was used based on uniform electric field obtained in Ref. [229] with 0.1 cm field rings placed at a pitch of 1.27 cm . These field rings were installed on a frame made with nylon rods. As shown in Figure 3.10, the miniature multiwire proportional chamber was connected at the top end of the field cage while the bottom end was connected to a copper plate cathode. Then the cathode was connected to the nearest drift field ring which was connected to the subsequent adjacent drift field rings through a $750 \text{ k}\Omega$ resistor to ensure that uniform drift field is maintained in the drift cage as the voltage is stepped down from its maximum potential on the cathode to about zero on the one-plane MWPC. This configuration of the field cage results in a maximum drift

3. MUX readout for CYGNUS-TPC

distance of 10 cm and fiducial volume of about $2.6 \text{ cm} \times 2.6 \text{ cm} \times 10 \text{ cm}$.

After, the one-plane MWPC and the cathode were coupled to the field cage to form the DRIFT-IIe pro miniature time projection chamber (TPC) detector, it was mounted in a 96 litre stainless steel vacuum vessel and commissioned with 250 Torr of CF_4 gas. For more on the stainless steel vacuum vessel used in this operational tests, see Section 3.5. In that operation the current drawn by the grid wires at different voltages and the drift field in the field cage were studied at different voltages. This was necessary to determine the operational grid and cathode voltages that can be used in the experiment. Results from the test of the miniature detector are shown in Figures 3.11 and 3.12 for the current in the grid wires and the drift fields, respectively, each shown as a function of voltages.

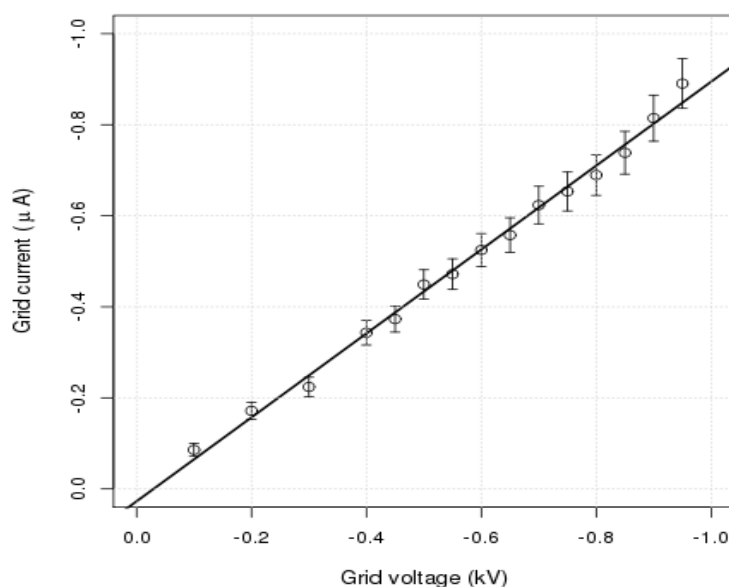


Figure 3.11: Current drawn by the grid channels at different grid bias voltages.

In Figure 3.11, the difference between consecutive data points in the range 0 kV to -0.4 kV is larger than the difference between consecutive data points at electrical potentials greater than -0.4 kV due to a potential ramp transition from -0.10 kV to -0.05 kV, respectively. Using the results in Figure 3.11 and 3.12, it can be seen that the expected current on the grid wires is about -650 nA to -850 nA when the grid wires are

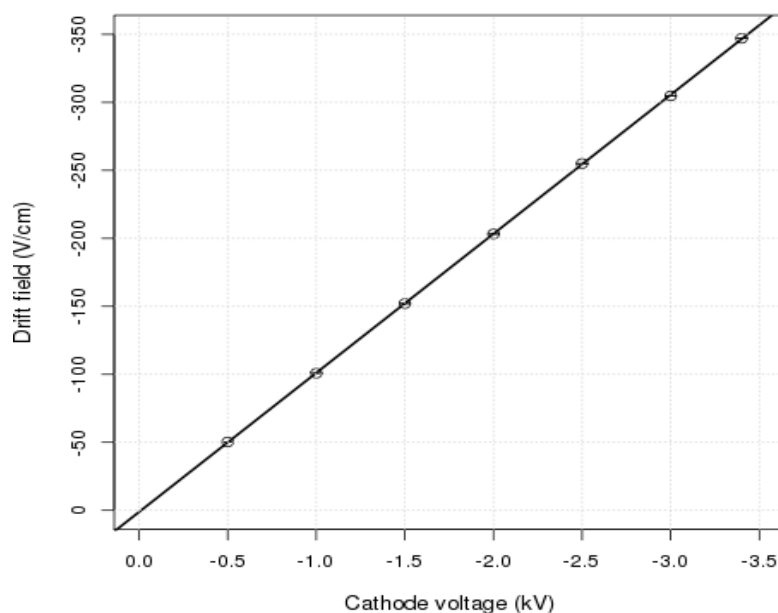


Figure 3.12: Variation of drift field as a function of the cathode bias voltage.

biased to potential V of -0.750 kV to -0.950 kV, respectively. These range of electric potential were used as operational grid V values in the rest of this experiment. Hence, an average corresponding avalanche field of about -8500 V cm $^{-1}$ is expected between the anode and grid wires. The expectation is that this electric field will induce signal amplification through electron avalanches on the more positive grounded anode wires after an interaction in the active volume of the detector. Negative electric potentials were used to ensure that when operated in a gas TPC, negative ions and electrons will be attracted to the MWPC plane for readout after an interaction in the active volume of the detector. These required negative potentials for the grid wires and cathode plane were generated using a Nuclear Instrumentation Module (NIM) cassette NHQ238L dual power supply acquired from the ETPS electronics. Hence, a uniform drift field of about -0.354 kV cm $^{-1}$ was obtained when the cathode plane of the detector was biased at a potential of -3.5 kV as shown in Figure 3.12. This cathode potential and electric drift field were used in the rest of this experiment.

In principle, higher drift fields can be achieved, but these higher fields are not

critical for these studies. The average uncertainty on the drift fields shown in Figure 3.12 is about $\pm 0.003 \text{ V cm}^{-1}$.

To investigate the nature of the electric fields closer to the grid and anode wires at relevant field, theoretical simulations were performed using Garfield [230] and HEED [231] software. The results indicate that at operational voltages that the electric field potential expected around the mid point distance between the anode and grid wires ranges from -0.55 kV to -0.35 kV . The variation between the electric field strength around the anode and grid wires can be seen in Figure 3.13. The zero electric field

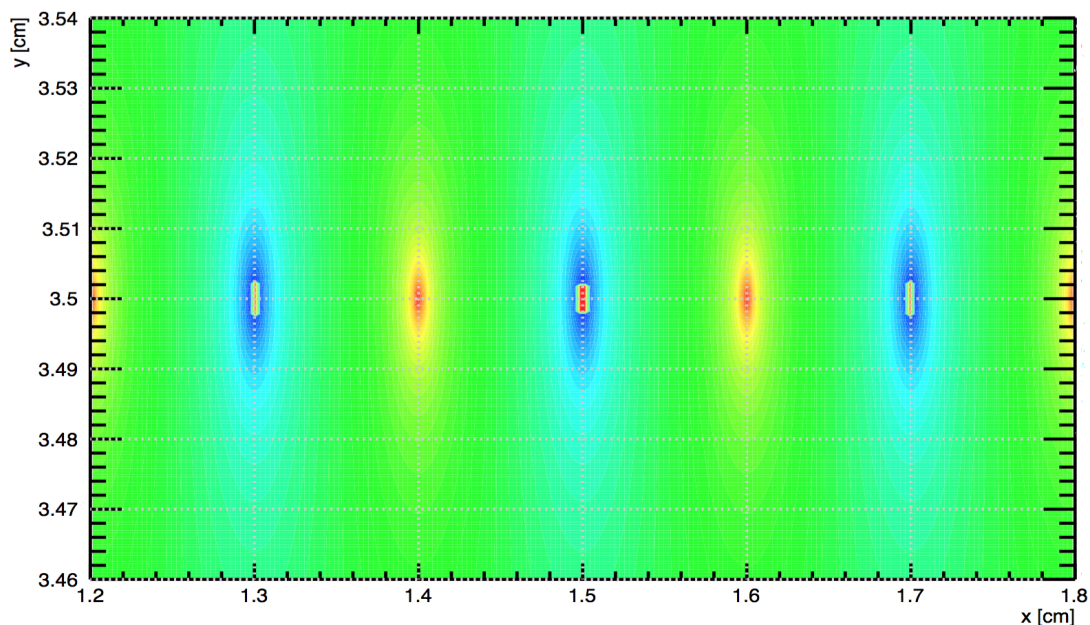


Figure 3.13: Illustration of the field strength variation between the anode and grid wires as determined with Garfield and HEED Monte Carlo. Regions with 0 and 850 V potentials are shown in red and blue, respectively while the regions with potentials >0 and $<850 \text{ V}$ are shown in green.

on the anode wires are shown with red while the -850 V on the grid wires are shown in blue. The regions whose absolute voltage potential is less than 850 V or greater than 0 is shown in green. It is expected that these variation in electric field strength (8500 V cm^{-1}) between the anode and grid wires will be enough to create the required electron avalanche after an interaction in the active volume of the detector. For a given interaction within the active volume of the detector, charge signals collected on anode and grid channels were passed through Cremat CR-111 [202] charge sensitive

preamplifiers and Cremat CR-200-4 μ s [203] gaussian shaping amplifiers, installed on CR-150-R5 and CR-160-R7 evaluation boards, respectively. The operational details of the amplifiers are discussed in section 3.3.

3.3 Front-end electronics

When an incoming particle loses some or all of its energy in the target gas, a number of electron-ion pairs (NIPs) are created through ionization. Due to the negative electric potential bias of the cathode, ionization electrons and anions drift towards the readout MWPC while positive ions drift toward the cathode and grid wires. These signals are drifted through the uniform electrostatic field created by the field cage. In the MWPC, signal multiplication occur through electron avalanches on the anode wires because of the drastic change in the electric field around the vicinity of the anode wires.

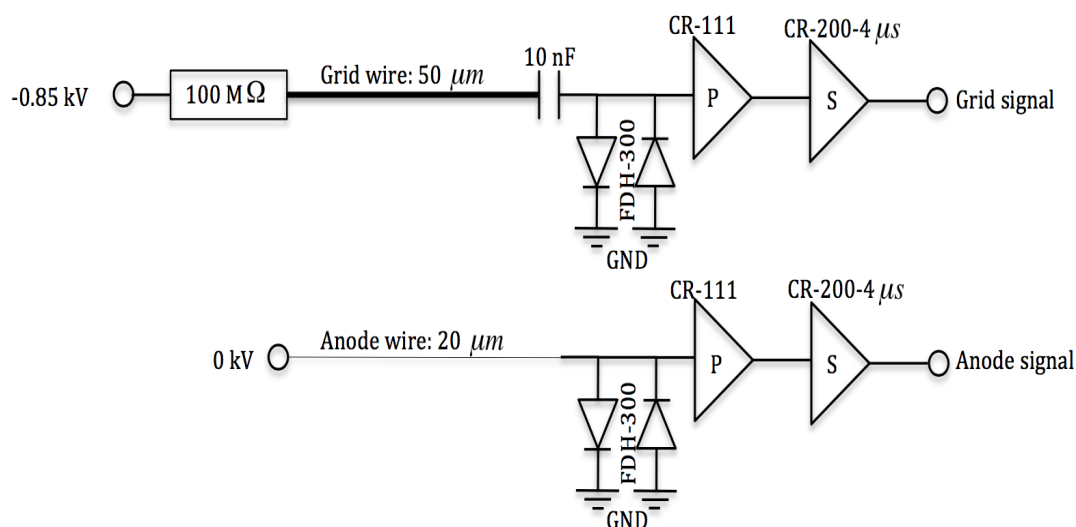


Figure 3.14: Electric circuit diagram showing the FDH-300 protection diode, other major electronic components and the operational potential biases of the grid and anode wires.

The current generated by the moving charges on the anode and grid wires are converted to equivalent voltage signals with ac coupled charge sensitive preamplifier front-end electronics operated with CR-150-R5 evaluation board. The details of the signal

3. MUX readout for CYGNUS-TPC

routing and components used are shown in Figure 3.14. Normally, the output signals from the detector should behave like a step function. At long time domain, the tail of this step function is returned to the base line due to discharging effects of a feedback capacitor C_f through a feed back resistor R_f in the charge sensitive preamplifier. The charge sensitive preamplifier was connected to the detector with a pair of FDH-300 protection diodes, with their respective polarities arranged in the opposite direction to be able to route any undesired discharge currents to the ground. This FDH-300 is a compact high conductance and low current leakage diode with pF capacitance. It has a maximum current rating of 600 mA which is higher than the expected $0.8 \mu\text{A}$ at operational grid voltage of -950 V . In Figure 3.14, the charge sensitive preamplifier is marked as P while the shaping amplifier is marked as S .

For the pictorial view and the electric circuit diagram of the Cremat CR-111 charge sensitive preamplifier which was used in this experiment, see Figures 3.15(a) and 3.15(b), respectively.

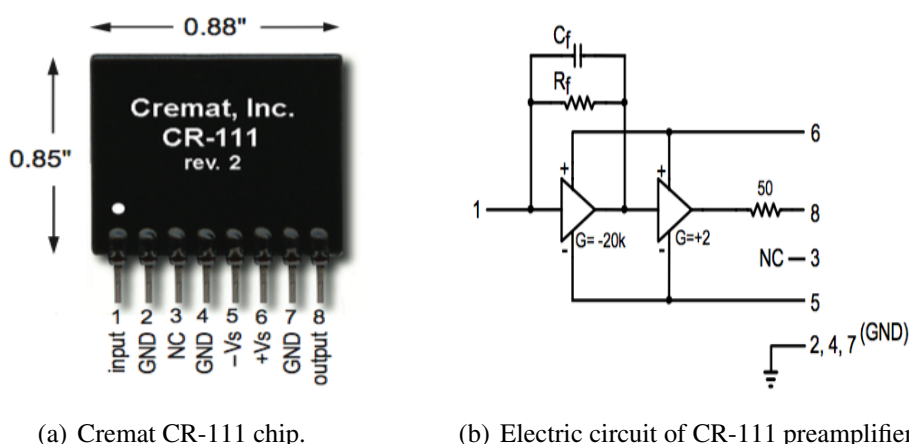


Figure 3.15: Pictorial view of the Cremat CR-111 chip and its simplified circuit diagram showing the major components [202].

The preamplifier chip is contained in about $22.4 \times 22.6 \text{ mm}$ single in-line (SIP) packaging with eight connection pins. It can be seen in Figure 3.15(a) that pin 1 is the input channel while pins 2, 4 and 7 provide reference ground to the preamplifier chip. Pins 5 and 6 are used to power the chip, pin 3 marked “not connected” (NC) in Figures 3.15(a) and 3.15(b) is reserved while pin 8 serves as the output channel of the chip. The circuit shown in 3.15(b) results in a rise time of 3 ns for the CR-111 preamplifier

3. MUX readout for CYGNUS-TPC

which is less than the expected sampling frequency of the data acquisition system used in this experiment.

In this experiment, raw charge signals from the wires were fed into the input pins of the charge sensitive preamplifiers for amplification. The Cremat CR-111 charge sensitive preamplifier is designed to produce a gain of $\times 10$. In the experiment described here, these preamplifier chips were mounted on a CR-150-R5 evaluation boards through which they were powered. In Figure 3.16 is the details of the electric circuit diagram of the CR-150-R5 evaluation board used to drive the CR-111 preamplifier chip.

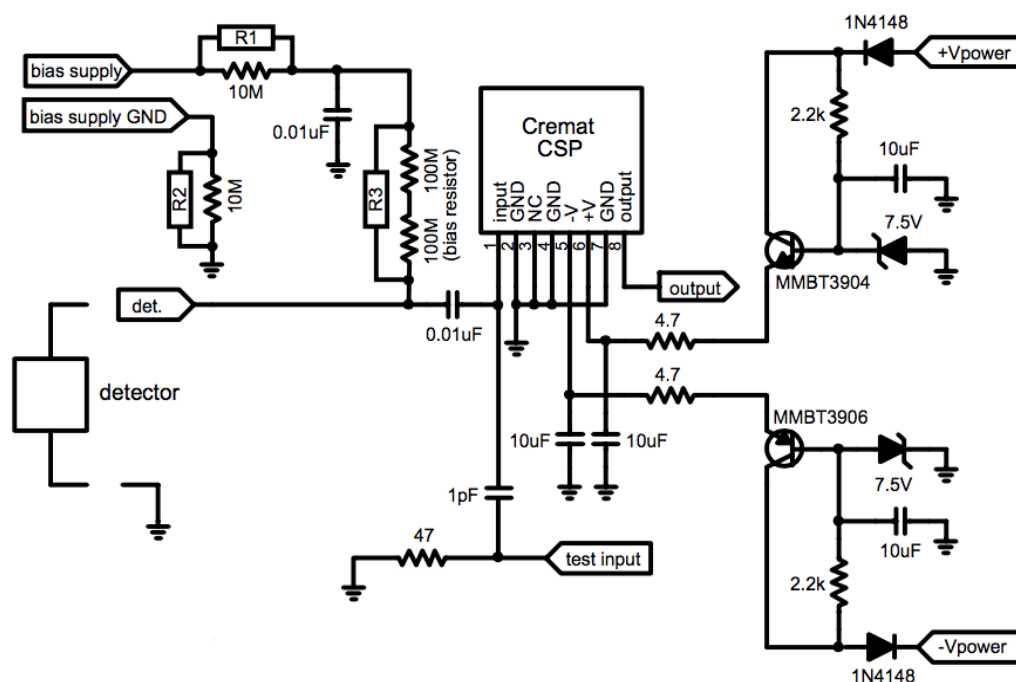


Figure 3.16: Electric circuit diagram of CR-150-R5 evaluation board used in driving the CR-111 charge sensitive preamplifier chip [232].

In that figure, a signal channel from the miniature detector is marked as *det.* and connected to the input of the preamplifier through a $0.01 \mu\text{F}$ capacitor. The filter resistors which are marked as R1, R2, and R3 in Figure 3.16 were left open since they were only needed in a case where large currents are expected from the decoupled signals. In that figure, the CR-111 preamplifier chip marked as *Cremat CSP*, was powered

through the power terminals marked as $-V_{power}$ and $+V_{power}$, using a dual channel PSM 2/2A high performance regulated dc power supply produced by British Standard Tester (BST) company. The operational voltages applied to the power terminals were ± 10 V to power the CR-150-R5 evaluation board and CR-111 charge sensitive amplifier. This was achieved through a PCB based feedthrough discussed in Section 3.4. The output of the charge sensitive preamplifiers were then connected to Cremat CR-200-4 μ s gaussian shaping amplifiers to ensure that exponential decaying signals from the preamplifiers are returned to baseline within the shaping time of the shaper. An operational voltage of ± 10 V was also used to power the CR-200-4 μ s shaper and its corresponding CR-160-R7 board. The evaluation board of the shaper can be used to achieve an additional gain of 10^3 .

3.4 Power and signal feedthrough

To be able to operate the DRIFT-IIe pro detector in vacuum, a vacuum vessel is needed. Hence, a stainless steel vacuum vessel of volume 96 L was used. High voltage cables used to power the cathode, field ring and the grid wires were fed into the stainless steel vacuum vessel through safe high voltage (SHV) connector feedthroughs. For the signals and the DC voltage of ± 10 V used to power the preamplifiers and the shapers, a PCB based feedthrough was designed and made on a converted blank flange for this purpose. A pictorial view of the blank flange after it was converted to a feedthrough using connectors installed on both sides of a two layer and circular PCB is shown in Figure 3.17.

Analogue signals from the detector and the ± 10 V for the preamplifiers and shaping amplifiers were connected into the vessel through MDR-50, LEMO and DB25 connectors mounted on the flange. Twenty signal channels were brought out from the vacuum vessel with a ribbon cable connected to the MDR-50 connector. The signal channels connected on the MDR-50 connector was arranged such that every signal channel was shielded by two adjacent grounded channels. Five channels in the far side of the either end of the ribbon cable were also grounded to provide additional shielding to the analogue signals. The DB25 connector was used to feed the DC voltages that were used to power the preamplifiers and signal shaping set-ups. The LEMO connectors were used to view any given signal channels with an oscilloscope. To study the response of each

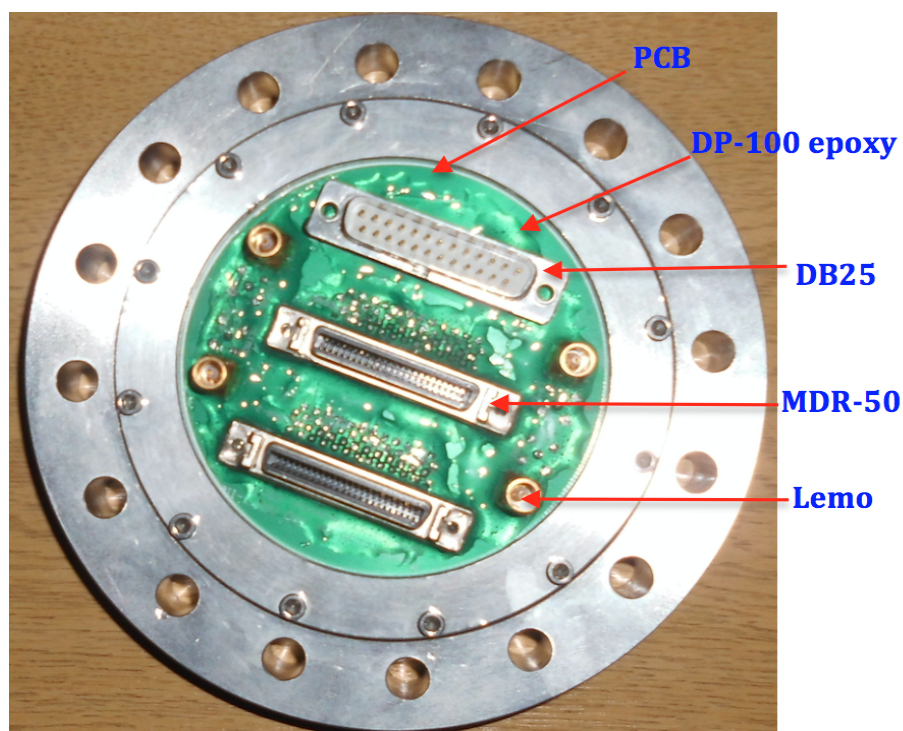


Figure 3.17: Signal feedthrough used to route signals out from the vacuum vessel and in, to power the amplifiers.

of the grid and anode wires, HAMEG HM03524 digital oscilloscope was used. For details on the detector response when it was commissioned, see Section 3.5.

3.5 Commissioning the one-plane MWPC based miniature detector

To be able to commission the detector, the set-up shown in Figure 3.14 for each of the wire channels were placed inside the 96 litres stainless steel vacuum vessel shown in Figure 3.18. The pictorial view of the miniature one-plane MWPC based DRIFT-IIe pro detector is shown in Figure 3.19.

To commission the DRIFT-IIe pro detector, the vacuum vessel was filled with CF_4 gas which is commonly used by leading directional WIMP search experiments for spin-dependent WIMP-proton sensitivity. The typical leak and out gassing rate of the stainless steel vacuum vessel used in this experiment was found to be about 0.22 Torr d^{-1}



Figure 3.18: Some of the major constituents of the experimental set-up used in commissioning the DRIFT-IIe pro detector. This comprises of a stainless steel vacuum vessel, high voltage power supply in NIM crate, CF_4 gas cylinder, DC power supply and pressure gauge.

which is less than 1% contamination allowed in the DRIFT-IIe experiment. Before using fresh CF_4 gas for a new detector operation, impurities in the stainless steel vacuum vessel such as air or old CF_4 gas was removed using a BOC Edwards XDS10 scroll vacuum pump. The vessel pressure was constantly monitored using a CERAVAC CTR-101 pressure gauge acquired from Oerlikon Leybold vacuum company. The CF_4 gas cylinder, the pressure gauge, 2 dc power supplies and the Nuclear Instrument Module (NIM) crate containing the high voltage (HV) power supply used to power the cathode and the grid wires are shown in Figure 3.18.

SRIM [233, 234] Monte Carlo computations were performed to determine the operational pressure for the DRIFT-IIe pro detector using CF_4 gas. This is to determine the pressure of the gas that can contain a 5.5 MeV alpha track from an Americium-241 (^{241}Am) source, located in diagonal position relative to the orientation of the wires.

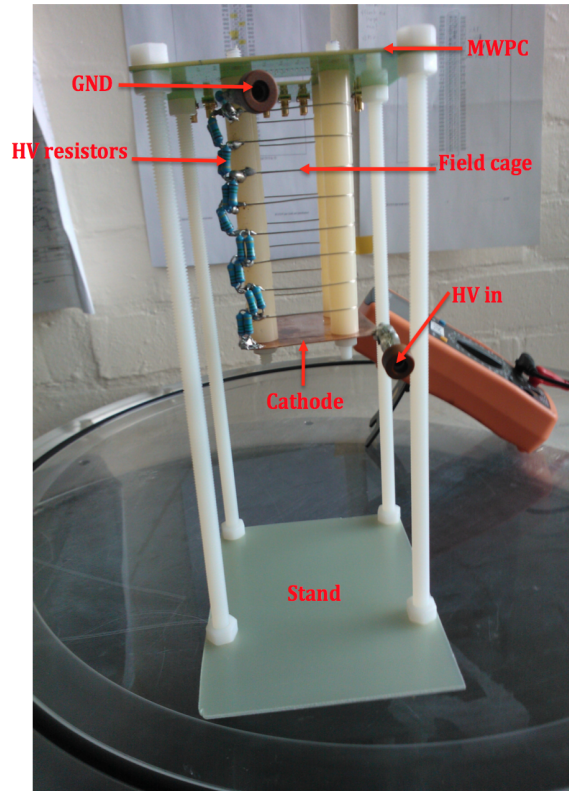


Figure 3.19: Miniature one-plane MWPC based DRIFT-IIe pro detector.

Americium-241 is the most prevalent isotope of americium that undergoes alpha decay with half life of about 432 yr. The 3D ranges of alpha tracks obtained in this simulation is shown as a function of CF_4 gas pressure in Figure 3.20. It can be seen that the 3D range of alpha tracks fall exponentially with increase in the CF_4 gas pressure. Result shown in Figure 3.20 indicate that when the fiducial volume of the one-plane miniature detector is diagonally placed relative to the direction of the collimated ^{241}Am source, allowing a source-field cage separation of about 1.5 cm, that about 250 Torr of CF_4 gas is required to contain the end of alpha tracks. To achieve this, the ^{241}Am source was attached to the tip of some M6 nylon studding of about 5 cm length. A pair of Neodymium disc magnets fixed to the stainless steel vacuum vessel and glue-tacked to the nylon studding was used. Then to be able to bring the source to position when needed and to be able to move it away from the detector when not in use, another pair of Neodymium disc magnets were employed outside the vessel. This was done such

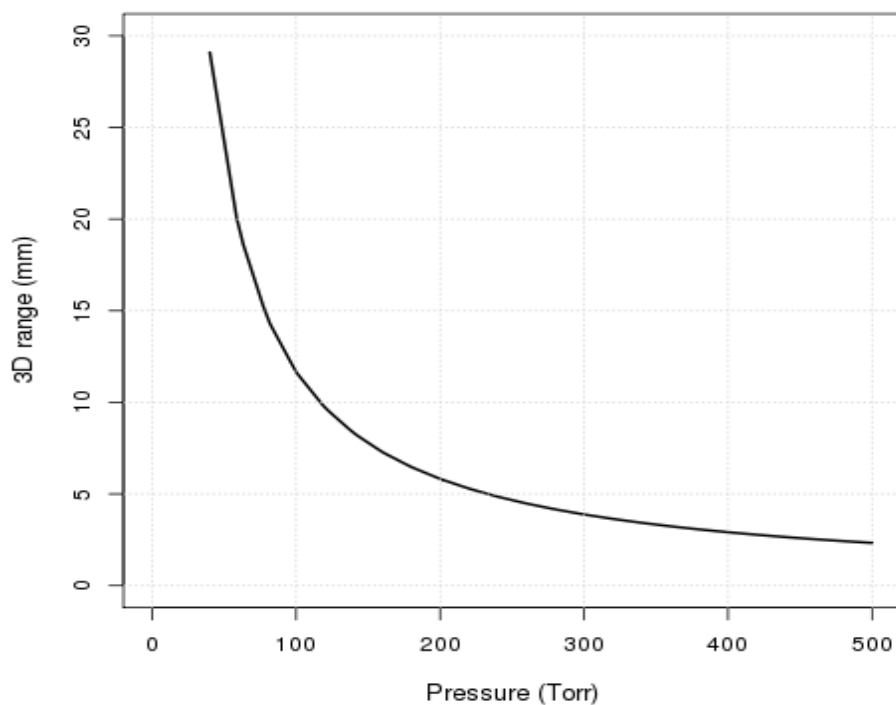


Figure 3.20: 3D alpha range in various pressures of CF_4 gas determined using SRIM Monte carlo.

that the force of attraction between unlike poles in both sets of magnets were used for regulating the position of the ^{241}Am source. This source exposure position and gas pressure were used in the remaining part of the experiment. Also an operational potential of -0.75 kV was used as the MWPC field ring voltage.

In Figure 3.21, is a sample of signal pulse from a single anode wire as observed with the oscilloscope when the source was brought to the exposure position. The polarity of the pulse shown in Figure 3.21 was inverted using the polarity switch on the CR-160-R7 evaluation board. This is to ensure that the signals on the grid and anode wires have common polarity. The pulse height of the signal shown in Figure 3.21 is about 2.9 V with a spatial resolution of ~ 10 μs and an undershoot of ~ 0.15 V, below the baseline. This undershoot effect can be seen in Figure 3.21 at the falling edge of the signal. The magnitude of the signal undershoot observed from each alpha event

3. MUX readout for CYGNUS-TPC

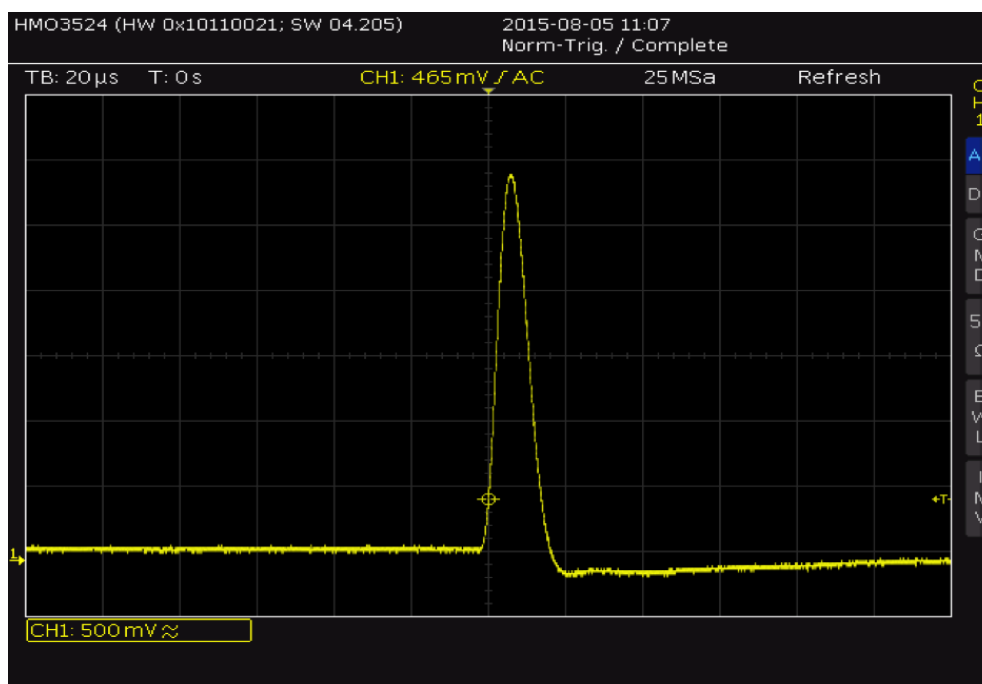


Figure 3.21: Oscillogram of signal pulse obtained from a single anode channel of the DRIFT-IIe pro detector .

depends on the fraction of the energy that is deposited on the wire under consideration. This undershoot effects was restored during data analysis using the transfer function of a simple high-pass filter discussed in [87]. When the amplifier gain is turned to the maximum value of $\times 10^4$, signals with more than 3 V amplitude saturated the amplification regime. However, channel events with amplitude of 3 V or more are not common while using 250 Torr of CF_4 gas with a regulated grid potential. For details on the response of a single signal channel from the one-plane miniature detector, see Figure 3.22.

As shown in Figure 3.22, the signal pulse heights show an exponential increase with the grid voltage. The observed increase is more apparent for grid voltages greater than -0.5 kV. At the operational voltage of about -0.85 kV, the pulse height reaches about 2200 mV. It is expected that the gas gain and hence, the signal pulse height will decrease with increase in gas pressure as discussed in Ref. [235, 236]. This is not a problem for this experiment because all measurements were performed using constrained gas pressures. The average uncertainty on the event pulse heights shown

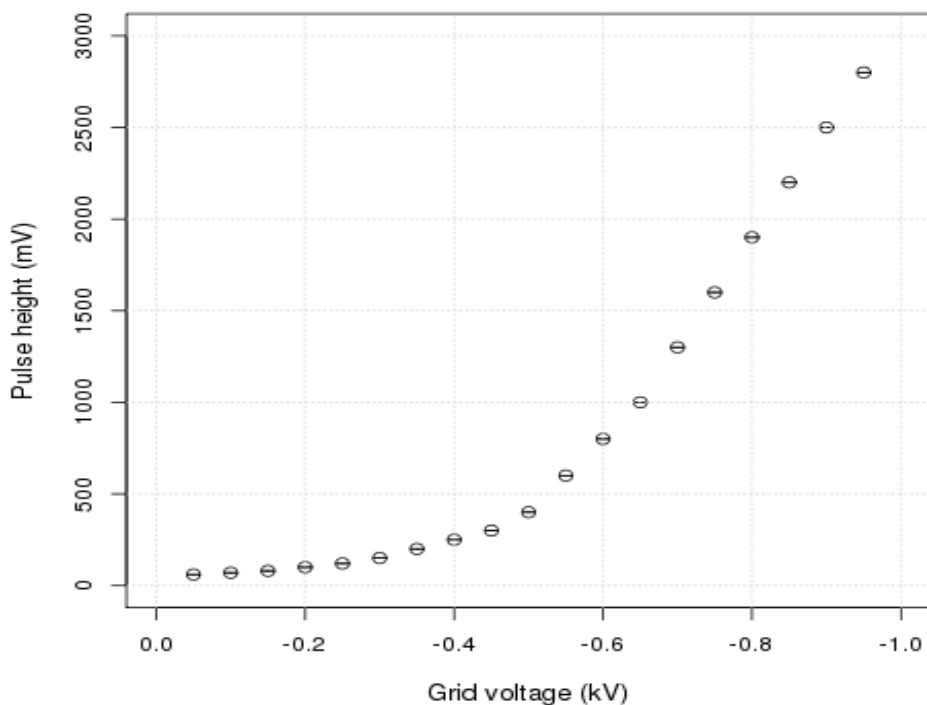


Figure 3.22: Signal pulse height recorded on a single anode wire due to an alpha track shown as a function of grid voltage.

in Figure 3.22 is ± 0.2 mV.

3.6 Gain of the one-plane MWPC based miniature detector

To calibrate the gain of the front-end electronics, a known voltage of 1.8 V was fed into the test input of the CR-111 charge sensitive preamplifier through a 1 pF test capacitor to obtain a charge signal of 1.8 pC. Then, the amount of energy E stored in the test capacitor can be determined using:

$$E = \frac{Q^2}{2C}, \quad (3.1)$$

where Q is the charge and C is the capacitance of the capacitor. This amounts to about 10 MeV energy which corresponds to 22.47×10^6 number of electron-ion pairs (NIPs). The NIPs value corresponds to the number of electron-ion pairs produced in the active volume of the detector by a given recoiling nucleus or interaction. The average energy required to produce an electron-ion pair in a given gas is known as W-value. The W-value of the CF_4 gas has been measured in Ref. [237] as 34.3 eV. Then, the NIPs value can be related to ionization energy E_i by:

$$NIPs = \frac{E_i}{W} = \frac{E_T q_{nc}}{W}, \quad (3.2)$$

as shown in Ref. [238], where E_T and q_{nc} are the total energy of the alpha particle before interaction and gas quenching factor [238, 239], respectively. For more discussions on gas quenching, see Section 4.4. The 1.8 pC charge signal was then shaped and the pulse heights from the signal was counted with an ORTEC 926 multichannel analyser (MCA). Details of the experimental set-up used in these gain calibration tests is shown in Figure 3.23. The oscilloscope (marked as ‘‘Scope’’) in Figure 3.23 was used to measure the raw pulse height of the analogue signals from a signal generator (marked as ‘‘G’’) before digitization in the MCA. It can be seen in that figure that the analogue signals from the signal pulse generator was digitized using the MCA data acquisition module before they were binned using a MAESTRO-32 pulse emulation software. The MCA data acquisition module used in this experiment has 8000 ADC (analogue to digital conversion) channels. Each of these can be used to bin gaussian shaped signal pulses that have positive rising edge of range 0 to +12 V [240]. In this calibration experiment, the average ADC channel of the MCA that recorded the highest number of signal counts during this test was channel 1820. The implication of this result is that about 22×10^6 NIPs will produce an energy peak on channel 1820 of the MCA using these front-end electronics. This can be compared to results obtained from energy spectrum of the 5.5 MeV alpha tracks when detected with the miniature one-plane MWPC based DRIFT-IIe pro detector and analysed with the MCA system to determine the gas gain of the set-up. Due to the separation of about 1.5 cm between the alpha source and the field cage, it is expected that at least 80% of the energy of

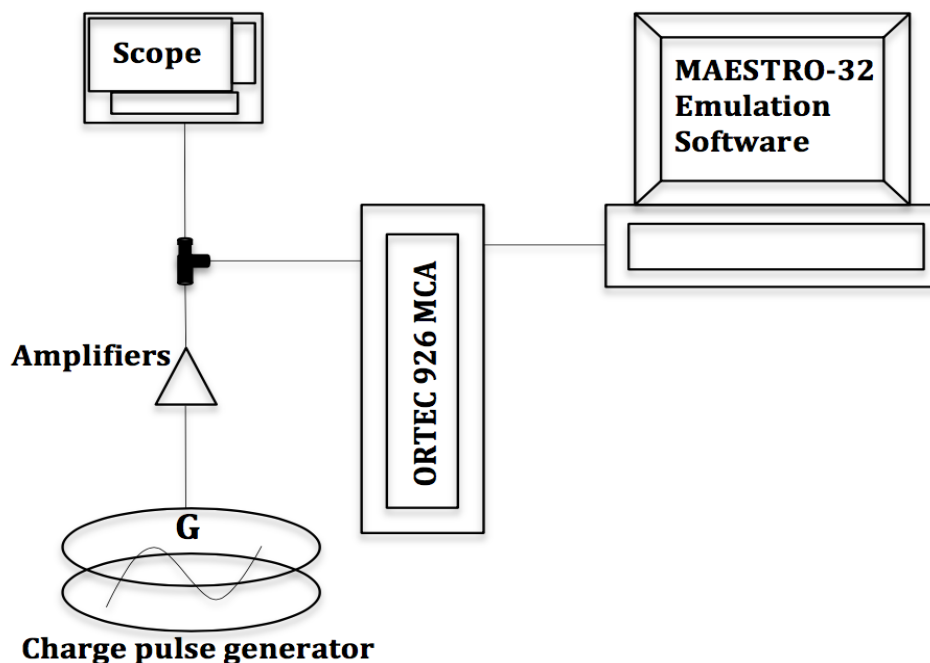


Figure 3.23: Experimental set-up used to calibrate the gain of the front-end electronics.

the alpha particles will be deposited within the fiducial volume of the detector. This is considering that the energy loss along a given ionization track induced by a charged particle obeys the Bethe-Bloch relation [120, 121, 241, 242, 243] by reaching a maximum value at the end of the track range. This is known as the Bragg curve while the end of the track range where the maximum ionization energy is deposited is known as the Bragg peak. This separation between the ^{241}Am source and the field cage could have been reduced and still contain the Bragg peak, if the detector was operated at a higher gas pressure. However, this would have decreased the length of the observed event tracks which can conceal any intrinsic Bragg effect.

Using equation 3.2, where q_{nc} for CF_4 gas is 0.28 (as measured in Ref. [238]), then the expected NIPs that can be induced by the fraction of the alpha track within the fiducial volume of the miniature detector is 35.92×10^3 . To be able to compare this result to the calibration data, the detector was operated in a single channel mode where all the anode signal channels were grouped. In this mode, the detector was exposed to the alpha source with the source-field cage separation described above in place. Then

3. MUX readout for CYGNUS-TPC

the resultant signal pulses from that exposure were analysed using the MCA. In that analysis, the average maximum alpha charge signal pulse peak was observed on MCA channel 1119. This is equivalent to 13.82×10^6 NIPs which implies that the gas gain G_g of the DRIFT-IIe pro detector set-up can be given by:

$$G_g = \frac{NIP_{SO}}{NIP_{SE}} = \frac{13.82 \times 10^6}{35.92 \times 10^3} = 385, \quad (3.3)$$

where NIP_{SO} and NIP_{SE} are the observed and the expected numbers of electron-ion pairs, respectively. The G_g value obtained for the one-plane MWPC based miniature detector in Equation 3.3 when operated in CF_4 gas shows that this one-plane MWPC technology can be adopted in designing larger area detector. Though, more studies can be conducted to understand how to improve this G_g value for better performance, comparable to about 1000 gain obtained from conventional three wire plane MWPC configuration as in Ref. [192]. This can be achieved by optimisation of the operational pressure and grid voltage for better gas gain. Another idea that can be used to improve the gas gain by up to 2 orders of magnitude is by operating the one-plane MWPC with a gaseous electron multiplier (GEM) [179] otherwise known as GEM+MWPC hybrid technology. In principle, the MWPC can be used for signal readout while the GEM provides the required gas gain in the proposed MWPC+GEM hybrid configuration. A simple illustration with examples of dimensions and possible readout configuration for the GEM+MWPC hybrid technology is depicted in Figure 3.24. In that figure, a one-plane MWPC, shown with black circular dots, set at zero potential can be used to readout negatively charged signals arriving from the GEMs after signal amplification via avalanches. The GEMs are shown with blue rectangular points in Figure 3.24 while the black thick lines are the cathode. The dimensions shown in that figure are for illustration purposes, only. It is expected that future experimental measurements can verify the possibility of these dimensions and hence can suggest the best operational dimensions for the hybrid set-up.

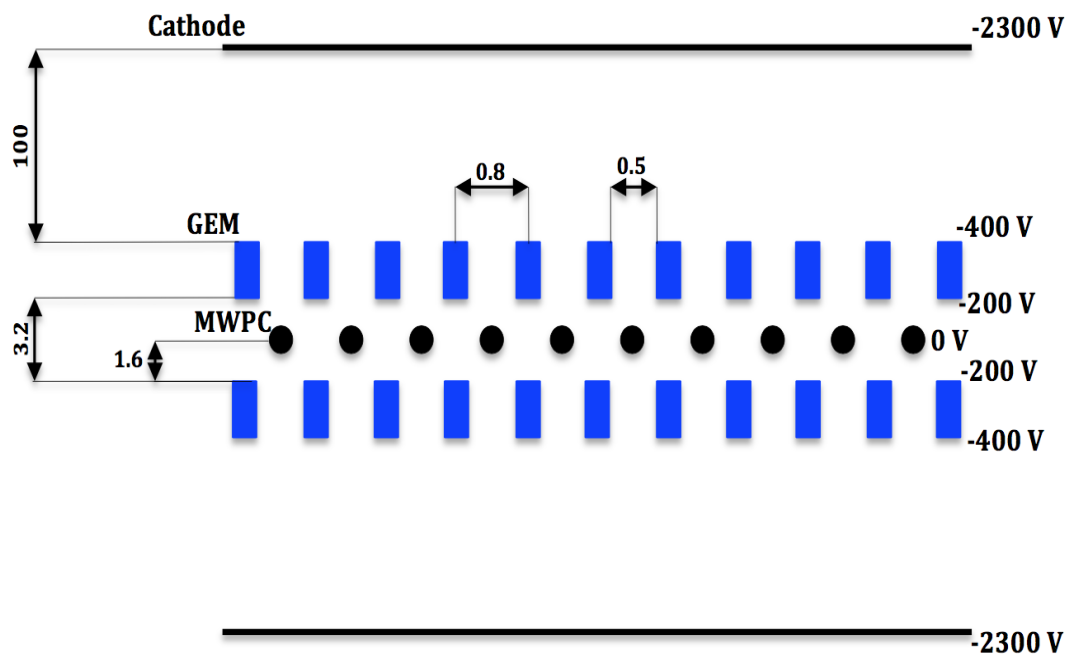


Figure 3.24: Simple illustration showing a possible configuration for GEM+MWPC readout technology. All dimensions are in mm.

3.7 LabVIEW based data acquisition system

National Instrument (NI), Laboratory Virtual Instrumentation Engineering Workbench (LabVIEW) [244, 245] was used to develop a data acquisition system (DAQ) to view more raw signal channels from the miniature one-plane MWPC based detector. This was achieved by using NI 5751 [246] digitizer adapter module with 16 ADC channels, operated with a NI FlexRIO PXI-7953R Field Programmable Gate Array (FPGA) [247] device. The NI FPGA module has a Xilinx Virtex-5 SX95T chip which was programmed with NI LabVIEW code. This can be seen in Figure 3.25, with the digitizer, an onboard dynamic random access memory (DRAM) and PXI express interface used for interacting with other external computers. In that figure the digitizer is marked as NI FlexRIO adapter module and shown on the left, while the FPGA module is on the right. Figure 3.26 is a pictorial view of the digitizer and the FPGA FlexRIO as they are installed in a NI PXIe-1078 chassis in the laboratory. The PCIe cable (with green strap) in Figure 3.26 is connected to the PXI express interface for pushing data to and

3. MUX readout for CYGNUS-TPC

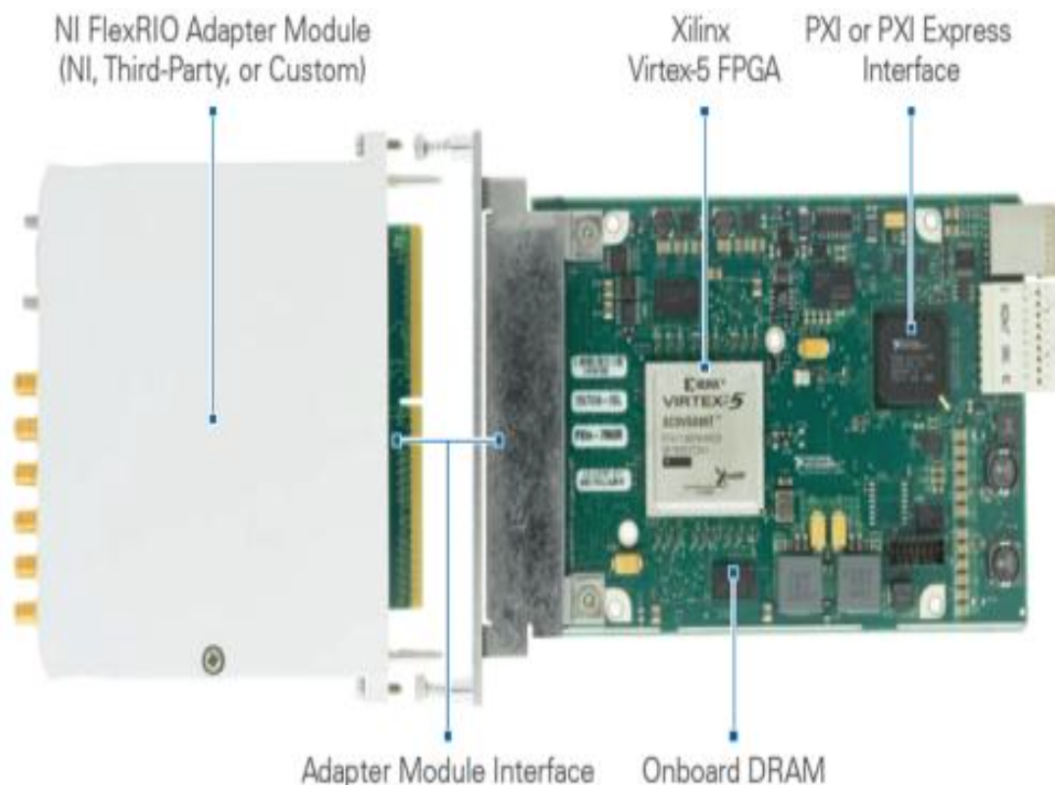


Figure 3.25: Constituents of the FPGA FlexRIO module from National Instrument [247].

from the NI modules to a personal computer. In the right hand side of that figure are two digitizer modules. It can be seen that each of the digitizers has 3 connectors. They serve as analogue inputs, external clock input and digital output.

LabVIEW programs and subroutines are known as virtual instruments (VIs). The major constituents of a VI can be classified into: a connector panel, a front panel and a block diagram parts. For instance, the block diagram of the LabView program used as a DAQ for the one-plane miniature MWPC based DRIFT-IIe pro detector is shown in Figure 3.27. In a LabVIEW code, a connector panel can be used to represent a given VI in block diagrams of other VIs where the code is called, while the front panel is the user interface of a LabVIEW program. For example, the front panel of the DAQ used in this experiment is shown in Figure 3.28. Control and indicator keys in the front panel can be used by the programmer as interaction interface to the program. LabVIEW

3. MUX readout for CYGNUS-TPC



Figure 3.26: National Instrument chassis used to power and interface the digitizer and FPGA FlexRIO.

programs are built in the block diagram by dragging, dropping and connecting virtual representation of different laboratory equipment in the direction of the data flow to create an application.

The expected cable delay, sample time, pre-trigger time, plot shift, trigger mode, trigger threshold, ADC select, run name, and filename are examples of input data to the DAQ. A cable delay of 5 ns was used in this experiment for the signal ribbon cable. Typically, the operational sample and pre-trigger times are 1000 μ s and 500 μ s, respectively. The trigger mode can be set to either rising edge, or falling edge, or free run for non triggered operations. At full operational cathode and grid wire voltages, a rising edge trigger threshold of 500 mV was used. This is to ensure that the signals recorded by the DAQ are clearly above noise. The ADC select was used to set the DAQ to single ADC operation or to multiple ADC operation. A run name and a filename

3. MUX readout for CYGNUS-TPC

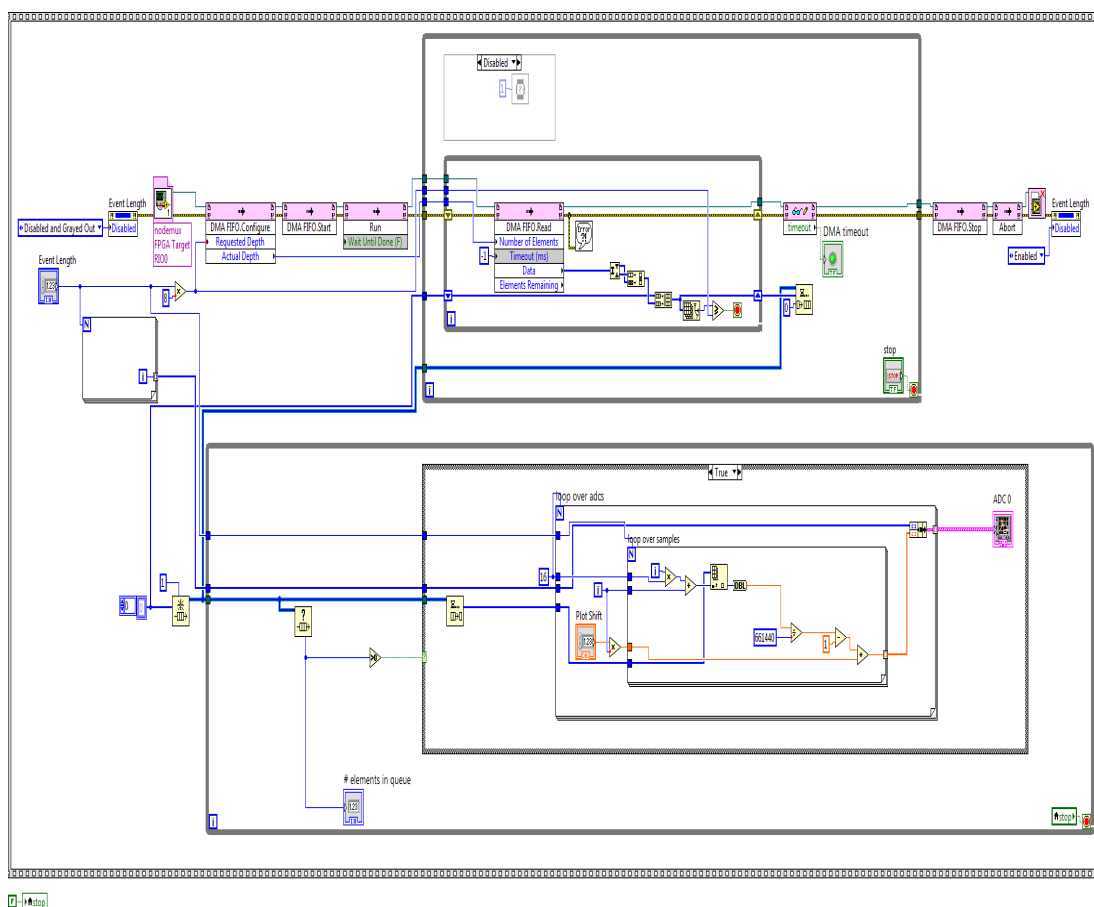


Figure 3.27: Block diagram of the LabVIEW based data acquisition system for the DRIFT-IIe pro detector.

was used to ensure that data from each detector run was saved with a unique name. Event numbers were added to the run names as suffixes to ensure that no two event share the same name.

A sample of the response of the DAQ when the miniature one-plane MWPC based DRIFT-IIe pro detector was exposed to an alpha source can be seen in Figure 3.28. It can be seen that only 16 signal channels are visible in Figure 3.28 because this is the maximum number of signal channels that the ADC can allow. The remaining first four channels of the detector which could not be displayed due to the capacity of the ADC were terminated for non-multiplexed operations. The Bragg curve of the alpha particle can be seen along the ionization track shown in that figure. In particular, the Bragg peak of that ionization event track is more apparent around the 4th and 6th signal

3. MUX readout for CYGNUS-TPC

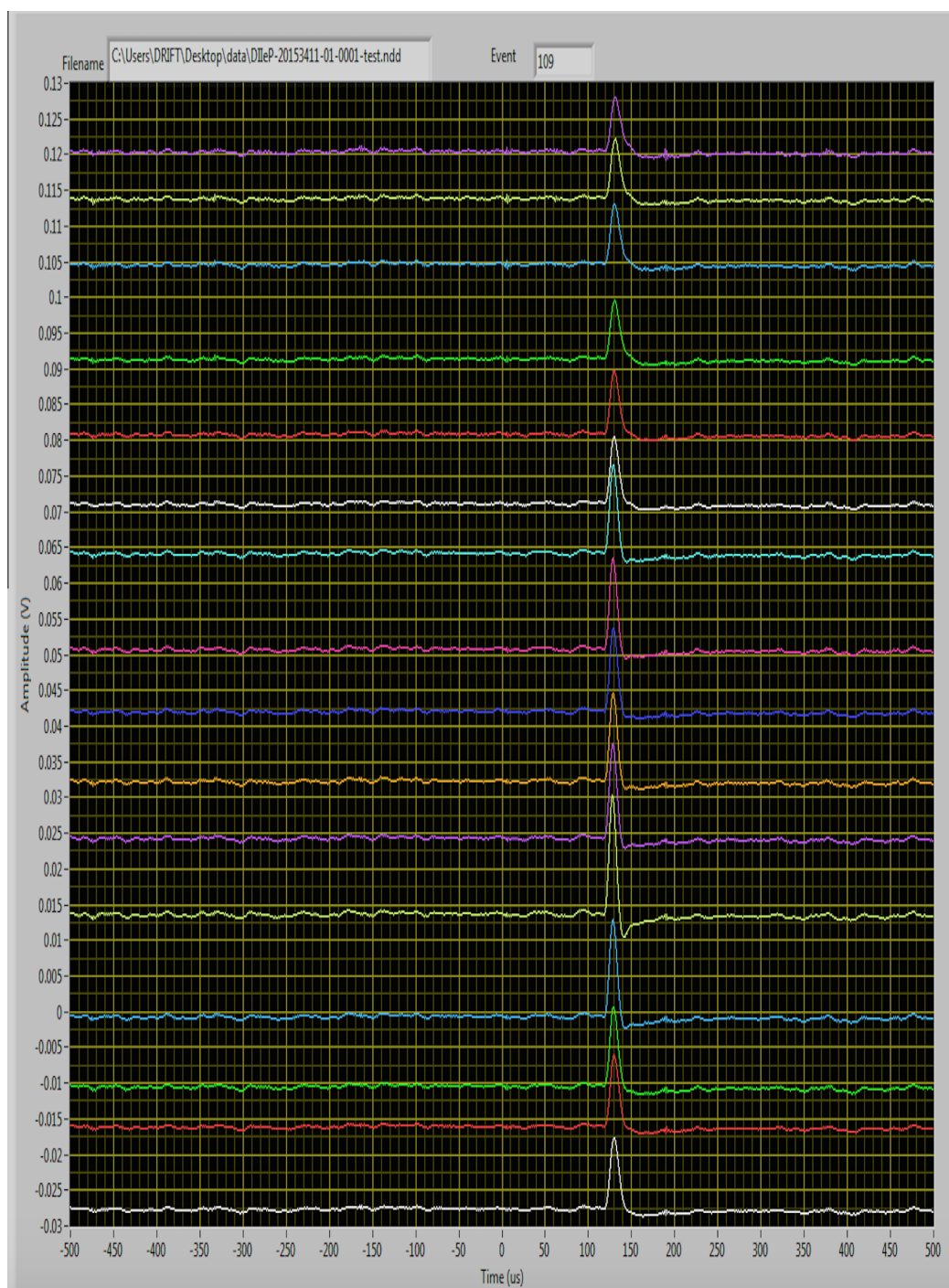


Figure 3.28: Front panel of the data acquisition system showing a sample of the detector response when exposed to an alpha source.

3. MUX readout for CYGNUS-TPC

channels (counting from bottom). This is because the top of DAQ shows signals from the wires that are closer to the alpha source and the bottom channels are from wires that are located further away from the source. The expected intrinsic temporal delay between two adjacent signal channels in Figure 3.28 is not apparent due to the fast drift velocities of charges in CF_4 gas. This is because the maximum drift distance z of charges in the CF_4 based DRIFT-IIe pro detector is not enough for even the expected overall intrinsic delay of 16 ± 4 ns between the first and the last signal channels of the detector to be detected with the micro-seconds scale resolution of the DAQ. The expected temporal separation between the signal wires can be determined using the expected electron drift velocity v_{drift} in pure CF_4 gas, which is given by $11 \text{ cm } \mu\text{s}^{-1}$ as measured in Ref. [248]. This is using the E/P and E/N values obtained from operational parameters of the DRIFT-IIe pro detector given by $1.35 \text{ kV cm}^{-1} \text{ atm}^{-1}$ and 5.5 Td , respectively.

To further understand the detector performance and sensitivity to energy loss of ionization particles along signal tracks, more studies were performed using Bragg curves obtained from alpha induced events. This was achieved by using the average of signal pulse heights induced on a given anode wire obtained after 10 separate detector exposures. These results are shown in Figure 3.29 as a function of distances of the alpha source from anode wires that recorded the charge signals. This does not account for about 15 mm offset between the source and the active volume of the detector. In this experiment the source position and the detector pressure was operated to ensure that the ionization tracks ends within the active volume of the detector using the results in Figure 3.20. The trend of the data in that figure indicate the presence of an alpha Bragg peak of about 649 ± 32 mV. This was observed on an anode wire located toward the end of the range of the event track, which is consistent with expectation. It can be seen that only 8 data points are recorded in Figure 3.29, this is because the 16 ADC channels were divided into 8 anode and 8 grid channels. Having established that the miniature detector is sensitive to Bragg peak effect using alpha tracks, hence, a new multiplexing device can be developed to investigate if the effect of energy loss of alpha particles along event tracks will be affected when analogue signals from the miniature one-plane MWPC based DRIFT-IIe pro detector are multiplexed and recovered through demultiplexing. This is the subject of the work described in Section 3.8.

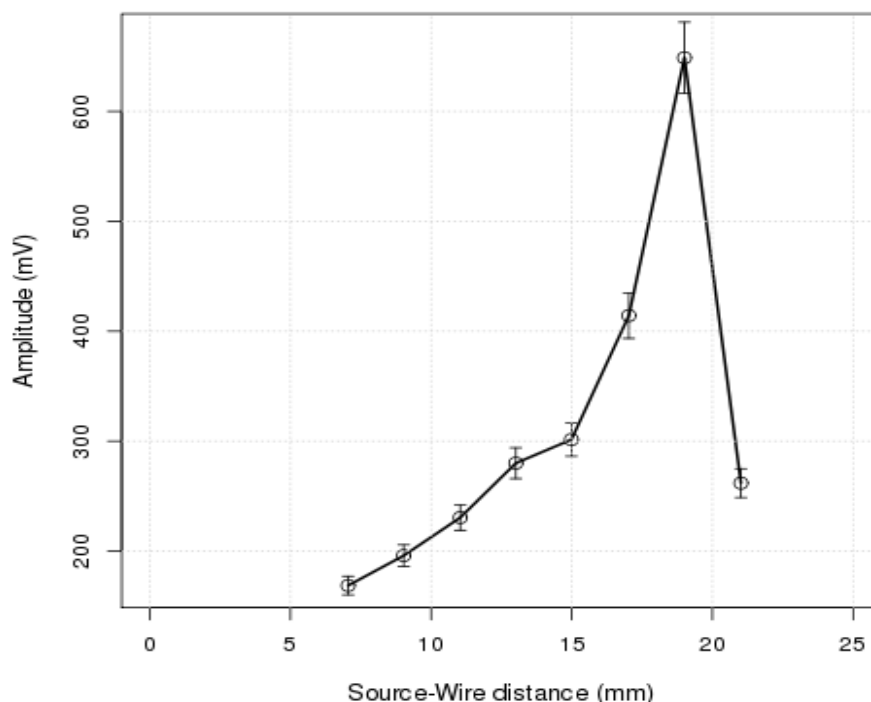


Figure 3.29: Average event pulse height on anode wires as obtained from 10 alpha induced signal tracks detected with the miniature one-plane MWPC based DRIFT-IIe pro detector showing a Bragg curve effect. Note that larger Source-Wire distances are closer to the tail of the observed alpha tracks.

3.8 Design and construction of a 20:1 signal multiplexer (MUX)

The viability of signal multiplexing as a potential readout to reduce the number of front-end channels in the proposed CYGNUS-TPC detector was investigated using analogue signals from the miniature one-plane DRIFT-IIe pro detector and a new analogue multiplexing scheme. Analogue multiplexers are produced, mainly from field-effect transistors (FET) known as FET analogue switches which allow one channel from several other channels to be selected and passed through to a common output channel at a given temporal interval [249, 250]. In this experiment, 5 of 4:1 LMH6574 multiplexer (MUX) chips from Texas Instruments were used. The principles of oper-

ation of the 4:1 multiplexer chips used in this experiment is illustrated in Figure 3.30.

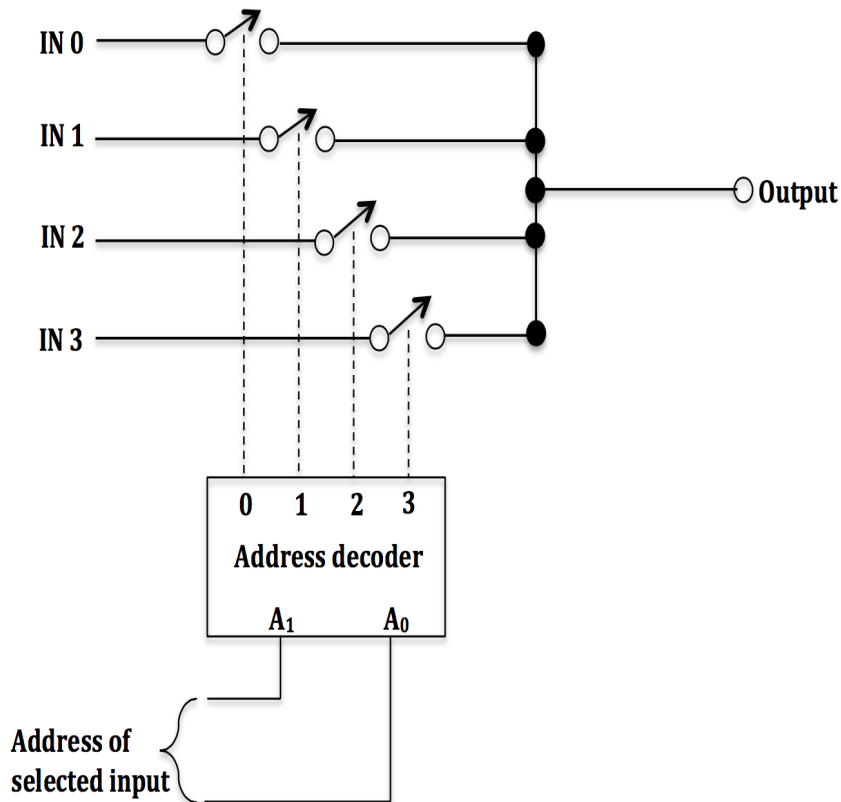


Figure 3.30: Principles of operation of a 4:1 analogue multiplexer.

The four input channels in each of the MUX chips are marked IN 0, IN 1, IN 2, and IN 3 in Figure 3.30. During an operation, each of these input channels is selected and passed as the output of the chip at different times using a unique signal address generated with a pair of A_0 and A_1 digital control signals [224]. Each of the input channels was terminated with a 550Ω resistor to reduce signal reflections and to ensure that any excess current due to charge surge were properly grounded. The LMH6574 MUX chip is a 14-pin device embedded in a small outline integrated circuit (SOIC) surface mount package. See Figure 3.31 for a schematic illustration of the pin configuration.

In Figure 3.31, the input termination resistors are marked as $R_{IN0} \dots R_{IN3}$, back termination resistors are marked as R_T , current feedback output buffer resistor is marked

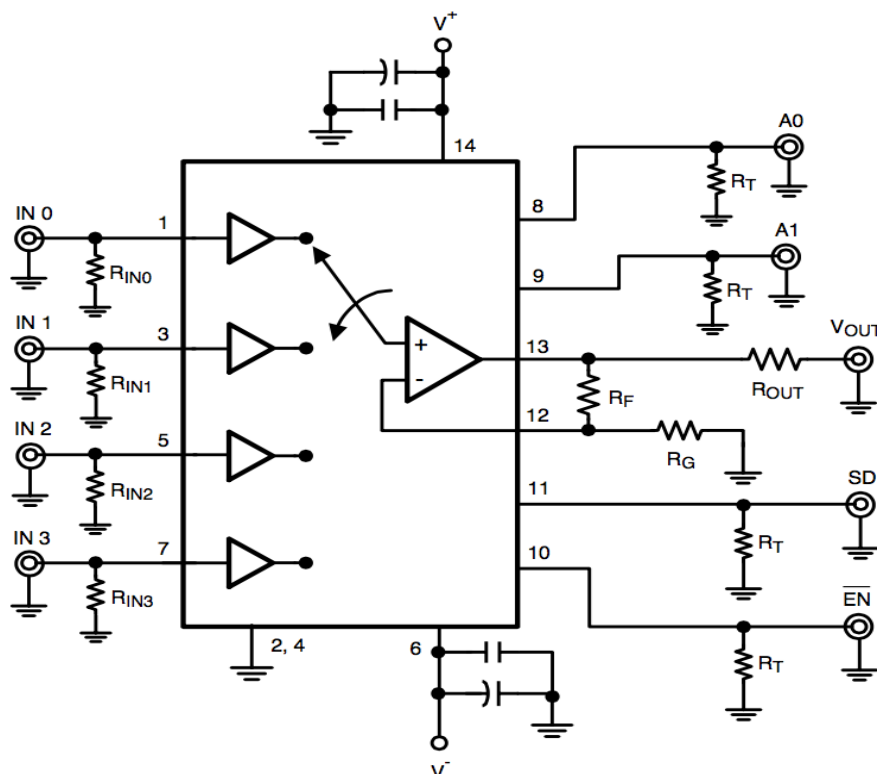


Figure 3.31: Pin layout of a single LMH6574, 4:1 analogue signal multiplexer [224].

as R_F , gain set resistor is marked as R_G while output load resistor is marked as R_{OUT} . The resistance of each of the R_T and R_G resistors used in this experiment is 550Ω while that of the R_{OUT} is 50Ω . In the figure, signal pins are marked with integers 1, 2, 3, ..., 14. It can be seen that pins 1, 3, 5, and 7 are the four analogue input channels while pin 13 is the common output channel and pin 12 provides performance feedback to the chip. Pins 2, and 4 were grounded and used as shielding to their respective adjacent signal input channels. In the chip shown in Figure 3.31, pins 8 and 9, carry the A_0 and A_1 digital control signals, respectively. The A_0 and A_1 digital signals have common amplitude of 3 V, though the frequency of the A_0 signal is required to be a factor of 2 higher than that of A_1 signal.

Typically, the frequency of the A_0 signal was 2 MHz while that of the A_1 signal was set at 1 MHz per channel in this experiment. This difference between the frequencies of these two digital control signals is necessary because every one full cycle of the A_1 signal, requires two cycles of the A_0 signal to be able to generate the required set of

3. MUX readout for CYGNUS-TPC

four digital addresses, one for selecting each of the analogue input channels. Typically, the following A_0, A_1 digital signal combinations: 1,1; 0,1; 1,0 and 0,0 can be used as digital control addresses for input channels: 0, 1, 2 and 3, respectively. A digital signal in pin 10 can be used to enable and disable the chip. The chip is disabled when the signal is high and becomes enabled when the signal is low. For this experiment, pin 10 was enabled in each of the chips throughout this experiment. Chip pins 11, and 12 are used to supply the chip with a shut down (SD_{sig}) signal, and feed back reference to the output channel, respectively. The SD_{sig} is the chip switching signal used for moving controls from one chip to another while in the expanded mode operations. See Figure 3.32 for illustration of a method that can be used to operate the MUX chips in the expanded mode.

As shown in Figure 3.32, two or more chips are connected to increase the number of analogue signal inputs that can be multiplexed to a single output in the expanded mode operations. For this experiment, the chip expansion was done by joining similar digital control pins in all of the five chips. Then, a single output line was obtained by connecting the individual outputs of the constituent chips with a common R_{out} resistor for enhanced chip-switching speed.

This process of chip expansion was used to build a 20:1 multiplexer device using 5 of the LMH6574 4:1 MUX chips. The chips were operated in the expanded mode using a specifically EAGLE designed PCB board. To achieve the required operational specification, the analogue ground was separated from the digital ground to avoid noise coupling between the analogue and digital signals. However, when this is not properly managed it can introduce crosstalk in the circuit since both planes may radiate noise or act as slot noise antennas. Such noise is due to return currents flowing beneath each signal line. This return current will always prefer to follow the path with lowest impedance hence disconnecting these return paths with separated grounds may result in potential current loops especially when there are signal traces over the ground breaks. A circuit with a resultant current loops can experience high ground inductance which is susceptible to signal interference. In this design, the issue of crosstalk induced by separated analogue-digital grounds was avoided by not cross running traces between the grounds. The ground-signal-ground trace stack-up arrangement was adopted to reduce electromagnetic interference (EMI) on the board.

Micro-strip trace technology was used in this design due to its characteristics of

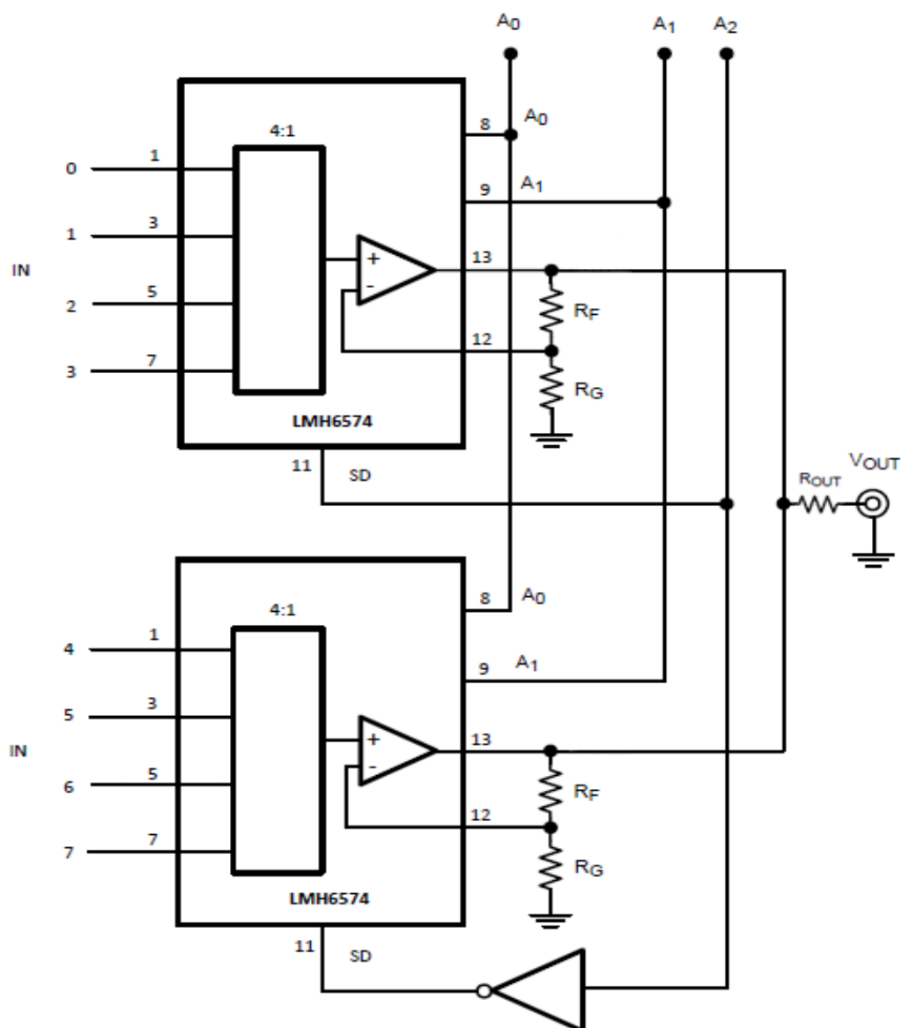


Figure 3.32: Principles of operation of the LMH6574 MUX chips in the expanded mode [224].

having less dielectric losses. For instance, electrons in a strip-line trace can transfer energy to neighbouring electrons in the FR4 material which can be converted to heat and then lost in that form which can result in undesired corresponding dielectric losses. There are no risks of such dielectric losses in the micro-strip technology. Also, micro-strips are easily accessible for maintenance, they are also cheaper and much easier to manufacture compared to the strip-line technology.

In this type of high frequency circuit, it is vital that the resultant impedance of

the circuits are controlled to achieve consistent amplitude and phase responses. These were factored into the design by maintaining a consistent trace width, trace thickness and dielectric material thickness to ensure uniform dielectric constant across the board. The worst case of signal reflection in high frequency circuits are expected when the effective trace impedance is either infinite with reflection coefficient $r_{\text{coef.}}$ of +1 or 0 when $r_{\text{coef.}}$ approaches -1 . The relationship between this $r_{\text{coef.}}$ parameter, the effective trace resistance R_{trace} and the wire resistance R_{wire} is given by:

$$r_{\text{coef.}} = \frac{R_{\text{wire}} - R_{\text{trace}}}{R_{\text{wire}} + R_{\text{trace}}}. \quad (3.4)$$

Considering the signal traces in the board design and a ribbon cable, an average reflection coefficient of 0.38 ± 0.08 was obtained. This is not +1 or 0 which indicates that the expected effect of signal reflection in this design should be minimal.

While operating the MUX in the expanded mode, an inter-chip switching delay of less than 145 ns would be expected. This estimate of the inter-chip switching delay is based on the measurement in the data sheet of LMH6574 chip [224] and independent measurement in Ref. [251]. The inter-chip switching delays are one of the major challenges of modular analogue multiplexers. It implies that for the 20:1 multiplexer board, a total of about 0.73 μs inter-chip switching delay would be expected. This should not affect the sampling time of each channel as chip input channels are sampled for 14 ns. Hence, the total time spent in a single chip while sampling the four different input channels is 55 ns which indicates that a total of 1 μs is required to be able to sample all the inputs of the 5 chips used in the 20:1 MUX board at 20 MHz. The implication of this is that, for a signal pulse from CR-200-4 μs shaping amplifier with a total duration of about 30 μs , the 20:1 multiplexer records about 30 data sampling cycles. This can then be used to reconstruct the original signal when demultiplexed.

The EAGLE board layout view of the MUX PCB is shown in Figures 3.33. After the design process, the 131 mm \times 131 mm, two layer MUX board was manufactured by the Quick-Teck, electronics company. To ensure good electrical contact between the two layers of the board, about 300 vias were used. In Figure 3.33, the positions of the five LMH6574 MUX chips are marked M-1, M-2, M-3, M-4, and M-5 while that of connectors are labelled C-1, C-2, C-3, and C-4. C-1 provides the soldering pad for a 236-412 wire-to-board terminal connector used for powering the chips while C-2, C-3,

3. MUX readout for CYGNUS-TPC

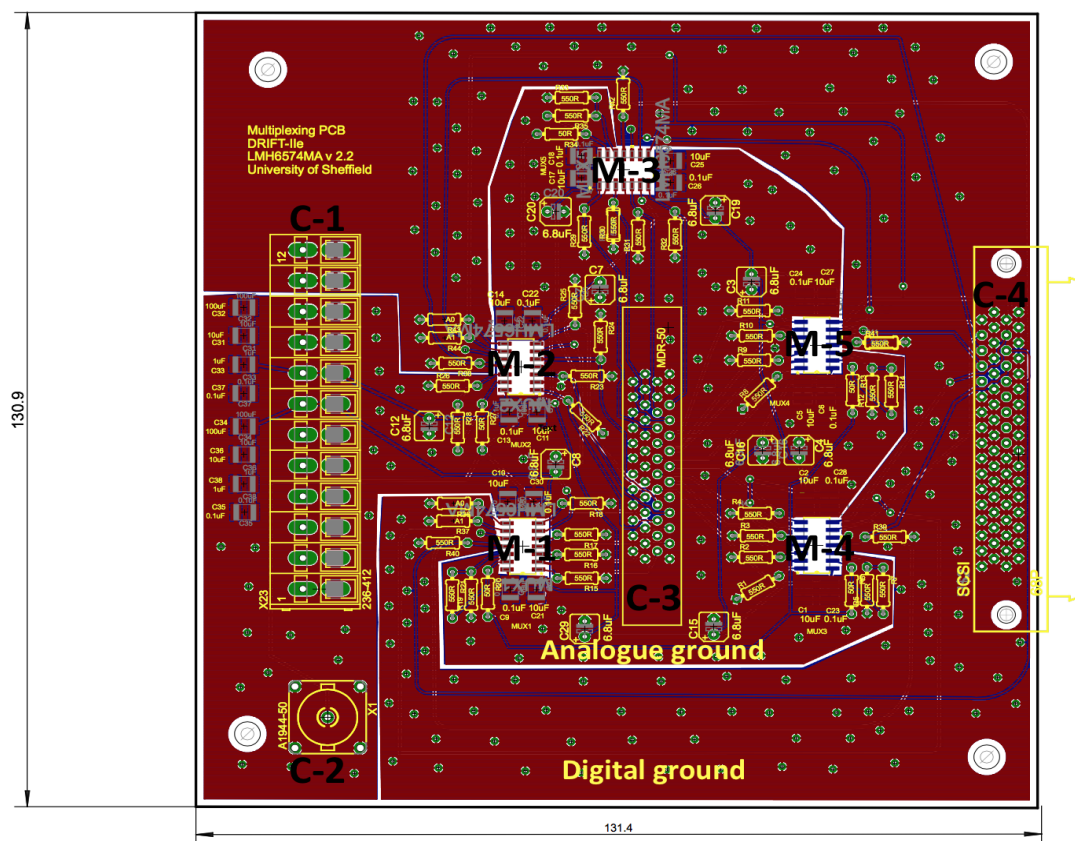


Figure 3.33: EAGLE board layout for the 20:1 signal multiplexing PCB. Positions of four connectors used for routing power to the chips, analogue signal output, analogue signal input and digital signal input are marked as C-1, C-2, C-3 and C-4, respectively. Positions of the five LMH6574 MUX chips are labelled M-1, M-2 . . . , M-5.

and C-4 are for BNC analogue output, MDR-50 analogue input and SCSI-68 digital input for the National Instrument (NI) digitizer, respectively. A pictorial view of the printed MUX board is shown in Figure 3.34 as it is installed in a shielding box, ready for operation. Operational details of the MUX board are discussed in Section 3.9.

3.9 Operations of the MUX data acquisition system

To be able to operate the MUX electronics with the DRIFT-IIe pro detector, parallel capacitors of 17 μF effective capacitance were used to provide power to the board in order to minimize the effect of harmonic distortions. Harmonic distortions can arise

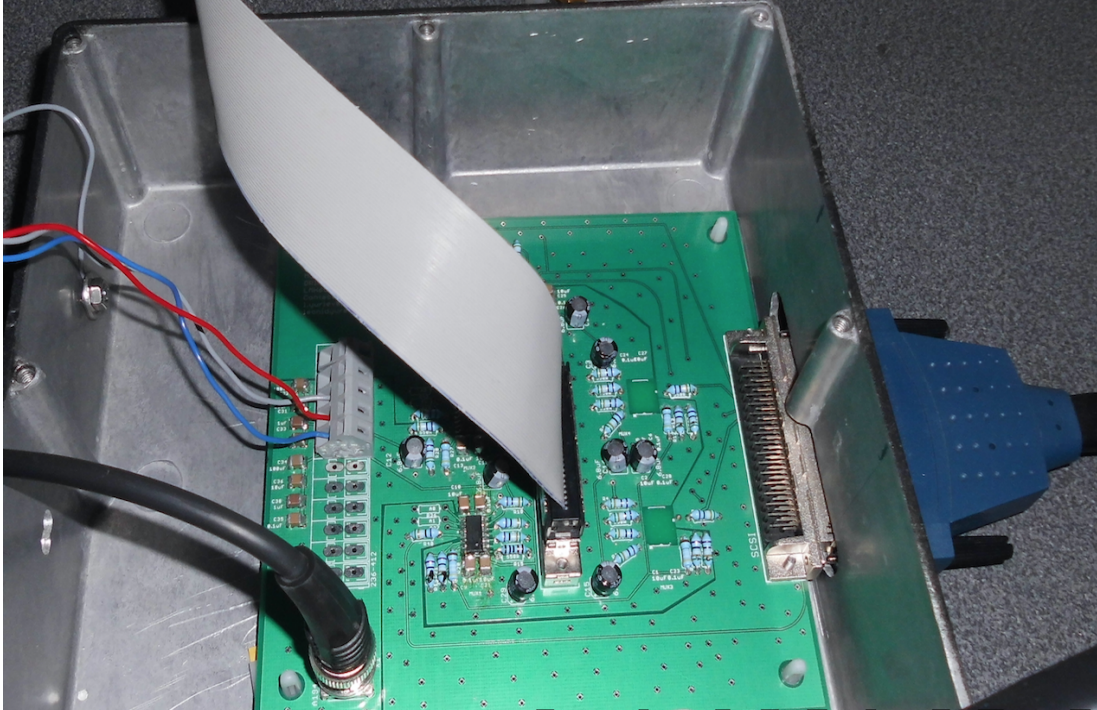


Figure 3.34: Pictorial view of the 20:1 printed multiplexer device in a shielding box, ready for operation. The grey ribbon cable carries the analogue signal from the detector and the blue connector carries digital signals from the FPGA device to the multiplexer. The 3 electric cables (blue, red, grey) are used to power the chips while the black BNC cable carries the analogue output signal.

due to corruption in output signals in the presence of induced harmonics. The integer multiples of fundamental frequencies of signals correspond to their harmonics. A BST dual dc power supply was used to provide the required +5 V and -5 V for the operation of the MUX board. The dc power supply was connected to the board using a blue, red and grey single core wires, shown in Figure 3.34. The BNC connector and cable shown in that figure was used to route multiplexed analogue output signal from the board to the NI FPGA and digitizer for demultiplexing and data storage in a disk for further analysis. This process of signal multiplexing and demultiplexing is illustrated in Figure 3.35.

Raw signals from the miniature detector were connected to the 20:1 MUX board through the MDR-50 connector through a ribbon cable while the SCSI-68 connector was used to feed digital control signals needed for driving the chips from the NI instru-

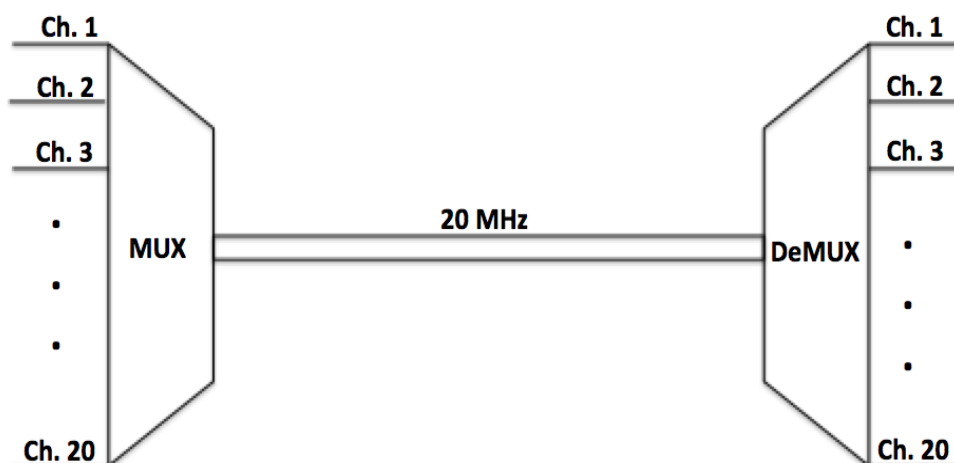


Figure 3.35: Cartoon illustration of signal multiplexing and demultiplexing of 20 analogue input channels at a total frequency of 20 MHz. The point in time where the input signals are multiplexed is marked as MUX while the point where they are demultiplexed is marked as DeMUX. Signal channels are marked such that ch. 1 stands for channel 1, ch. 2 stands for channel 2, etc.

ment to the MUX board (for a pictorial view, see Figure 3.34). As illustrated in Figure 3.35, 20 analogue signal inputs from the miniature one-plane MWPC based DRIFT-IIe pro detector can be multiplexed at a frequency of 1 MHz per signal channel resulting in a full signal cycle of 20 MHz. This can be demultiplexed before the data is recorded in a disk using the same frequency. The block diagram of major electronics components of the experimental set-up used for the signal multiplexing is shown in Figure 3.36.

It can be seen in Figure 3.36 that when an alpha source induces signal pulses in the miniature one-plane MWPC based DRIFT-IIe pro detector, the resultant signals are amplified, shaped and multiplexed. The signals were amplified and shaped inside the stainless steel vacuum vessel before multiplexing to avoid signal loss due to the low gain of the detector discussed earlier in Section 3.6. This is to ensure that any signal that is multiplexed has an amplitude that is greater than the expectation from electronics noise. In future studies for instance, analogue signals from a GEM+MWPC based hybrid detector can produce the gain that can allow raw signals from the detector to be multiplexed before any electronics amplification are applied. In order to view and recover the original data, the resultant multiplexed signal was demultiplexed using a new LabVIEW based data acquisition system. The LabVIEW VI for this demultiplexing

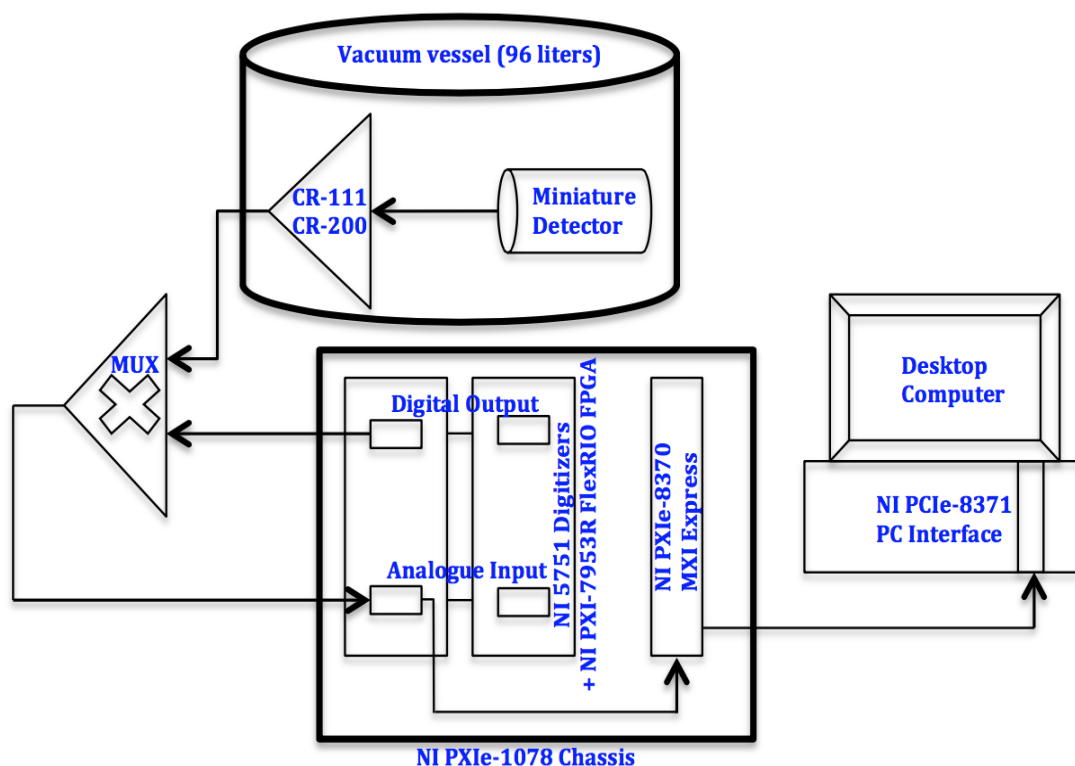


Figure 3.36: Block diagram of the experimental set-up used for the signal multiplexing and demultiplexing.

DAQ is shown in Figure 3.37.

As earlier discussed, the data were demultiplexed using the signal multiplexing frequencies. Then, the demultiplexed data can be saved on disk in a Desktop Computer as shown in figure 3.36 for further analysis. To do this, the analogue output of the 20:1 MUX board was digitized using the NI 5751 adapter module which was operated with the FlexRio NI FPGA device discussed in Section 3.7. The four digital control signals needed by the MUX DAQ to be able to multiplex analogue signals from the DRIFT-IIe pro detector were generated by programming the NI FPGA device. Hence, the resultant digital control signals from the NI machine were fed into the MUX board through a NI SHC68-68-RMIO shielded cable to the SCSI-68 connector as shown in Figure 3.34.

A sample of reconstructed demultiplexed alpha signal track pulses is shown in Figure 3.38 as obtained with a demultiplexing frequency of 625 kHz. This is after these

3. MUX readout for CYGNUS-TPC

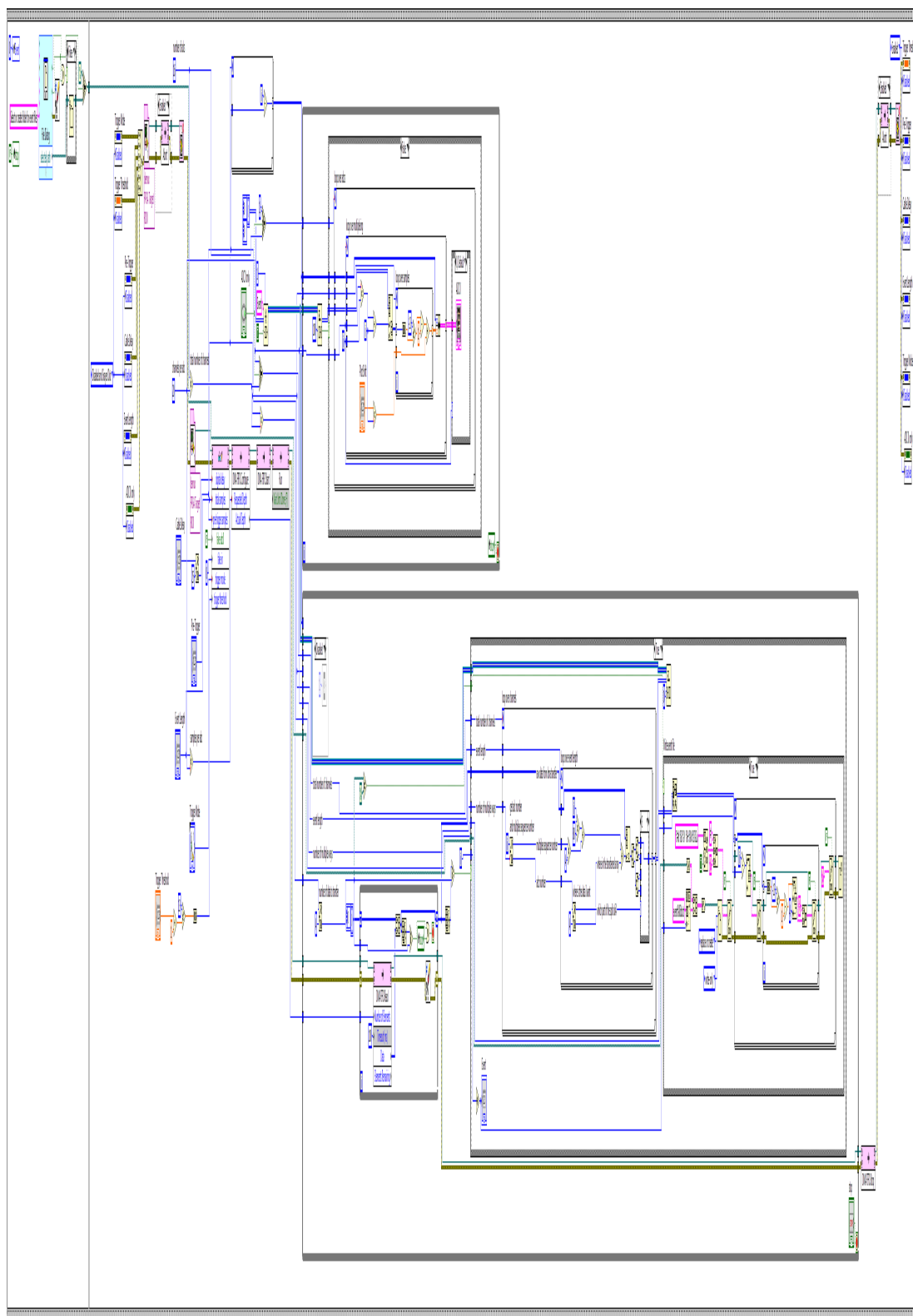


Figure 3.37: LabVIEW virtual instrument used as the signal multiplexer and demultiplexer data acquisition system.

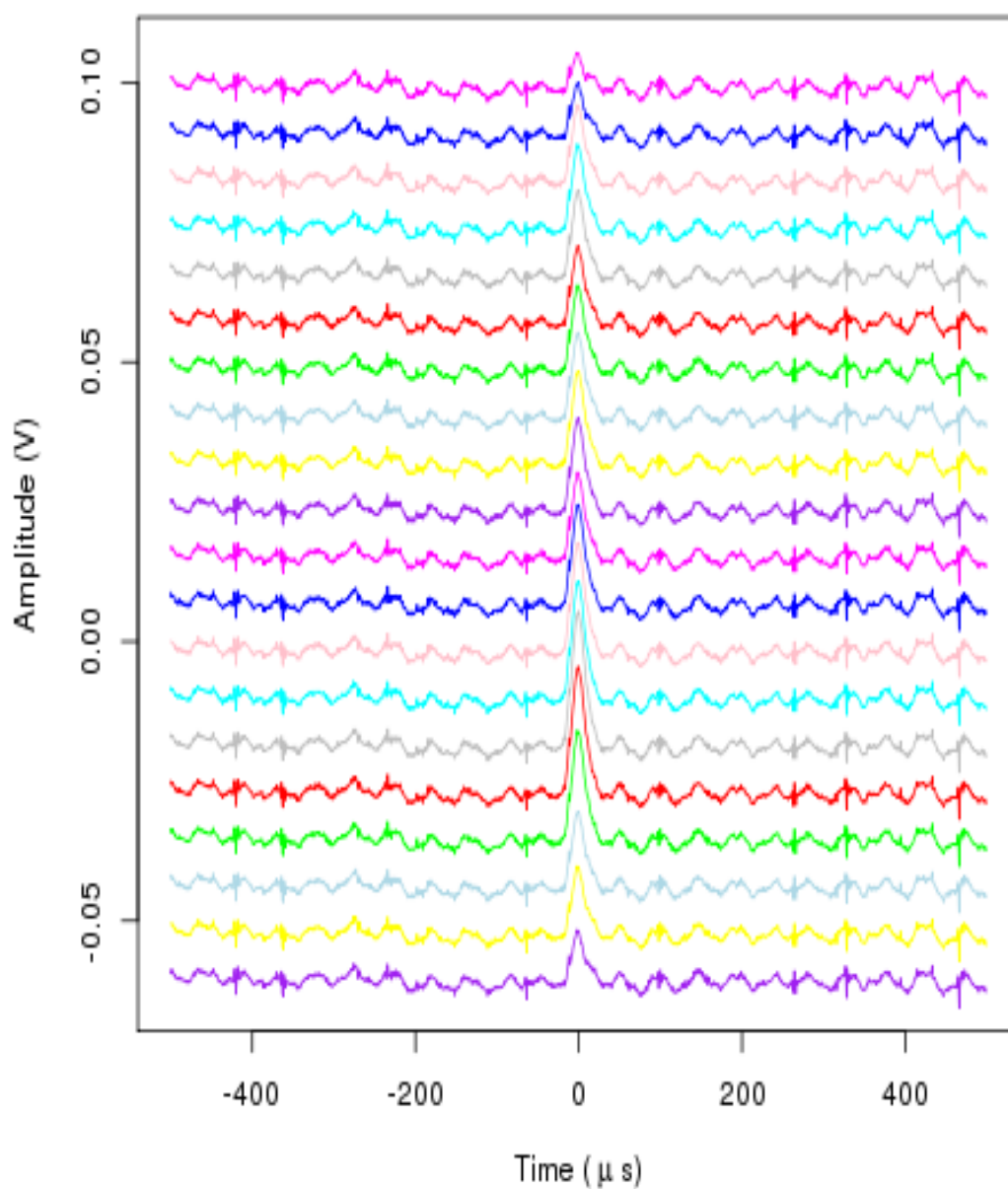
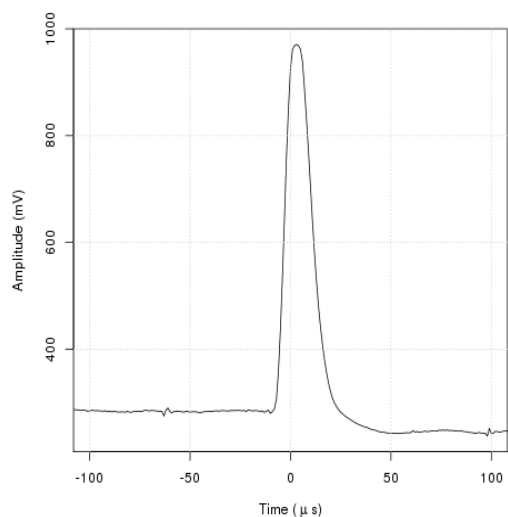


Figure 3.38: Sample of demultiplexed signals (multiplexed at 625 kHz) showing signal channels of the DRIFT-IIe pro detector when exposed to an alpha source.

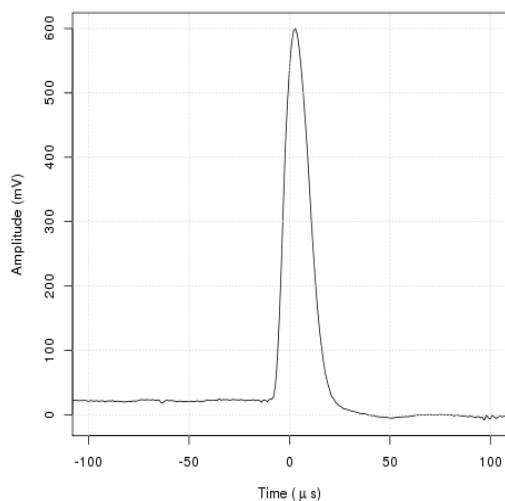
signals were multiplexed at the same frequency using the multiplexer data acquisition system discussed in Section 3.8. The Bragg curve effect due to energy loss of an alpha particle along the detected signal track can be seen in Figure 3.38. This is with a background low frequency sinusoidal waveform noise on each of the observed signal channels shown in that figure. These low frequency noise were not present before the signals were multiplexed. Hence, they must have been coupled to the signals during the multiplexing or demultiplexing processes or both. This type of noise can be suppressed in future design of this type of multiplexing data acquisition system by isolating the power channel, analogue and digital channel grounds using different PCB ground layers while designing the multiplexer board. The quality of the signal input to the multiplexer can be improved if coaxial (relative to ribbon) cables are used to route signals from detector to the multiplexer board. Also, shorter conducting traces can reduce the MUX board susceptibility to radiated and other extraneous low frequency noise. Further investigations show that the observed signal to noise ratio decays with increase in multiplexing frequency. An exponential decay in signal to noise ratio was observed when operating with multiplexing frequencies that are >1 MHz.

To understand the effect of signal multiplexing on the intrinsic Bragg curve effect on alpha tracks after these signals are demultiplexed, 1000 alpha event tracks were considered. The observed low frequency background noise on each of the channels of these events were suppressed by fitting and subtracting harmonics of low frequency waveform on each of the demultiplexed signal channel. This was followed by a $30 \mu\text{s}$ Savitzky-Golay smoothing to further reduce the noise. Reconstructed pulse samples from demultiplexed alpha signal tracks are shown for different channels of the detector in Figures 3.39(a) to 3.39(d). As performed in the previous study done without using the signal multiplexing and demultiplexing data acquisition system, the average of signal pulse heights recorded on each of the anode signal wire channels due to alpha event tracks obtained from 1000 separate detector exposures were computed and shown for each of these anode signal channels in Figure 3.40. The results in that figure indicate that Bragg curve effects due to energy loss along the track of alpha particles can be observed after signal multiplexing and demultiplexing. The peak of the measured Bragg curve effect is 584 ± 0.6 mV obtained with a lower signal to noise ratio (>10) compared to the signals before they were multiplexed and subsequently demultiplexed. The magnitude of the observed Bragg peak is a few mV less than the previous

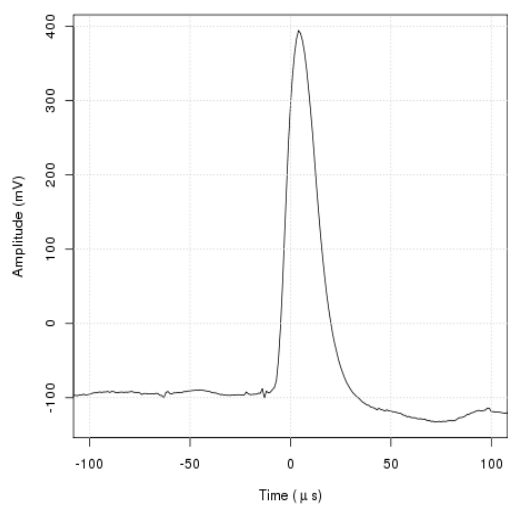
3. MUX readout for CYGNUS-TPC



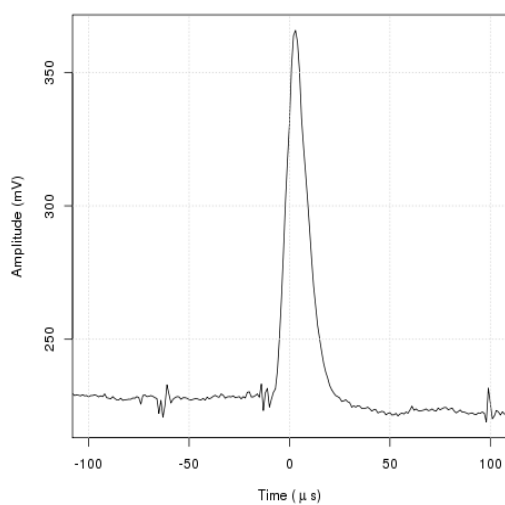
(a) Demultiplexed 686.3 mV pulse.



(b) Demultiplexed 579.6 mV pulse.



(c) Demultiplexed 486.9 mV pulse.



(d) Demultiplexed 141.1 mV pulse.

Figure 3.39: Samples of demultiplexed signal pulses obtained from different channels of the one-plane MWPC based DRIFT-IIe pro detector when exposed to an ^{241}Am alpha source.

3. MUX readout for CYGNUS-TPC

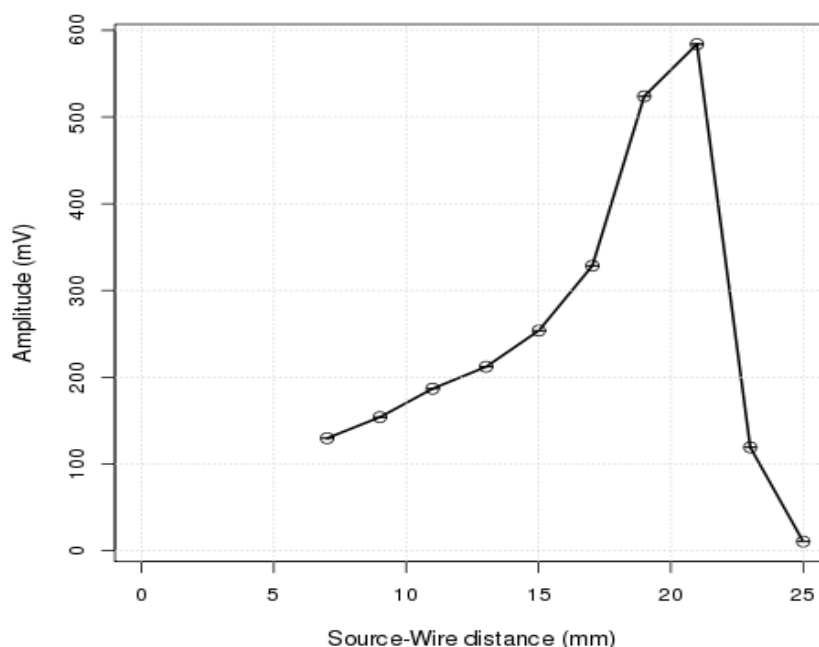


Figure 3.40: Average event pulse heights on anode signal wires obtained from 1000 demultiplexed alpha induced signal tracks detected with the miniature one-plane MWPC based DRIFT-IIe pro detector showing a Bragg curve effect.

result obtained without any signal multiplexing. This suggests that this few mV scale pulse could have been lost during the multiplexing and demultiplexing processes. The anode wire (counting from the location closer to the source) on which the Bragg peak was observed in Figure 3.29 is different from the result in Figure 3.40 obtained before and after the signal multiplexing, respectively. This could be due to systematic effects resulting from harmonic noise coupled to the analogue signals in the MUX circuit and the efficiency of the low-frequency wave fits and smoothening applied to the data after demultiplexing. Also, the average signal pulse heights (energy resolution) recovered after the multiplexing are also less than the results in Figure 3.29 by $\sim 10\%$. This may be due to variation in the detector gain or due to signal loss in the MUX circuit. Future work can focus on understanding these effects.

3.10 Conclusion

A single plane MWPC based miniature time projection chamber detector was designed, built and used to test the feasibility of a new 20:1 analogue signal multiplexer as a possible readout for a future massive directional WIMP search detector known as CYGNUS-TPC. The motivation was to study this as a possible means to reduce the cost of signal readouts without compromising the detector sensitivity to event x-y position. The results from this experiment is encouraging because it was possible to reconstruct alpha induced tracks and measure energy loss along the tracks. These measurements were performed before and after the signals were multiplexed and reconstructed through signal demultiplexing. In the future, these results can be validated using nuclear recoil events with lower energy threshold as required in WIMP search experiments.

An additional conclusion that emerged from this work is that the gas gain of the one-plane MWPC based detector is less than the results from conventional three plane MWPC configuration. In the one-plane MWPC, grounded anode wires are sandwiched between two grid wires biased at appropriate voltage to create electron avalanches. To overcome this low gas gain issue in the one-plane MWPC, a new GEM+MWPC hybrid readout technology is proposed. In the proposed configuration, GEMs can be used to create the required signal amplification through electron avalanches before the signals are readout using a grounded one-plane MWPC as discussed in the text. Further work is needed to test this GEM+MWPC hybrid readout technology.

Chapter 4

Directionality measurements with the DRIFT-II detector

4.1 Introduction

Signal directionality in a WIMP search detector refers to the ability to reconstruct the direction of an incident particle after it has scattered off a target nucleus using its nuclear recoil ionization track information. The possibility of signal directionality with fiducialisation in the proposed CYGNUS-TPC detector was investigated. This is using data from an existing fiducialised m^3 scale DRIFT-II detector. Signal directionality can be achieved in the DRIFT-II detector through the measurement of vector or axial components of nuclear recoil tracks. The vector or sense directionality component determines on which end of the track the event collision vertex is located. It is expected that there should be highest charge density at the beginning (tail) of a recoil track when compared to the end (head) of the track. This is because the maximum transferred energies are gained from the scattering particle at the point of first contact with the target nucleus and decreases as the recoiling nucleus comes to rest. Hence, this asymmetry in the distribution of signal charge along nuclear recoil tracks is known as the head-tail effect. The ability to measure this head-tail effect can potentially improve detector sensitivity by a factor of 10 [139, 140] and as a result, is vital to the proposed CYGNUS-TPC detector.

In the DRIFT experiment, the existing measurements of these directional capabil-

4. Directionality measurements with the DRIFT-IIId detector

ities that were reported in Refs. [87, 252, 253, 254, 255] were performed prior to the addition of oxygen to the target gas. As discussed in Section 2.8.4, the oxygen admixture was required to fiducialise the DRIFT-IIId detector. The aim of the work covered in this chapter is to establish if the important directionality information is still retained in this new operational regime. Some of the results obtained from these measurements have been published by the author in Ref. [256]. To achieve this, it was considered that theoretical computations show that neutron induced nuclear recoil tracks can mimic WIMP induced signals [253, 257]. Hence, the energy spectra of neutron (from ^{252}Cf source) induced events in a given detector are expected to be similar to expected spectra from WIMPs of similar energies. Thus, in this experiment neutron induced recoil tracks were generated as discussed in Section 4.2 to be able to quantify these directional effects in nuclear recoil ionization tracks. To do this, a new analysis algorithm was developed to aid the reconstruction of any available intrinsic head-tail effects and axial directional range component parameters in these neutron data obtained from the new fiducialisation mode operations.

4.2 Directed neutron exposures

To quantify the signal directionality, the DRIFT-IIId detector was exposed to neutrons from a ~ 338 kBq ^{252}Cf source from different directions for about seven days. The ^{252}Cf source is a radioisotope and an intense neutron emitter [258]. These neutrons are produced as the source decays to a more stable ^{248}Cm atom through spontaneous fission. The neutron exposures were performed without source collimation to minimise neutron back scattering. Illustration of the detector and details on the directions of the neutron exposures are depicted in Figure 4.1.

After neutrons from the ^{252}Cf source interact with target nuclei in the fiducial volume of the detector, the neutron transfers some of its energy to the target atom which induces ionization in the gas. Free electrons resulting from this interaction are quickly attached to surrounding electronegative CS_2 molecules to form CS_2^- as described in Section 2.8.4. These electrons and the CS_2^- are expected to be distributed along the nuclear recoil track. The CS_2^- anions are then drifted towards the MWPC readout. This is because the central cathode is biased with a more negative voltage relative to the MWPC readout plane. Drifting CS_2^- anions reduces the signal diffusion to thermal

4. Directionality measurements with the DRIFT-II detector

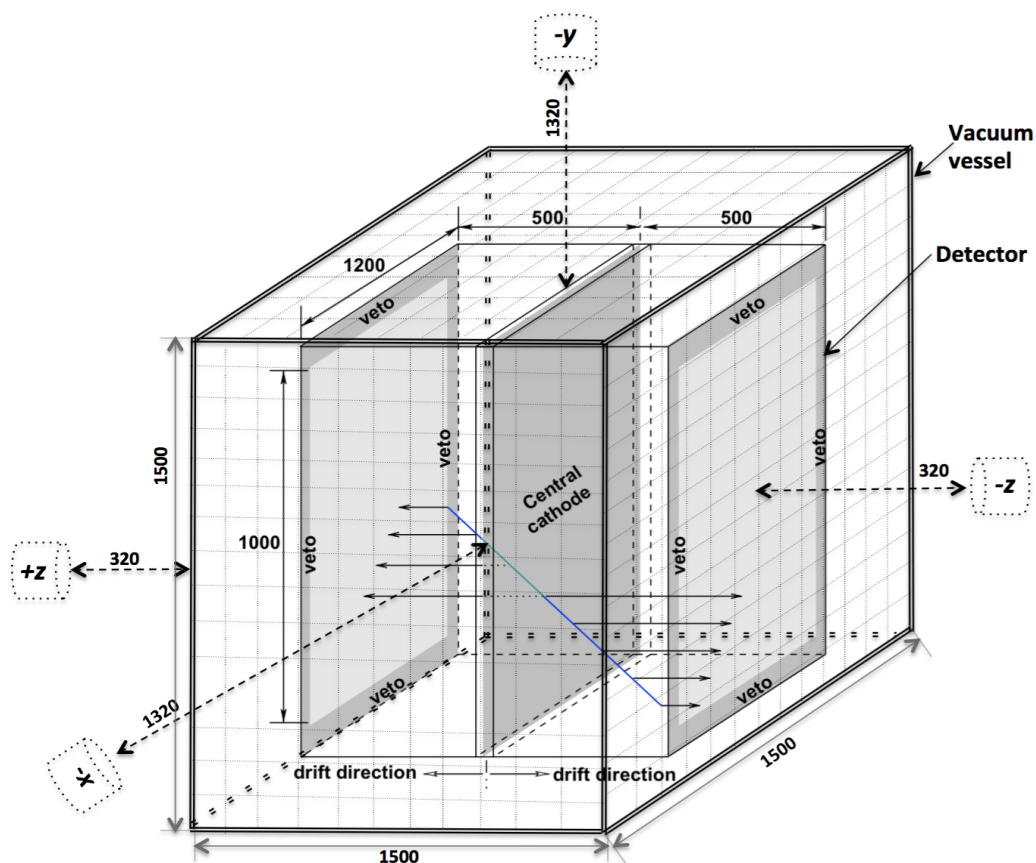


Figure 4.1: DRIFT-II detector showing different directions of neutron exposures, central cathode, veto, field direction and stainless steel vacuum vessel. Positions of the ^{252}Cf neutron source during the +z, -x, -z and -y runs are shown with small cylinders, which represent the lead canister used as the source container. The dotted double-headed arrows show the separation distance between the neutron source and the vacuum vessel during the runs. There is a separation of 250 mm (150 mm) between the detector and the vacuum vessel from the +z and -z (-y and -x) directions. Dimensions in mm.

scale [229]. During drift, some population of the CS_2 anions undergo three-body electron attachments through Block-Bradbury mechanisms [194, 195, 196, 197, 198] in the presence of O_2 to form three minority charge carrier species in addition to the main CS_2^- charge cloud. Closer to the readout plane, the presence of higher electric field in this region of the detector causes the charge signals to avalanche on the grounded anode wires. This frees large amount of electrons, creating electron avalanche and CS_2 cations. The electrons continue on the anode wires while the CS_2^+ drift in the electric

4. Directionality measurements with the DRIFT-IIId detector

field to the grid wires. For more on target gas, detector operation principles, configuration and principle of operation of the MWPC readout used in the DRIFT-IIId detector, see Section 2.8.4 and references therein.

The hardware threshold of the detector was set to 15 mV throughout this experiment, resulting in a typical trigger rate of 5 Hz and minimum detected recoil energy of ~ 300 NIPs (~ 20 keV_r ^{19}F equivalent energy). NIPs is the number of electron ion pairs produced by recoiling nuclei. Detector gas gain and energy calibrations were performed 4 times in a day as described in Section 4.4. Throughout this experiment, the 30:10:1 Torr of $\text{CS}_2:\text{CF}_4:\text{O}_2$ gas mix was operated in the continuous flow mode using the automated gas handling system discussed in Section 2.8.4.

The source position was chosen such that the mean neutron direction (MND) pointed along the z -direction (perpendicular to the central cathode and MWPCs), x -direction (parallel to the grid wires), and y -direction (parallel to the anode wires). In previous studies the DRIFT detector was found to be most sensitive to head-tail for events from the z -directions since microsecond sampling, coupled with the anion drift speed, results in a spatial sampling of about $60\ \mu\text{m}$ along this direction. These are termed the optimal directions (see Ref. [253]). The detector was exposed from these optimal ($+z$ and $-z$) and anti-optimal ($-x$ and $-y$) directions. In the exposure with the MND along the $+z$ direction, the source was placed to the left of the MWPCs such that neutron induced recoils in the left detector were predominantly oriented towards the central cathode, while in the right detector neutron induced recoils were predominantly oriented away from the central cathode. Inversely, in the exposure with the MND along the $-z$ direction, the source was placed to the right of the MWPCs such that neutron induced recoils in the right detector were predominantly oriented towards the central cathode, while in the left detector neutron induced recoils were mainly oriented away from the central cathode. The runs where the source was centered on the central cathode from the x and y -directions are known as $-x$ and $-y$ runs. Hence, charge signals obtained from the left and right back-to-back detectors in each of the neutron exposures can be used in analyses to account for any bias from shaping electronics.

In each of these exposures, the source was placed at a distance of 32 cm (107 cm) and 132 cm (207 cm) away from the vessel (geometric center of the central cathode) for the optimal and anti-optimal directed neutron runs, respectively. These distances result in neutron interaction angular spread of about 25° (14°) for the optimal (anti-

4. Directionality measurements with the DRIFT-IIId detector

optimal) directed neutron exposures. In these measurements, the source neutron-vessel separation distances for the optimal and anti-optimal runs were maximised subject to available space in the underground laboratory during the exposures. The exposure from the optimal directions was done to ascertain if the sensitivity of the DRIFT-IIId detector to signal head-tail (earlier reported in Ref [253]) was affected by addition of the oxygen that aided the full fiducialisation of the detector while the anti-optimal runs were expected to provide the required reference for null results. However, in the axial case, the range components of nuclear recoil tracks can be reconstructed for the optimal and anti-optimal neutron events, and then, the expected modulation in the observed amplitude of the axial range component parameters can be used to infer the direction of the original particle.

4.3 Introduction to DRIFT data and analyses

As discussed in Section 2.8.4, signal waveform tracks from each of the grid and anode MWPC wire planes are grouped down to 8 channels before the data is stored for analysis. The amplitude of raw signal pulses from these 8 grid and 8 anode signal channels with 3 veto channels are shown as a function of event duration in Figure 4.2 for a neutron induced nuclear recoil. It can be seen that signals from both the right and left MWPCs are shown in that panel. The signals from the left MWPCs are marked with labels starting with L (for left) while those from the right MWPC are marked with labels starting with R (for right). The second letter in each of these labels shows whether the data was obtained from an anode, a grid or a veto signal channel. In the end of each of the labels is either S, 1 . . .8, A or G which stands for signals obtained from integral charge in the given channels, channel numbers, anode and grid channels, respectively. For example, a channel that is marked LA1 was obtained from the first signal channel in the anode MWPC in the left detector while LAS is the integral charge in all the signals for that MWPC etc. Signal pulses from a neutron induced recoil can be seen in Figure 4.2 on the fourth and fifth channels of the right detector. In the grid channels, the observed signal pulses are scaled by a factor of 5 due to low gain from cations.

After the directed neutron exposure data have been recorded on disk, a set of analyses were performed to discriminate nuclear recoil tracks from noise (for instance,

4. Directionality measurements with the DRIFT-II detector

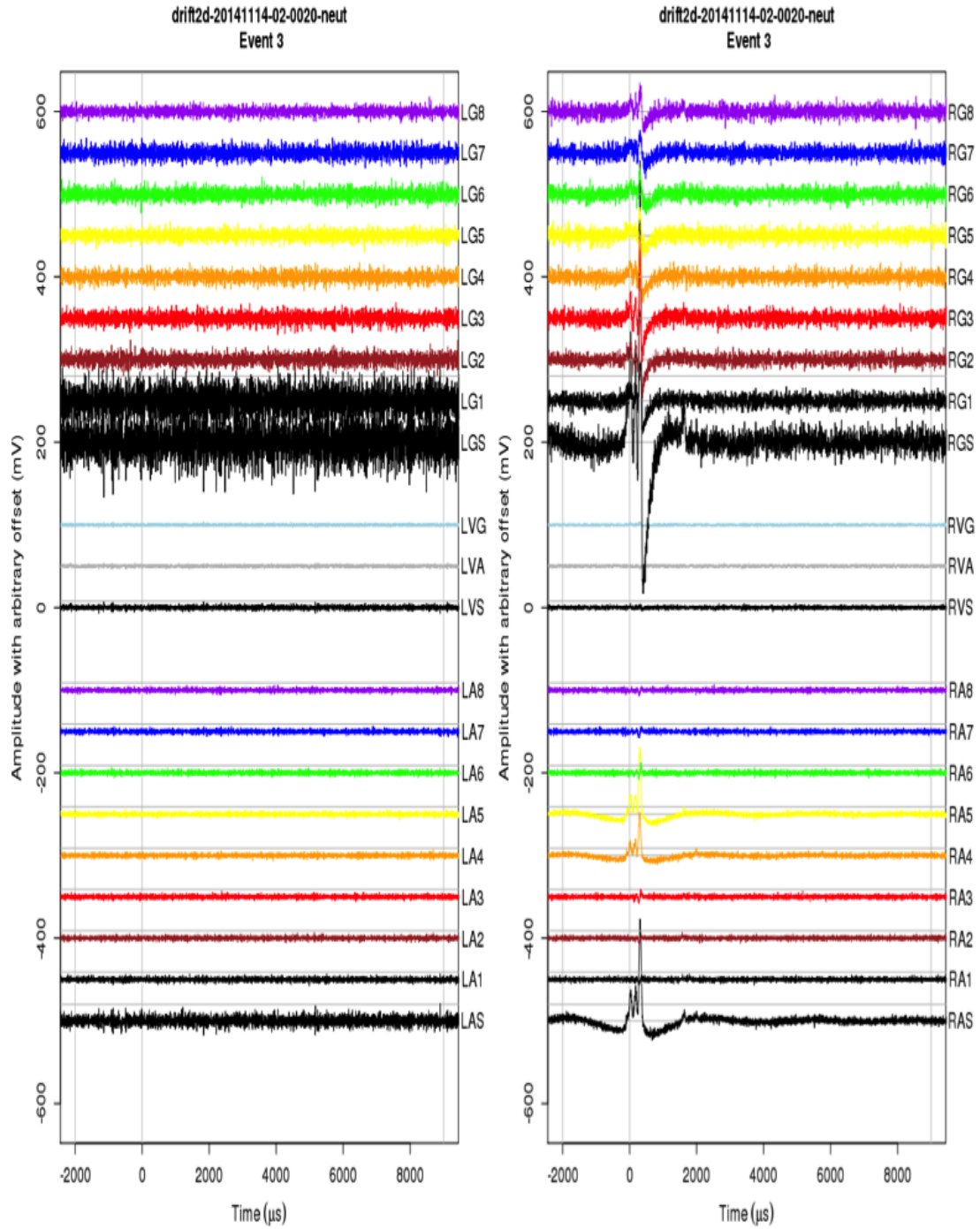


Figure 4.2: Sample of raw nuclear recoil event recorded by the DRIFT-II detector.

4. Directionality measurements with the DRIFT-II detector

alpha tracks from radioactive decays in the active volume of the detector or sparks near the MWPC) and also to reconstruct the ionization energy of the interactions and distances of their interaction vertex from the readout plane etc. The methods used in these analyses are summarized in Figure 4.3. It can be seen that there are four main types of nuclear recoil data which can be obtained from the DRIFT-II detector. These are the directed neutron data, neutron calibration data, shielded WIMP search data and unshielded rock neutron measurement data. An example of a set-up used to generate directed neutron data is discussed in Section 4.2. For more on the shielded WIMP search, neutron calibration and unshielded data, see Chapter 5.

As shown in Figure 4.3, there are three main stages of the nuclear recoil data analyses after which further analyses are required to extract any available intrinsic directionality information in the neutron induced nuclear recoil tracks. All raw data from the DRIFT-II detector come with some simple harmonic noise waveforms with kHz scale frequency and low (Hz) frequency noise from the power mains. The high frequency scale noise is removed by notching out the unwanted frequency from the Fourier transform of the recorded waveform data and reconstructing the good signals. For the low frequency noise, a set of 5 low frequency harmonics are subtracted from the experimental waveform data. Signal undershoot introduced by the shaping electronics are corrected using a two stage, time-constant function developed for the CR-200-4 μ s shaper used in this experiment. A set of noise introduced by the readout electronics is reduced using a 50 μ s Savitzky-Golay signal smoothing function. After these noise reduction procedures, the Stage 1 cuts (see Figure 4.3) are applied. For more discussion on these cuts, see Sections 4.5 and 4.6, also further discussions on analyses cuts are presented in Chapter 5.

In the next stage of the analyses, an analyses region of interest is defined from where the ionization energy of the event and distance of the event vertex from the readout plane are reconstructed. The details used in the reconstruction of ionization energies for interactions that occur within the active volume of the DRIFT-II detector are discussed in Section 4.4. Also at this stage of the analyses, a new set of highly efficient alpha rejection cuts can be implemented on the data. These stage 2 and stage 3 computations are discussed in more details in Section 4.5. More details on the head-tail (HT) analyses, axial directional component (Axial) analyses and WIMP analyses are discussed in Sections 4.6, 4.7 and Chapter 5, respectively.

4. Directionality measurements with the DRIFT-II detector

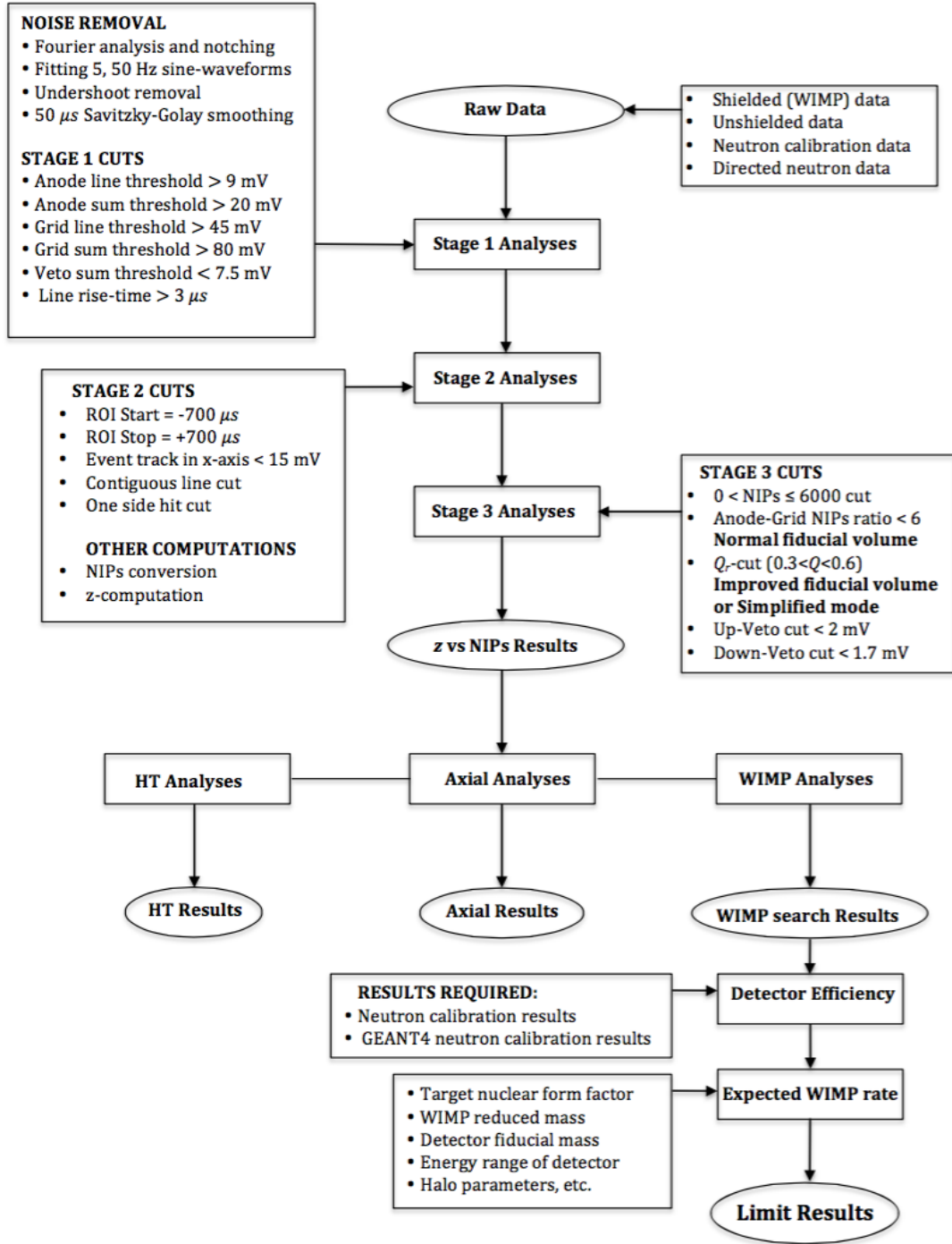


Figure 4.3: Block diagram showing the major analyses steps.

4.4 Energy calibration

To determine an energy conversion constant required for determination of the ionization energy of interactions, the detector was calibrated at intervals of 6 h. This was achieved using 5.9 keV X-rays emitted from two internal ^{55}Fe sources mounted near the two MWPCs as they decay to ^{55}Mn through the electron capture process. The sources were mounted in stainless steel containers, each covered with an automated shutter. One of the sources contained in the automated shutter set-up was installed on a perspex strong back support at the centre of the right hand side of the right MWPC. The second ^{55}Fe source was installed on a similar set-up on a strong back support located at the centre of the left hand side of the left MWPC. The X-ray windows in the automated shutters open only during the energy calibration runs. This is to ensure that X-rays from these ^{55}Fe decays do not cause ionization events during WIMP search operations but only when energy calibration is needed.

During an energy calibration operation, the shutter of the left MWPC source opens and exposes the fiducial volume of the left detector to ionization events from X-rays. The ^{55}Fe data in all the wires are then recorded to disk continuously for few minutes without any hardware threshold and trigger. This is because the ionization due to these ^{55}Fe events is very small and at high rate. Afterwards, the left shutter is closed while the right shutter opens for the process to be repeated in the right detector. The data are then gathered and analysed with a threshold of 2.3 mV. This is done by computing the resultant area of the ionization charge pulse Q_{Fe55} (in mV μs) for all the ^{55}Fe events that pass the analysis threshold and used as reference for reconstructing all nuclear recoil events in the fiducial volume of the detector within the latest 6 h interval. To do this, the average expected number of electron ion pairs (NIPs) from each ^{55}Fe event can be computed using:

$$NIP_{S_{Fe55}} = \frac{E_{Fe55}}{W}, \quad (4.1)$$

similar to Equation 3.2, where the W is the average amount of energy required to produce an electron ion pair during ionization in a given gas mixture [237] and E_{Fe55} is the energy of the X-rays. The ionization energy depends on a property of the gas mixture known as the quenching or Lindhard factor (see Ref. [238, 239]). This gas quenching factor q_{nc} measures the fraction of energy that goes into ionization for a given recoil. For example, the quenching factor is 0.53 for a 50 keV fluorine recoil

4. Directionality measurements with the DRIFT-II detector

in a 30:10 Torr of $\text{CS}_2:\text{CF}_4$ gas mixture, and so a recoil of this energy will produce 1055 electron ion pairs [113, 238]. For analyses presented here in this Chapter 4 and Chapter 5, we assumed a W value of 25.2 ± 0.6 eV as discussed in Ref. [113]. This shows that the expected $NIP_{S_{Fe55}}$ value is 234 ± 6 as measured in Ref. [259]. Hence, for each energy calibration runs, a histogram of individual ionization charge pulse areas from different signal channels in either side of the detector is generated and fitted to a gaussian. The mean of this resultant gaussian is used as the Q_{Fe55} value for computing the corresponding energy calibration constants E_C for that particular time interval via:

$$E_C = \frac{NIP_{S_{Fe55}}}{Q_{Fe55}}. \quad (4.2)$$

In Figure 4.4, the E_C values obtained for the left and the right detectors during the optimal directed neutron exposures is presented as a function of time. It can be seen

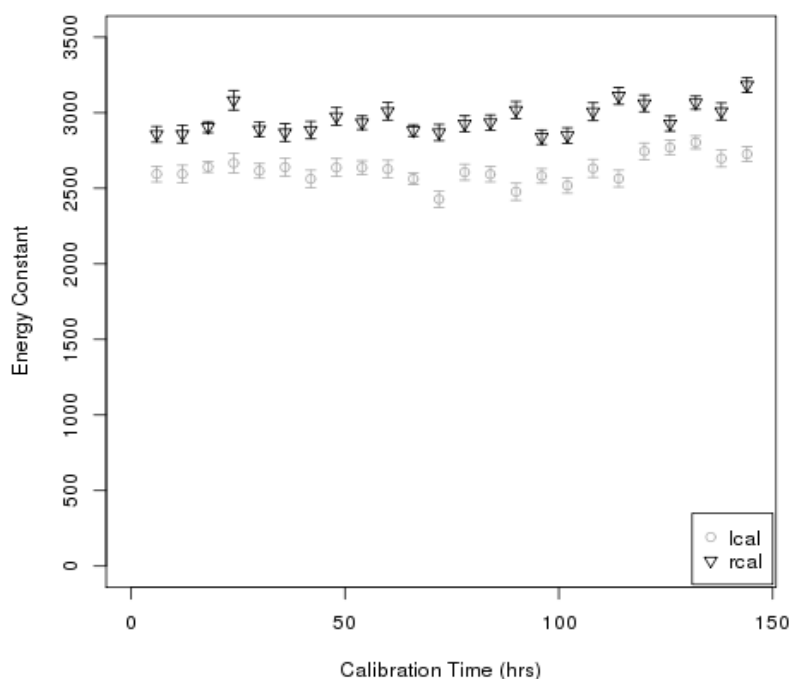


Figure 4.4: Energy calibration constant E_C obtained during the optimal directed neutron exposures shown as a function of time. The circle grey points are the E_C values for the left detector while the down pointing triangles in black are for the right detector.

4. Directionality measurements with the DRIFT-II detector

in that figure that the average gas gain scaled E_C parameter for the left detector is 2622 ± 70 . This has a 14% spread compared to 2956 ± 60 obtained for the right detector with a spread of 12%. The implication is that the gain of the right detector is higher than that of the left detector by $\sim 11\%$. This may be due to non-uniformity of tension on the wires in the two MWPCs. However, these right and left E_C values can be smoothed in analysis to account for this non homogeneity of the detector gains. Hence, using these parameters, the NIPs value of any nuclear recoil event $NIPs_{event}$ that occurred within the fiducial volume of the detector in a given time period can be determined using:

$$NIPs_{event} = E_C Q_{event} . \quad (4.3)$$

These NIPs values can then be transformed to the corresponding ionisation energies E_{events} using:

$$E_{events} = q_{nc} E_{in} = NIPs_{event} W , \quad (4.4)$$

where E_{in} is equivalent to the energy which the incident particle transferred to the recoiling nucleus before scattering off. The gas quenching factors q_{nc} are not the same for different recoiling nuclei of the same energy in the same gas medium. Therefore, absolute event E_{in} cannot be reproduced in detectors with many target nuclei (as in the DRIFT-II detector) unless the constituent recoil components can be separated. In the DRIFT collaboration, this is avoided by representing event energies using the NIPs equivalent parameters.

4.5 Fiducialisation of events z position in DRIFT-II detector

Radon progeny recoils (RPRs) [110, 111, 112] emanating from the central cathode were major source of backgrounds before the DRIFT-II detector was fiducialised. Nuclear recoil events due to RPRs are known to have common vertex with corresponding coincident alpha signals. This becomes problematic when the coincident alpha signal is concealed in the central cathode leaving only the nuclear recoil component signature which cannot be easily discriminated. As earlier discussed in Sections 2.8.4 and 4.1, the addition of 1 Torr of oxygen to the CS_2+CF_4 mixture results in several mi-

4. Directionality measurements with the DRIFT-II detector

minority carriers in addition to the main charge cloud, each drifting at a slightly different speed in the DRIFT detector. These minority carriers are believed to be due to different species of anions [199]. The three minority charge carriers and the main charge cloud are labeled as D, P, S, and I in Figure 4.5, with I being the primary ionization, equivalent to the charge cloud observed in the absence of oxygen [199]. The minority carriers exhibit various characteristics with their behaviour depending mostly on the z -position of the event as illustrated in Figures 4.5(a) to 4.5(d). The four signal pulses shown in Figure 4.5 are from four different neutron induced nuclear recoils obtained from the anode wire that recorded the highest voltage after the respective events at different z positions.

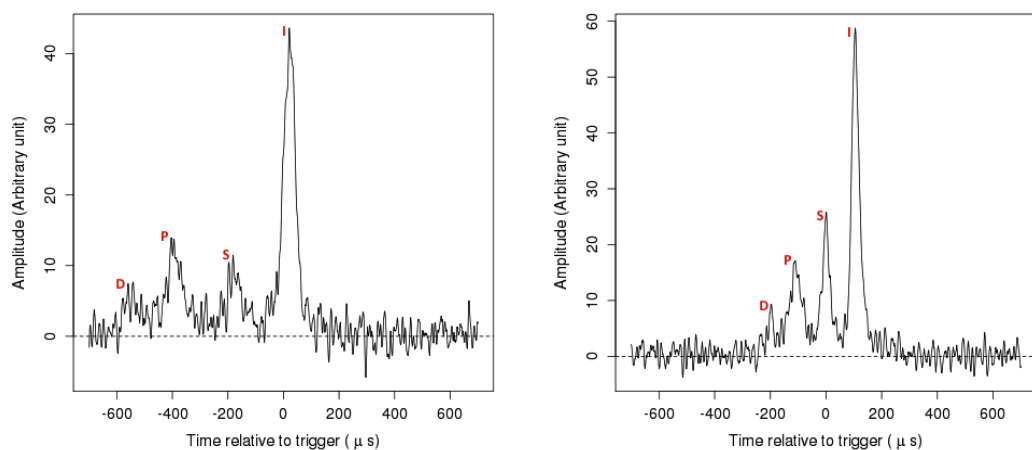
The I peak contains about 50% of the total ionization products in each event while the remaining $\sim 50\%$ is shared between the D, P, and S peaks [199]. The separation in arrival times of the anions in these peaks at the $x - y$ charge readout plane allows for the absolute position of an event vertex along the z -axis to be determined, and hence the detector is fiducialised. The absolute position of an event in the z -direction is given by:

$$z = (t_i - t_p) \left(\frac{v_i v_p}{v_p - v_i} \right), \quad (4.5)$$

where z is the distance between an event vertex and the readout plane, t_i and t_p are the arrival times of the anions in the I peak and P peak respectively, after drifting with corresponding velocities v_i and v_p . The events z positions increase from 0 (MWPC) to 50 cm (central cathode) for each of the two detectors. See the distribution of reconstructed neutron induced nuclear recoil events in the z -NIPs space in Figure 4.6 below.

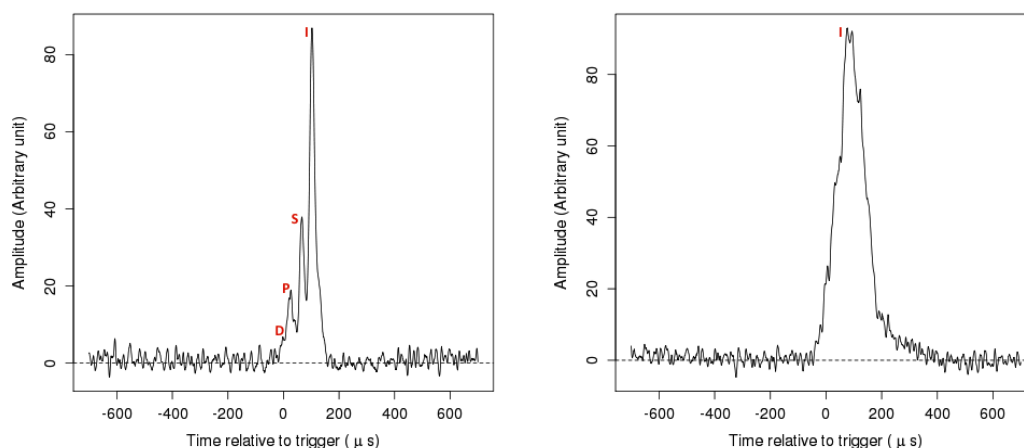
For the purpose of this analysis, events in the detector were grouped into three bins according to their z -position: low- z ($0 < z \leq 15$ cm), mid- z ($15 \text{ cm} < z \leq 35$ cm) and high- z ($35 \text{ cm} < z \leq 50$ cm). There are no events in the left part of the panel in Figure 4.6 because charge signal pulses diffuse as they drift to the readout plane. For low-energy, high- z events, diffusion broadens the pulse width and may reduce the maximum pulse amplitude below the data acquisition trigger. The trigger has since been modified to monitor the integral charge of the waveform, rather than the amplitude. This new upgraded trigger is expected to improve the efficiency for high- z events at low-energy. In the lower part of the panel, closer to the readout plane, the reconstruction cannot

4. Directionality measurements with the DRIFT-II detector



(a) High- z event at $z = 48.6$ cm, NIPs = 2300.

(b) Mid- z event at $z = 25.1$ cm, NIPs = 1504.



(c) Low- z event at $z = 9.2$ cm, NIPs = 1685.

(d) Low- z event at $z = ?$, NIPs = 1851.

Figure 4.5: Signal pulses from neutron-induced recoils at different z -positions within the active volume of the detector. The S specie charge carriers can change to other species of anions during drift, which reduces amplitude of the S peak (see (a)). Distinct D, P, S, and I peaks are shown for a mid- z event in (b). Typical behaviour of these peaks as they merge in the low- z region is shown in (c). The worst case in the very low- z region (closer to MWPC) is shown in (d). Events in the low- z region were rejected during analysis since their minority carriers become concealed under the main charge cloud. NIPs here stands for number of ion pairs.

4. Directionality measurements with the DRIFT-II detector

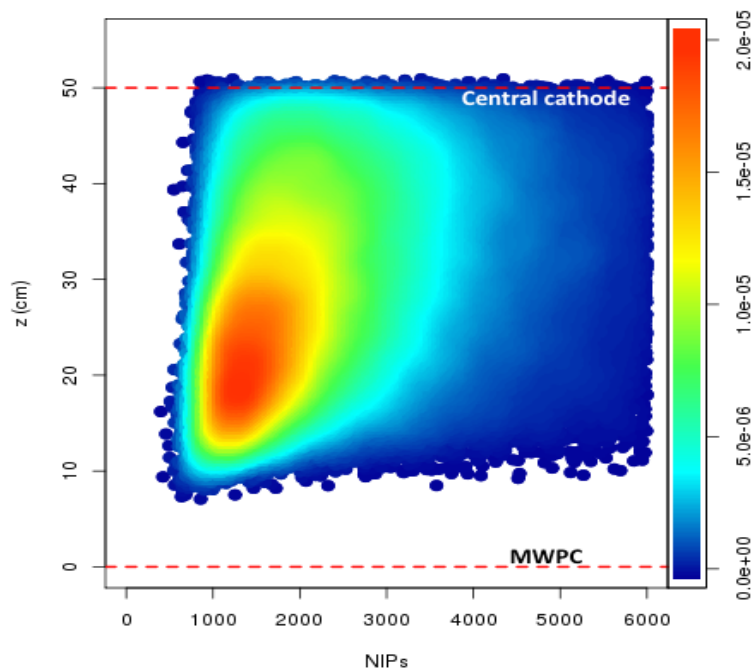


Figure 4.6: Event distribution in the z -NIPs space obtained from neutron exposure using a ^{252}Cf source. This is before the z cuts described in the text. The dashed red lines at 0 and 50 cm mark the locations of the readout plane and central cathode respectively. The colour scale represents the density of the events.

identify at least two of the D, P, and S peaks because of the short drift time, and so these events do not pass nuclear recoil selection cuts. The energy distribution of these events shown in Figure 4.6 is compared to the expected energy spectrum from ^{12}C , ^{19}F and ^{32}S recoil candidates generated with GEANT4 [260] program in Figure 4.7. It can be seen from these two spectra that the distribution of the experimental data and theoretical expectation from ^{12}C , ^{19}F , ^{32}S candidates all reach maximum at about 1000 NIPs, each with an exponential fall-off at higher NIPs. Hence, it is likely that there are some fractions of ^{12}C , ^{19}F and ^{32}S recoil candidates in this data set. However, the energy spectrum obtained from the GEANT4 simulation (see Figure 4.7(b)) has a slower high-energy fall-off with a steeper cut-off at low-energy when compared to the experimental data shown in Figure 4.7(a). These discrepancies may be related to unexplained systematics discussed in Section 4.6.1.

Relative to the I peak, the amplitude of the S peak is known to decrease with in-

4. Directionality measurements with the DRIFT-II detector

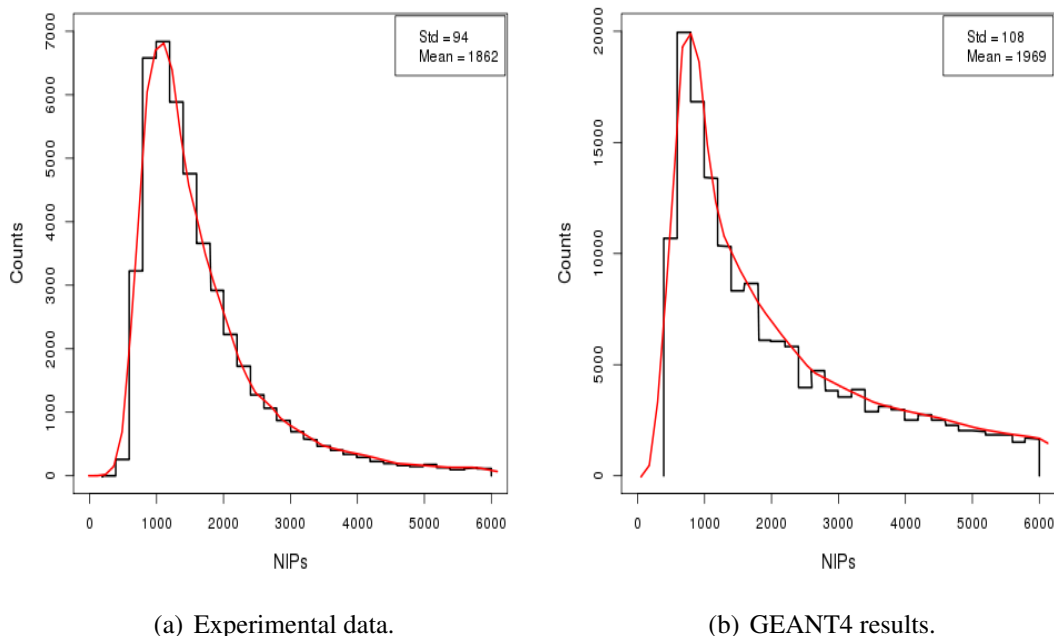


Figure 4.7: Energy spectra of neutron-induced nuclear recoils with the source in the optimal direction. (a) Experimental data before the z cuts (described in the text) from a $+z$ run. (b) Results of a GEANT4 Monte Carlo simulation. Red line is a density fit. The exposure live time of the experimental data is about a factor 4 less than that of the simulated data set.

creasing z [199]. This suppression of the S peak for the high- z events can be seen in Figure 4.5(a). In this work, many high- z events did not have a clear S peak, and so the z -position of each event was calculated from timing of the I and P peaks. For mid- z events, clear and distinct separation between the main and minority peaks was observed as depicted in Figure 4.5(b). In this region, the amount of charge in the peaks decreases from the I to the D peak, in that order. In the low- z region, closest to the MWPC, the total drift time of the anions is short, and so the temporal spacing between the peaks is small. For many of the low- z events, the four peaks are not resolved in time and hence, were not precisely fiducialised. As a result, we omit the low- z region from this analysis. The implication is that data from 30% of the active volume of the detector were not included in this analysis. New work to allow inclusion of these events is highly motivated within the DRIFT collaboration.

4. Directionality measurements with the DRIFT-IIId detector

As earlier discussed at the beginning of this section and also in Refs. [110, 111, 112, 113], a population of nuclear recoil events known as RPRs occurring near $z = 50$ cm are produced by radioactive decays on the central cathode. The effect of this contamination on the high- z sample is negligible because (1) the intrinsic decay rate is low compared to the neutron interaction rate (observed as <3 events/day vs. $\sim 2.3 \times 10^4$ events/day), (2) about half of the total number of these RPR events with $z > 50$ cm were not included in the analysis. These RPR events have z values that are larger than the expected maximum drift distance of 50 cm for the DRIFT-IIId detector due to z reconstruction uncertainty of the analysis.

In the work presented here, the high- z and mid- z bins were selected and used as a means to investigate the possible effect of diffusion on the head-tail asymmetry and the axial signatures for events closer to the central cathode and middle of the detector respectively.

4.6 Measurement of nuclear recoil track vector sense

The vector sense of nuclear recoil tracks also known as the head-tail effect can be measured using the charge distribution asymmetry on a given signal track. It is expected that larger charge density should be recorded at the tail relative to the head of nuclear recoil tracks. As described in Section 2.8.4, charge signal clouds due to interactions in the DRIFT-IIId detector are drifted through a uniform field to the MWPC readouts. In this work, only the main charge clouds known as the I peaks were analysed to determine the head-tail effect. This is because the I peak retains most of an event charge compared to D, P, and S peaks. In the analysis, a nuclear recoil candidate must pass a series of initial cuts described in Ref. [113, 253]. There are five main reasons to reject some events in this first stage. Events emanating from the central cathode (RPR events) may have hits (charge signals that cross the analysis threshold) on both sides of the cathode - such events are rejected, as are events with hits on non-contiguous wires, which may be two independent events in the same time window. Also, these repudiated non-contiguous signals can arise due to multiple scatter events within the allowed time window. An analysis threshold of 9 mV allowed for identification of the D, P, and S peaks since events are typically triggered by the I peak. Apart from the I peak, at least any two of the D, P, and S peaks must pass the analysis threshold for an

4. Directionality measurements with the DRIFT-II detector

event to be analysed further as a nuclear recoil candidate. Events with all eight wires in a group hit are cut to reject all contained alpha events with track length in the x - y plane greater than 15 mm. This is because there are no contained alphas with x - y range < 15 mm in the DRIFT-II detector design [112]. To reject other alphas and all other events emanating from outside the active volume of the detector, events with hits on the veto wires are rejected. Also, events with rise-times less than $3 \mu\text{s}$ are rejected to remove noise (for instance sparks).

In the next stage of the analysis, the integral charge from each event in ADC units was converted to corresponding NIPs equivalent. To do the NIPs conversions, a region of interest (ROI) was defined from $+700 \mu\text{s}$ to $-700 \mu\text{s}$ relative to the trigger time for all anode channels with signal above the analysis threshold. This ROI contains the D, P, S, and I peaks. The sum of the integrated charge values was converted to the NIPs equivalent value using the most recent ^{55}Fe detector gain calibration constant and W -value of the gas mixture as described earlier in Section 4.4. Events with $\text{NIPs} \leq 6000$ were considered further, no low-energy cut was applied.

Additionally, to quantify the relative amount of ionization in the minority peaks to the main charge cloud, a parameter called the minority peak ratio (mp.ratio) Q_r , defined as:

$$Q_r = \frac{Q_{DPS}}{Q_T}, \quad (4.6)$$

was also computed using the signal pulse on the anode wire that recorded the highest voltage in each event, where Q_{DPS} is the integral charge in the D, P, and S peaks, and Q_T is the total integral charge in the D, P, S, and I peaks. See Figure 4.8 for the spectrum of the Q_r obtained from all the directed neutron events. Three distinct peaks can be seen in that figure, the first two peaks are due to events with $Q_r < 0.30$ which have no or negligible minority peaks. These are sparks and events that occur near the MWPC readout plane which do not possess enough drift time for the minority charge carriers to separate from the main charge cloud. In these events, Q_{DPS} is less than 50% of the Q_T parameter. In the analysis, events whose Q_r values are greater than 0.30 and less than 0.65 were analysed further. This cut was found to be a powerful tool for discriminating nuclear recoils from radon progeny recoil events emanating from the MWPC charge readouts and some low- z events whose minority charge carrier peaks are completely concealed under the main charge cloud, respectively. These noise

4. Directionality measurements with the DRIFT-II detector

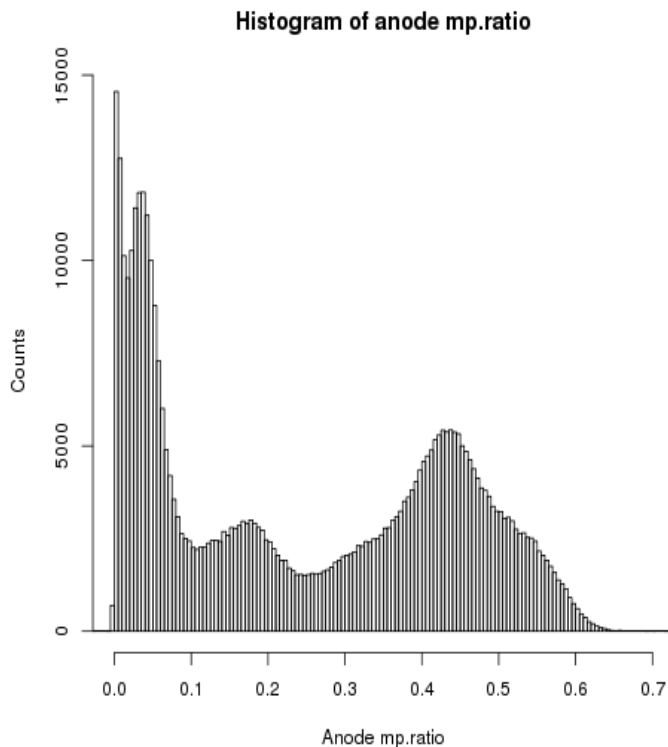


Figure 4.8: Spectrum of minority peak ratio (mp.ratio) for neutron induced nuclear recoil events obtained in all the directions of exposure before Q_r cuts.

events are expected to have little or no minority charge carrier peaks, which result in small Q_{DPS} values with $Q_r < 0.3$ (see Figure 4.8). The upper cut on $Q_r > 0.65$ is used to remove any residual spark events with continuous waveform pulses resulting in large Q_{DPS} values relative to expectations from nuclear recoil events.

To investigate the presence of the head-tail effect in the nuclear recoil tracks, the charge distribution in the main charge cloud from every nuclear recoil event was used, as illustrated in Figure 4.9. This is because of the expectation that any available head-tail signature will cause a temporal asymmetry in the charge distribution along the nuclear recoil tracks [253, 257]. The asymmetry was measured by comparing the integral charge in the first and second halves of the I peak using the signal pulse in the anode wire with the highest voltage for that event. Specifically, the temporal extent of the I peak was defined as the region where the signal is larger than 25% of the peak amplitude which is more than 5σ above noise (see Figure 4.9). This region was then

4. Directionality measurements with the DRIFT-II detector

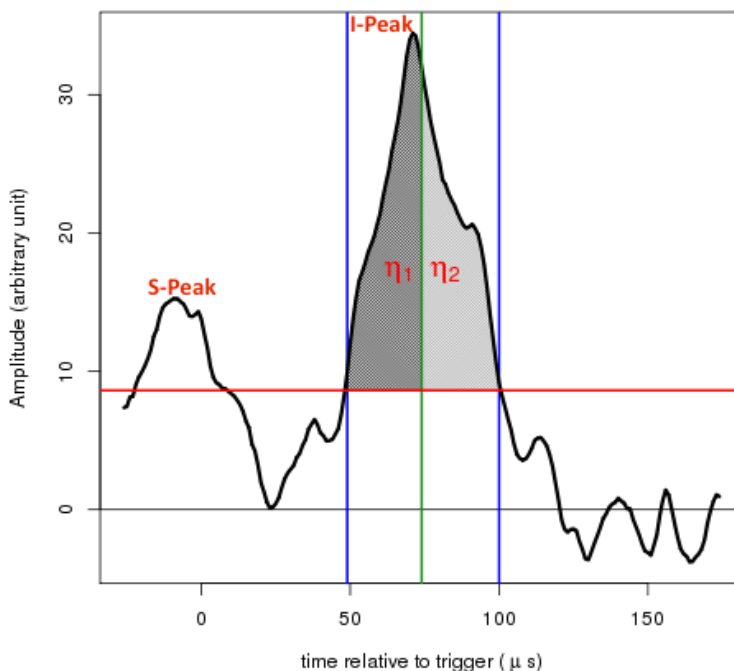


Figure 4.9: Event waveform from a single wire showing the analysed I peak with η_1 (integral charge in the first half of region of interest) shaded dark grey and η_2 (integral charge in the second half of the region of interest) shaded light grey. The two blue lines mark the region where the signal exceeds 25% of the peak amplitude. The green line is the mid-point time (half of signal duration above analysis threshold) between the first and second halves of the signal and the red line shows the 25% of the I peak used as the analysis threshold.

split into two equal-length regions, and the integral charges η_1 and η_2 were computed for each of the events that passed the cuts. The vector direction of the track was then determined from the ratio:

$$\alpha \equiv \frac{\eta_1}{\eta_2}, \quad (4.7)$$

which is equivalent to the magnitude of any asymmetry in charge distribution in a given nuclear recoil track pulse. Because the ionization density for nuclear recoils is larger at the start of the track than the end, a nuclear recoil whose velocity vector points towards the MWPC should have $\eta_1 < \eta_2$, and therefore $\alpha < 1$. Tracks with $\alpha > 1$ correspond

4. Directionality measurements with the DRIFT-II detector

to recoils that point toward the central cathode.

The head-tail asymmetry parameter α was computed for the events in left and right TPCs and termed α_L and α_R , respectively. Then, the mean value of α was computed separately for events in the left and right detectors: $\langle\alpha\rangle_L$ and $\langle\alpha\rangle_R$, respectively. There is a temporal asymmetry introduced by the shaping electronics in the measured waveforms. To account for this effect, we compute $\Delta\alpha \equiv \langle\alpha\rangle_L - \langle\alpha\rangle_R$ between the mean asymmetry parameters for the left and right detectors for each neutron exposure. This excellent electronics effect correction was possible due to the back-to-back nature of the DRIFT-II TPC detector. The expectation is that the largest head-tail effect should come from the $+z$ and $-z$ neutron source runs. In contrast, no head-tail effect is expected in the dataset from the anti-optimal $-x$ and $-y$ runs.

To understand the head-tail effect further, the percentage difference of the head-tail asymmetry parameter was determined and termed δ . This δ parameter, given by:

$$\delta = 100 \frac{|\Delta\alpha|}{\frac{1}{2}(\langle\alpha\rangle_L + \langle\alpha\rangle_R)}, \quad (4.8)$$

is the ratio of $|\Delta\alpha|$ to the mean of $\langle\alpha\rangle_R$ and $\langle\alpha\rangle_L$, expressed as a percent. The δ parameter quantifies the measurability of the head-tail effect, including both the intrinsic head-tail signature and the sensitivity of the detector to that signature. This δ parameter was measured using events from the optimal and anti-optimal directions. From the details in Equation 4.8, it can be seen that the δ parameter cannot be obtained on event-by-event basis due to the nature of the signal readouts in the DRIFT-II detector design. Details of the results obtained in this analysis for each of the directed neutron exposures are discussed in Section 4.6.1.

4.6.1 Nuclear recoil track vector sense results

The dependence of δ on energy is shown in Figure 4.10 for both the optimal and the anti-optimal runs, using bins of width 200 NIPs. It can be seen in that figure that the δ parameter measured in the anti-optimal runs is consistent with zero for all energies indicating that no head-tail effect was detected. This is expected because the mean directions of event tracks in these anti-optimal runs are the same for both TPCs, re-

4. Directionality measurements with the DRIFT-II detector

sulting in null $|\Delta\alpha|$ and δ parameters. Conversely, events from the optimal runs, where the mean direction of recoil tracks is oriented along the drift direction of anions, show a δ parameter that increases with energy. The δ parameter obtained from the optimal case is significant at 750 NIPs (~ 38 keV F-recoil energy equivalent). These results demonstrate the sensitivity of the detector to the head-tail directional signature and, furthermore, increased sensitivity with higher energy tracks.

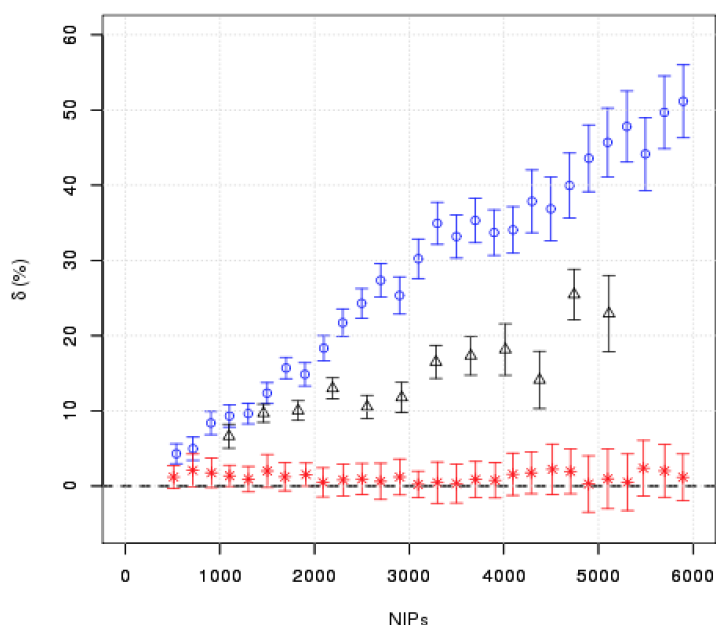


Figure 4.10: Percentage difference δ parameter for different recoil energies represented by NIPs equivalent. Results from this analysis (obtained with ^{12}C , ^{19}F and ^{32}S tracks) are shown with blue circle points for the optimal runs and red asterisk points for the anti-optimal runs. The black triangle points are 2009 results obtained with only ^{32}S tracks in pure CS_2 (see Ref. [253]). Colour online.

In Figure 4.10, the δ parameter obtained in this new gas mode is compared to the result obtained in a previous measurement performed in 2009 using pure CS_2 gas [253]. It was shown in that study that event tracks used in the measurement were primarily from ^{32}S recoils. The lower analysis threshold used in this measurement yielded the observed head-tail sensitivity below the ~ 1000 NIPs threshold obtained from the pure CS_2 data. Above 2000 NIPs, the measured values for δ in this work are approximately a factor of 2 larger than in the 2009 study.

To explain this, we hypothesize that the observed increase in the δ parameter in

4. Directionality measurements with the DRIFT-II detector

Figure 4.10 is due to the inclusion of ^{12}C and ^{19}F recoils in this data set which were not included in the 2009 study. A longer recoil track is expected to yield a larger head-tail effect because it allows for a more distinct separation between the beginning and the end of the recoil track. For instance, a SRIM [234] calculation of the ranges for ^{12}C , ^{19}F , and ^{32}S recoils that produce 1000 NIPs in 30:10:1 Torr of $\text{CS}_2:\text{CF}_4:\text{O}_2$ gives 1.70 mm, 1.51 mm and 0.98 mm, respectively. However, the gas quenching for each of the ^{12}C , ^{19}F and ^{32}S recoil candidates is different [257]. This gas quenching effect is expected to increase with mass of a given nucleus. Hence, in the context of this experiment, ^{32}S nuclear recoil tracks should suffer more energy loss per given recoil distance relative to ^{12}C or ^{19}F recoil candidates. Earlier studies in Ref. [144] reported the presence of head-tail effects in nuclear recoil tracks obtained with a CF_4 based TPC detector with potential ^{12}C and ^{19}F recoil candidates.

To check for the presence of nuclear recoil candidates with track ranges that are greater than the expectations from only ^{32}S recoils, the full width half maximum (FWHM) range $\Delta z = FWHM \times v_i$, was computed for each of the optimal (+z and -z) events. This Δz range was used because of its high resolution (<0.1 mm). The results obtained from this analysis is shown in Δz -NIPs space in Figure 4.11. The SRIM range (in 3D) R_3 as a function of NIPs was computed for ^{32}S , and the maximum expected Δz parameter for ^{32}S recoils was then determined by accounting for track thermal diffusion σ_d , shaping electronics σ_τ , and the differences in charge-carrier trajectories σ_f due to non-uniform electric field line distribution near the anode readout wires using $\Delta z = \sqrt{R_3^2 + \sigma_d^2 + \sigma_\tau^2 + \sigma_f^2}$ [229]. In this, $\sigma_d^2 = 2kTz/eE$ [243], $\sigma_\tau = 9.4 \mu\text{s} \times v_i$ and $\sigma_f = 8.23 \mu\text{s} \times v_i$ [229], where k , T , e and E are the Boltzmann constant, temperature, electronic charge and drift field, respectively. Results from these measurements show a significant number of events with Δz in excess of the expectations for ^{32}S , but consistent with presence of longer recoil tracks.

The spectrum of α_L and α_R parameters for events in all the bins for each of the optimal runs are depicted in Figures 4.12(a) to 4.12(d). Using the directions of neutron exposures depicted in Figure 4.1 to read the spectra in Figure 4.12, it can be seen that there are more events in the right TPC relative to the left TPC for -z run. Conversely, in the +z run, more events were recorded in the left TPC when compared to the right detector. Hence, this shows that the detector closer to the neutron source recorded the highest number of events in each of the optimal runs. This is expected because the

4. Directionality measurements with the DRIFT-II detector

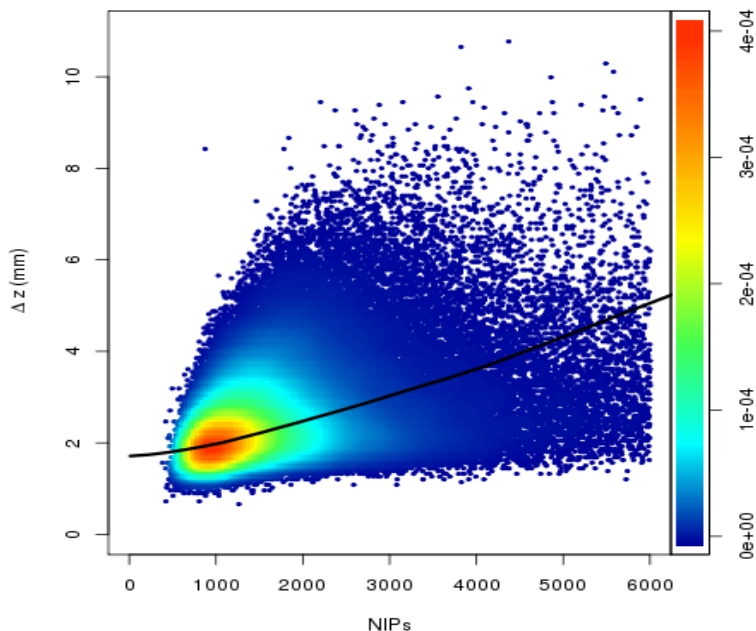


Figure 4.11: Experimental data overlaid with the maximal Δz predictions for ^{32}S recoils in 30:10:1 Torr of $\text{CS}_2:\text{CF}_4:\text{O}_2$ gas mix obtained using SRIM. The heat map is the experimental data while the black line is the maximum Δz predictions for ^{32}S recoils. The colour scale represents the density of the events.

neutron flux at any point in the detector is proportional to the subtended solid angle of the neutron source at that point [261].

The head-tail asymmetry parameter $\Delta\alpha$ obtained from the high- z and mid- z bins in the $+z$ and $-z$ runs are shown in Tables 4.1 and 4.2. Significant head-tail effects are apparent in both the high- z and mid- z regions as well as the combined data in Table 4.3.

Naively, it is expected that a lower value of $\Delta\alpha$ will be observed in the high- z region compared to the mid- z region of the detector due to diffusion effects. This is because diffusion can reorganise the actual charge distribution along a recoil track when it is exposed to longer drift distance which tends to conceal the head-tail effect. However, the opposite was observed because there are more high-energy ($\text{NIPs} > 1500$) events in the high- z region of the detector compared to the mid- z region of the detector. This is because the trigger efficiency on low-energy ($\text{NIPs} \leq 1500$) events decreases for events closer to the central cathode due to accumulated diffusion effects along the drift direction.

4. Directionality measurements with the DRIFT-II detector

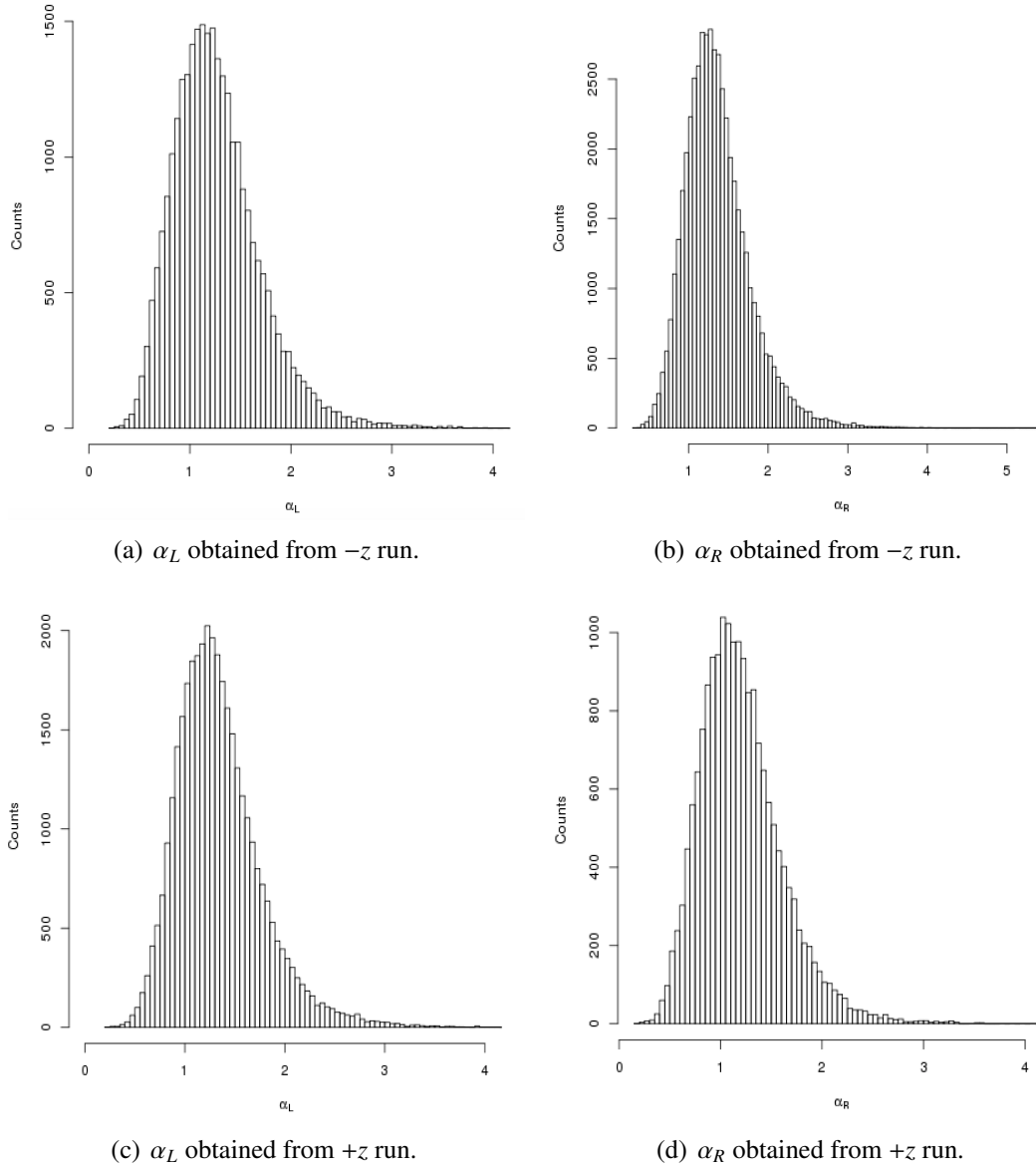


Figure 4.12: Spectrum of α parameter in the left and right detector obtained from optimal runs. The top panels are $-z$ events while the bottom panels are $+z$ events.

In fact, the fraction of high-energy events in the high- z is about an order of magnitude greater than that in the mid- z regions of the detector. To investigate this effect, 19800 events were selected from the optimal high- z and mid- z regions using a fixed energy spectrum of GEANT4 generated ^{32}S recoil events. These selected events were

4. Directionality measurements with the DRIFT-II detector

Table 4.1: Head-tail parameter obtained from high- z events in the $+z$, $-z$ runs. Only statistical uncertainties are quoted. The n is the number of events, other symbols used here are defined in the text.

MND	n	live-time (days)	$\langle\alpha\rangle_L$	$\langle\alpha\rangle_R$	$\Delta\alpha \pm \sigma_{\Delta\alpha}$
$+z$	19955	1.909	1.294 ± 0.003	1.146 ± 0.004	0.148 ± 0.005
$-z$	21054	3.713	1.175 ± 0.004	1.316 ± 0.003	-0.141 ± 0.005

Table 4.2: Head-tail parameter obtained from mid- z events in the $+z$, $-z$ runs. Only statistical uncertainties are quoted. Symbols are defined in Table 4.1.

MND	n	live-time (days)	$\langle\alpha\rangle_L$	$\langle\alpha\rangle_R$	$\Delta\alpha \pm \sigma_{\Delta\alpha}$
$+z$	31267	1.909	1.359 ± 0.003	1.256 ± 0.004	0.103 ± 0.005
$-z$	49005	3.713	1.303 ± 0.003	1.377 ± 0.002	-0.074 ± 0.004

Table 4.3: Head-tail parameter obtained from combined high- z and mid- z events in the $+z$, $-z$, $-x$, and $-y$ runs. Only statistical uncertainties are quoted. Symbols are defined in Table 4.1.

MND	n	live-time (days)	$\langle\alpha\rangle_L$	$\langle\alpha\rangle_R$	$\Delta\alpha \pm \sigma_{\Delta\alpha}$
$+z$	51222	1.909	1.336 ± 0.002	1.203 ± 0.003	0.133 ± 0.003
$-z$	70059	3.713	1.258 ± 0.003	1.360 ± 0.002	-0.102 ± 0.003
$-x$	5094	0.915	1.408 ± 0.009	1.411 ± 0.009	-0.003 ± 0.013
$-y$	2873	0.561	1.345 ± 0.011	1.350 ± 0.012	-0.005 ± 0.016

analysed using the same procedure described above. The resultant $\Delta\alpha$ parameter of 0.098 ± 0.005 and 0.104 ± 0.006 were obtained from the high- z and mid- z regions, respectively. This result demonstrates that both diffusion and recoil energy affect the head-tail reconstruction.

The larger fraction of high-energy events in the high- z region of the detector is expected to produce longer recoil tracks with distinct track head-tail separation and

4. Directionality measurements with the DRIFT-II detector

higher signal to noise ratio which yield higher values of the head-tail asymmetry parameter $\Delta\alpha$, compared to the mid- z region. Results obtained from all the events in the optimal ($+z$ and $-z$ data) and anti-optimal ($-x$ and $-y$ data) runs are presented in Table 4.3. It can be seen from this table that a higher value of the head-tail parameter $\Delta\alpha$ was obtained from $+z$ and $-z$ directions when compared to $-x$ and $-y$ runs. This confirms that $+z$ and $-z$ are the optimal directions for head-tail detection in the DRIFT-II detector design as reported in Ref. [253]. Also as expected, $-x$ and $-y$ exposures returned null head-tail effect. It can be seen in Tables 4.1 to 4.3 that $\langle\alpha\rangle_R$ and $\langle\alpha\rangle_L$ for $+z$ and $-z$ neutrons, respectively, are not less than 1 as expected. As described in Section 4.6, this is due to the effect of the shaping electronics, which is accounted for in the computation of $\Delta\alpha$ parameter. Even with the effect of the shaping electronics, it can be seen that $\langle\alpha\rangle_L > \langle\alpha\rangle_R$ for the $+z$ run and $\langle\alpha\rangle_L < \langle\alpha\rangle_R$ for the $-z$ run, as expected.

Using the observed results from the optimal and anti-optimal directions shown in Table 4.3, the number of nuclear recoil events required for a 3σ head-tail effect detection can be constrained. This is in the context of the expected modulation in observed $\Delta\alpha$ parameter due to the motion of the Cygnus constellation (expected mean direction of WIMPs) across the Earth in a sidereal day. This can be achieved by considering the case where the Cygnus constellation moves from the $+z$ or $-z$ to either $-x$ or $-y$ directions of the detector. Then, considering that the $\Delta\alpha$ parameter expected from $-x$ and $-y$ directions should be consistent with zero and statistically insignificant as shown in Table 4.3. It can be obtained that the magnitude of head-tail effect of about 44.3σ and 34σ is expected, when the Cygnus constellation moves from the $+z$ and $-z$ directions to the anti-optimal directions of the detector, respectively. These results suggest that about 258 to 589 nuclear recoil events could be enough for a 3σ head-tail detection in the DRIFT-II detector design.

Some cross-checks can be done on the results presented in Tables 4.1, 4.2 and 4.3. For each of the tables, the difference between the magnitude of the $\Delta\alpha$ parameter for the $+z$ and $-z$ runs should be zero within uncertainties. The differences are 0.007 ± 0.007 (Table 4.1, high- z region), 0.029 ± 0.006 (Table 4.2, mid- z region) and 0.031 ± 0.004 (Table 4.3, combined mid- z and high- z regions). These checks indicate agreement of the two measurements of $\Delta\alpha$ for the high- z events, but also indicate the presence of a systematic effect for the two measurements of $\Delta\alpha$ for the mid- z events of Table 4.2 and the combined data in Table 4.3. Although, the observed head-tail asymmetry parameter

4. Directionality measurements with the DRIFT-II detector

remains statistically significant after allowing for this systematic effect.

Additionally, two other alternative measures of the $\Delta\alpha$ parameter can be formulated by using only one side of the detector (left or right) with both $+z$ and $-z$ runs. This can be done by subtracting $\langle\alpha\rangle_L$ (for a $-z$ run) from $\langle\alpha\rangle_L$ (for a $+z$ run) and also by subtracting $\langle\alpha\rangle_R$ (for a $-z$ run) from $\langle\alpha\rangle_R$ (for a $+z$ run). These two alternate calculations yielded 0.119 ± 0.005 and -0.170 ± 0.005 for the high- z region of the detector. For the mid- z events, the alternate measures were found to be 0.056 ± 0.004 and -0.121 ± 0.004 , while for the combined runs the alternate measures are 0.078 ± 0.004 and -0.157 ± 0.004 . The differences between the magnitude of each pair of these numbers obtained from the alternate measures are 0.051 ± 0.007 (high- z), 0.065 ± 0.006 (mid- z) and 0.079 ± 0.006 (combined mid- z and high- z). The presence of these differences again indicate systematic effects, since the magnitude of the numbers obtained from the alternative measures are not equal within uncertainty. The differences reported above are estimates of the size of the systematic effects, which are larger than the statistical uncertainties reported in Tables 4.1 - 4.3.

After allowing for the systematic effects described above, the head-tail effect remains clearly present for the optimal runs. It should be noted that the systematic effects were not observed in Ref. [253]. However, the experimental conditions for this work were different in comparison to Ref. [253]. For mechanical reasons, the neutron source had to be placed closer to the detector for this work. In addition, for this work there existed an asymmetric distribution of materials surrounding the detector. Hence, the angular spread of neutrons from the source and any effect of neutron path reorientation due to scattering interactions in surrounding materials are expected to be different relative to the previous measurements.

To understand the possible cause of this systematic effect, a careful GEANT4 [260] simulations of the detector was performed. In this simulation, the steel vacuum vessel, wooden box container surrounding the detector for polypropylene pellet shielding and about 50 cm of polypropylene pellets buried beneath the laboratory floor, directly under the stainless steel vacuum vessel used for shielding the detector from underneath background rock neutrons were included. The simulated detector was then exposed to neutrons from a ^{252}Cf source from the optimal directions with the source at the same distance as in the measurement. About 1000 neutrons were fired from the source and their step by step interactions were recorded until they come to rest. The result shows

4. Directionality measurements with the DRIFT-II detector

that the initial directions of about 60% of the neutrons were reoriented after scattering off from the wooden boards, underfloor polypropylene pellets and stainless steel vacuum vessel. But back scattered neutrons can change the MND for a given directed run and this likely contributed to the observed systematic effects. Full recoil track simulation can be used for more detailed understanding of the systematics. Though, the head-tail effect, observed in [253], is still present while operating in this new fiducialised mode.

4.7 Measurement of axial directional components of nuclear recoil tracks

Using nuclear recoil ionization tracks in the fiducial volume of the detector, three dimensional information about the track can be extracted. This track information has its x component along the grid wires, y components along the anode wires and z component along the drift direction (i.e. perpendicular to the MWPCs and the central cathode). These three ionization track informations are known as Δx , Δy and Δz range for the x , y and z components, respectively. Hence, the three dimensional range R_3 of a given nuclear recoil track can be determined by summing these Δx , Δy and Δz parameters in quadrature.

It is important to point out that this analysis can only reconstruct the absolute z position of events as discussed in Section 4.5 but cannot unambiguously reconstruct their absolute x and y positions. This is because of the multiplicity of the anode and the grid wires in the grouped signal channels, see Section 2.8.4. For instance, a hit on the first anode readout channel could be due to a hit on wire 53, 61, 69, 77, 85, 93, etc. However, knowing the absolute x and y positions of events are not useful for WIMP search detectors. The most important nuclear recoil ionization track axial informations for directional WIMP search experiments are the track range and recoil angle. It has been established in Refs. [87, 254, 255] that the DRIFT-II detector can measure these nuclear recoil ionization track properties before the recent fiducialisation operations. This work aims to investigate if this detector capability was affected by the addition of oxygen to the target gas using a new analyses algorithm.

The methods used for calculating each of these nuclear recoil track axial directional

4. Directionality measurements with the DRIFT-II detector

components are different due to the nature of the readout hardware. Each of these methods are described below.

4.7.1 Reconstruction of track Δx range

For each of the neutron induced recoil tracks, the maximum values of Δx range for the tracks can be reconstructed by counting the number of anode wires n that recorded parts of the ionization charges distributed along the recoil tracks, using:

$$\Delta x_{max} = 2n \pm 1 \text{ mm} . \quad (4.9)$$

The factor of 2 in Equation 4.9 is due to the 2 mm anode wire pitch in x -direction. This shows that the resolution of any measurement performed with Equation 4.9 is 2 mm. Hence, the relation in equation 4.9 cannot reconstruct Δx values that are less than 2 mm. Also, the minimum possible value of the Δx range can be determined using:

$$\Delta x_{min} = (n - 1) \times 2 \pm 1 \text{ mm} . \quad (4.10)$$

But Equation 4.10 assigns zero to Δx of nuclear recoil tracks that has all its charges recorded on a single wire (i.e. when $n = 1$). To account for these issues, the average of the maximum and minimum values was adopted in this analysis. This is given by:

$$\Delta x = \frac{\Delta x_{max} + \Delta x_{min}}{2} = 2n - 1 . \quad (4.11)$$

In this way, the resolution of the analysis in reconstructing the Δx parameter is improved by 50% relative to the method shown in Equation 4.9.

4.7.2 Reconstruction of track Δy range

As discussed in Section 4.2, after an interaction within the fiducial volume of the detector, cations resulting from signal avalanches near the anode wires drift to the grid wires where they induce voltage signals. In this process, the highest voltage signal pulse is deposited on the grid wire that is nearest to the position of the avalanche and event vertex. The induced signal pulses on other further grid wires grow progressively smaller.

4. Directionality measurements with the DRIFT-II detector

Hence, it is expected that the Δy range for nuclear recoil tracks should be encoded in the charge distribution between these grid wires. However, this Δy parameter cannot be determined by counting the number of grid wires with hits as in the Δx computations, rather, this can be done using the position of the centroid of the cations [254, 262, 263, 264].

To determine the Δy range component for each of the events that passed all the cuts described in Section 4.6, the grid channel that recorded the highest voltage and corresponding four contiguous signal channels (i.e. two contiguous grid signal channels on either side of the channel with the maximum voltage) were used. This is because the magnitude of the charge deposited on each channel depends on the location of the avalanche [262]. Hence, it is expected that more than 60% of the total cations from the signal avalanche should be deposited on these five grid wires.

In this analysis, to extract the charge centroid from these selected grid channels, a gaussian was fitted to their respective I peak charges and the charge centroid determined from that fit using:

$$y_n = \frac{\sum_{j=1}^k Q_j y_j}{\sum_{j=1}^k Q_j}, \quad (4.12)$$

where y_n is the centroid of the charge of width w deposited on the n^{th} grid channel, Q_j is the amount of charge that are deposited on a given grid wire at j^{th} time and y_j is the position of that charge from the beginning of the charge cloud. This y_j parameter is given by:

$$y_j = v_i t_j, \quad (4.13)$$

where v_i is the drift velocity of the I peak charge cloud and t_j is the temporal extent of charge Q_j from the beginning of the signal pulse. Also for each of the selected signal pulses, the z extent of the track range given by $z_n^y = w_n v_i$ was determined and plotted against the channel charge centroid y_n . Then, the Δy range is the product of the gradient $\frac{y_n}{z_n^y}$ of this plot and average of the z_n^y parameter. This is to neutralise the effect of z_n^y parameter on the determined Δy range.

4.7.3 Reconstruction of track Δz range

The Δz range was computed using the full width at half maximum (FWHM) parameter and the drift velocity of the I peak charge as described in Section 4.6.1. The steps used

4. Directionality measurements with the DRIFT-II detector

in computing this FWHM parameters are illustrated in Figure 4.13. It can be seen from

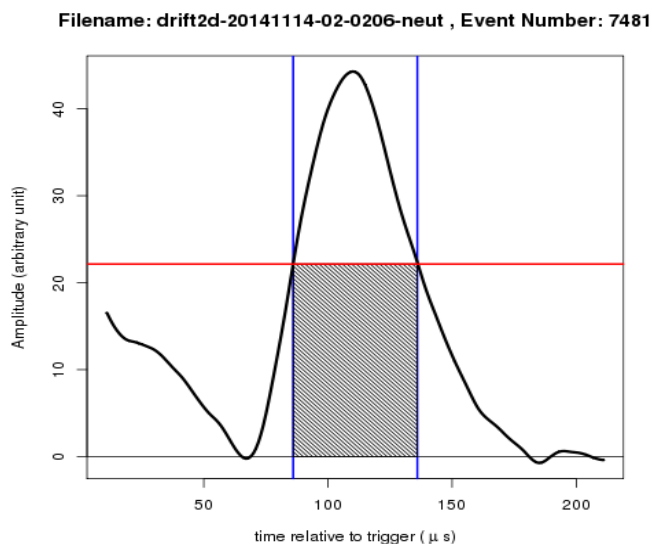


Figure 4.13: Event waveform showing the analysed I peak and the determined full width half maximum (FWHM) parameter. The red line marks 50% of charge amplitude in the I peak, the two blue lines are the lower and upper temporal bounds of the FWHM while the shaded region is the area under the determined FWHM.

that figure that the FWHM time for a given signal pulse was defined as the temporal extent between the 50% of the peak amplitude at the rising and falling edges of the the signal pulse. The Δz analyses presented here were performed using signal charges in the I peak which are obtained from the anode channel that recorded the highest voltage for events that passed all the required analysis cuts. See Section 4.6 for more discussion on the details of the applied nuclear recoil selection cuts.

4.7.4 Other nuclear recoil axial parameters

When a particle scatters off a target nucleus within the fiducial volume of the detector, it transfers part of its energy to the target and sets the nucleus to recoil at a given recoil angle θ . This recoil angle can be better reconstructed from the recoil track signature. This is especially easier if the three dimensional vector components of the nuclear recoil track can be determined. However, the DRIFT-II detector readout hardware does not allow for reconstruction of these three dimensional vector components of a

4. Directionality measurements with the DRIFT-II detector

nuclear recoil track. Even in an idealised readout technology, it is known that nuclear recoil tracks undergo straggling and diffusion as they drift to the readout plane [193, 229, 265]. These effects can also affect the reconstruction of nuclear recoil angle from track information.

For this analysis, the three dimensional axial components of nuclear recoil tracks (Δx , Δy and Δz) discussed earlier can be employed to estimate this θ parameter using:

$$\theta = \arctan\left(\frac{\Delta y}{\Delta x}\right). \quad (4.14)$$

But this computation is a two dimensional approach to resolving the recoil angle with an assumption that the track is contained in a minimum cuboid. The three dimensional component of the recoil angle θ_3 can then be determined using the quadrature sum of the axial range components given by:

$$\theta_3 = \arccos\left(\frac{\Delta z}{R_3}\right) = \arccos\left(\frac{\Delta z}{\sqrt{\Delta x^2 + \Delta y^2 + \Delta z^2}}\right), \quad (4.15)$$

where R_3 is the 3-D range of the nuclear recoil track.

To understand how these axial parameters vary from the average values for events in the perpendicular directions, the average difference between each of axial range parameters from the two perpendicular direction ΔR_{\perp} was computed. For instance for Δx from the x directions, the $\Delta R_{\perp x}$ was determined using:

$$\Delta R_{\perp x} = \frac{1}{2} \left(\frac{\sum_{a=1}^{n_x} (\Delta x_{x_a} - \overline{\Delta x_z})}{n_x} + \frac{\sum_{a=1}^{n_x} (\Delta x_{x_a} - \overline{\Delta x_y})}{n_x} \right), \quad (4.16)$$

where n_x and $\overline{\Delta x_z}$ ($\overline{\Delta x_y}$) are number of events in the $-x$ neutrons and average Δx parameter obtained from z (y) directed neutron exposures, respectively. Each of the individual Δx parameters obtained from x neutrons is denoted with Δx_{x_a} , where a is the number of computation iterations in n_x . A similar process as in Equation 4.16 were employed for Δx , Δy and Δz in other directions of neutron exposure.

The magnitude of the expected oscillation A_o when the source is moved from a direction of neutron exposure or one axis of the detector to another can be estimated using the $\overline{\Delta z}/\overline{\Delta x}$ parameter from the given axes [87, 254]. If each of the neutron

4. Directionality measurements with the DRIFT-II detector

induced nuclear recoil tracks considered in this analysis can be described as a minimum cuboid with range components that obey Pythagoras theorem, hence, this ratio can be defined in terms of the third range component by:

$$\frac{\Delta z}{\Delta x} = \sqrt{1 + \frac{\Delta y^2}{\Delta x^2}}, \quad (4.17)$$

for each of the runs. However, using the information in Equation 4.15 where R_3 is defined as $\sqrt{\Delta x^2 + \Delta y^2 + \Delta z^2}$, it can be seen that the assumptions in Equation 4.17 are not valid for Δx , Δy and Δz parameters in this analysis. Empirically, the $(\overline{\Delta z}/\overline{\Delta x})$ parameter can be determined using:

$$\frac{\overline{\Delta z}}{\overline{\Delta x}} = \frac{\sum_{a=1}^n \left(\frac{\Delta z_a}{\Delta x_a} \right)}{n}, \quad (4.18)$$

where Δz_a and Δx_a are the Δz and Δx parameters obtained from a^{th} event while n is the total number of events in the considered exposure. In particular, the expected oscillation can be investigated in terms of event recoil energies as the source is moved from x to z directions in a given energy bin via:

$$A_{o_{zx}} = \left(\frac{\frac{\overline{\Delta z}}{\overline{\Delta x_z}} - \frac{\overline{\Delta z}}{\overline{\Delta x_x}}}{\frac{1}{2} \left(\frac{\overline{\Delta z}}{\overline{\Delta x_z}} + \frac{\overline{\Delta z}}{\overline{\Delta x_x}} \right)} \right) 100, \quad (4.19)$$

where $A_{o_{zx}}$ is equivalent to the magnitude of the expected oscillation as the source is moved from z to x direction. The $\overline{\Delta z}/\overline{\Delta x_z}$ and $\overline{\Delta z}/\overline{\Delta x_x}$ parameters are the average range component ratios obtained from Equation 4.18 for the z and x neutron events, respectively. Results from these computations and other axial track range reconstruction parameters are shown in Section 4.7.5 for different directions of neutron exposures.

4.7.5 Results from analysis of axial directional components of nuclear recoil tracks

The average Δx , Δy and Δz nuclear recoil range components obtained from each of the directed neutron exposures is shown in Table 4.4. In general, it can be seen from that table that the values of the Δx parameter are bigger for each of the runs compared to

4. Directionality measurements with the DRIFT-II detector

Table 4.4: Axial range components of nuclear recoil tracks obtained from $+z$, $-z$, $-x$, and $-y$ directed neutron events. The mean neutron directions (MND) are shown in the first column, number of events n are in the second column while run live-time for each of the neutron exposures are in the third column. In columns four to six are the average Δx , Δy , and Δz parameters for each of the runs. The $\overline{\frac{\Delta z}{\Delta x}}$ parameter obtained for each of these runs is shown in column seven. Only statistical uncertainties are quoted. Event energies are in the range of about $300 \leq \text{NIPs} \leq 6000$.

MND	n	live-time (days)	Δx (mm)	Δy (mm)	Δz (mm)	$\overline{\frac{\Delta z}{\Delta x}}$
$+z$	51222	1.909	3.662 ± 0.009	1.205 ± 0.009	2.560 ± 0.005	1.016 ± 0.004
$-z$	70059	3.713	3.672 ± 0.008	1.164 ± 0.005	2.526 ± 0.004	0.999 ± 0.003
$-x$	5094	0.915	4.619 ± 0.043	1.368 ± 0.024	2.087 ± 0.009	0.710 ± 0.009
$-y$	2873	0.561	3.869 ± 0.044	1.439 ± 0.025	2.188 ± 0.014	0.857 ± 0.013

their corresponding Δy and Δz range parameters. This is because of the larger detector resolution in determining the Δx parameters as discussed earlier in Section 4.7.1. Hence, resolution errors of at least ± 1 mm are expected on the determined Δx values. In contrast, the Δy values were found to be smaller for each of the runs when compared to Δx and Δz parameters obtained from that run. This is due to the effect of differences in charge-carrier trajectories due to curvature of electric field lines closer to the grid signal wires, as discussed in Refs. [253, 229]. In the vicinity of the anode wires, electrostatic field lines are curved which also results in curved signal paths around these regions. It is expected that this effect will be worst along the anode wires corresponding to the y axis of the detector. It is important to note that the best resolution for measurement of nuclear recoil axial range components in the DRIFT detector is in the Δz parameters [254, 256].

Statistically consistent Δx results were obtained from the $+z$ and $-z$ exposures. However, the Δy , Δz and $\overline{\frac{\Delta z}{\Delta x}}$ parameters obtained from these two runs did not agree within statistical errors. This could be due to the systematic effect caused by path curvature of electric field lines closer to the grid signal wires and the systematic effect discussed earlier in Section 4.6.1. The Δx values obtained from $-y$ run is greater than

4. Directionality measurements with the DRIFT-II detector

the results from the optimal directions. This is expected because larger areas of the anode wires were covered by the neutron MND during the $-y$ run compared to the optimal exposures. In general, it can be seen that the Δx and Δz results obtained in this analysis are larger than the results from only ^{32}S recoil candidates in Ref. [254]. This new result is consistent with expectations from inclusion of longer ^{12}C and ^{19}F nuclear recoil tracks.

Each of the axial range component parameters shown in Table 4.4 returned a larger value where the mean neutron direction (MND) is oriented in a direction parallel to the respective axes of the range components. For instance, the Δx parameter obtained from x directed neutron exposure is greater than the values obtained from $+z$, $-z$, and $-y$ exposures. This is because the MND in this direction is perpendicular to the orientation of the anode wires. In this MND direction, the detector has the best Δx resolution, compared to the MND in other directions of neutron exposures. Similarly, this is also true for the Δy parameter obtained from y directed neutron exposure and Δz value obtained from the optimal exposures. These directions have their MNDs oriented in the directions with best detector resolution for the respective range components. The distribution of each of these measured axial range component parameters for nuclear recoil tracks from the respective directions of neutron exposures are shown in Figure 4.14. In that figure, the distribution of Δx parameters are shown in Figures 4.14(a) to 4.14(d), the Δy parameters are shown in Figures 4.14(e) to 4.14(h) while the Δz parameters are shown in Figures 4.14(i) to 4.14(l), each for neutron events obtained from $+z$, $-z$, $-x$, $-y$, respectively. It is the average values obtained from each of these distributions in Figure 4.14 that are quoted in Table 4.4 with their corresponding statistical errors.

The difference between these axial range components in a particular direction and average values of events in the other two perpendicular directions ΔR_{\perp} were computed as a way to better understand the detector response in measuring these axial range components from a given axis of the detector relative to other perpendicular directions. In principle, this effect can be used for possible detection of modulation in the range components of WIMP induced nuclear recoils as the Cygnus constellation (expected mean direction of WIMPs) moves from one axis of the detector to another over a sidereal day. The results from this analysis are depicted in Figure 4.15.

As expected, it can be seen from that figure that the maximum ΔR_{\perp} parameters

4. Directionality measurements with the DRIFT-II detector

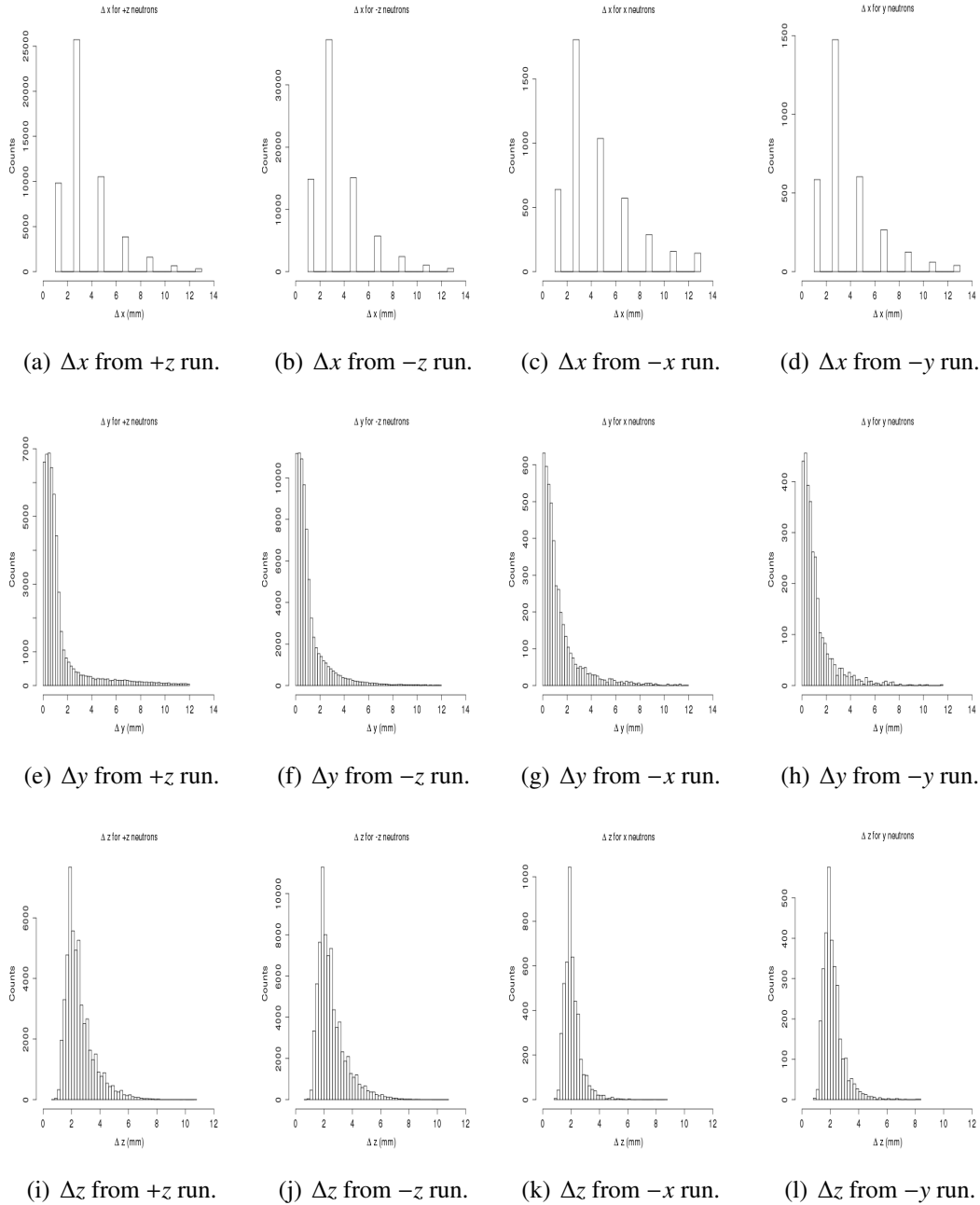


Figure 4.14: Distribution of Δx , Δy and Δz axial nuclear recoil range components obtained from different directions of neutron exposure. The top panels show the Δx parameters, the middle panels are the Δy parameters while the bottom panels are the Δz parameters obtained from $+z$, $-z$, $-x$, and $-y$, respectively.

4. Directionality measurements with the DRIFT-II detector

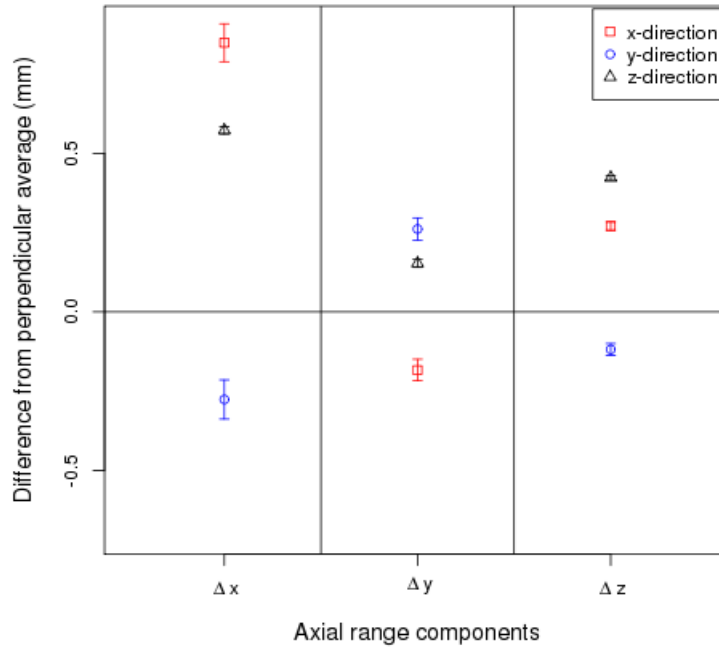


Figure 4.15: Average difference of the axial range components obtained from the average results in each of the two perpendicular directions shown for neutron events from $-x$, $-y$ and $+z$ directions. Results from $-x$ neutrons are shown in red square points, the circular blue points are results from $-y$ directed neutron exposure while results from the $+z$ neutrons are shown in black triangular points. Only statistical uncertainty are shown.

were observed from the Δx , Δy and Δz axial range components in the x , y and z directed neutron exposures, respectively. These are the directions where the best detector performance for detecting each of the respective axial range components are expected. Generally, the absolute magnitude of Δy parameters from all the directions of exposure are small compared to Δx and Δz results from the same direction of exposure. This result indicates that the detector reconstruction power for the Δy parameters is poor compared to its Δx and Δz reconstruction efficiency. This is due to the effect of the differences in charge-carrier trajectories due to electric field line distribution near the readout wires on the reconstructed Δy parameter as earlier discussed and as in Refs. [254, 229].

4. Directionality measurements with the DRIFT-IIId detector

Using these axial range component results, the expected modulation in magnitude of the measured axial range parameters can be investigated as the source is moved from one detector axis to another for application in directional WIMP searches. This can be applied by tracking the mean direction of WIMP signals reaching the detector from the direction of Cygnus as the constellation moves from one detector axis to another over a sidereal day. It has been proposed in [253, 254] that this effect will be more useful in the DRIFT-IIId design if the optimal directions of the detector are oriented along the Earth north-south axis illustrated in Figure 2.8. The magnitude of this expected oscillation can be estimated using the ratio $\overline{\Delta z/\Delta x}$ for events from x and z directions. In this computation the Δy values were not used because of the effects of the distribution of charge-carrier trajectories near the grid wires, on the y component results. These $\overline{\Delta z/\Delta x}$ results for each of the runs are shown in column seven of Table 4.4. With this computation, the maximum $\overline{\Delta z/\Delta x}$ values were observed from events in the optimal exposures and minimum results from $-x$ events as expected, due to larger Δx parameters observed in this axis. In Table 4.4, an oscillation of 0.306 ± 0.010 can be seen by comparing the $\overline{\Delta z/\Delta x}$ results from $+z$ and $-x$ exposure directions. This results to an oscillation of 30.6σ as the source is interchanged between these two neutron source locations. This is a factor of about 2.6 greater than 11.8σ observed with only ^{32}S recoils in Ref. [254]. Hence, considering the case where the Cygnus constellation moves from $+z$ to $-x$ or from $-z$ to $-x$ axes of the detector, the number of nuclear recoil events required for a 3σ axial range component oscillation effect can be constrained. Results shown in Table 4.4 suggest that about 541 to 656 nuclear recoil events could be enough for a 3σ axial range component oscillation effect detection in the DRIFT-IIId detector design. This is a factor of 2 greater than the number predicted with vector head-tail sensitivity using $+z$ optimal events as discussed in Section 4.6.1.

To investigate the magnitude of oscillation expected from moving the source from the optimal direction to the x axis of the detector, the $A_{o_{zx}}$ parameter was computed and shown in Figure 4.16. This is using events obtained from the $+z$ and $-x$ directed neutron exposures and that of $-z$ and $-x$ runs as shown in Equation 4.19. In this computation, the $+z$, $-z$ and $-x$ events were binned at an interval of 200 NIPs and then the average NIPs values and the $A_{o_{zx}}$ parameter for each of the bins were determined separately for the $+z$ to $-x$ and $-z$ to $-x$ case as shown in Figure 4.16. The $+z$ neutrons in that figure were not combined with $-z$ neutron events in order to investigate any

4. Directionality measurements with the DRIFT-II detector

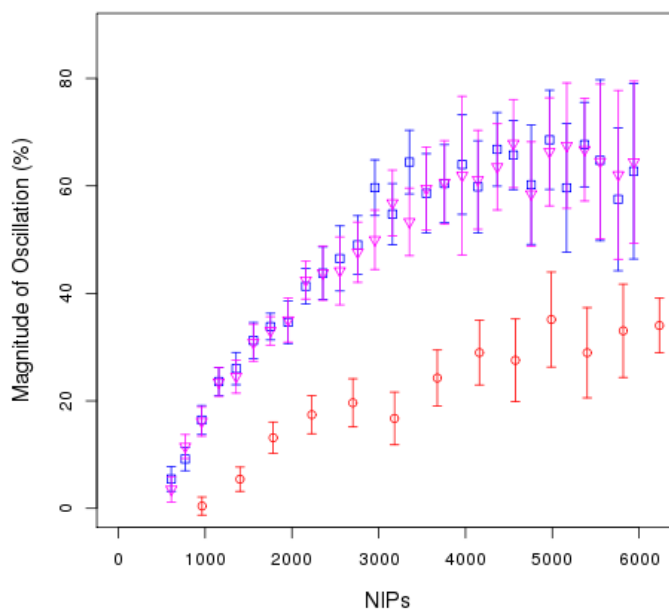


Figure 4.16: Magnitude of oscillation as the neutron source is moved from $+z$ to $-x$ and from $-z$ to $-x$ ($A_{o_{zx}}$) expressed in percent and shown as a function of nuclear recoil NIPs equivalent energy. Data from this analysis which are average values from bins of 200 NIPs interval are shown with blue square points for $+z$ to $-x$ oscillation. Pink triangular points show results from $-z$ to $-x$ oscillation and red circle points are results obtained with only ^{32}S recoil tracks in Ref. [254].

effect of the systematics earlier discussed in Section 4.6.1 on measured axial directional components.

It can be seen in Figure 4.16 that the magnitude of oscillation obtained by moving the source from $+z$ to $-x$ directions and that obtained from moving the source from $-z$ to $-x$ increase with nuclear recoil energy. The magnitude of oscillation observed by moving the neutron source from $+z$ to $-x$ is consistent with the results obtained from moving the source from $-z$ to $-x$. The maximum $A_{o_{zx}}$ parameters obtained at high-energy region of Figure 4.16 can be compared to the maximum values from the high-energy region of ^{32}S recoil tracks in Ref. [254]. In this, the magnitude of the oscillation observed with this new operational gas is larger than the maximum values in Ref. [254] by a factor of about 2.6. This is because of the expected increase in

4. Directionality measurements with the DRIFT-II detector

the $\overline{\Delta z/\Delta x_z} - \overline{\Delta z/\Delta x_x}$ due to inclusion of longer nuclear recoil tracks from the ^{12}C and ^{19}F components of the target gas in this analyses relative to results in Ref. [254]. For instance, an improved Δz parameters are expected from optimal events when compared to only ^{32}S recoil tracks. Similarly, an improved Δx parameters are expected from events whose MND are oriented along the x axis of the detector.

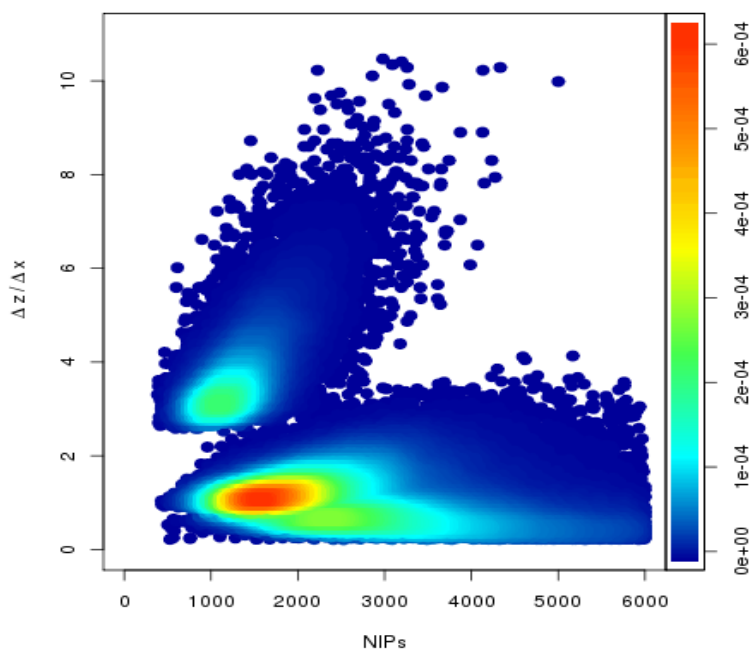


Figure 4.17: Axial range component ratio ($\Delta z/\Delta x$) obtained from the optimal neutron events shown as a function of NIPs recoil energy equivalent. The colour scale represents the density of the events.

To further investigate the presence of these expected longer recoil tracks in this data set, the axial range component parameters obtained from the optimal directed neutron exposures were used. This is to understand if there are any patterns or unique signatures from each of the recoil candidates that can be used to identify them in the recoil population. This analysis was performed using the $\Delta z/\Delta x$ parameters obtained from individual events. The results obtained from this analysis are depicted in Figures 4.17 to 4.19. It can be seen from Figure 4.17 that there are three distinct recoil species on the $\Delta z/\Delta x$ -NIPs space. The first nuclear recoil data cluster with $2.3 \leq \Delta z/\Delta x < 11$ has higher event population compared to the other two recoil candidates whose $\Delta z/\Delta x$ values are < 2.3 . It can be seen from that figure that the gradient of the first two

4. Directionality measurements with the DRIFT-II detector

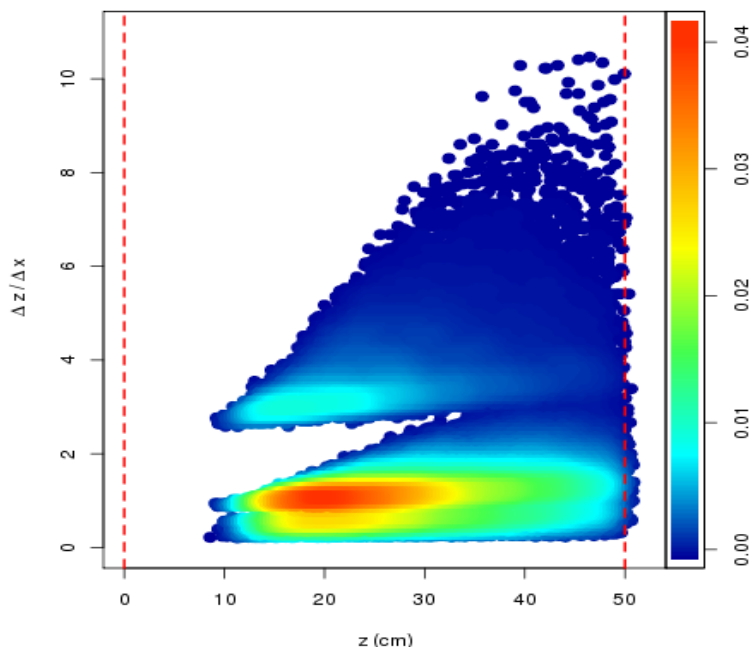


Figure 4.18: Axial range component ratio ($\Delta z/\Delta x$) obtained from optimal neutron events shown as a function of distance of the event vertex from the MWPC readout plane. Events from the low- z region of the detector were added to demonstrate how diffusion smears the separation between these recoil candidates at the high- z region. The two dotted red lines on 0 and 50 cm represent the MWPC and central cathode, respectively. The colour scale represents the density of the events.

nuclear recoil data clusters (with higher $\Delta z/\Delta x$ values) are positive while that of the third nuclear recoil data cluster tends to be negative. This is because some events from the second nuclear recoil data cluster could not be unambiguously separated from the third nuclear recoil data cluster.

The effect of diffusion on each of the data clusters for high- z events can be seen in Figure 4.18. It is important to note that the number of events in each of the respective data clusters in Figures 4.17 and 4.18 are consistent, this is not considering the extra low- z population (with $z < 15$ cm) added in Figure 4.18. This extra low- z events were included to demonstrate how diffusion can smear any intrinsic separation between the data clusters for events with longer drift distances. These results suggest that the events in each of the respective clusters in both figures are from the same recoil candidate. The distribution of these $\Delta z/\Delta x$ parameters is depicted in Figure 4.19

4. Directionality measurements with the DRIFT-II detector

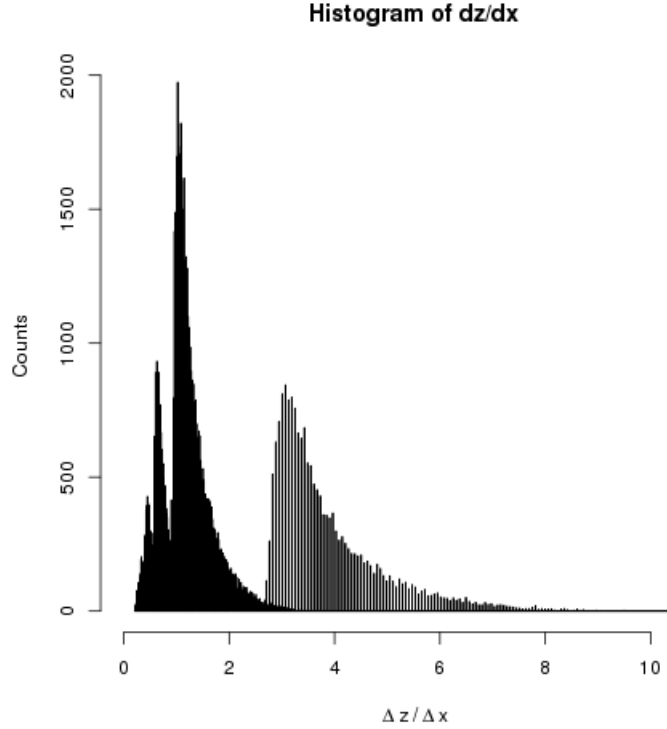


Figure 4.19: Spectrum of $\frac{\Delta z}{\Delta x}$ parameter showing populations of distinct nuclear recoil data clusters.

where these data clusters were also distinct. But this time with a new visible smaller population with $0 < \Delta z / \Delta x < 0.8$. Having observed these distinct separations between these nuclear recoil population, the big questions are “Does each of these data clusters represent group of nuclear recoils from ^{12}C , ^{19}F and ^{32}S candidates?” and if yes “How do we know the group from each of the candidates?”. Also another question is “Could these data clusters occur as a result of discretization due to the coarse detector resolution in disentangling the Δx parameters?”. These discretization effects for Δx parameters can be seen in Figures 4.14(a) to 4.14(d). At the time of compiling this thesis, more work was underway to unambiguously answer these questions. However, few potential answers can be proposed and discussed for future empirical investigations. Hence, starting from the last question, if these data clusters are due to the discretization effect in the observed Δx then a total of 7 data clusters would be expected and not the observed 3 data clusters. Where the number “7” is equivalent to the maximum

4. Directionality measurements with the DRIFT-IIId detector

number of Δx discretization clusters observed in Figure 4.14(a).

Considering each of these data clusters as a recoil candidate from either of ^{12}C , ^{19}F , and ^{32}S components, then the ratio of the number of events in each of the data cluster can be compared to the expectations from each of these nuclear recoil candidates. In this analysis, it was found that about 20% of the events were in the first cluster with $2.3 < \Delta z/\Delta x$ while the remaining ~80 % are in the data clusters with $2.3 > \Delta z/\Delta x$. To compare this result to the expectation from 30:10:1 Torr of $\text{CS}_2:\text{CF}_4:\text{O}_2$ gas mixture using 3.72 g cm^{-3} as the density of CF_4 gas and 1.26 g cm^{-3} as the density of CS_2 gas. It was found that the ratio of the expected $^{32}\text{S} : (^{12}\text{C}+^{19}\text{F})$ recoil population is 27% : 73% in this gas mixture, assuming that the number of O_2 recoils are negligible. This result is similar to 25% : 75% ratio obtained for $^{32}\text{S} : (^{12}\text{C}+^{19}\text{F})$ recoil candidates with GEANT4 simulation after applying the energy threshold cut. All these results are of the same trend and similar to the experimental result. More work is required to better understand this potential method of isolating and identifying different nuclear recoil candidates in the detector. See Chapter 5 for more details on the detector nuclear recoil calibration, detection efficiency and WIMP search results.

4.8 Conclusion

Neutron induced nuclear recoil tracks were generated using neutrons from a ^{252}Cf source placed at different locations around the DRIFT-IIId directional WIMP search detector. This is to investigate the possible effect of newly added CF_4 and O_2 gases to the detector sensitivity in resolving head-tail effect and axial directional components of nuclear recoil tracks. The CF_4 gas was added to the detector targets to achieve the spin-dependent coupling detection sensitivity while the O_2 gas was used for the detector fiducialisation. This new analysis is after these directional signatures were previously reported considering only ^{32}S recoils in pure CS_2 target gas.

The data presented here indicate that the DRIFT-IIId detector is still sensitive to the signal head-tail effect and the axial directional range component signatures. The longer recoil tracks due to ^{12}C and ^{19}F components in the new data were found to yield a more distinct separation between signal track head and tail resulting to higher detector efficiency for detecting the directional signatures at a given energy relative to the previous results obtained from only ^{32}S tracks. Studies done at different z regions

4. Directionality measurements with the DRIFT-IIId detector

of the detector yielded higher values of the head-tail asymmetry parameter in the high- z region compared to the mid- z region. This was found to be because the high- z bin is dominated by high-energy events, mostly because low-energy events in this region of the detector do not pass the analysis threshold due to larger diffusion effects.

The $+z$ and $-z$ directions were confirmed as the optimal directional axes for the DRIFT-IIId detector while nuclear recoil events induced from $-x$ and $-y$ directions produced null head-tail results, as expected. This observed head-tail effect from the optimal direction and null effects from the anti-optimal directions can be combined to track the modulation in signal directionality from WIMP wind reaching the detector from the direction of the Cygnus constellation. This oscillation can be observed as the mean direction of the WIMP wind moves from one detector axis to another over a sidereal day. An oscillation was also observed as expected while comparing the axial directional signatures obtained from neutron events in the optimal and anti-optimal runs. These observed oscillations can be better utilised for directional WIMP searches in the DRIFT-IIId design when the optimal axes of the detector are aligned along the Earth north-south axis as proposed in the earlier studies and illustrated in Figure 2.8.

These new results are encouraging for the possibility of developing a large volume TPC for directional dark matter detection where an appropriate readout technology, sensitive to head-tail effect and the axial directional signatures can be combined with full detector fiducialisation. Further work is strongly encouraged towards developing a more sophisticated analysis for extracting the concealed directional signatures due to peak pile-up in the low- z region of the detector which is expected to improve the overall directional sensitivity further.

Chapter 5

WIMP search analyses and results from the DRIFT-II detector

5.1 Introduction

In this chapter, WIMP search analyses were performed to investigate the possibility of event fiducialisation and a low cost readout technology in the proposed CYGNUS-TPC detector. This is using data from the fiducialised DRIFT-II directional dark matter detector. The WIMP search results presented in this chapter were determined using 57.4 live-time days of shielded data from the DRIFT-II detector and the theoretical differential rate earlier discussed in Section 2.3. In each of the analyses, the expected WIMP rate in the detector was determined and used to constrain the likely WIMP-proton cross sections for different WIMP mass candidates, if no WIMP induced nuclear recoil events are detected. During these WIMP search runs the automated gas handling system was operated in the continuous flow mode resulting in about one detector gas change per day. The detector was fully shielded with ~ 50 cm of loose polypropylene pellets from all directions which provided an average shielding of 44 g cm^{-2} from all directions. This is to ensure that the number of neutrons emanating from the walls of the laboratory cavern that can reach the fiducial volume of the detector is reduced to about < 1 neutron event per year. These neutron events due to the laboratory cavern are referred to as rock neutrons. Data obtained in this polypropylene pellet shielding mode are referred to as shielded data (see Figure 4.3). After every two weeks, on av-

5. WIMP search analyses and results from the DRIFT-II detector

erage, the shielded WIMP search operations were stopped for detector nuclear recoil calibration measurements. In these calibrations, nuclear recoil tracks were generated using a ^{252}Cf neutron source placed on the centre of the vacuum vessel in the $-y$ direction (see exposure directions in Figure 4.1) such that the source is in-line with the central cathode. As earlier discussed in Chapter 4, a ^{252}Cf neutron source was used for these calibration operations because it has been shown in Refs. [253, 254] that energy spectra of neutron induced recoils are consistent with expectations from WIMPs. The method used in this analysis for energy calibration, data reduction, nuclear recoil identification and selection are mainly as described in Chapter 4. Details of further analyses methods used for each given specific computation purpose are discussed in the following sections.

A big aspect of the new analysis presented here is: (1) development of a new technique to extend the fiducial volume of the detector by fiducialising low- z events which were previously rejected in analyses. Hence, after analysing the WIMP data using the normal fiducial volume of the detector ($11 \text{ cm} \leq z \leq 48 \text{ cm}$ and $700 \leq NIPs \leq 6000$), an alternative method for estimating the distance z of an event vertex from the readout plane was developed for events at the low- z region of the detector. With the recovery of this low- z region, a new effective 18% of active volume of the detector was recuperated as part of the detector fiducial volume which is expected to improve the overall constraints set on the likely WIMP interaction properties. (2) To test the viability of a simplified readout technology which can reduce the cost of front-end electronics and data acquisition systems in the proposed CYGNUS-TPC detector design discussed in Sections 2.10 and 3.1 by a few orders of magnitude relative to channel-by-channel readouts. This test was achieved by simulating a simple $1 \text{ m} \times 1 \text{ m}$ one dimensional readout scheme with no x - y information using neutron calibration and WIMP search data obtained from the DRIFT-II detector.

To determine the rate of rock neutrons that can be detected in the fiducial volume of the detector when the detector is not shielded with the polypropylene pellets, another 45.4 live-time days of unshielded data were recorded to disk and analysed. This is without altering the automated gas handling mode. Operating the detector in this automated continuous gas flow mode helps to reduce the effect of gas ageing and minimize radon decays in the gas as earlier discussed and as in Ref. [266]. The details of the methods used and the results obtained from each of these analyses are subjects of

the following sections in this chapter.

5.2 WIMP and background neutron data and analyses

The details of the raw DRIFT-IIId data used in these WIMP search and background neutron analyses are shown in Tables 5.1. The first column of that table marked as “Science run”, shows names that summarise the nature and aim of each of the operations. The second column of that table, marked as “Name of data file” shows the names of event data files obtained in each of the operations, while the third column marked as “live-time” shows the total live time of each of the runs. The set of data marked as “Shielded” in Table 5.1 were obtained from the detector during WIMP search operations performed with full detector shielding in place. The “Nuclear recoil calibration” (or neutron calibration) data were obtained during nuclear recoil track calibrations done with a ^{252}Cf neutron source. Data for the rock neutron measurements were obtained with 80% of the total detector shielding removed and hence, are marked as “Unshielded” in Table 5.1.

The format of the DRIFT-IIId data files in the second column of Table 5.1, is of the form: Detector-YYYYMMDD-RunNumber. The “Detector” is the detector name, “YYYY” is the year, “MM” is the month and “DD” is the day on which each of the operational runs were performed. The sum of the differences between the start and the end times of each of the run data files are computed as their total operational live times, see the third column of Table 5.1. In each of the science run days, the “RunNumber” starts from 1 for the first run of the day and grows by 1 when the old run is stopped and a new data run is started. For instance, the data in the file called drift2d-20141204-03 were recorded with the DRIFT-IIId detector on the 4th day of December 2014, during the 3rd run of the day. In total, a total of 821 data cycles were recorded on disk during the shielded WIMP search operations. A typical data cycle in a continuous run set-up comprises 10000 events. However, this is not applicable to short runs and in the last data cycle for each run because such runs can be stopped before the 10000 maximum number of events is reached. Data files in the “Nuclear recoil calibration” runs are good examples of short run files which resulted in only 51 data cycles. In the “Unshielded” runs, a total of 786 data cycles were recorded. Each set of these data were analysed using the methods described in the following sections for each of the respective data

5. WIMP search analyses and results from the DRIFT-II detector

Table 5.1: Names of data files and total live times of events recorded during the WIMP search runs, nuclear recoil calibrations runs and rock neutron measurements. See text, for details of the row and column labels.

Science run	Name of data file	live-time (days)
Shielded	drift2d-20141204-03	
	drift2d-20141209-02	
	drift2d-20141218-02	
	drift2d-20141219-01	
	drift2d-20141219-05	
	drift2d-20150219-03	
	drift2d-20150220-02	
	drift2d-20150226-02	
	drift2d-20150302-02	
	drift2d-20150308-03	
	drift2d-20150312-02	
	drift2d-20150317-02	
	drift2d-20150319-01	
		54.7
Nuclear recoil calibration	drift2d-20141209-01	
	drift2d-20141218-01	
	drift2d-20150220-01	
	drift2d-20150223-01	
	drift2d-20150226-01	
	drift2d-20150302-01	
	drift2d-20150312-01	
	drift2d-20150317-01	
		0.803
Unshielded	drift2d-20141021-01	
	drift2d-20141106-01	
	drift2d-20141121-04	
	drift2d-20151026-02	
	drift2d-20151029-01	
	drift2d-20151103-02	
	drift2d-20151106-01	
	drift2d-20151107-01	
	drift2d-20151112-03	
	drift2d-20151113-01	
	drift2d-20151117-02	
drift2d-20151118-02		
		45.4

sets.

5.2.1 Detector efficiency for nuclear recoil tracks

As shown in Figure 4.3, after stages 1, 2 and 3 analyses are applied to a WIMP search data, the detector performance needs to be determined before further progress can be made in the WIMP analyses. To measure the detector performance in detecting nuclear recoil tracks, the neutron induced recoil data obtained during the nuclear recoil calibration runs discussed in Section 5.1 were used. This detector nuclear recoil detection efficiency ϵ measurement was performed by comparing the rate of the observed neutron induced nuclear recoil events after all cuts to the predicted event rate generated with GEANT4 simulations. This ϵ parameter expressed in percent can be defined as:

$$\epsilon = \frac{100f_{exp}}{f_{mc}}, \quad (5.1)$$

where f_{exp} and f_{mc} are the event rates obtained from the experimental data and GEANT4 Monte Carlo simulations, respectively. In the context of this analysis, to determine the expected neutron induced nuclear recoil rate for the DRIFT-IIId detector, the detector was simulated using GEANT4 code. The diagram of the simulated detector in the laboratory cavern is shown in Figure 5.1.

The simulation included the walls of the laboratory cavern which comprises rock salts, the polypropylene pellet shielding, plaster boards used as shielding walls for holding the loose polypropylene pellets in place, stainless steel vacuum vessel, drift cage, acrylic back cover surrounding the field cage used in the detector design to minimize high voltage discharge. The concentration of Uranium (U) and Thorium (Th) contaminations in the rock salts were populated based on the measurements and results in Refs. [267, 268, 269]. An active volume of the simulated detector was defined similar to that of the real detector. This active volume was filled with 25×41 Torr (750:250:25 Torr) of $\text{CS}_2:\text{CF}_4:\text{O}_2$ gas mixture. The actual density of the gas in the detector was scaled by a factor of 25 to minimize computation time. This is possible because it is expected that the rate of nuclear recoil interactions in the active volume of the detector should scale linearly with pressure of target gas used, as discussed in Refs. [266, 270]. Hence, this factor of 25 increase in the rate of the Monte Carlo neutron

5. WIMP search analyses and results from the DRIFT-II detector

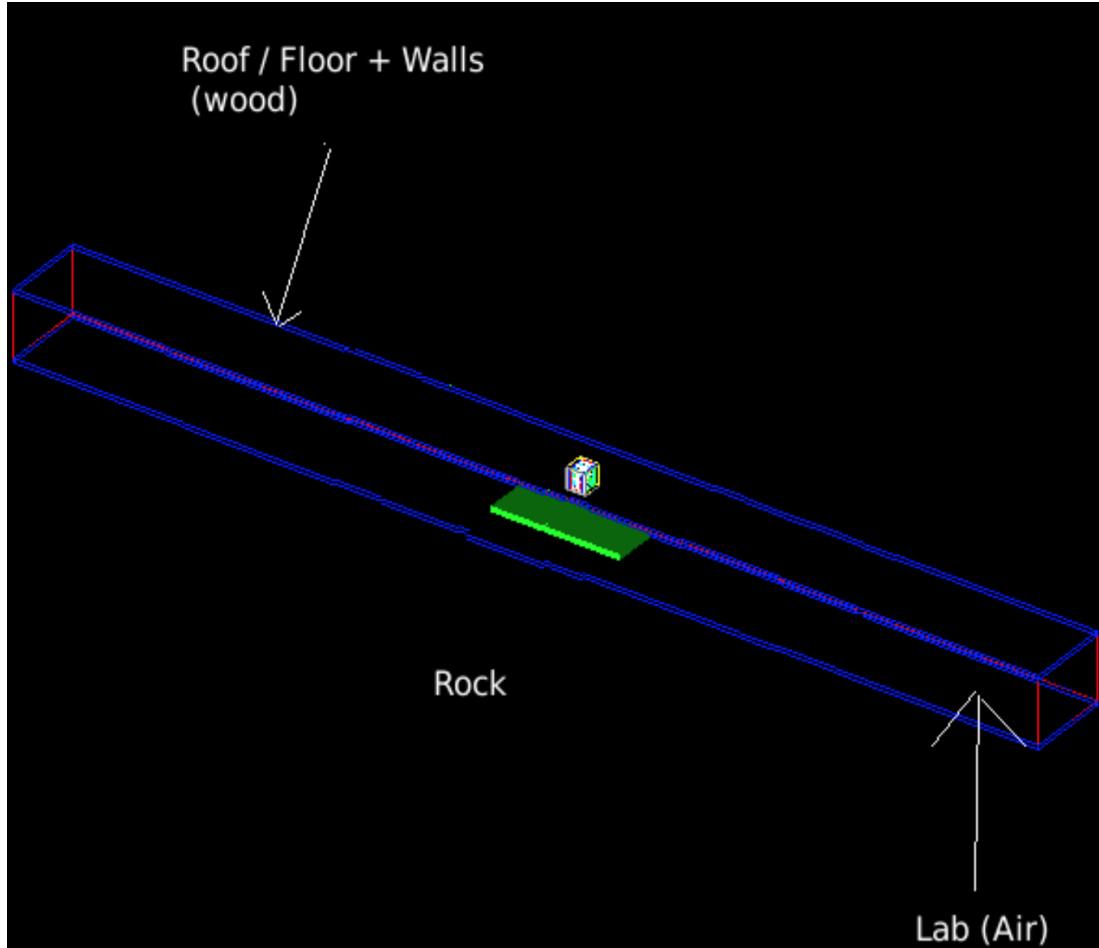


Figure 5.1: Pictorial view of the GEANT4 simulated DRIFT-II detector in the underground laboratory cavern. Blue and red lines are simulated wood that marks the underground laboratory cavern, the rectangular green box is underfloor polypropylene pellet shielding. The cubic volume above the green box is the simulated DRIFT-II detector.

event rates will be accounted for before any comparison to the experimental results.

To generate neutron induced nuclear recoil events, a SOURCE-4C [271] simulated ^{252}Cf source was placed on the vacuum vessel such that it was centered on the central cathode from the $-y$ direction. This was achieved using the GEANT4 Neutron Hadronic Process based Physics List. The energy spectrum of the SOURCE-4C simulated neutron source ranges from 0 to 10 MeV with an average energy value of 2 MeV. For each of the generated event recoil species within the active volume of the detector,

5. WIMP search analyses and results from the DRIFT-II detector

the energy and distance of the first event's interaction vertex from the readout plane were recorded for further analysis. These nuclear recoil events can be from ^{12}C , ^{16}O , ^{19}F or ^{32}S candidates. The gas quenching factor for each of the recoil species and the W-value of the gas were used to determine the number of ion pairs (NIPs) produced from each of the recoils. However, the readout electronics and full recoil tracks of the generated nuclear recoil events were not simulated. This is because the readout electronics and recoil tracks do not contribute to the observed rates in the detector.

To determine the detector and analyses nuclear recoil acceptance efficiency, the neutron induced nuclear recoil calibration data obtained during the shielded runs which passed all the nuclear recoil event selection cuts described in Chapter 4 were binned. As discussed earlier in Chapter 4, due to overlap of the charge carriers at the low- z region of the detector and events emanating from the central cathode, events with $z < 11$ cm and $z > 48$ cm were not considered in this analysis. Also events with NIPs < 700 were removed to avoid the accumulated effects of diffusion on low-energy events in the high- z region of the detector. Hence, the allowed fiducial volume of the detector after these cuts is bounded by the following z and NIPs conditions: $11 \text{ cm} < z < 48 \text{ cm}$ and $700 < \text{NIPs} < 6000$, respectively. The distribution of neutron induced recoil events that passed all the cuts with a total fiducial rate of 17815 ± 148 neutrons per day obtained from the nuclear recoil calibration data during the shielded runs are shown in Figure 5.2. In that figure, the region where background events are expected due to Radon Progeny Recoils (RPRs) emanating from the central cathode of the detector is marked with red lines while the analysis fiducial volume is marked with blue lines. The RPR region is above the fiducial volume. The rate of these RPR events will be measured using the shielded WIMP search data set (see Table 5.1 for details) in Section 5.3.1. Then, events that passed the afore described z and NIPs cuts were binned in widths of 2.05 cm and 294.4 NIPs, respectively. This resulted in 18×18 (rows \times columns) data bins. The rate of events f_{exp} in each of the bins were determined using:

$$f_{exp} = \frac{N_{b_{exp}}}{t_{L_{exp}}}, \quad (5.2)$$

where $N_{b_{exp}}$ is the number of events in a given z -NIPs bin and $t_{L_{exp}}$ is the total exposure live-time (in days) of the nuclear recoil calibration runs.

To determine the predicted rate for each of these bins, 0.9×10^9 neutrons were fired

5. WIMP search analyses and results from the DRIFT-II detector

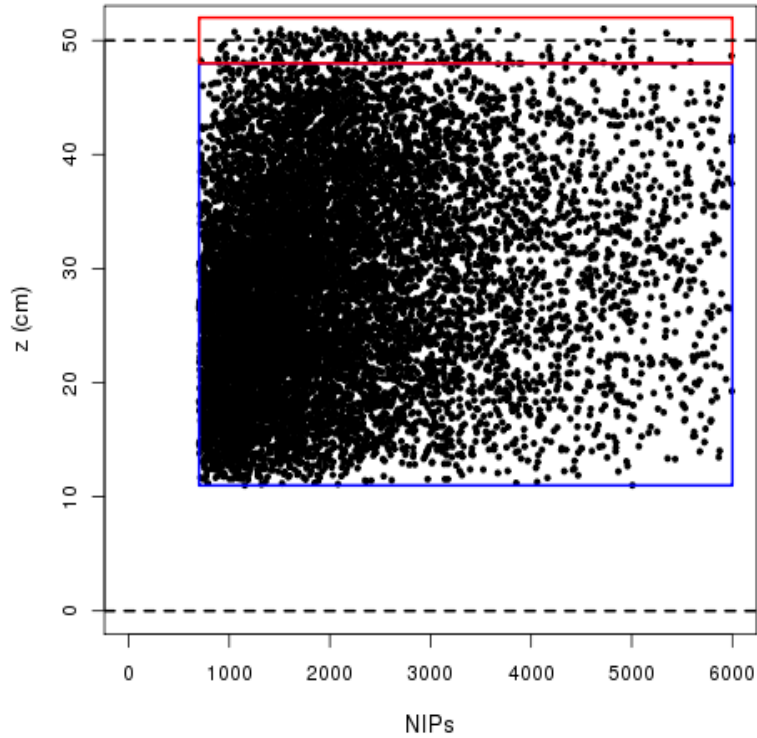


Figure 5.2: Distribution of neutron induced nuclear recoil events obtained from a 0.803 live-time days of nuclear recoil calibration data shown in z -NIPs space. The red lines show the region where background contaminations are expected from Radon Progeny Recoils (RPRs) emanating from the central cathode while the blue lines mark the fiducial volume used in this analysis. The bottom boundary of the RPR region and the top boundary of the fiducial volume are bounded with a red line on $z = 48$ cm.

from the simulated ^{252}Cf neutron source to the active volume of the simulated detector and the NIPs and z values of the resulting events were recorded. Similarly, the Monte Carlo events that passed the earlier discussed z and NIPs cuts were binned using the z and NIPs bin widths that were applied to the experimental data. To determine the rate of events in each of the bins of the Monte Carlo data set, an equivalent neutron exposure live-time was estimated using a measured neutron emission rate for the ^{252}Cf source obtained during the nuclear recoil calibration runs, the number of fired neutrons and the pressure scale factor. This resulted in an estimated equivalent neutron exposure

5. WIMP search analyses and results from the DRIFT-II detector

live-time of 9.401 days for the Monte Carlo events. This is about a factor of 12 more than the exposure live-time of the experimental data, but should be accounted for in the computation of f_{mc} and f_{exp} parameters used to determine the detector efficiency defined in Equation 5.1. Using this equivalent exposure live-time for the Monte Carlo data set, the f_{mc} parameter for each of the simulated z -NIPs bins was determined using:

$$f_{mc} = \frac{N_{b_{mc}}}{t_{L_{mc}}}, \quad (5.3)$$

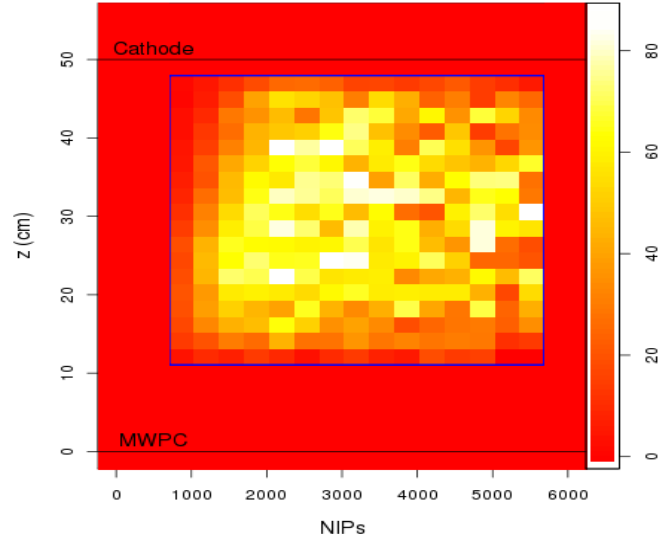
where $N_{b_{mc}}$ and $t_{L_{mc}}$ are the number of events in each of the bins and the equivalent neutron exposure live-times for the Monte Carlo data set, respectively.

The f_{exp} and f_{mc} rates obtained for each of the bins bounded by a given set of z and NIPs values were used to determine the detector nuclear recoil detection efficiency for that bin using Equation 5.1. The results from each of the bins are shown in Figure 5.3.

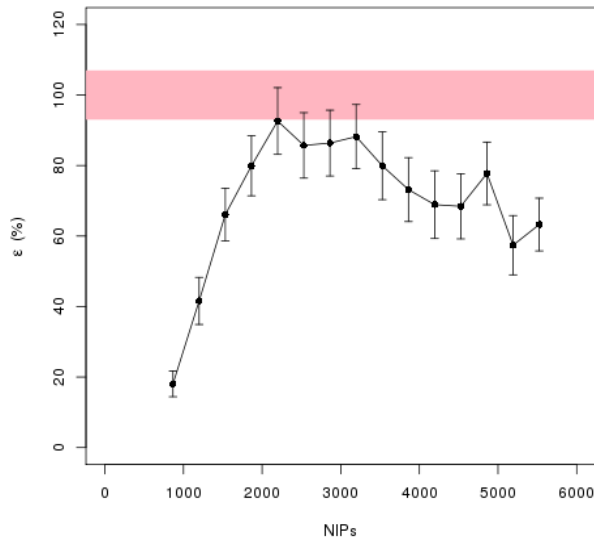
It can be seen from Figures 5.3(a) and 5.3(b) that the average detector nuclear recoil detection efficiency is higher for events with about 1500 to 4000 NIPs relative to events with energies >4000 NIPs. In fact, this is more apparent in Figure 5.3(b). The efficiency increased in the lower energies and reached 90% at 2000 NIPs and then decays to about 60% at about 6000 NIPs. This is mainly because charge signals in the main charge cloud are more than 50% of the total charge in an event for high energy events hence, resulting in a lower Q_r parameter defined in Equation 4.6. Due to this effect, the reconstruction can reject high energy events especially when the charge ratio Q_r parameter cut is applied. This could be improved by using a lower Q_r cutoff at higher energies. Since the minority charge clouds are small compared to the main charge cloud, the reconstruction algorithm may fail to find three equidistance peaks on some of these high-energy events thereby rejecting them in analyses. However, the low-energy window is likely to be a more promising parameter space for WIMP interaction searches relative to higher energies as discussed in Ref. [1, 9, 47, 97].

To compute the expected WIMP event rate in the detector from which the most probable WIMP-proton cross sections limit are determined as shown in Section 5.3.1, then an average nuclear recoil detection efficiency for different energy bins were determined, this is shown in Figure 5.3(b).

5. WIMP search analyses and results from the DRIFT-II detector



(a) Efficiency map for z -NIPs bins.



(b) Efficiency map for energy bins.

Figure 5.3: Nuclear recoil detection efficiency for the DRIFT-II detector. This is without considering events from low- z regions of the detector with $z < 11$ cm. In (a) is the efficiency map for different z and NIPs bins while (b) shows the average efficiency in a given energy bin. The colour scale in (a) is the bin efficiencies presented in percent.

5.3 Unshielded background rock neutron measurements

This section aims to understand the number of background rock neutron events that can reach the fiducial volume of the detector and be detected if 80% of the total passive polypropylene pellet shielding were not used around the detector. To do this, the unshielded rock neutron measurement data (shown in Table 5.1) were analysed using the methods discussed in Chapter 4. The event z reconstruction and NIPs equivalent energy conversion methods discussed in Sections 4.5 and 4.4, respectively, were applied on all the data that passed the earlier discussed nuclear recoil selection cuts. The distribution of these good events in the z -NIPs space is shown in Figure 5.4 as obtained from the rock neutron measurement data analyses. In that figure, the normal

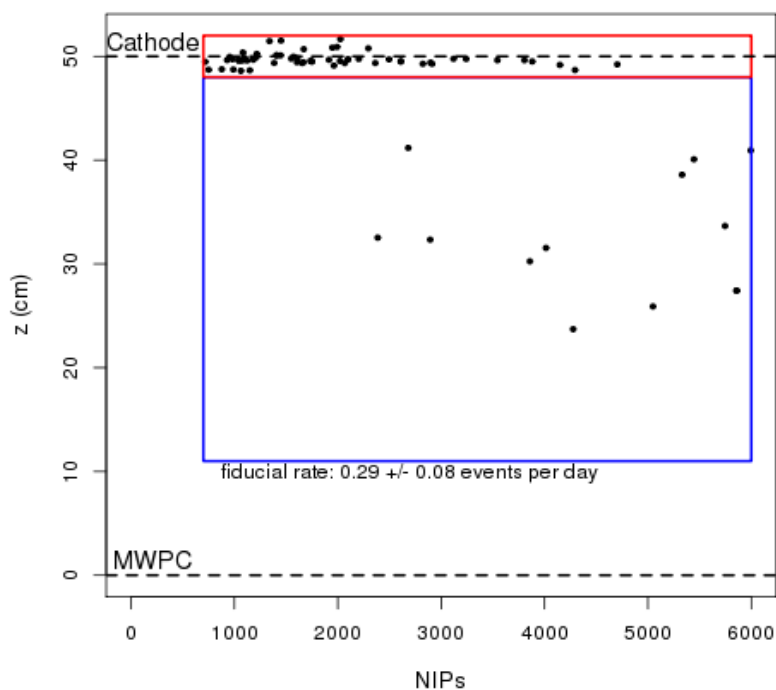


Figure 5.4: Distribution of nuclear recoil events as obtained from the rock neutron measurement data. The fiducial volume and the region where RPR events were expected are marked with blue and red lines, respectively. The red lines on $z=48$ cm separates the fiducial volume and the RPR region. The black dashed lines on $z = 0$ and $z = 50$ cm represent the readout MWPC and central cathode, respectively.

5. WIMP search analyses and results from the DRIFT-II detector

fiducial volume of the detector (see Section 5.2.1) is marked with blue lines while the region closer to the central cathode where radon progeny recoil (RPR) events are expected is marked with red lines. It can be seen that there are more events closer to the central cathode than in the fiducial volume of the detector. This indicates that more RPR events were observed relative to the number of observed rock neutron events in this 20% shielded mode. In fact, the rate of fiducial nuclear recoil events obtained from this measurements is 0.29 ± 0.08 events per day while the total event rate recorded during these measurements is 1.63 ± 0.19 events per day. The measured fiducial rock neutron rate in this unshielded detector mode is consistent with 0.24 ± 0.02 background neutron events per day expected from the laboratory caverns. This expected rate was determined using results from a GEANT4 simulation as obtained in Ref. [272] and the average detector efficiency obtained in this analyses. The implication of these rock neutron results is that there would be at least 1 background nuclear recoil event induced by rock neutrons in the fiducial volume of the detector after every 3.5 days if the detector is unshielded from every other direction except from the laboratory floor which was shielded using passive underfloor polypropylene pellets. Using this fiducial rock neutron event rate and the total event rate, then the rate of RPR events can be estimated from this rock neutron measurement data set. This results in 1.34 ± 0.21 RPR events per day which is consistent with 1.41 ± 0.16 RPR events per day, obtained earlier in Section 5.3.1 using the shielded background WIMP search data set. The detector sensitivity to these rock neutrons validates that the detector operates as expected. See Section 5.3.1 for results obtained from the shielded WIMP search operations.

5.3.1 WIMP search results from the normal fiducial volume

To search for the presence of any WIMP-induced nuclear recoil events in the fiducial volume (without considering low- z region) of the detector within the allowed 54.7 live-time days-operational time window, the shielded WIMP search data set (see Table 5.1) were used. These data were analysed using the nuclear recoil selection methods and data reduction cuts described in Chapter 4 and illustrated in Figure 4.3. As in that figure, the z -NIPs results from this analyses is shown in Figure 5.5.

It can be seen that no nuclear recoil events were detected within the fiducial volume of the detector during these shielded WIMP search operations. This result is consistent

5. WIMP search analyses and results from the DRIFT-II detector

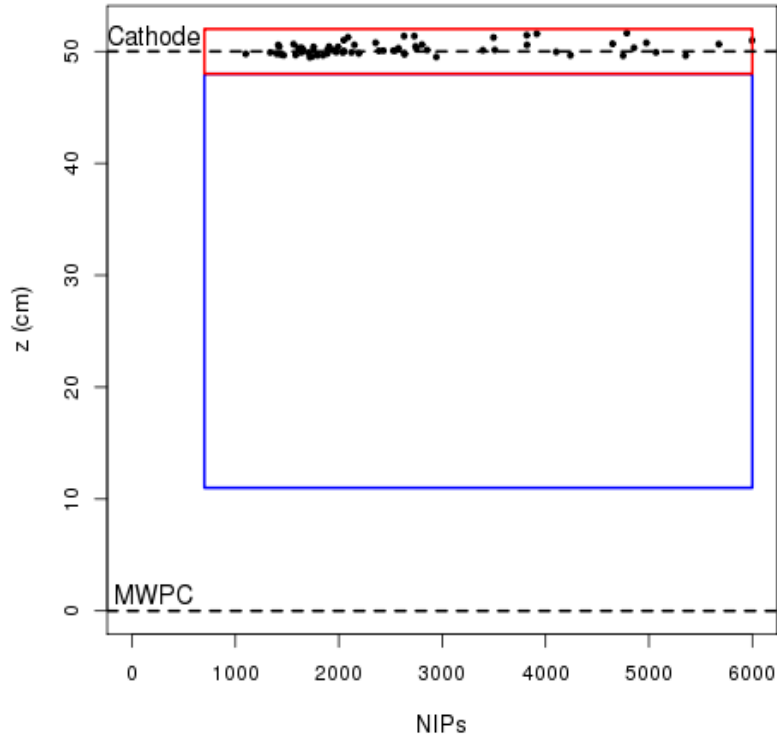


Figure 5.5: Distribution of background events recorded during the 54.7 days of WIMP search runs. The RPR regions are marked with red lines and the fiducial volume is bounded by the blue lines. The black dashed lines on $z = 0$ and $z = 50$ cm represent the readout MWPC and central cathode, respectively.

with expectations from the total background neutron events emanating from the rocks and the stainless steel vacuum vessel in the fiducial volume of the detector during these WIMP search runs as shown in Table 5.2. This is after gammas are ruled out as possible source of any observed events given the gamma rejection factor of the detector measured in Refs [266, 272]. All the observed events were located near the central cathode and are due to the background RPR events emanating from the central cathode as earlier discussed in Section 4.5. These are group of RPR events (termed Film RPR events in Ref. [112]) with coincidence alpha signals that are completely concealed in the central cathode, leaving only the corresponding nuclear recoil signatures which could not be rejected in analyses. The rate of these events can be determined using

5. WIMP search analyses and results from the DRIFT-II detector

Table 5.2: Expected background neutrons in the fiducial volume of the detector and RPR events during the 54.7 shielded data days, considering the detector efficiency.

Source of neutrons	Expected neutrons	Detected events
Lab carven rocks	0.164 ± 0.002 [272]	0
Stainless steel vessel and detector materials	$0.0014 \pm 0.07 \times 10^{-10}$ [272]	0
	0.1654 ± 0.002	0
Central cathode (RPR region)	60 ± 8 [112]	77 ± 9

the information in Figure 5.5. This results in a RPR rate of 1.41 ± 0.16 events per day. The implication of these results is that there were no WIMP-induced interactions in the background free fiducial volume of the detector. Hence, the detector efficiency and the expected WIMP event rates in the detector which were determined using the methods earlier discussed in Chapter 2 were used to set an upper limit on the most likely cross section for 10^4 bins of WIMP masses within $10 \leq M_W \leq 10^4 \text{ GeV } c^{-2}$ range.

To achieve this, all the information obtained in the earlier discussed WIMP search analyses and other detector parameters needed for the computation of a 90% confidence limit on expected WIMP interaction cross section in the detector is summarised in Table 5.3. To determine the upper limit on the expected number of WIMP events in the detector at 90% confidence level for the allowed time window, the Poisson statistics for 0 (0) observed WIMP (background) event shown in Table IV of Ref. [273] was adopted. This results in 3.09 events which was converted to the expected number of WIMP events in $\text{kg}^{-1} \text{d}^{-1}$. This was achieved by considering the detector efficiency, then the obtained theoretical event rate was divided by the fiducial mass (in kg), the exposure live-time (in days) and the average detector efficiency to obtain the final expected event rate of $2.44 \text{ events kg}^{-1} \text{d}^{-1}$ if only spin-dependent interactions were considered. For the spin-dependent WIMP-proton interaction sensitivity, only the mass contributions of ^{19}F within the 0.74 m^3 fiducial volume of the detector were consid-

5. WIMP search analyses and results from the DRIFT-II detector

Table 5.3: Details of the parameters used for computation of the WIMP exclusion limit.

WIMP limit parameter	Used values
Confidence limit	90%
Expected upper limit on number of events at 90% CL	2.44 events kg ⁻¹ d ⁻¹
WIMP search live time days	4726080 s (54.7 days)
Energy range	700 - 6000 NIPs (30 - 205 keV _r)
Target atom	¹⁹ F
Coupling sensitivity	WIMP-proton spin-dependent
Fiducial volume	0.74 m ³
Fiducial SD target mass	31 g
Number of fiducial WIMP-induced recoil events	0
Number of fiducial background events	0
Detector efficiency	as shown in Figure 5.3

ered further. Hence, this fluorine only consideration reduces the total fiducial mass of the detector to 31 g (0.031 kg). After all the cuts, the fiducial energy window for this analysis was found to be 30 keV to 205 keV_r fluorine nuclear recoil energy equivalent. Then, the corresponding detector efficiency for the given nuclear recoil ¹⁹F-equivalent energy bins were obtained from Figure 5.3(b). It should be noted that the detector efficiency shown in that figure was determined without any isolation of constituent ³²S, ¹⁹F, ¹⁶O and ¹²C nuclear recoil candidates that may be in this data set. Hence, the detector nuclear recoil detection efficiency shown in Figure 5.3(b) are average values obtained from all the constituent nuclear recoil candidates. This detector efficiency was used for the spin-dependent WIMP-proton limit calculation.

To obtain an event rate for each of the 10⁴ bins of WIMP masses, an arbitrary

5. WIMP search analyses and results from the DRIFT-II detector

WIMP cross section of 100 pb was used. Then, the expected integrated overall WIMP interaction rates in the detector for a giving bin of WIMP mass was computed using Equation 2.44. The 90% confidence level, spin-dependent WIMP-proton cross section for each of the WIMP masses was determined by scaling down the arbitrarily chosen cross section until the overall WIMP event rate obtained is equal to the 2.44 events $\text{kg}^{-1} \text{d}^{-1}$ benchmark. The upper limit for WIMP-proton spin-dependent cross sections obtained in this analysis are shown in Figure 5.6 as a function of bins WIMP masses.

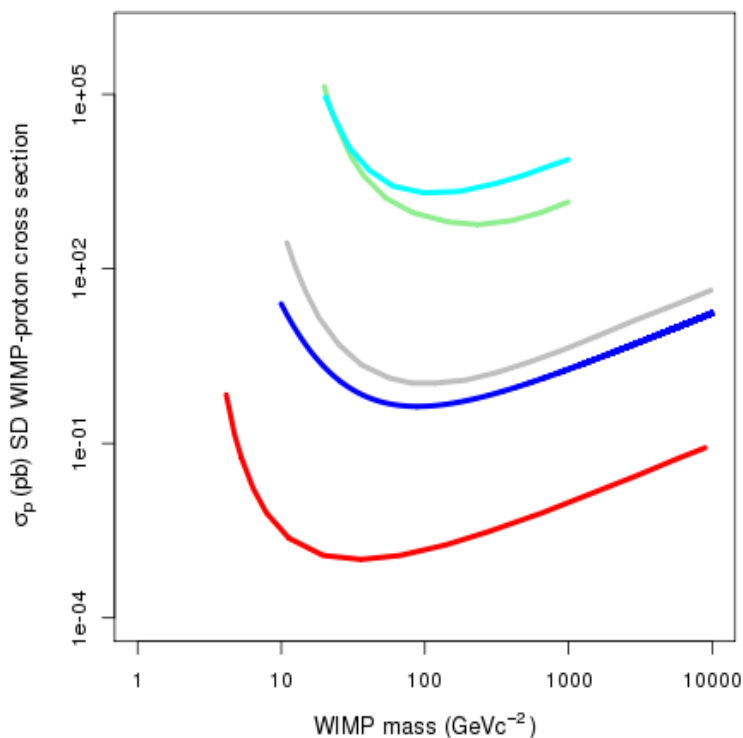


Figure 5.6: Spin-dependent WIMP-proton cross section limit at 90% confidence level shown as a function of WIMP masses. The results from this analyses obtained with the DRIFT-II directional detector is shown in blue, cyan line is the latest result from DMTPC [177], light green line is that from NEWAGE [144], grey line is 2015 DRIFT-II result obtained with a higher hardware threshold [113] while red line is the latest PICO (non-directional detector) result [157].

5. WIMP search analyses and results from the DRIFT-II detector

In that figure, all the spin-dependent WIMP-proton cross sections above the blue line are excluded by this analysis. It can be seen that the detector reached its highest sensitivity at about 0.33 pb spin-dependent WIMP-proton cross section for a WIMP of mass $\sim 100 \text{ GeV c}^{-2}$. In Figure 5.6, the results obtained in this analysis are compared to results obtained with the DRIFT-II detector in 2015 [113] (grey line). This old results were obtained using a hardware threshold higher than an improved hardware and trigger thresholds used in this data by a factor of 2. These results are compared to the latest WIMP exclusion limits from the DMTPC [177], NEWAGE [144] and PICO [157] experiments shown with cyan, light green and red lines, respectively. The observed improvement in Figure 5.6 between the spin-dependent WIMP-proton cross section obtained in this analysis for a given WIMP mass relative to the results in Ref [113] is due to the lower detector threshold, increase in exposure live-time for this data and a lower detector efficiency in the old data due to effects of gas ageing in sealed operations. The results from the PICO non-directional detector excluded some parameter spaces where this analysis was unable to explore. The expectation is that the CYGNUS-TPC detector, if built and future directional WIMP search detectors will be able to affirm or invalidate these non-directional results. The results in Figure 5.6 indicate that the DRIFT-II detector remains the world most sensitive directional WIMP-search detector with the results from this analysis as the most stringent spin-dependent WIMP-proton cross section limit from a directional detector to date. In fact, this result is a factor 6060 and 2345 better than the 2000 pb and 774 pb spin-dependent WIMP-proton cross sections for WIMPs of masses 115 GeV c^{-2} and 100 GeV c^{-2} obtained by the DMTPC and NEWAGE directional experiments, respectively.

In Section 5.4, data from the DRIFT-II detector were used to study the feasibility of reducing the number of signal readout front-end electronics for possible application in the proposed CYGNUS-TPC project.

5.4 Simulated simplified readout configuration

It is of interest to investigate if zero background WIMP search results can still be observed in this detector even if all the x, y information is switched off. This can be viewed as simulating a detector that has only 1D- z dimension directional sensitivity with head-tail vector sense recognition but with no axial directional components. Such

5. WIMP search analyses and results from the DRIFT-II detector

a detector (for instance as might be viable for the proposed CYGNUS-TPC) would still have directional sensitivity but be a lot cheaper to build due to reduced cost of front-end electronics and data acquisition system. To test this, charge pulses recorded on signal sum-lines of the DRIFT-II detector were used. For example, the anode sum-lines are labeled as “LAS” and “RAS” for the left and right anode MWPCs, respectively, in Figure 4.2. This new arrangement where only information on the sum-lines are considered in analyses is known as a simplified readout mode. In this simplified readout mode, each of the 448 signal wires in the anode and grid wire planes were grouped separately for the left and right detectors. Hence, this results in a total of 3 (1 anode, 1 grid and 1 veto) signal channels from the left MWPC and another 3 (1 anode, 1 grid and 1 veto) signal channels from the right MWPC readout.

To be able to estimate the absolute z positions and reconstruct the NIPs equivalent ionization energies of events in this new data mode, a new z reconstruction algorithm and ^{55}Fe energy calibration data analyses were developed. These new z reconstruction and NIPs computation algorithms were based on the methods discussed in Sections 4.5 and 4.4, respectively, but in this case they were applied to the sum-lines. This new ^{55}Fe data analysis was necessary to avoid the effect of induced signal pulses on adjacent wires when events ionization energies are reconstructed using signal pulses obtained from the sum-lines. As earlier discussed in Sections 2.8.4 and 4.4, ^{55}Fe energy calibrations are performed every 6 h for the left and the right MWPCs during data recording operations in DRIFT. These calibration data were recorded without any trigger and hardware threshold. Each of the energy calibration operations comprises of 100 event files recorded within a 13 ms time window. For this new simplified readout analyses, the recorded ^{55}Fe data were analysed using charge signal pulse areas (in $\text{mV } \mu\text{s}$) determined with an analyses threshold of 2.3 mV. This was used to obtain the energy spectrum of charge signals induced by X-rays from the 5.9 keV ^{55}Fe source. To do this for each of the 13 ms long data, the charge area obtained from all the signal pulses on the anode sum-lines which have enough charge amplitude to cross the analysis threshold, were used.

Then, the position of the peak obtained from the energy spectrum for any given ^{55}Fe energy calibration operation in the left or right detectors was stored and used to determine the required energy calibration constant for that operation. This was used in analyses for reconstructing the ionization energy for all nuclear recoil events that

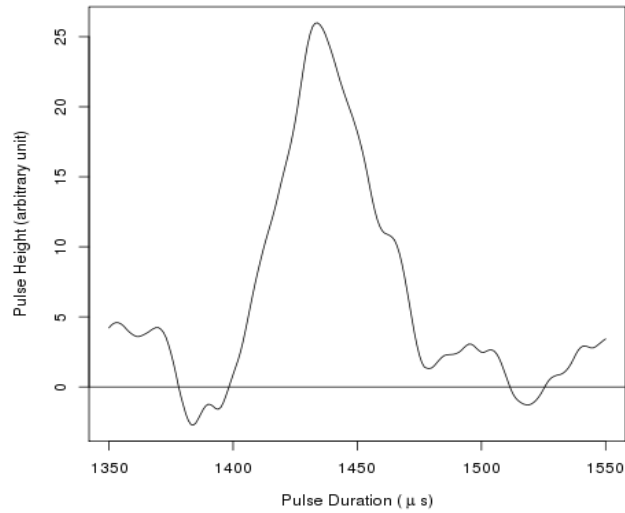
5. WIMP search analyses and results from the DRIFT-IIId detector

occur during the next 6 h after that ^{55}Fe calibration. For example, the average value of the energy constant obtained for the left and the right detector as determined in these analyses is 3128 ± 368 and 3449 ± 337 , respectively. This is larger than the values obtained from the individual channels by about 18 %. A sample of ^{55}Fe event pulse obtained from the anode sum-line is shown in Figure 5.7(a) while in Figure 5.7(b) is a sample of ^{55}Fe energy spectrum obtained from one calibration operation for the left MWPC.

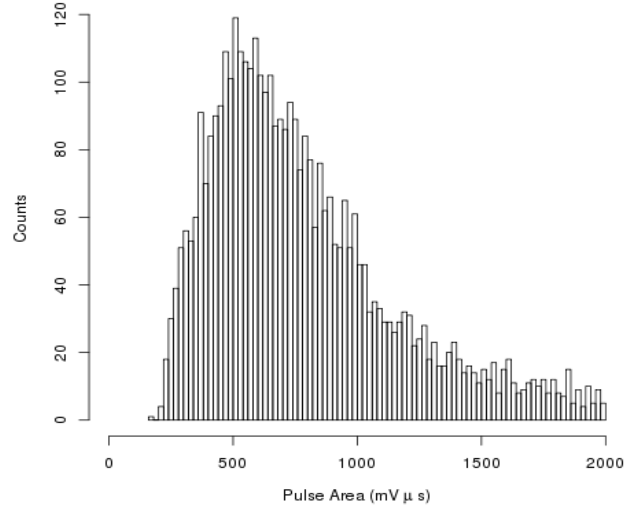
It can be seen that the energy spectrum shown in Figure 5.7 reaches its peak at about $510 \text{ mV } \mu\text{s}$ and tails off at higher pulse areas $>1500 \text{ mV } \mu\text{s}$. Results show that this is because signal pulses recorded at the same time on different anode signal channels can merge (pile-up) on the sum-line. For instance, this is illustrated in Figure 5.8 using a raw ^{55}Fe charge signal pulses. In analysis, this merged signal pulses can be recorded by the algorithm as one pulse sample from the ^{55}Fe calibration for that time which can result in a systematic effect due to over estimation of the actual calibration pulse. This does not apply to triggered nuclear recoil events which are recorded on the sum-lines. In principle, these merged signals can be discriminated from single ^{55}Fe pulses using their charge duration parameter, if more energy calibration data samples were recorded for a given operation. However, in this analysis where only 100 event files were recorded for a given operation, this discrimination tends to reject most of the energy calibration events that passed the analysis threshold. This charge merger at the sum-line is a caveat of this energy calibration method for the simplified readout technology.

For nuclear recoil events, an alternative alpha rejection algorithm was developed using the average signal charge amplitude between the time before (down-veto) and after (up-veto) the ROI. The cuts applied to the up and down-vetos are shown in Figures 5.9(a) and 5.9(b), respectively. It can be seen that there are two distinct event species with different range parameters. This is because long alpha tracks with range $>15 \text{ mm}$ are expected to induce continuous waveform pulses on a signal channel especially in the regions outside the ROI in the DRIFT-IIId detector design. The group of events with smaller values of up and down-veto parameters are due to short nuclear recoil tracks relative to long event tracks from alphas, resulting in larger up and down-veto values. Hence, to reject these alpha events, all events whose up and down-veto values are greater than 2 mV and 1.7 mV , respectively, were rejected as shown in Fig-

5. WIMP search analyses and results from the DRIFT-II detector



(a) ^{55}Fe pulse obtained from the sum-line.



(b) Spectrum of ^{55}Fe events from the sum-line.

Figure 5.7: Sample of a ^{55}Fe events obtained from the DRIFT-II detector when set to the simplified readout mode. In (a) is a signal pulse from ^{55}Fe event as observed from the sum-line while in (b) is a typical energy spectrum of these ^{55}Fe events from a set of calibration.

5. WIMP search analyses and results from the DRIFT-II detector

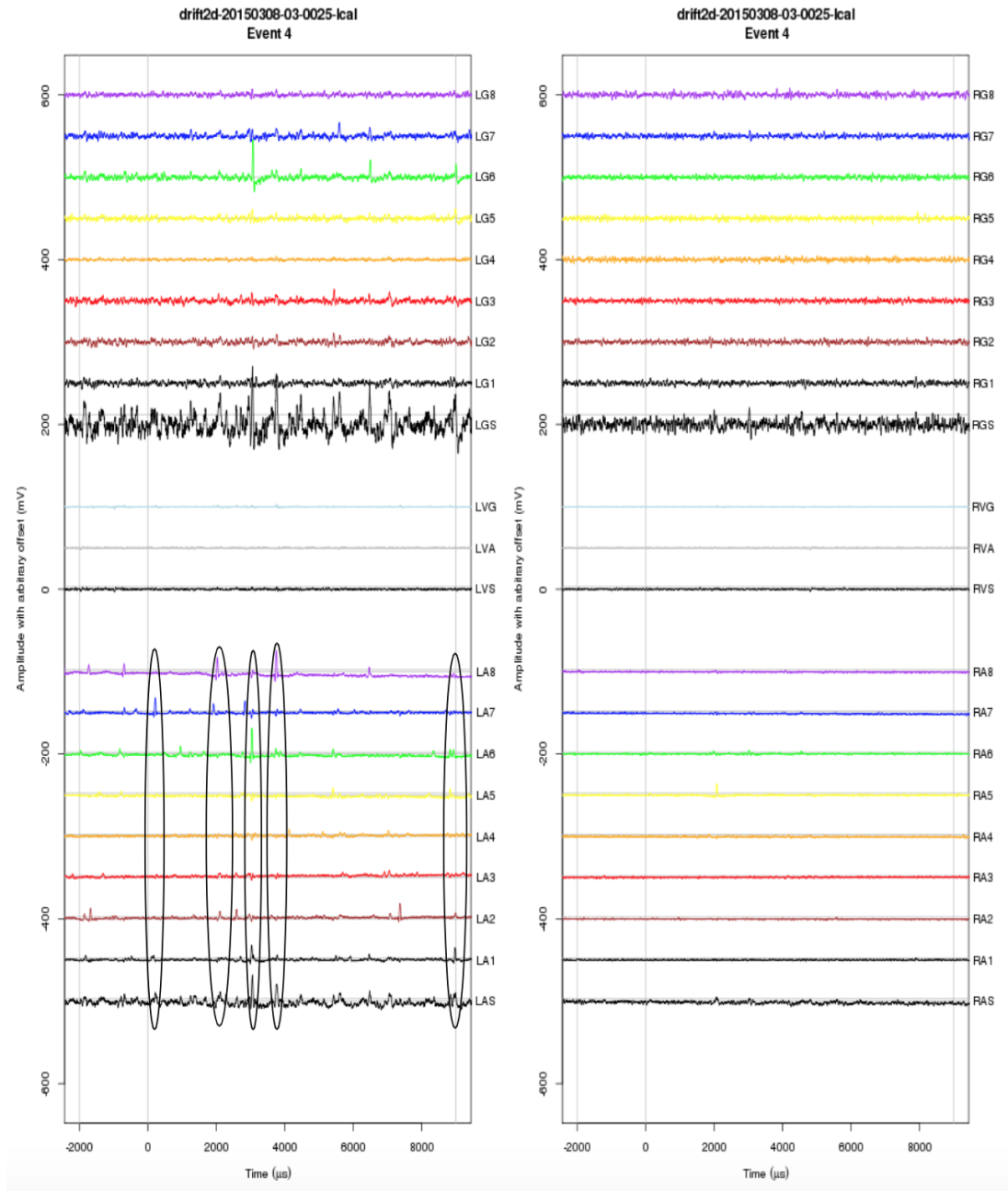
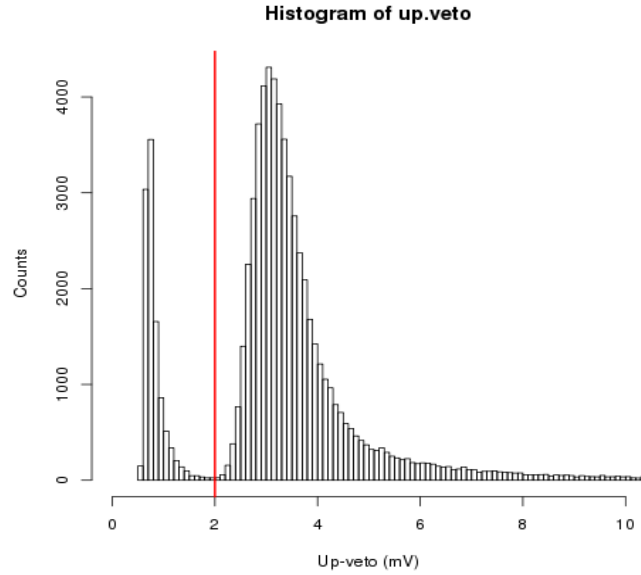


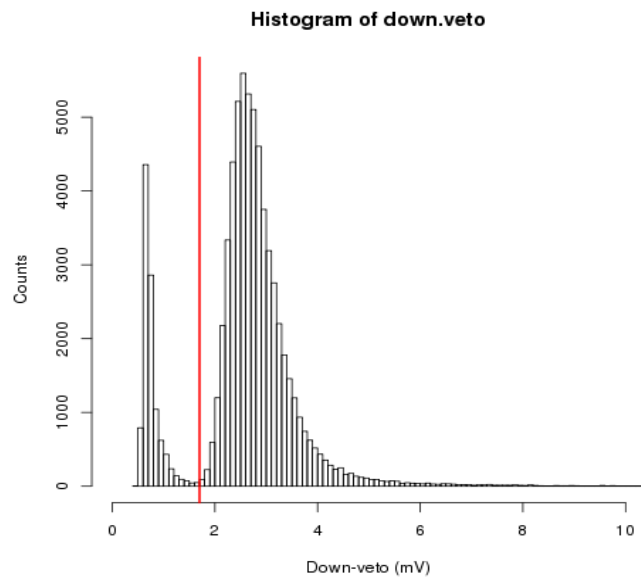
Figure 5.8: Sample of ^{55}Fe event showing merged charge pulses on the sum-line after energy calibration operations on the left detector. The anode sum-line is labelled as LAS. Black circular lines show merged ^{55}Fe charge pulses.

ure 5.9. This new alpha rejection method is needed because the previous algorithm

5. WIMP search analyses and results from the DRIFT-II detector



(a) Up-veto.



(b) Down-veto.

Figure 5.9: Spectra of up and down-veto parameters obtained from events in the detector, without any Q_r cut. In (a) is spectrum of up-veto parameter while (b) is that of the down-veto. All events beyond the red lines (to the right) were rejected in this analysis.

5. WIMP search analyses and results from the DRIFT-II detector

requires information from each of the eight signal channels which are not available in this simplified readout mode. Also, events that recorded charge signals on the veto sum channels were rejected to avoid longer alpha tracks and events emanating from outside the active volume of the detector. After determining the NIPs values of events using their respective energy constants, then, their NIPs values determined from the anode sum-lines were compared to that obtained from the grid sum-lines. Hence, all events with anode-grid NIPs ratio greater than 6, were rejected in analyses as done in the previous analyses to remove events that are in coincidence with sparks or charge surge in the anode wire readout plane. After the nuclear recoil selection cuts, the z values of all the good events were computed.

5.4.1 Results from the simplified 1D readout analyses

Using these simplified readout analyses methods, the feasibility of the simplified readout technology was investigated with the neutron calibration and the shielded data sets shown in Table 5.1. The results from this analysis for neutron calibration events is shown in Figure 5.10. It can be seen that the z and NIPs reconstruction algorithms used in this analysis were sensitive to neutron induced nuclear recoil events that occurred within the normal fiducial volume of the detector. These results demonstrate that detector fiducialisation is possible with a simplified readout. However, due to the effect of merging signal pulses from many channels on the sum-line, the NIPs values shown in Figure 5.10 were not precisely calibrated and can be improved. For nuclear recoil events, it was found that the z position of events obtained from the sum-line analyses were different by few mm from the results of analyses reported in Section 5.3.1 which were obtained with signal pulses deposited on the individual anode channels. This could be as a result of charge losses due to induced pulses on adjacent channels relative to the wire that recorded the actual signal charge from an event. Also, it was found that more than 70% of the observed neutron induced nuclear recoil events produced NIPs equivalent energies < 3000 . This is because the charge density induced by signal pulses on adjacent signal channels and number of channels on which these signals are induced scale with event energy. Hence the effect of charge loss due to inverted induced signal pulses on the sum-line is more on higher energy events. Due to these effects and a different set of nuclear recoil selection cuts used, this analysis

5. WIMP search analyses and results from the DRIFT-II detector

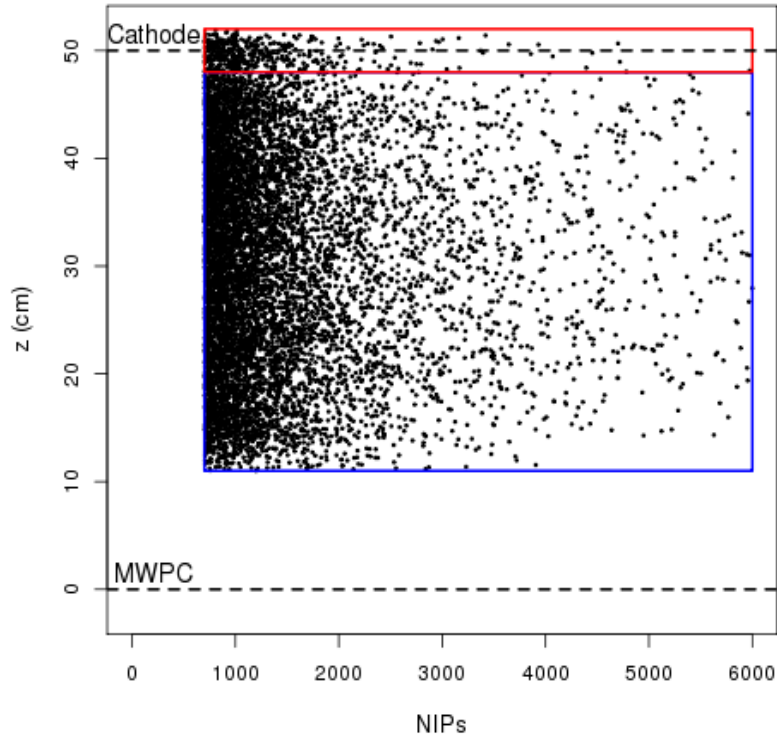


Figure 5.10: Distribution of neutron induced nuclear recoil events obtained from the 0.803 live-time days of neutron calibration data. The normal detector fiducial volume is marked with blue lines while red lines show the RPR region. The boundary between this RPR region and the fiducial volume is shown with a red line. The black dashed lines on $z = 0$ and $z = 50$ cm represent the readout MWPC and central cathode, respectively.

was unable to precisely reproduce results obtained from the normal DRIFT analyses algorithms discussed in Section 5.2. For instance, the rate of neutron induced nuclear recoil events obtained from the simplified 1D readout analyses shown in Figure 5.10 is 12557 ± 115 events d^{-1} . This is less than the previous results by about 30%.

Using these observed neutron events and the GEANT4 simulation data, the nuclear recoil detection efficiency of the detector can be determined for this simplified 1D readout analyses mode as earlier described in Section 5.2.1. The detector efficiency results obtained from this analysis are depicted in Figures 5.11(a) and 5.11(b) for the

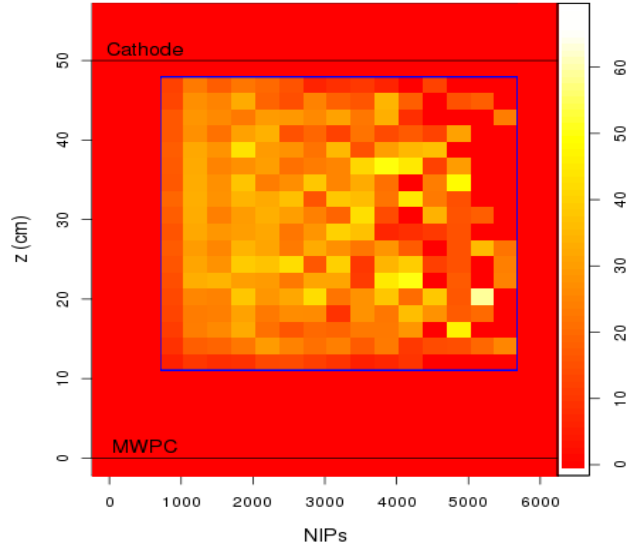
5. WIMP search analyses and results from the DRIFT-II detector

efficiency map shown in the z -NIPs space and the average detector efficiency for different energy bins, respectively. It can be seen in Figure 5.11(b) that the detector when operated in this mode recorded highest efficiency of about 60% for events with energy of 1000 to 4000 NIPs. This decreased at higher energies above 4000 NIPs reaching a minimum of about 20%. This low efficiency at higher energies is because of the earlier discussed charge losses and energy calibration effects for high energy events on the sum-line. Also, the detector efficiency obtained for < 1000 NIPs events is larger than the results obtained in the normal analysis and that obtained for > 5000 NIPs events by a factor of ~ 2 . This implies that more low-energy events passed the nuclear recoil selection cuts used in this 1D readout analyses relative to high-energy events and low-energy events in the normal analysis.

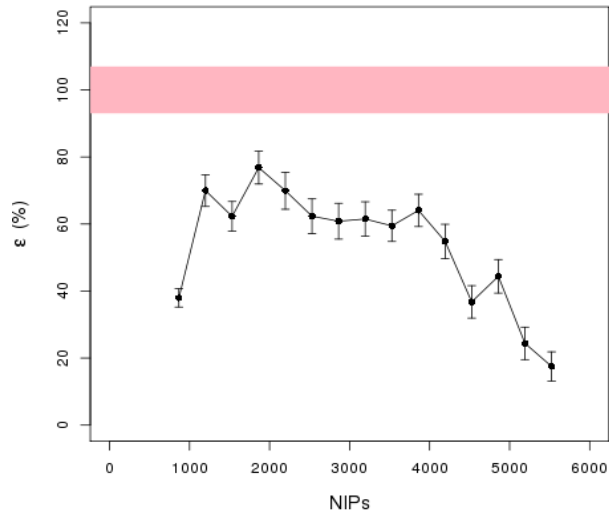
To be able to estimate the detector performance for a WIMP search operation in this simplified 1D readout mode, the WIMP search data was used. Results obtained from the analysis of the WIMP search data in this detector mode is shown in Figure 5.12. It can be seen that no nuclear recoil event was observed within the fiducial volume of the detector. However, the observed z positions, NIPs values and event rate (1.01 ± 0.14 events d^{-1}) of RPR events that passed the earlier described simplified 1D readout nuclear recoil selection cuts are different from the results obtained in the normal analyses shown in Figure 5.5. This is due to different set of nuclear recoil selection cuts used in this simplified 1D readout analysis. These new results can be used to estimate the spin-dependent WIMP-proton cross section at 90% confidence level as previously discussed in Section 5.3.1. To determine this WIMP exclusion limit, the detector efficiency shown in Figure 5.11, WIMP search results obtained from this simplified 1D readout mode analyses and other detector parameters discussed in Section 5.3.1 were used.

The 90% confidence level spin-dependent WIMP-proton cross section results obtained from this computation is shown in Figure 5.13 as a function of WIMP masses. In that figure, the results from this simplified 1D readout analysis are shown with a blue line while the previous result obtained from the normal DRIFT analysis is shown with a red line. As before, these results were compared to recent results from other leading directional experiments. The DMTPC and NEWAGE results are shown with cyan and light green lines, respectively while the 2015 result obtained from the DRIFT-II detector with a higher hardware threshold and results from the PICO non-directional

5. WIMP search analyses and results from the DRIFT-IIId detector



(a) Efficiency map for z -NIPs bins from simplified readout data.



(b) Energy bin efficiency from simplified readout data.

Figure 5.11: Nuclear recoil detection efficiency of the detector obtained from the simulated simplified 1D readout mode analyses. In (a) is efficiency map for different z and NIPs bins while (b) is the average efficiency in a given energy bin. The colour scale in (a) is the bin efficiencies presented in percent.

5. WIMP search analyses and results from the DRIFT-II detector

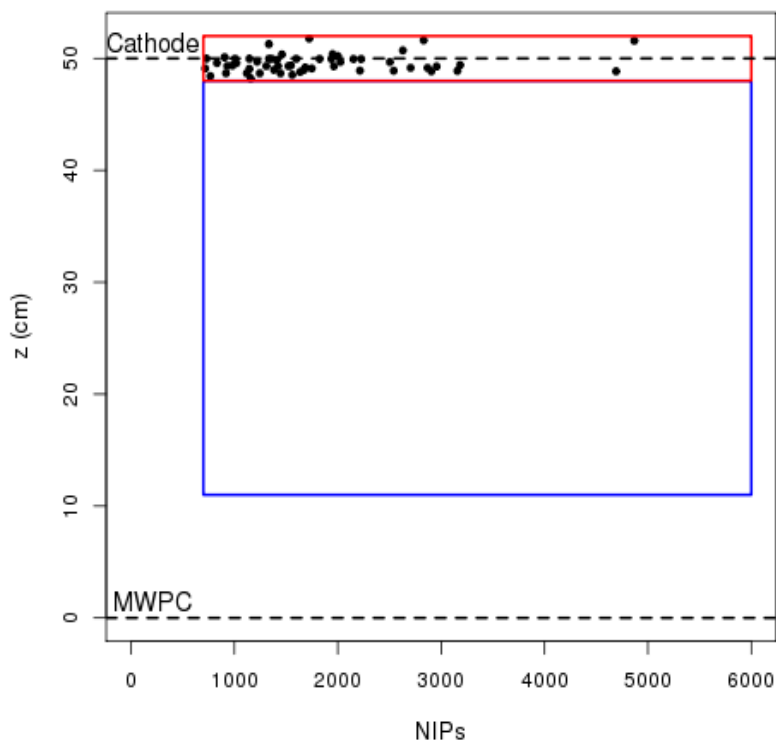


Figure 5.12: Background events that passed the simplified 1D readout nuclear recoil selection cuts obtained from the 54.7 live-time days of WIMP search data. The normal detector fiducial volume is marked with blue lines while red lines show the RPR region. The boundary between this RPR region and the fiducial volume is shown with a red line. The black dashed lines on $z = 0$ and $z = 50$ cm represent the readout MWPC and central cathode, respectively.

experiment are shown with grey and black lines, respectively. It can be seen that in this new readout mode that the detector reached a spin-dependent WIMP-proton cross section sensitivity of about 0.41 pb for WIMPs of mass $\sim 100 \text{ GeV } c^{-2}$. This result is worse than the previous result obtained from the previous normal DRIFT analysis by only 0.1 pb. But, this does not account for the systematic uncertainties due to the events energy calibration used and the simplified assumptions made in the detector simulation. These 1D readout results can be improved further using a better alternative energy calibration method. The results obtained in this analysis are encouraging

5. WIMP search analyses and results from the DRIFT-II detector

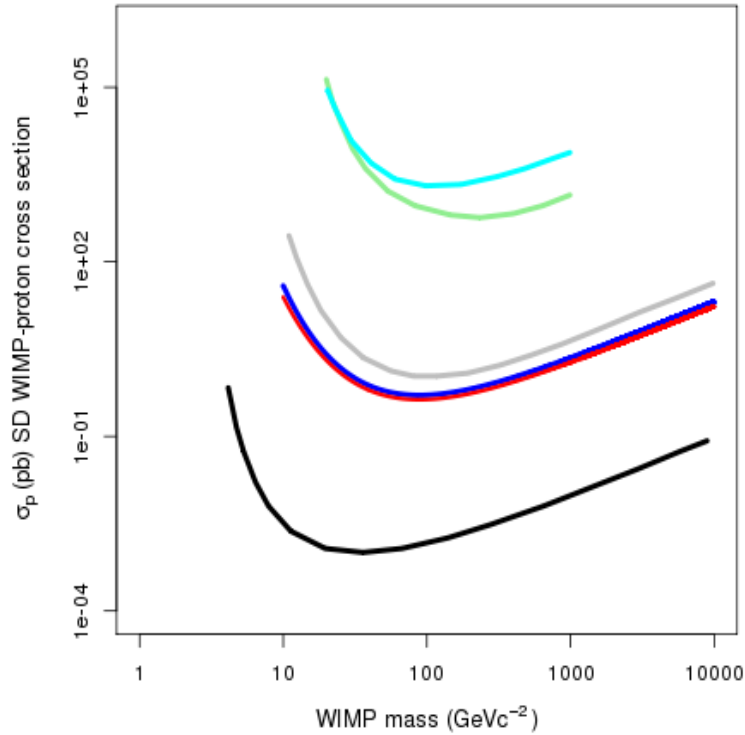


Figure 5.13: Spin-dependent WIMP-proton cross section limit set at 90% confidence level obtained from the simplified 1D readout mode analyses shown as a function of WIMP masses. The results obtained from this simplified 1D readout analyses is shown with a blue line, cyan line is the latest result from DMTPC [177], light green line is that from NEWAGE [144], grey line is 2015 DRIFT-II result obtained with a higher hardware threshold [113], red line is the result obtained with the normal fiducial volume analyses shown in Figure 5.6 while black line is the latest non-directional result from PICO [157].

which suggest that a 1D readout technology may be a possible path towards reducing the cost of front-end electronics and data acquisition systems in large area TPC detectors. However, it is important to point out that more work is required to understand the implication for rejection of electron recoils and gamma event backgrounds for this one dimensional readout scheme especially in longer WIMP search operations. Also, the results obtained in this study were determined from integral charge pulse in the sum-line of the DRIFT-II detector which did not simulate any possible effect of capacitive

noise which may arise from signal grouped wires.

5.5 Extending the fiducial volume to the low- z region of the detector

In this section, an alternative analyses method that is sensitive to neutron induced nuclear recoil events which can be used to extend the detector fiducial volume to the low- z region of the detector is discussed. This is important for the proposed CYGNUS-TPC detector to ensure that the detector fiducial volume and sensitivity are maximised when built. In fact, one way to improve the detector spin-dependent WIMP-proton cross section sensitivity further, is to increase the fiducial volume which can result in an enhanced fiducial target mass. For the DRIFT-II detector, this can be achieved by extending the analyses described in Sections 4.5 and 5.2 to the low- z region of the detector. As earlier discussed, signal charges due to interactions in the low- z region of the detector arrive at the readout plane within a very short period after the interaction. This makes it hard for the previous analysis to find the charge carrier peaks and determine the required temporal separations between the minority charge carriers (resulting in the D, P and S peaks) and the main charge cloud (resulting in the I peak). Hence, the z reconstruction algorithm described in Chapter 4 that uses the temporal separations between these peaks (as shown in Equation 4.5) to reconstruct event z positions, fails for low- z events which leads to their rejection in analyses. The behaviour of these D, P, S, and I peaks at different regions of the detector are illustrated in Figure 4.5 using signal pulses from various neutron induced nuclear recoil events. In Figure 5.14 is a zoomed version of Figure 4.5(b) for easy reference. This figure shows distinct D, P, S and I peaks as observed from a typical nuclear recoil event in the mid- z region of the detector.

To be able to develop a new z reconstruction algorithm that can be sensitive to events at the low- z region, more understanding of the behaviour of these signal peaks at the high- z and mid- z regions of the detector is required which can potentially be extrapolated to low- z events. This was studied using signal pulses from neutron induced tracks. As before, the signal channel that recorded the highest voltage was analysed for each of these neutron events. The data were binned using their respective z positions.

5. WIMP search analyses and results from the DRIFT-II detector

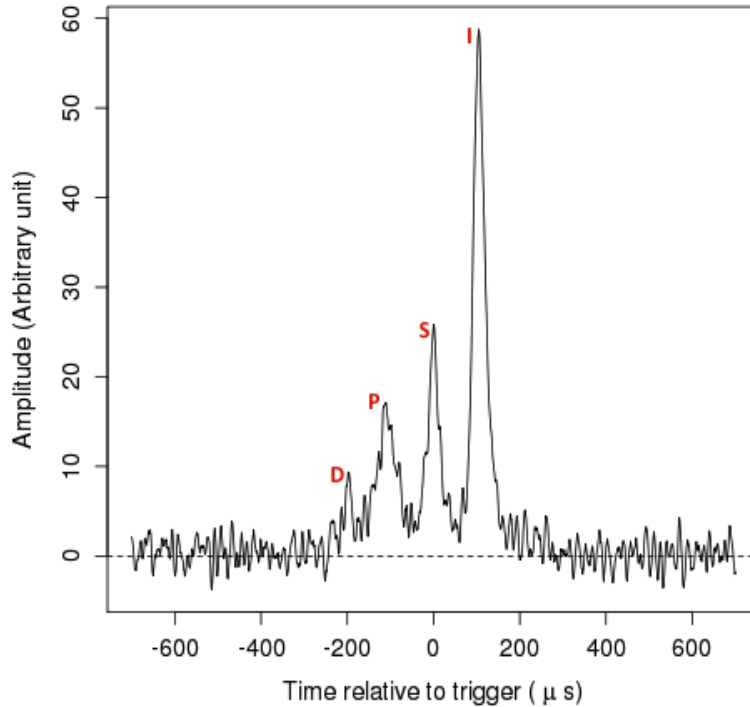
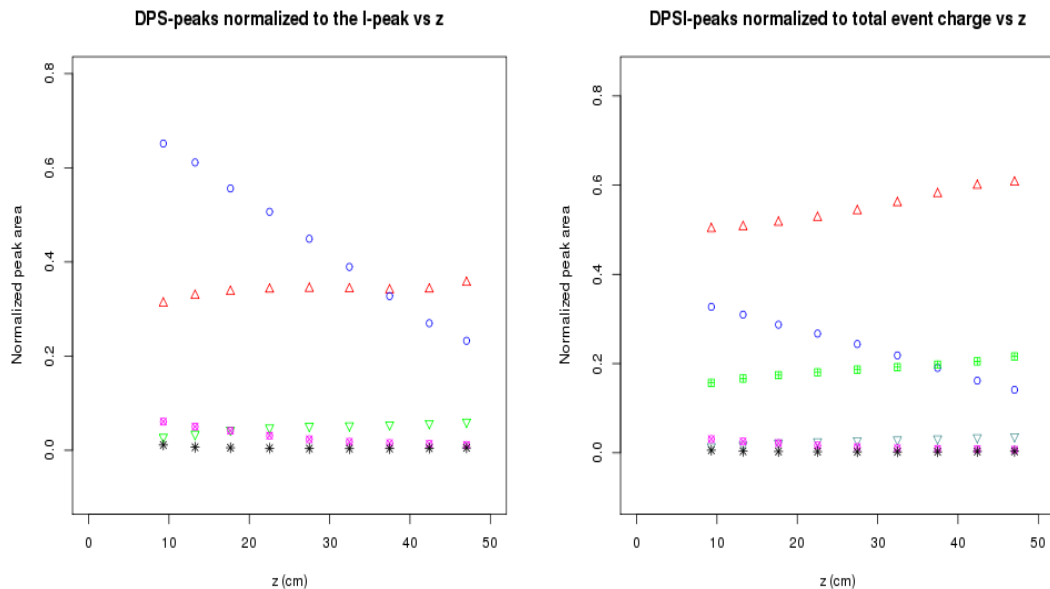


Figure 5.14: Minority charge carrier species (D, P and S charge carrier species) after arriving to the read out plane ahead of the main charge cloud (I charge carrier species) obtained from a nuclear recoil event in the DRIFT-II detector.

In that analysis, the positions of each of the peaks were recorded and boundaries of the respective charge carrier species were marked using their pulse widths. Then, the ratio of the integral charge in the D, P and S charge carriers were determined relative to the integral charge in the I charge carrier species. Also, the ratio of the integral charge in each of the signal carriers (D, P, S, I) relative to the overall integral charge obtained from all the charge carrier species in any given event was computed. The results from these analyses are shown in Figures 5.15(a) and 5.15(b), respectively.

In each of these computations, the average charge ratio obtained from the ROI down-veto (ROI-down) and up-veto (ROI-up) regions of signal pulses were computed for each of the bins and shown in Figure 5.15. The results in Figure 5.15(a) show that the S charge carrier species decrease with increase in z relative to the I charge carrier

5. WIMP search analyses and results from the DRIFT-II detector



(a) D, P and S relative to I charge carriers.

(b) D, P, S, I relative to their integral charges.

Figure 5.15: Behaviour of integral charges in the D, P, S and I charge carrier species shown as a function of event z positions. The integral charge in D (green downward triangular points), P (red upward triangular points) and S (blue circular points) charge carrier species were normalized to the integral charges in the I charge carrier species in (a) while integral charges in each of the D (grey downward triangular points), P (green square points), S (blue circular points) and I (red upward triangular points) charge carrier species were normalized to the overall integral charge obtained from each of the events in (b). The integral charge between the beginning of the ROI and the start boundary of the D charge carrier is shown with purple square point in (a) and (b) while the integral charge between the end of the I charge carrier boundary and the end of the ROI is shown with black asterisk points in (a) and (b).

species. For the P charge carrier species, a small increase can be seen relative to the I charge carrier species with increase in z . The charges in the D charge carrier species, the ROI-down and ROI-up vetos are negligible relative to the I charge cloud and to the overall charge from all the charge carrier species (see Figures 5.15(a) and 5.15(b), respectively). The results in Figure 5.15(b) show that the integral charge in the P and I species increase with z while that of S decrease with increase in z . These results suggest that charges in the S charge carrier species may be changing to either the P or the I charge carriers after drifting longer distances.

5. WIMP search analyses and results from the DRIFT-II detector

The temporal separation Δt between the arrival times of the S and I and that between the P and S charge carrier species to the readout plane are shown in Figure 5.16. The Q_r cuts discussed in Chapter 4 were not applied to the data in Figure 5.16 in order

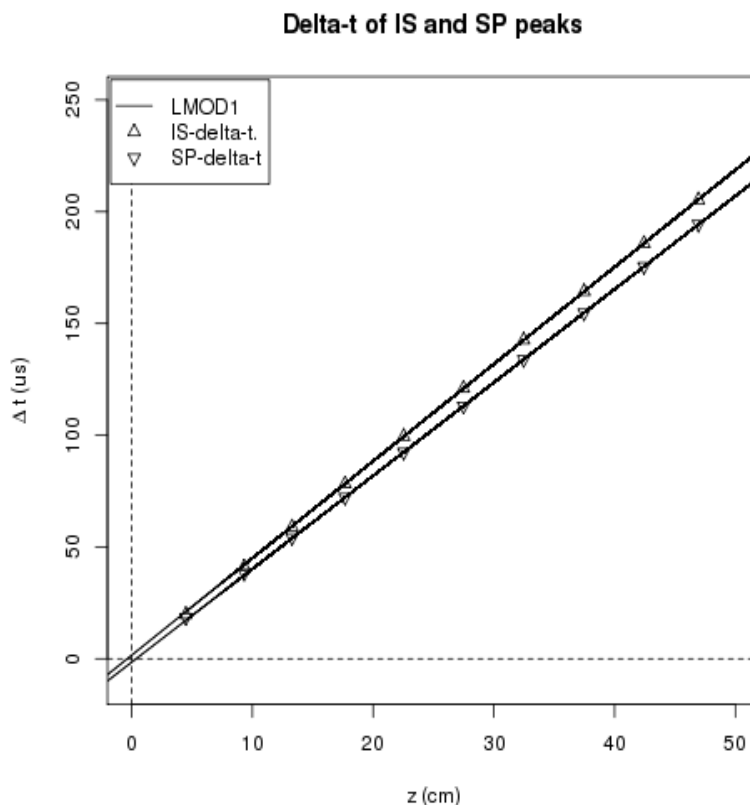


Figure 5.16: Temporal separation Δt between the arrival times of two different charge carrier species at the readout plane. The upward triangular points are the Δt between the arrival times of I and S charge carrier species while the downward triangular points are Δt between the S and P charge carrier species. The lines are fitted linear models. No Q_r cuts were applied to this dataset.

to allow some low- z events to be sampled. It can be seen in that figure that there is a linear relationship between the Δt parameter obtained from S and I charge carrier species and that obtained from P and S charge carrier species. The results show that these Δt parameters are the same within statistical errors especially for events from the low- z region of interest. Then, Equation 4.5 can be rewritten in a more simplified form

5. WIMP search analyses and results from the DRIFT-II detector

using the Δt parameter as:

$$z = \frac{v_i v_p \Delta t_{ip}}{v_p - v_i}, \quad (5.4)$$

where $\Delta t_{ip} = t_i - t_p$ is the temporal separation between charge cloud in the I and P peaks. This is after the charges in the I and P peaks have arrived at the readout plane at times t_i and t_p with drift velocities v_i and v_p , respectively.

This implies that if a Δt parameter can be determined for any two of the charge carrier species in a given event then, Equation 5.4 can be used to estimate the z position of that event. To do this, the information in Figure 5.16 can be used to define a linear relationship between the temporal separation Δt and the z -position of events using any two consecutive peaks given by:

$$\Delta t = \beta z, \quad (5.5)$$

where β is the slope of the linear relationship between Δt and z parameters for a given event. However, Equation 5.5 can only be used to determine the Δt parameter for events with known z -positions but, the absolute z of the low- z events of interest, are not precisely known. Then, combining the information in Figure 5.16 and Equation 5.5, it can be seen that the overall pulse duration $\Delta\tau$ of events can be defined in terms of Δt using:

$$\Delta\tau = 4\Delta t + \Delta\phi. \quad (5.6)$$

The $\Delta\phi$ parameter is a correction factor added to account for duration of signal pulse from events that occur on the MWPC (i.e. with $z = 0$). This $\Delta\phi$ parameter is about 10 μs equivalent to the expected minimum pulse width from the shaping electronics used in this experiment. In Figure 5.17, the boundaries of the $\Delta\tau$ parameter in a sample of nuclear recoil event pulse are marked with blue lines. In that figure, the $\Delta\tau$ parameter can be determined by finding the difference between the upper and lower boundaries. The temporal separation between any two of the four charge carrier species (D, P, S and I) can then be determined using:

$$\Delta t_{is} = \frac{(\Delta\tau - \Delta\phi)}{4}, \quad (5.7)$$

when the S and I charge carrier species are considered. In this case, the Δt_{is} parameter obtained in Equation 5.7 can be substituted in Equation 5.4 for the Δt_{ip} parameter,

5. WIMP search analyses and results from the DRIFT-II detector

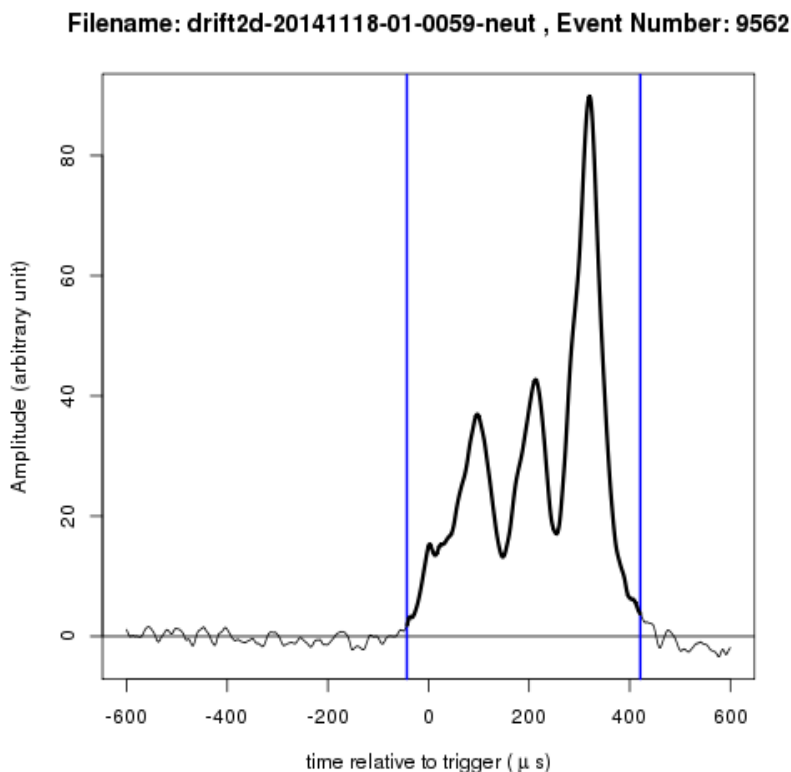


Figure 5.17: Signal pulse duration $\Delta\tau$ shown for a neutron induced nuclear recoil event obtained from the DRIFT-II detector. The boundaries of the $\Delta\tau$ parameter are marked with blue lines.

using v_s and v_i as the drift velocities of the S and I peaks, respectively. Then, it can be obtained that:

$$z = \frac{v_i v_s \Delta t_{is}}{v_s - v_i} = \frac{v_i v_s (\Delta\tau - \Delta\phi)}{4(v_s - v_i)}. \quad (5.8)$$

Hence, Equation 5.8 can be used as an alternative method to estimate the absolute distance between an event vertex and the readout plane for all events and especially for the low- z candidates.

To understand the performance of this method, a new z reconstruction algorithm was developed. This is based on the method shown in Equation 4.5, which was used at the first instance, when it fails then the alternative method shown in Equation 5.8 was then applied. To do this, the Q_r cuts were not applied to the data in this analysis in order not to reject low- z events. Rather, a $\Delta\tau$ cut was developed which monitors the

5. WIMP search analyses and results from the DRIFT-IIId detector

signal pulse duration (see Figure 5.17) and rejects spark events with $\Delta\tau < 9 \mu\text{s}$. It is expected that this cut should reject spark events as done previously with the $Q_r < 0.3$ cut. Also a cut on the up-veto $< 2 \text{ mV}$ and down-veto $< 1.7 \text{ mV}$ parameters were used to reject other spark events with continuous waveform pulses (as previously done with the $Q_r < 0.6$ cut) and long alpha event tracks. By this recovery of the low- z region of the detector, the fiducial volume of the detector could be improved by about 18% of the active volume of the detector by using $2 \text{ cm} \leq z \leq 48 \text{ cm}$. The remaining 2 % of the active volume, at the very low- z region, closer to the MWPC readouts can then be used to record any background events due to radioactive (for instance: ^{238}U , ^{234}U , ^{210}Po , ^{222}Rn , ^{218}Po , ^{220}Rn and ^{214}Po [112]) decays on the stainless steel MWPC readout wires, plexiglas frame, epoxy and other materials used in building the MWPCs. As discussed in Section 5.3.1, these events can become problematic when the alpha signature resulting from the interactions are completely concealed in the MWPC readout wires. This set of new analysis was performed on the shielded WIMP search data and their corresponding neutron calibration data discussed in Section 5.2. The results from this analysis are presented in Section 5.5.1.

5.5.1 WIMP results from the improved fiducial volume

Detector performance and WIMP search results obtained from analyses of the neutron calibration and the shielded WIMP search data (see Table 5.1) using the alternative z reconstruction algorithms discussed in Section 5.5 are presented in this section. To be able to extract a WIMP search result from this analysis, a new detector efficiency was determined using event rates from the neutron calibration and GEANT4 Monte Carlo simulation data as earlier discussed in Section 5.2.1. In this efficiency analyses, the neutron data shown in Figure 5.18 were binned using the methods described in Section 5.2 and compared to the GEANT4 data. In that figure, it can be seen that indeed, the alternative z reconstruction is sensitive to events closer to the MWPC readouts. The rate of these observed low- z events was found to be smaller compared to the rates at high- z and mid- z regions of the detector. This is because some real nuclear recoil events in the low- z region tends to share similar characteristics with noise events, hence the nuclear recoil discrimination algorithm fails to recover all the events in this region of the detector. Also, it is expected that the rate of neutron induced events should scale

5. WIMP search analyses and results from the DRIFT-II detector

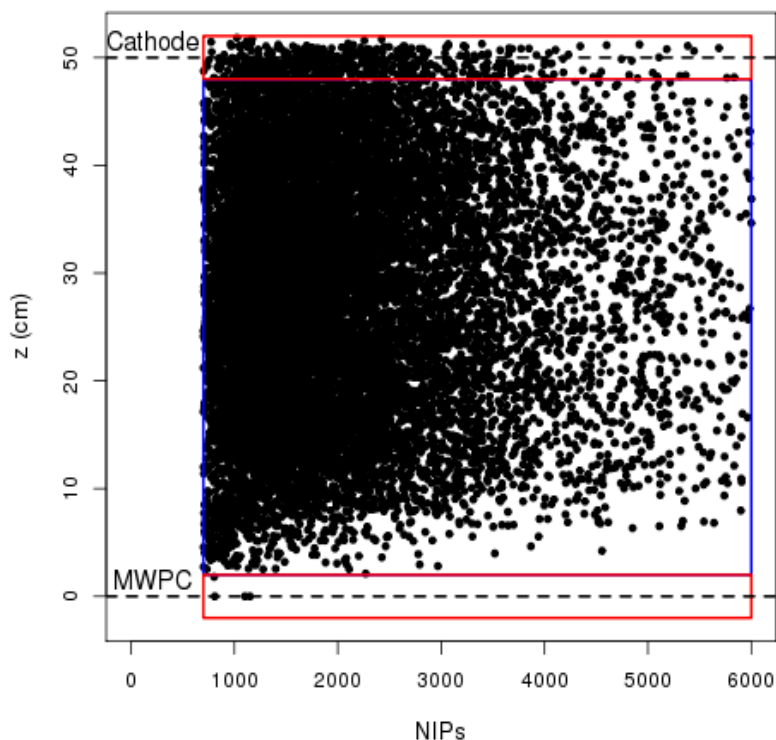


Figure 5.18: Distribution of neutron induced nuclear recoil events recorded during the 0.803 days of neutron calibration operations. The RPR regions are marked with red lines while the fiducial volume of the detector is bounded in the left and right with blue lines and with red lines from the top and bottom sides. The black dashed lines on $z = 0$ and $z = 50$ cm represent the readout MWPC and central cathode, respectively.

with the solid angle subtended by the neutron source at any point in the detector. As earlier discussed in Section 5.1, the neutron source was placed closer to the central cathode during the neutron calibration operations. This position is closer to the high- z and mid- z regions of the detector when compared to the low- z region. The results show that the total fiducial rate for neutron induced nuclear recoil events recorded with this new z reconstruction algorithm is 18403 ± 152 neutrons per day. This is more than the rate obtained in the previous normal fiducial volume analysis by 3%. This is mainly due to extra events that were recovered from the low- z region of the detector in this extended fiducial volume analyses.

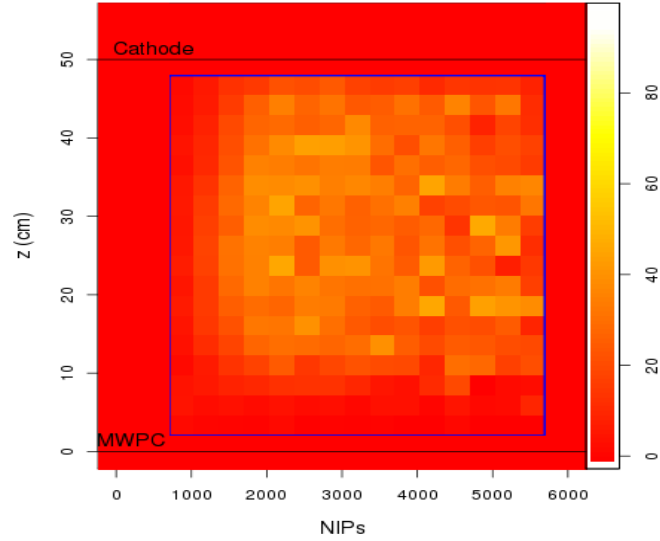
5. WIMP search analyses and results from the DRIFT-II detector

Using these neutron calibration and the GEANT4 results, then the detector nuclear recoil detection efficiency can be determined for this improved fiducial volume analysis. These detector efficiency results are shown in Figure 5.19. It can be seen that the observed efficiency at the low- z region is lower than as in the mid- z and the high- z regions. This is as a result of the lower analyses nuclear recoil acceptance efficiency for low- z events, because event discrimination in this low- z region is more complicated due to the behaviour of minority carriers at this region of the detector. Hence, some real nuclear recoil events in the low- z region did not pass the required nuclear recoil selection cuts used in this analyses. More work is required to optimise this method so that higher percentage of real nuclear recoil events in this low- z region can be recovered. This can be achieved by using a more efficient cut which can discriminated more low- z events from unwanted noise events.

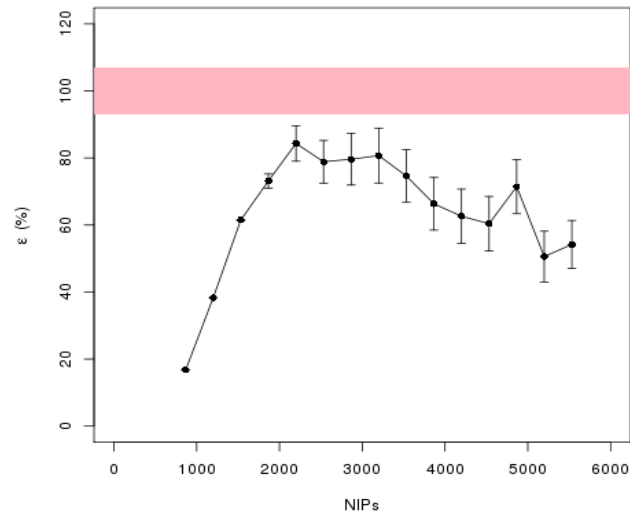
However, using the obtained detector efficiency shown in Figure 5.19 and the shielded WIMP search data, a new upper limit at 90% confidence level can be determined on the spin-dependent WIMP-proton cross section sensitivity of the detector in this new extended fiducial volume analyses mode. To do this, the shielded WIMP search data was analysed using the new set of nuclear recoil selection cuts which were developed for the extended fiducial volume analyses and the new z reconstruction algorithm as earlier described. The results from that analyses are shown in the z -NIPs space in Figure 5.20. It can be seen in that figure that no RPR events were observed around the MWPC readouts. This is due to lower efficiency of the new nuclear recoil selection cuts used in this analysis in discriminating low- z events from unwanted background noise for events closer to the MWPCs (see Figures 5.18 and 5.19). The implication of this is that the observed zero events at the MWPC readout for the 54.7 live-time days should be validated with a more efficient low- z nuclear recoil discrimination algorithm. Also the rate of RPRs near the central cathode as obtained from this analyses is 0.42 ± 0.09 events per day. This is a factor of 3 less than the results from the previous normal fiducial volume analyses. This indicates that, in principle, this observed rate of events emanating from the MWPC readouts may increase if a higher nuclear recoil discrimination can be achieved in this analyses that includes low- z events.

Then using the detector information in Figures 5.19 and WIMP search results in Figure 5.20, an upper limit can be set for the spin-dependent WIMP-proton cross section sensitivity as described earlier in Section 5.3.1 for the normal fiducial volume

5. WIMP search analyses and results from the DRIFT-II detector



(a) Efficiency map for z -NIPs bins for the improved fiducial volume.



(b) Energy bin efficiency for the improved fiducial volume.

Figure 5.19: Nuclear recoil detection efficiency of the detector obtained from data in the extended fiducial volume mode. This is considering all events including the low- z events. In (a) is efficiency map for different z and NIPs bins while (b) is the average efficiency in a given energy bin. The colour scale in (a) is the bin efficiencies presented in percent.

5. WIMP search analyses and results from the DRIFT-II detector

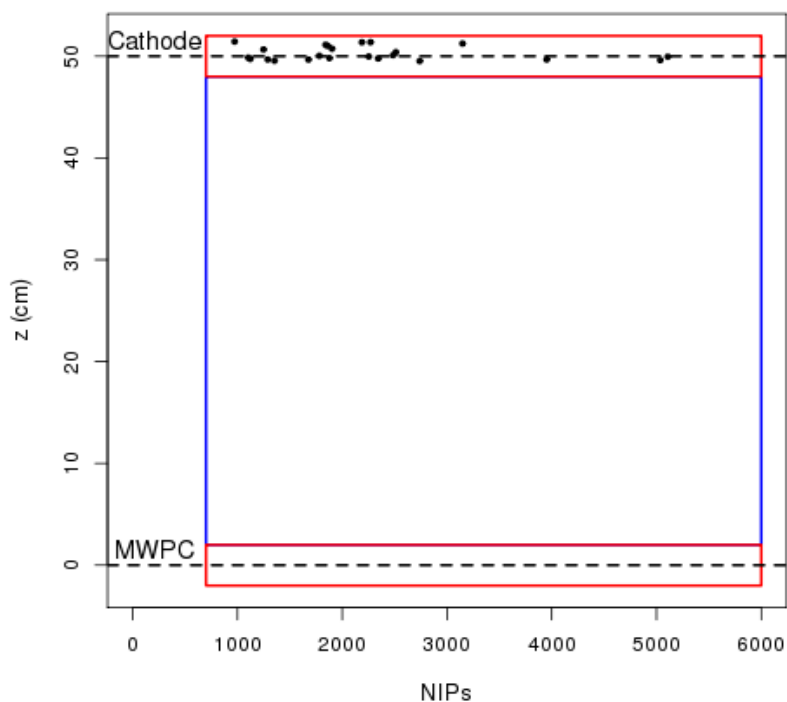


Figure 5.20: Distribution of nuclear recoil events shown in z -NIPs space as obtained from the 54.7 live-time days of shielded WIMP search data using the new extended fiducial volume z reconstruction algorithm. The regions where RPRs are expected from the cathode and MWPC readouts are marked with red lines while the fiducial volume of the detector is bounded in the left and right with blue lines and with red lines from the top and bottom sides. The black dashed lines on $z = 0$ and $z = 50$ cm represent the readout MWPC and central cathode, respectively.

analyses. This is using 92% of the active volume of the detector as analyses fiducial volume resulting in a fiducial mass of 0.038 kg. Using these new parameters and other detector parameters shown in Table 5.3, then, the expected WIMP rate can be computed as earlier described in Sections 5.3.1. These computations for this analysis yielded the results shown with blue line in Figures 5.21 and 5.22.

In Figure 5.21, the new results are compared to the results from the normal fiducial volume analysis shown with a red line, also in cyan, light green and black lines are the latest results from the DMTPC, NEWAGE and PICO experiments, respectively, while

5. WIMP search analyses and results from the DRIFT-II detector

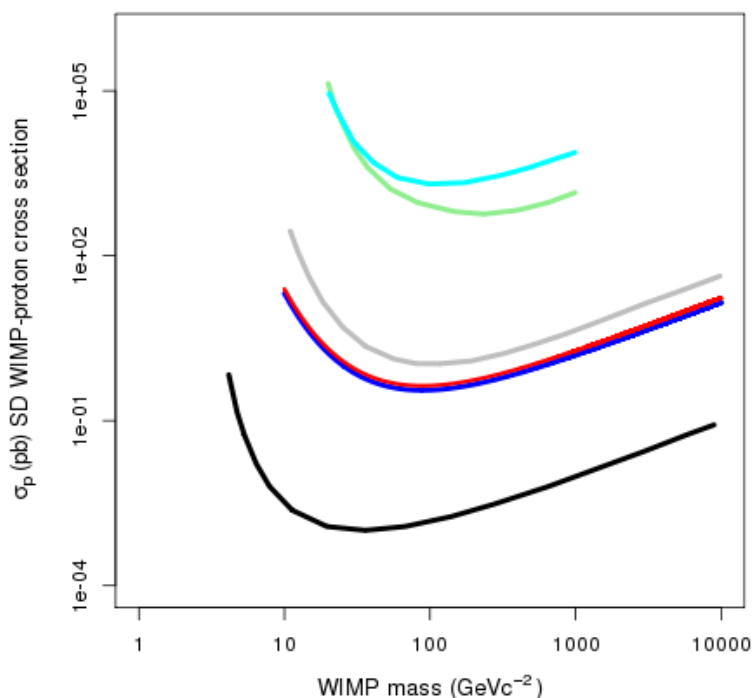


Figure 5.21: Spin-dependent WIMP-proton cross section exclusion limit set at 90% confidence level shown as a function of WIMP masses obtained from the extended fiducial volume analyses. The results obtained from the improved fiducial volume analyses is shown in blue, cyan line is the latest result from DMTPC [177], light green line is that from NEWAGE [144], grey line is 2015 DRIFT-II result obtained with a higher hardware threshold [113], red line is the result obtained with the normal fiducial volume analyses shown in Figure 5.6 while black line is the latest non-directional result from PICO [157].

the grey line is the 2015 results from the DRIFT-II detector. It can be seen from these new results that the detector reached highest sensitivity for spin-dependent WIMP-proton cross section at 0.29 pb for WIMPs of mass $\sim 100 \text{ GeV } c^{-2}$. This new limit obtained with a bigger fiducial target mass is better than the previous result obtained from the normal fiducial volume analyses by 0.04 pb. For more details, see the zoomed version of this improved fiducial volume results in Figure 5.22 for better comparison to other results obtained from the simplified 1D readout analysis and that from the normal analyses. In that figure, the results from the simplified 1D readout, the normal

5. WIMP search analyses and results from the DRIFT-IIId detector

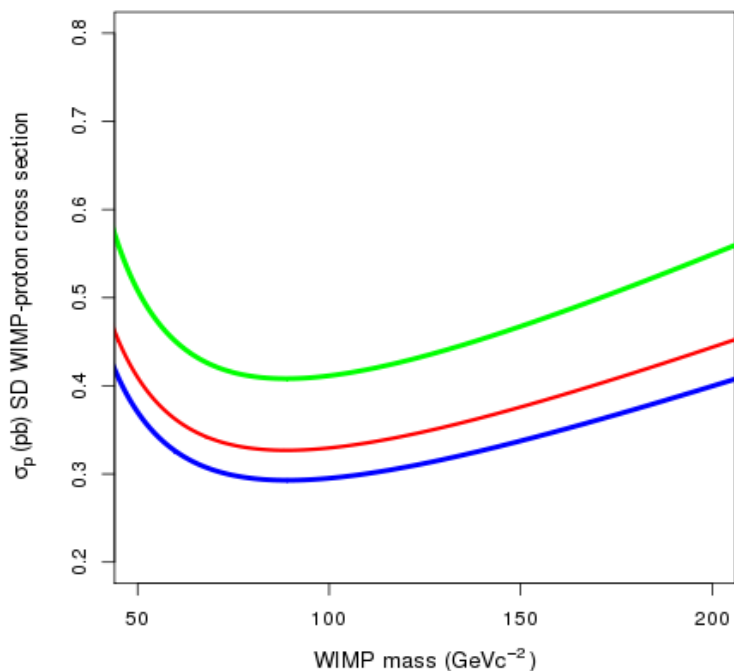


Figure 5.22: Comparison of the spin-dependent WIMP-proton cross section sensitivity of the DRIFT-IIId detector obtained using the simplified 1D readout, normal and the improved fiducial volume analyses at 90% confidence level. Results from the simplified 1D readout analysis is shown with a green line while that from the normal and improved fiducial volume analyses are shown with red and blue lines, respectively.

and the improved fiducial volume analyses are shown with green, red and blue lines, respectively. More studies can be done to improve the nuclear recoil discrimination cuts for this improved fiducial volume mode analyses thereby optimising the detector efficiency and sensitivity.

5.6 Conclusion

Data analyses algorithms were developed to investigate possible WIMP interactions and background events in the DRIFT-IIId detector using a set of shielded WIMP search, neutron calibration and unshielded rock neutron measurement data. Results from the

5. WIMP search analyses and results from the DRIFT-II detector

54.7 live-time days of shielded WIMP search data set, show no WIMP-induced nuclear recoil events within a smaller fiducial volume of the detector. Using the information from these analyses and the nuclear recoil detection efficiency obtained from comparing the neutron calibration data analyses results to that of GEANT4, an upper limit on the most probable WIMP interaction cross section was determined. This results in highest detector sensitivity to the spin-dependent WIMP-proton cross section at 0.33 pb for WIMPs of mass $\sim 100 \text{ GeV } c^{-2}$.

The results obtained from the unshielded rock neutron measurements show that at least 1 nuclear recoil event can be observed within the fiducial volume of the detector in every ~ 3.5 days, if about 80% of the polypropylene pellet shielding are not used around the detector during operations. Hence, in order to improve the detector sensitivity and reduce the number of background events during WIMP search operations, enough polypropylene pellet shielding should be used to obtain a tolerable neutron background rate of ~ 1 event per year in the detector.

A new z reconstruction algorithm was developed to extend the detector sensitivity to the low- z region of the detector which can improve the detector fiducial volume by 18% with an improved fiducial mass. Results obtained from combining this new z reconstruction algorithm with the previous method for the 54.7 live-time days of shielded WIMP search data also showed no background events within the improved fiducial volume of the detector with a reduced detector efficiency in different energy bins. These new WIMP search results were used to obtain a 90% C.L. upper limit of 0.29 pb on the spin-dependent WIMP-proton cross section for $\sim 100 \text{ GeV } c^{-2}$ WIMP mass. This improved sensitivity relative to results obtained in the normal fiducial volume analyses is mainly due to a larger fiducial target mass used in this case.

Also, the possibility of a simplified one dimensional readout technology was simulated using only the informations on the signal sum-line channels of the DRIFT-II detector. The results obtained from the neutron calibration and the WIMP search data in this simplified readout mode analyses show that z positions and ionization energies of nuclear recoil tracks can be reconstructed in this mode. However, the accuracy of this event energy reconstruction can be optimised with a more efficient energy calibration technique.

Chapter 6

Conclusions

The nature of the Universe was introduced in Chapter 1. This is using baryonic and non baryonic matter contributions to the energy density of the Universe as measured by the *Planck* mission. These *Planck* results show that 85% of matter content of the Universe is made up of a non baryonic dark matter. More empirical evidences obtained from velocity dispersion of galaxies, galaxy rotation curves, gravitational lensing effects, Bullet Cluster, Big Bang nucleosynthesis and cosmic microwave background radiations which also support the existence of this non baryonic dark matter were discussed. Gravitational evidence, present-day thermal relic abundance and expectations from the large scale structure formation suggest that dark matter is composed of particles that interact in weak scale with non baryonic matter. Hence, all the particles that possess major characteristics of these putative dark matter are referred to as Weakly Interacting Massive Particles (WIMPs).

Theoretical formulations and detection strategies used in searching for these WIMP dark matter particles are the subject of Chapter 2. These WIMP search methods can be either direct, indirect or through WIMP production at the large hadron collider. However, efforts toward WIMP production at the large hadron collider have not been successful. Some progress have been made by indirect WIMP search experiments which aim to detect product of WIMP annihilation. The most promising WIMP search strategies is through the direct detection channel which aims to observe WIMP induced nuclear recoil tracks in detectors. Current status and results from some direct WIMP search experiments were discussed. These experiments can be directional or non-directional. Directional experiments can reconstruct the energy and directions from

which interactions occur in the fiducial volume of the detector while non-directional detectors can reconstruct only the energy of interactions. As a result, directional detectors have the capability to observe the expected galactic sidereal modulation in WIMP rate. Also, it is expected that there should be an annual modulation in WIMP event rate reaching a detector over a year. This galactic WIMP signature can be detected by some non-directional WIMP search detectors. However, in principle, the directional galactic signatures are potentially more powerful than the annual modulation signals because the later can be mimicked easily by background events. This implies that non-directional WIMP search detectors may be unable to probe WIMPs beyond a background rich neutrino floor. Neutrinos coherently scattering off target nuclei are expected to be a major source of backgrounds beyond the neutrino floor. Hence, a massive directional WIMP search detector with enough sensitivity will be needed to probe these background rich parameter space. Global efforts towards building a massive directional detector called CYGNUS-TPC which can be used to probe for WIMPs beyond this neutrino floor was presented. This directional detector can also be used in the future to confirm the direction of any WIMP event detected in non-directional detectors.

In Chapter 3, the viability of a 20:1 signal multiplexing data acquisition system (DAQ) was investigated for possible use in the CYGNUS-TPC design. It is expected that this multiplexer DAQ will reduce the overall cost of signal readout in the CYGNUS-TPC project by a factor of 20 relative to a channel-to-channel readout configuration. The design, construction and operation of the signal multiplexing scheme with a one-plane miniature MWPC based DRIFT-IIe pro detector built for this experiment was presented. Measurements performed with this set-up show that even after signals from the DRIFT-IIe pro detector were multiplexed and demultiplexed that the effect of charge distribution along an alpha track can be reconstructed with about 10% signal loss.

Methods used in measurement of directional signatures in the DRIFT-IIe WIMP search detector are presented in Chapter 4. New directional measurements were performed in the current mode of detector where minority charge carriers due to addition of 1% of O₂ to the target were used for event fiducialisation. Also in the current mode, 28% of the target gas is CF₄ which provides an excess proton needed for spin-dependent coupling sensitivity. These new directional measurements were done

to ascertain if directional efficiency of the DRIFT-IIId detector was affected by recent changes in the detector target material. The detector measurability of nuclear recoil head-tail sense and axial directional range components were determined using neutron events. In these measurements, the head-tail effects were determined through a charge distribution asymmetry along nuclear recoil tracks while the axial directional signatures were reconstructed from event range components. Results show that longer nuclear recoil candidates from ^{12}C and ^{19}F components of the target gas improved the detector measurability of these directional signatures by about a factor of 2 relative to results obtained with only ^{32}S recoil tracks. These new directional results show prospects for events fiducialisation with directionality in the CYGNUS-TPC project.

Sensitivity of the DRIFT-IIId detector to the spin-dependent WIMP-proton cross section coupling was investigated in Chapter 5. This is using a 54.7 live-time days of shielded WIMP search data obtained while the detector was operated in steady automated gas flow mode with a cumulative of one detector gas change per day. During the WIMP search time window, no WIMP interaction event was observed within the fiducial volume of the detector. Using the detector efficiency and the expected WIMP interaction rate, a 90% C.L. spin-dependent upper cross section limit of 0.33 pb was obtained for $\sim 100 \text{ GeV } c^{-2}$ WIMPs. A new data analysis method was developed and used to extend event fiducialisation to the low- z region of the DRIFT-IIId detector resulting in improved fiducial target mass. Detector parameters and theoretical event rates obtained in this new mode improved the previous WIMP search results by 12%. These new results are currently the most stringent limit obtained from a direction sensitive WIMP search detector and also show the possibility of an optimal sensitivity for the proposed CYGNUS-TPC detector.

References

- [1] J. L. Feng. Dark matter candidates from particle physics and methods of detection. *Annu. Rev. Astron. Astrophys.* 48 (2010), pp. 495–545 (cit. on pp. [1](#), [3](#), [4](#), [19–23](#), [178](#)).
- [2] P. A. R. Ade et al. Planck 2015 results. *Astronomy and Astrophysics* 594 (2016) (cit. on pp. [1](#), [3](#), [13](#), [15](#), [16](#), [21](#)).
- [3] C. L. Bennett et al. Nine-year Wilkinson Microwave Anisotropy Probe (WMAP) observations: final maps and results. *Astrophys. J. Suppl. Ser.* 208.2 (Oct. 2013), p. 20 (cit. on p. [1](#)).
- [4] J. L. Sievers et al. The Atacama Cosmology Telescope: cosmological parameters from three seasons of data. *J. Cosmol. Astropart. Phys.* 61.10 (Oct. 2013), p. 060 (cit. on p. [1](#)).
- [5] C. C. Onuchukwu and A. C. Ezeribe. Constraining the Hubble parameter using distance modulus and Redshift relation. *Journal of Physics and Astronomy* 4.2 (2013), FP140–FP144 (cit. on p. [1](#)).
- [6] M. Roos. *Introduction to Cosmology*. 3rd ed. John Wiley and Sons, Ltd, 2003 (cit. on pp. [1](#), [2](#)).
- [7] S. R. Golwala. Exclusion Limits on the WIMP-Nucleon Elastic-Scattering Cross Section from the Cryogenic Dark Matter Search. PhD thesis. University of California at Berkeley, 2000 (cit. on pp. [1](#), [2](#)).

REFERENCES

- [8] T. M. Davis and D. Parkinson. Characterising Dark Energy through supernovae. *Handbook of Supernovae*. Ed. by A. W. Alsabti and P. Murdin. Springer International Publishing, Nov. 2016, pp. 1–23 (cit. on p. 3).
- [9] G. Bertone, D. Hooper, and J. Silk. Particle dark matter: evidence, candidates and constraints. *Phys. Reports* 405 (5 – 6 2005), pp. 279–390 (cit. on pp. 3, 5–7, 23, 178).
- [10] K. A. Olive et al. Review of particle physics. *Chinese Phys. C*. 38.9 (2014), p. 090001 (cit. on pp. 3, 13).
- [11] W. N. Cottingham and D. A. Greenwood. *An Introduction To The Standard Model Of Particle Physics*. 2nd ed. Cambridge University Press, 2007 (cit. on p. 3).
- [12] J. L. Hewett et al. Fundamental Physics at the Intensity Frontier. *Preprint: arXiv1205.2671* (2012) (cit. on pp. 3, 4).
- [13] K. Freese. *The Cosmic Cocktail: Three Parts Dark Matter*. Princeton University Press, 2014 (cit. on pp. 4, 5, 10, 13, 19, 20, 23).
- [14] A. Ibarra. Dark matter theory. *Nucl. and Phys. Proc.* 267–269 (2013), pp. 323–331 (cit. on pp. 4, 22, 23).
- [15] F. Zwicky. Die Rotverschiebung von extragalaktischen Nebeln. *Helv. Phys. Acta* 6 (1933), pp. 110–127 (cit. on p. 5).
- [16] V. C. Rubin and W. K. Ford Jr. Rotation of the Andromeda nebula from a spectroscopic survey of emission regions. *Astrophys. J.* 159 (1970), pp. 379–403 (cit. on pp. 5, 6).
- [17] V. Rubin. Dark matter in spiral galaxies. *Sci. Am.* 248 (1983), pp. 9–106 (cit. on p. 6).
- [18] V. Rubin. A brief history of dark matter. *Dark Universe. Matter, Energy Gravity*. Ed. by M. Livio. Baltimore: Cambridge University Press, 2001, pp. 1–13 (cit. on p. 6).

REFERENCES

- [19] K. G. Begeman, A. H. Broeils, and R. H. Sanders. Extended rotation curves of spiral galaxies: dark haloes and modified dynamics. *Mon. Not. R. Astr. Soc.* 249 (Aug. 1991), pp. 523–537 (cit. on p. 7).
- [20] E. M. Burbidge et al. The Rotation and Mass of NGC 6503. *Astrophysical Journal* 139 (Feb. 1964), p. 539 (cit. on p. 7).
- [21] F. Iocco, M. Pato, and G. Bertone. Evidence for dark matter in the inner Milky Way. *Nature Physics* 11 (Feb. 2015), pp. 245–248 (cit. on p. 8).
- [22] M. Milgrom. A modification of the Newtonian dynamics as a possible alternative to the hidden mass hypothesis. *Astrophys. J.* 270 (1983), pp. 365–370 (cit. on p. 8).
- [23] A. Einstein. Die grundlage der allgemeinen relativitatstheorie. *Annalen der Physik* 354.7 (1999), pp. 769–822 (cit. on p. 9).
- [24] B. P. Abbott et al. Observation of gravitational waves from a binary black hole merger. *Phys. Rev. Lett.* 116.061102 (Jan. 2016), pp. 061102-1 —061102-16 (cit. on p. 9).
- [25] D. Walsh, R. F. Carswell, and R. J. Weymann. 0957+561 A, B: twin quasistellar objects or gravitational lens? *Nature* 279 (1979), pp. 381–384 (cit. on pp. 9, 10).
- [26] D. Wittman et al. Detection of weak gravitational lensing distortions of distant galaxies by cosmic dark matter at large scales. *Nature* 405 (May 2000), pp. 143–148 (cit. on p. 9).
- [27] T. Treu. Strong lensing by galaxies. *Annu. Rev. in Astron. Astrophys.* 48 (2010), pp. 87–125 (cit. on pp. 9, 10).
- [28] I. Morison. *The Night Sky January 2012*. University of Manchester, 2012 (cit. on p. 10).
- [29] R. Massey, T. Kitching, and J. Richard. The dark matter of gravitational lensing. *Rep. on Prog. in Phys.* 73 (2010), pp. 1–26 (cit. on pp. 10, 11).

REFERENCES

- [30] Y. Shu et al. The SLOAN lens ACS survey. XII. extending strong lensing to lower masses. *The Astrophy. Journ.* 803.71 (2015), pp. 1–17 (cit. on pp. [10](#), [11](#)).
- [31] D. Clowe et al. A direct empirical proof of the existence of dark matter. *Astrophys. J.* 648 (2006), pp. L109–L113 (cit. on p. [11](#)).
- [32] D. Clowe, A. Gonzalez, and M. Markevitch. Weak-lensing mass reconstruction of the interacting cluster 1E0657-558: direct evidence for the existence of dark matter. *Astrophys. J.* 604 (2004), pp. 596–603 (cit. on p. [11](#)).
- [33] M. Markevitch. Chandra Observation of the most interesting cluster in the universe (2005) (cit. on p. [11](#)).
- [34] M. Markevitch et al. Direct Constraints on the Dark Matter Self-Interaction Cross Section from Merging Galaxy Cluster IE 0657-56. *The Astrophysical Journal* 606.2 (2004), pp. 819–824 (cit. on pp. [11](#), [12](#)).
- [35] S. W. Randall and M. Markevitch. Constraints on the self-interaction cross section of dark matter from numerical simulations of the merging galaxy cluster 1E 0657–56. *Astrophys. J.* 679 (2008), p. 1173 (cit. on pp. [11](#), [12](#)).
- [36] L. J. King et al. The Distribution of Dark and Luminous Matter in the Unique Galaxy Cluster Merger Abell 2146. *Mon. Not. R. Astron. Soc.* 549 (2016), pp. 517–527 (cit. on p. [12](#)).
- [37] A. Robertson, R. Massey, and V. Eke. What does the Bullet Cluster tell us about Self-Interacting Dark Matter? (May 2016) (cit. on p. [12](#)).
- [38] K. Jedamzik and M. Pospelov. Big Bang nucleosynthesis and particle dark matter. *New Jour. of Phy.* 11.105028 (2009), pp. 21–20 (cit. on p. [13](#)).
- [39] R. H. Cyburt, B. D. Fields, and K. A. Olive. An update on the big bang nucleosynthesis prediction for ${}^7\text{Li}$: the problem worsens. *J. Cosmol. Astropart. Phys.* 2008.11 (Nov. 2008), p. 012 (cit. on p. [13](#)).

REFERENCES

- [40] R. H. Cyburt et al. Big bang nucleosynthesis: Present status. *Rev. Mod. Phys.* 88 (1 Feb. 2016), p. 015004 (cit. on p. 13).
- [41] R. Cooke. Big Bang Nucleosynthesis and the Helium Isotope Ratio. *Astrophys. Journ. Lett.* 812.L12 (2015), pp. 1–5 (cit. on p. 13).
- [42] E. W. Kolb and M. S. Turner. *The Early Universe*. Vol. 69. Front. Phys., 1994, pp. 1–547 (cit. on pp. 13, 22).
- [43] J. Chluba. Which spectral distortions does Λ CDM actually predict? *Mon. Not. R. Astron. Soc.* 460.1 (Apr. 2016), pp. 227–239 (cit. on p. 16).
- [44] R. Tojeiro. *Understanding the Cosmic Microwave Background Temperature Power Spectrum*. Lecture note. 2006 (cit. on p. 17).
- [45] A. Faessler et al. Search for the Cosmic Neutrino Background and KATRIN. *Rom. J. Phys.* 58.9-10 (2014), pp. 1221–1231 (cit. on p. 18).
- [46] G. Huang and S. Zhou. Discriminating between thermal and nonthermal cosmic relic neutrinos through an annual modulation at PTOLEMY. *Phys. Rev. D.* 94 (11 Dec. 2016), p. 116009 (cit. on p. 18).
- [47] G. Bertone. *Particle Dark matter: Observations, Models and Searches*. Cambridge University Press, 2010 (cit. on pp. 19, 20, 23, 178).
- [48] J. E. Kim and G. Carosi. Axions and the strong CP problem. *Rev. of Mod. Phys.* 82.1 (Mar. 2010), pp. 557–601 (cit. on pp. 19, 22, 23).
- [49] N. J. C. Spooner. *PHY326/426: Dark Matter and the Universe*. Lecture note series. Sheffield, 2016 (cit. on pp. 19, 20, 23).
- [50] L. Baudis. Dark Matter Searches. *Ann. Phys.* 528.1—2 (Jan. 2016), pp. 74–83 (cit. on pp. 19, 22, 23).

REFERENCES

- [51] T. Baldauf et al. LSS Constraints with controlled theoretical uncertainties. *ArXiv preprint arXiv:1602.00674* (2016) (cit. on p. 19).
- [52] V. Springel, C. S. Frenk, and S. D. M. White. The large-scale structure of the Universe. *Nature* 440.7088 (Apr. 2006), pp. 1137–1144 (cit. on p. 19).
- [53] J. M. Kubo et al. Dark matter structures in the Deep Lens Survey. *Astrophys. J.* 702.2 (Sept. 2009), pp. 980–988 (cit. on p. 19).
- [54] G. Jungman, M. Kamionkowski, and K. Griest. Supersymmetric dark matter. *Phys. Rep.* 267 (1996), pp. 195–373 (cit. on pp. 20, 21, 37).
- [55] G. Steigman, B. Dasgupta, and J. F. Beacom. Precise relic WIMP abundance and its impact on searches for dark matter annihilation. *Phys. Rev. D* 86 (2 July 2012), p. 023506 (cit. on p. 20).
- [56] G. Steigman and M. S. Turner. Cosmological constraints on the properties of weakly interacting massive particles. *Nuclear Physics B* 253 (1985), pp. 277–281 (cit. on p. 20).
- [57] L. Bergstrom. Dark matter candidates. *New J. Phys.* 11.10 (Oct. 2009), p. 105006 (cit. on p. 22).
- [58] L. Bergstrom and A. Goobar. *Cosmology and Particle Astrophysics*. 2nd ed. Stockholm: Springer, 2008 (cit. on p. 22).
- [59] Atlas Collaboration. *Searches for new phenomena in the $Z(\rightarrow \ell\ell) + E_T^{\text{miss}}$ final state at $\sqrt{s} = 13 \text{ TeV}$ with the ATLAS detector*. Tech. rep. ATLAS-CONF-2016-056. Geneva, Aug. 2016 (cit. on p. 22).
- [60] D. N. Spergel. Motion of the Earth and the detection of weakly interacting massive particles. *Phys. Rev. D.* 37 (6 Mar. 1988), pp. 1353–1355 (cit. on pp. 22, 46).

REFERENCES

- [61] M. O. Tahim and C. A. S. Almeida. Gauge hierarchy from a topological viewpoint? *Phys. Lett. B* 600 (2004), pp. 151–156 (cit. on p. 22).
- [62] M. Holthausen, K. S. Lim, and M. Lindner. Planck scale boundary conditions and the Higgs mass. *J. of High Energy Phys.* 2012.2 (2012), p. 37 (cit. on p. 22).
- [63] R. Peccei and H. Quinn. Constraints imposed by CP conservation in the presence of pseudoparticles. *Phys. Rev. D* 16.6 (May 1977), pp. 1791–1797 (cit. on p. 22).
- [64] L. Covi. Gravitino Dark Matter confronts LHC. *Jour. of Phys.: Conf. Series* 485.012002 (2014) (cit. on p. 23).
- [65] D. Bauer et al. Dark matter in the coming decade: Complementary paths to discovery and beyond. *Physics of the Dark Universe* 7–8 (Sept. 2015), pp. 16–23 (cit. on p. 23).
- [66] J. Hisano, S. Matsumoto, and M. Nojiri. Explosive dark matter annihilation. *Phys. Rev. Lett.* 92.3 (Jan. 2004), p. 031303 (cit. on p. 25).
- [67] A. Ibarra. Neutrino bounds on dark matter. *Nucl. Phys. B - Proc. Suppl.* 237–238 (Apr. 2013), pp. 242–245 (cit. on p. 25).
- [68] D. N. Spergel and P. J. Steinhardt. Observational evidence for self-interacting cold dark matter. *Phys. Rev. Lett.* 84.17 (Apr. 2000), pp. 3760–3763 (cit. on p. 25).
- [69] C. Weniger. A tentative gamma-ray line from dark matter annihilation at the Fermi Large Area Telescope. *J. Cosmol. Astropart. Phys.* 2012 (Aug. 2012), p. 007 (cit. on p. 25).
- [70] J. Buckley et al. Working Group Report: WIMP Dark Matter Indirect Detection. *Proceedings, Community Summer Study 2013: Snowmass on the Mississippi (CSS2013): Minneapolis, MN, USA, July 29-August 6, 2013.* 2013 (cit. on p. 25).
- [71] M. Klasen, M. Pohl, and G. Sigl. Indirect and direct search for dark matter. *Prog. in Part. and Nucl. Phys.* 85 (2015), pp. 1–32 (cit. on p. 25).

REFERENCES

- [72] D. Hooper, C. Kelso, and F. Queiroz. Stringent constraints on the dark matter annihilation cross section from the region of the Galactic Center. *Astroparticle Physics* 46 (2013), pp. 55–70 (cit. on p. 25).
- [73] M. L. Ahnen et al. Limits to dark matter annihilation cross-section from a combined analysis of MAGIC and Fermi-LAT observations of dwarf satellite galaxies. *J. Cosmol. Astropart. Phys.* 2016.02 (2016), p. 039 (cit. on pp. 25, 26).
- [74] M. G. Aartsen et al. Search for dark matter annihilations in the sun with the 79-string IceCube detector. *Phys. Rev. Lett.* 110.0031-9007 (Mar. 2013), p. 131302 (cit. on p. 25).
- [75] M. G. Aartsen et al. Improved limits on dark matter annihilation in the sun with the 79-string detector and implications for supersymmetry. *J. Cosmol. Astropart. Phys.* 022.04 (Mar. 2016) (cit. on p. 25).
- [76] S. Y. Hoh, J. R. Komaragiri, and W. A. T. Wan Abdullah. Dark matter searches at the Large Hadron Collider. *AIP Conf. Proc.* 1704 (2016), p. 020005 (cit. on p. 26).
- [77] A. Barr et al. *Searches for Supersymmetry at the high luminosity LHC with the ATLAS detector*. Tech. rep. Geneva: CERN, 2013, pp. –17 (cit. on p. 26).
- [78] O. Buchmueller, M. J. Dolan, and C. McCabe. Beyond effective field theory for dark matter searches at the LHC. *J. High Energy Phys.* 2014.1 (2014) (cit. on p. 26).
- [79] G. Aad et al. Search for dark matter candidates and large extra dimensions in events with a jet and missing transverse momentum with the ATLAS detector. *J. of High Energy Phys.* 2013.4 (Apr. 2013), p. 75 (cit. on p. 26).
- [80] A. Askew et al. Searching for Dark Matter at Hadron Colliders. *Int. J. Mod. Phys.* A29 (23 Sept. 2014), p. 1430041 (cit. on p. 26).
- [81] J. Abdallah et al. Simplified models for dark matter searches at the LHC. *Physics of the Dark Universe* 9-19 (Dec. 2015), pp. 8–23 (cit. on p. 26).

REFERENCES

- [82] G. Aad et al. Search for new phenomena in final states with an energetic jet and large missing transverse momentum in pp collisions at $\sqrt{s} = 8$ TeV with the ATLAS detector. *The European Physical Journal C* 75.7 (Apr. 2015), p. 299 (cit. on p. 26).
- [83] M. Schumann. Dark Matter 2014. *EDP sciences* 01027.96 (2015) (cit. on p. 27).
- [84] J. D. Lewin and P. Smith. Review of mathematics, numerical factors, and corrections for dark matter experiments based on elastic nuclear recoil. *Astroparticle Physics* 6.96 (1996), pp. 87–112 (cit. on pp. 27–30, 32–35).
- [85] D. R. Tovey et al. A new model-independent method for extracting spin-dependent cross section limits from dark matter searches. *Phys. Lett. B* 488 (2000), pp. 17–26 (cit. on pp. 27, 37).
- [86] E. Daw. A review of the theory of WIMP scattering off target nuclei. *Priv. Commun.* (2011) (cit. on pp. 28–30, 32).
- [87] S. Sadler. Towards the DRIFT-III Directional Dark Matter Experiment. PhD thesis. Sheffield: University of Sheffield, 2015 (cit. on pp. 30, 32, 99, 127, 153, 157).
- [88] M. Pipe. Limits on Spin-Dependent WIMP-Proton Cross-Sections using the DRIFT-IIId Directional Dark Matter Detector. PhD thesis. University of Sheffield, 2011 (cit. on p. 30).
- [89] B. J. Kavanagh and A. M. Green. Model Independent Determination of the Dark Matter Mass from Direct Detection Experiments. *Phys. Rev. Lett.* 111.11 (3 July 2013), p. 031302 (cit. on p. 32).
- [90] B. J. Kavanagh. Discretising the velocity distribution for directional dark matter experiments. *J. Cosmol. Astropart. Phys.* 111.07 (July 2015), p. 019 (cit. on p. 32).
- [91] J. Engel. Nuclear form factors for the scattering of neutralinos. *Nuclear Physics B - Proceedings Supplements* 28.1 (1992), pp. 310–313 (cit. on pp. 35, 36).

REFERENCES

- [92] J. Engel, S. Pittel, and P. Vogel. Nuclear Physics of dark matter detection. *Int. J. Mod. Phys. E* 1.1 (1992), pp. 1–37 (cit. on pp. [35](#), [36](#)).
- [93] J. Engel and P. Vogel. Spin-dependent cross sections of weakly interacting massive particles on nuclei. *Phys. Rev. D* 40.1 (9 Nov. 1989), pp. 3132–3135 (cit. on p. [35](#)).
- [94] J. Engel. Nuclear form factors for the scattering of weakly interacting massive particles. *Phys. Lett. B* 264.1 (1991), pp. 114–119 (cit. on p. [36](#)).
- [95] V. I. Dimitrov, J. Engel, and S. Pittel. Scattering of weakly interacting massive particles from ^{73}Ge . *Phys. Rev. D* 51 (2 Jan. 1995), R291–R295 (cit. on p. [36](#)).
- [96] J. Menéndez, D. Gazit, and A. Schwenk. Spin-dependent WIMP scattering off nuclei. *Phys. Rev. D* 86 (10 Nov. 2012), p. 103511 (cit. on p. [36](#)).
- [97] F. Mayet et al. A review of the discovery reach of directional Dark Matter detection. *Phys. Rep.* 627 (2016), pp. 1–49 (cit. on pp. [36](#), [48](#), [60](#), [75](#), [178](#)).
- [98] E. Daw et al. Spin-dependent limits from the DRIFT-II_d directional dark matter detector. *Astroparticle Physics* 35.7 (2012), pp. 397–401 (cit. on pp. [37](#), [65](#)).
- [99] D. R. Tovey. A study of pulse shape discrimination in scintillator dark matter detectors. PhD thesis. Sheffield: University of Sheffield, 1998 (cit. on p. [37](#)).
- [100] D. Chitwood et al. Improved measurement of the positive-muon lifetime and determination of the Fermi constant. *Phys. Rev. Lett.* 99.3 (July 2007), p. 032001 (cit. on p. [37](#)).
- [101] W. R. Leo. *Techniques for Nuclear and Particle Physics Experiments: A How-to Approach*. 2nd ed. Springer-Verlag, 1987 (cit. on p. [40](#)).
- [102] S. N. Ahmed. *Physics and Engineering of Radiation Detection*. 1st ed. Elsevier, 2007 (cit. on p. [40](#)).

REFERENCES

- [103] D.-M. Mei and A. Hime. Muon-induced background study for underground laboratories. *Phys. Rev. D* 73 (5 Mar. 2006), p. 053004 (cit. on pp. [41](#), [42](#)).
- [104] M. Robinson et al. Measurements of muon flux at 1070 m vertical depth in the Boulby underground laboratory. *Nucl. Inst. and Meth. in Phys. Res. Sect. A: Accel., Spectrometers, Detect. and Assoc. Equip.* 511.3 (Oct. 2003), pp. 347–353 (cit. on pp. [41](#), [42](#)).
- [105] V. A. Kudryavtsev, N. J. C. Spooner, and J. E. McMillan. Simulations of muon induced neutron flux at large depths underground. *Nucl. Instrum. Meth. A* 505.2 (2003), pp. 688–698 (cit. on p. [41](#)).
- [106] L. Liu and P. Solis. The Speed and Lifetime of Cosmic Ray Muons (Nov. 2007) (cit. on p. [41](#)).
- [107] V. A. Kudryavtsev. Muon simulation codes MUSIC and MUSUN for underground physics. *Computer Physics Communications* 180.3 (2009), pp. 339–346 (cit. on p. [41](#)).
- [108] G. Remmen and E. McCreary. Measurement of the Speed and Energy Distribution of Cosmic Ray Muons. *Journal of Undergraduate Research in Physics* (Feb. 2012), pp. 1–8 (cit. on p. [41](#)).
- [109] T. Marrodan Undagoitia and L. Rauch. Dark matter direct-detection experiments. *J. Phys. G* 43.1 (2016), p. 013001 (cit. on pp. [41](#), [42](#)).
- [110] J. B. R. Battat et al. Radon in the DRIFT-II directional dark matter TPC: emanation, detection and mitigation. *JINST* 9.11 (2014), P11004 (cit. on pp. [42](#), [43](#), [136](#), [141](#)).
- [111] J. B. R. Battat et al. Long-term study of backgrounds in the DRIFT-II directional dark matter experiment. *JINST* 9 (2014), P07021 (cit. on pp. [42](#), [43](#), [136](#), [141](#)).
- [112] J. B. R. Battat et al. Reducing DRIFT backgrounds with a submicron aluminized-mylar cathode. *Nucl. Inst. and Meth. in Phys. Res. A: Accel., Spectrometers, Detect. and Assoc. Equip.* 794.11 (Sept. 2015), pp. 33–46 (cit. on pp. [42](#), [65](#), [136](#), [141](#), [142](#), [182](#), [183](#), [204](#)).

REFERENCES

- [113] J. B. R. Battat et al. First background free limit from a directional dark matter experiment: results from a fully fiducialised DRIFT detector. *Physics of the Dark Universe* 9–10 (2015), pp. 1–7 (cit. on pp. [42](#), [43](#), [48](#), [60](#), [65](#), [66](#), [69](#), [135](#), [141](#), [185](#), [186](#), [197](#), [209](#)).
- [114] G. Angloher et al. Limits on WIMP dark matter using sapphire cryogenic detector. *Astroparticle Physics* 18 (Apr. 2002), pp. 43–55 (cit. on p. [43](#)).
- [115] J. Cherwinka et al. First data from DM-Ice17. *Phys. Rev. D* 90.092005 (2014) (cit. on pp. [43](#), [56](#)).
- [116] R. Bernabei et al. Investigating Earth shadowing effect with DAMA/LIBRA-phase1. *The European Physical Journal C* 75.239 (May 2015), pp. 138–146 (cit. on p. [43](#)).
- [117] R. Agnese et al. Silicon detector dark matter results from the final exposure of CDMS II. *Phys. Rev. Lett.* 111.25 (Dec. 2013), p. 251301 (cit. on pp. [43](#), [45](#), [48](#), [55](#), [56](#)).
- [118] D. S. Akerib et al. Improved limits on scattering limitsof Weakly Interacting Massive Particles from Reanalysis of 2013 LUX data. *Phys. Rev. Lett.* 116.161301 (2016) (cit. on pp. [43](#), [48–51](#), [59](#)).
- [119] G. Angloher et al. Results on light dark matter particles with a low-threshold CRESST-II detector. *The European Physical Journal C* 76.1 (2016), pp. 1–8 (cit. on pp. [43](#), [53](#), [54](#)).
- [120] S. H. Morgan and P. B. Eby. Corrections to the Bethe-Bloch formula for average ionization energy loss of relativistic heavy nuclei Close collisions. *Nucl. Inst. and Meth.* 106.3 (May 1973), pp. 429–435 (cit. on pp. [44](#), [102](#)).
- [121] J. Mompert et al. Calculation of range and energy loss of fast ions with $Z \geq 30$ using a corrected Bethe-Bloch formula. *Nucl. Inst. and Meth. in Phys. Res. Sect. B: Beam Interactions with Materials and Atoms* 107.1–4 (1996), pp. 56–61 (cit. on pp. [44](#), [102](#)).

REFERENCES

- [122] B. Morgan. Dark Matter Detection with Gas Time Projection Chambers. PhD thesis. Sheffield, United Kingdom: University of Sheffield, 2004 (cit. on pp. 45–47).
- [123] R. Bernabei et al. The Annual Modulation Signature for Dark Matter: DAMA/LIBRA-Phase1 Results and Perspectives. *Adv. High Energy Phys.* 2014 (2014), p. 605659 (cit. on pp. 45, 56).
- [124] R. Bernabei et al. Final model independent result of DAMA/LIBRA–phase1. *The European Physical Journal C* 73.12 (Dec. 2013), pp. 1–11 (cit. on pp. 45, 56, 58).
- [125] C. E. Aalseth et al. Results from a search for light-mass dark matter with a p-type point contact germanium detector. *Phys. Rev. Lett.* 106.13 (Mar. 2011), p. 131301 (cit. on p. 45).
- [126] J. Klinger and V. A. Kudryavtsev. Muon-induced neutrons do not explain the DAMA data. *Phys. Rev. Lett.* 114.151301 (2015), pp. 151301-1—151301-5 (cit. on pp. 45, 46, 59).
- [127] G. Angloher et al. Results from 730 kg days of the CRESST-II dark matter search. *The European Physical Journal C* 72.4 (Apr. 2012), p. 1971 (cit. on pp. 45, 54).
- [128] V. A. Kudryavtsev, M. Robinson, and N. J. C. Spooner. The expected background spectrum in NaI dark matter detectors and the DAMA result. *Astroparticle Physics* 33 (2 2010), pp. 91–96 (cit. on p. 46).
- [129] J. H. Davis. Fitting the annual modulation in DAMA with neutrons from muons and neutrinos. *Phys. Rev. Lett.* (Aug. 2014), p. 081302 (cit. on pp. 46, 59).
- [130] C. J. Copi and L. M. Krauss. Angular signatures for galactic halo weakly interacting massive particle scattering in direct detectors: prospects and challenges. *Phys. Rev. D.* 63.043507 (2001), pp. 043507-1–043507-13 (cit. on pp. 46, 47).
- [131] C. A. J. O’Hare. Dark matter astrophysical uncertainties and the neutrino floor. *Phys. Rev. D* 94.063527 (6 Sept. 2016), pp. 063527-1—063527-16 (cit. on p. 47).

REFERENCES

- [132] J. Va’vra. A new possible way to explain the DAMA results. *Phys. Lett. B* 735 (2014), pp. 181–185 (cit. on p. 47).
- [133] K. Abe et al. Solar neutrino measurements in Super-Kamiokande-IV. *Phys. Rev. D* 94 (5 Sept. 2016), p. 052010 (cit. on p. 47).
- [134] T. Kajita. Atmospheric neutrinos and discovery of neutrino oscillations. *Proceedings of the Japan Academy Series B, Physical and Biological Sciences*. Vol. 86. Apr. 2010, pp. 303–321 (cit. on p. 47).
- [135] J. F. Beacom. The Diffuse Supernova Neutrino Background. *Annual Review of Nuclear and Particle Science* 60.1 (2010), pp. 439–462 (cit. on p. 47).
- [136] R. Harnik, J. Kopp, and P. A. Machado. Exploring ν signals in dark matter detector. *J. of Cosmol Astropart. Phys.* 377.07 (2012), p. 026 (cit. on p. 47).
- [137] J. Kopp. New signals in dark matter detectors. *Journal of Physics: Conference Series* 485.1 (2014), p. 012032 (cit. on p. 47).
- [138] C. A. J. O’Hare et al. Readout strategies for directional dark matter detection beyond the neutrino background. *Phys. Rev. D* 92.063518 (Sept. 2015), pp. 063518-1—063518-16 (cit. on p. 48).
- [139] C. J. Copi, J. Heob, and L. M. Krauss. Directional sensitivity, WIMP detection, and the galactic halo. *Phys. Rev. B.* 461 (1-2 1999), pp. 43–48 (cit. on pp. 48, 126).
- [140] A. Green and B. Morgan. Optimizing WIMP directional detectors. *Astroparticle Physics* 27.2-3 (Mar. 2007), pp. 142–149 (cit. on pp. 48, 126).
- [141] S. Ahlen et al. The Case for a Directional Dark Matter Detector and the Status of Current Experimental Efforts. *Int. J. Mod. Phys. A* 25.01 (2010), pp. 1–51 (cit. on pp. 48, 75).

REFERENCES

- [142] R. Bernabei et al. Final Model Independent Results of DAMA/LIBRA-Phase1 and Prospectives of Phase2. *Physics of Particles and Nuclei* 46.2 (Mar. 2015), pp. 138–146 (cit. on pp. [48](#), [56](#), [58](#), [59](#)).
- [143] F. Ruppin et al. Complementarity of dark matter detectors in light of the neutrino background. *Phys. Rev. D* 90.3 (8 Oct. 2014), p. 083510 (cit. on p. [48](#)).
- [144] K. Nakamura et al. Direction-sensitive dark matter search with gaseous tracking detector NEWAGE-0.3b. *Prog. Theor. Exp. Phys.* 043F01 (Apr. 2015) (cit. on pp. [48](#), [60–62](#), [147](#), [185](#), [186](#), [197](#), [209](#)).
- [145] S. E. Vahsen et al. 3-D tracking in a miniature time projection chamber. *Nucl. Inst. and Meth. in Phys. Res. Sect. A: Accel., Spectrometers, Detect. and Assoc. Equip.* 788 (2015), pp. 95–105 (cit. on pp. [48](#), [70](#), [71](#)).
- [146] P. Grothaus, M. Fairbairn, and J. Monroe. Directional dark matter detection beyond the neutrino bound. *Phys. Rev. D* 90.055018 (Sept. 2014), pp. 055018-1–055018-15 (cit. on pp. [48](#), [75](#)).
- [147] J. Billard et al. Directional detection as a strategy to discover Galactic dark matter. *Phys. Lett. B* 691.3 (July 2010), pp. 156–162 (cit. on p. [48](#)).
- [148] D. S. Akerib et al. The large Underground Xenon (LUX) experiment. *Nucl. Instr. and Meth. in Phys. Res. A* 704 (2013), pp. 111–126 (cit. on p. [49](#)).
- [149] D. S. Akerib et al. First results from the LUX dark matter experiment at the Sanford Underground Research Facility. *Phys. Rev. Lett.* 112.091303 (2014) (cit. on p. [49](#)).
- [150] D. S. Akerib et al. Results on the spin-dependent scattering of Weakly Interacting Massive Particles on Nucleons from the run 3 data of the LUX experiment. *Phys. Rev. Lett.* 116.161302 (2016) (cit. on pp. [50](#), [51](#)).
- [151] D. S. Akerib et al. Results from a search for dark matter in LUX with 332 live days of exposure. *Preprint: 1608.07648* (2016) (cit. on pp. [50](#), [51](#)).

REFERENCES

- [152] O. Buchmueller et al. Characterising dark matter searches at colliders and direct detection experiments: vector mediators. *J. High Energy Phys.* 2015.1 (2015), p. 37 (cit. on p. 50).
- [153] S. A. Malik et al. Interplay and characterization of Dark Matter searches at colliders and in direct detection experiments. *Physics of the Dark Universe* 9-10 (2015), pp. 51–58 (cit. on p. 50).
- [154] J. Ellis and K. A. Olive. Revisiting the Higgs mass and dark matter in the CMSSM. *The European Physical Journal C* 72.5 (2005), p. 2005 (cit. on p. 50).
- [155] D. S. Akerib et al. LUX-ZEPLIN (LZ) Conceptual Design Report. *Preprint: arXiv1509.02910* (2015) (cit. on p. 52).
- [156] S. Archambault et al. Searching for Dark Matter with PICASSO. *Phys. Procedia* 61 (2015), pp. 107–111 (cit. on p. 52).
- [157] C. Amole et al. Dark Matter Search Results from the PICO-2L C₃F₈ Bubble Chamber. *Phys. Rev. Lett.* 114.23 (2015), p. 231302 (cit. on pp. 52, 53, 185, 186, 197, 209).
- [158] E. Behnke et al. First dark matter search results from a 4-kg CF₃I bubble chamber operated in a deep underground site. *Phys. Rev. D* 86.5 (2012), p. 052001 (cit. on p. 52).
- [159] E. Behnke et al. Improved Limits on Spin-Dependent WIMP-Proton Interactions from a Two Liter CF₃I Bubble Chamber. *Phys. Rev. Lett.* 106 (2011), p. 021303 (cit. on p. 53).
- [160] G. Angloher et al. EURECA Conceptual Design Report. *Physics of the Dark Universe* 3 (2014), pp. 41–74 (cit. on pp. 54, 55).
- [161] G. Angloher et al. Results on low mass WIMPs using an upgraded CRESST-II detector. *The European Physical Journal C* 74.12 (2014), pp. 1–6 (cit. on pp. 53, 54).

REFERENCES

- [162] M. Kiefer et al. In-situ study of light production and transport in phonon/light detector modules for dark matter search. *Nucl. Inst. and Meth. in Physics Res. Sect. A: Accel., Spectrometers, Detect. and Assoc. Equip.* 821 (2016), pp. 116–121 (cit. on p. 53).
- [163] R. Agnese et al. Improved WIMP-search reach of the CDMS II germanium data. *Phys. Rev. D* 92 (Oct. 2015), p. 072003 (cit. on pp. 55, 56).
- [164] K. van Bibber. Viewpoint: Scaling up the search for dark matter. *Physics 2.2* (Jan. 2009) (cit. on p. 55).
- [165] R. Agnese et al. Maximum likelihood analysis of low energy CDMS II germanium data. *Phys. Rev. D* 91 (Dec. 2015), p. 052021 (cit. on p. 55).
- [166] P. Fulde. Cooper pair breaking. *Mod. Phys. Lett. B* 24.26 (2010), pp. 2601–2624 (cit. on p. 55).
- [167] Y. G. Zhao et al. Optical Cooper pair breaking spectroscopy of cuprate superconductors. *Phys. Rev. B* 63 (13 Mar. 2001), p. 132507 (cit. on p. 55).
- [168] R. Bernabei et al. Searching for WIMPs by the annual modulation signature. *Phys. Lett. B* 424 (1998), pp. 195–201 (cit. on pp. 56, 58).
- [169] R. Bernabei et al. New results from DAMA/LIBRA. *The European Physical Journal C* 67 (Mar. 2010), pp. 39–49 (cit. on p. 56).
- [170] J. Cherwinka et al. A search for the dark matter annual modulation in South Pole ice. *Astroparticle Physics* 35 (June 2012), pp. 749–754 (cit. on pp. 56, 57).
- [171] J. Cherwinka et al. Measurement of Muon Annual Modulation and Muon-Induced Phosphorescence in NaI(Tl) Crystals with DM-Ice17. *Phys. Rev. D* 93.042001 (2016) (cit. on pp. 56, 57).

REFERENCES

- [172] E. Barbosa de Souza et al. First Search for a Dark Matter Annual Modulation Signal with NaI(Tl) in the Southern Hemisphere by DM-Ice17. *Preprint: arXiv1602.05939v2* (2016) (cit. on pp. [56–58](#)).
- [173] H. S. Lee et al. Search for low-mass dark matter with CsI(Tl) crystal detectors. *Phys. Rev. D* 502 (Sept. 2014), p. 052006 (cit. on p. [57](#)).
- [174] J. Amaré et al. The ANAIS Dark Matter Project: Status and Prospects. *14th Marcel Grossmann Meeting on Recent Developments in Theoretical and Experimental General Relativity, Astrophysics, and Relativistic Field Theories (MG14) Rome, Italy, July 12-18, 2015*. Vol. 39. May 2016 (cit. on p. [58](#)).
- [175] E. Shields, J. Xu, and F. Calaprice. SABRE: A New NaI(Tl) Dark Matter Direct Detection Experiment. *Physics Procedia* 61.1 (Mar. 2015). 13th International Conference on Topics in Astroparticle and Underground Physics, TAUP 2013, pp. 169–178 (cit. on p. [58](#)).
- [176] K. Miuchi et al. First underground results with NEWAGE-0.3a direction-sensitive dark matter detector. *Phys. Lett. B* 686 (2010), pp. 11–17 (cit. on pp. [60–62](#)).
- [177] S. Ahlen et al. First dark matter search results from a surface run of the 10-L DMTPC directional dark matter detector. *Phys. Lett. B* 695 (2011), pp. 124–129 (cit. on pp. [60](#), [62](#), [63](#), [185](#), [197](#), [209](#)).
- [178] D. Santos et al. MIMAC: A micro-TPC matrix for directional detection of dark matter. *Journal of Physics: Conference Series* 309 (Aug. 2011), p. 012014 (cit. on pp. [60](#), [64](#)).
- [179] F. Sauli. The gas electron multiplier (GEM): Operating principles and application. *Nucl. Inst. and Meth. in Phys. Res. Sect. A: Accel., Spectrometers, Detect. and Assoc. Equip.* 805 (Aug. 2016). Special Issue in memory of Glenn F. Knoll, pp. 2–24 (cit. on pp. [60](#), [103](#)).

REFERENCES

- [180] K. Nakamura et al. Low pressure gas study for a direction-sensitive dark matter search experiment with MPGD. *JINST* 7 (Feb. 2012), p. C02023 (cit. on p. 60).
- [181] K. Nakamura et al. Newage. *Journal of Physics: Conference Series* 375.1 (July 2012), p. 012013 (cit. on p. 60).
- [182] C. Deaconu et al. Track Reconstruction Progress from the DMTPC Directional Dark Matter Experiment. *Phys. Procedia* 61 (2015), pp. 39–44 (cit. on p. 63).
- [183] J. P. Lopez et al. Background rejection in the (DMTPC) dark matter search using charge signals. *Nucl. Inst. and Meth. in Phys. Res. Sect. A: Accel., Spectrometers, Detect. and Assoc. Equip.* 696 (2012), pp. 121–128 (cit. on pp. 62, 63).
- [184] M. Leyton. Directional dark matter detection with DMTPC m³ experiment. *Proceedings of the 14th International Conference on Topics in Astroparticle and Underground Physics (TAUP) 2015 edition. Journal of Physics: Conference Series*. Vol. 718. 2016, p. 042035 (cit. on p. 63).
- [185] J. B. Battat et al. The Dark Matter Time Projection Chamber 4-Shooter directional dark matter detector: Calibration in a surface laboratory. *Nucl. Inst. and Meth. in Phys. Res. Sect. A: Accel., Spectrometers, Detect. and Assoc. Equip* 755 (2014), pp. 6–19 (cit. on p. 63).
- [186] Q. Riffard et al. Dark Matter directional detection with MIMAC. *Proceedings, 48th Rencontres de Moriond on Very High Energy Phenomena in the Universe*. arXiv Prepr. arXiv1306.4173. 2013, pp. 227–23 (cit. on pp. 64, 65).
- [187] J. Billard et al. In situ measurement of the electron drift velocity for upcoming directional dark matter detectors. *JINST* 9.P01013 (2014) (cit. on p. 64).
- [188] F. Iguaz et al. New Developments in Micromegas Microbulk Detectors. *Physics Procedia* 237–238 (2012), pp. 448–455 (cit. on p. 64).

REFERENCES

- [189] P. Abbon et al. The Micromegas detector of the CAST experiment. *New Journal of Physics* 9.6 (June 2007), p. 170 (cit. on p. [64](#)).
- [190] D. Santos et al. MIMAC: A micro-TPC matrix for directional detection of dark matter. *PoS IDM2010* (Aug. 2011), p. 012014 (cit. on pp. [64](#), [65](#)).
- [191] S. M. Paling and A. S. J. Murphy. The Boulby Mine Underground Science Facility: the search for dark matter, and beyond. *Nucl. Phys. News* 22.1 (2012) (cit. on p. [65](#)).
- [192] G. Alner et al. The DRIFT-II dark matter detector: design and commissioning. *Nucl. Inst. and Meth. in Phys. Res. Sect. A: Accel., Spectrometers, Detect. and Assoc. Equip.* 555.1-2 (Dec. 2005), pp. 173–183 (cit. on pp. [65](#), [76](#), [103](#)).
- [193] E. H. Miller. Mitigating Backgrounds with a Novel Thin-Film Cathode in the DRIFT-II Dark Matter Detector. PhD thesis. Albuquerque, New Mexico: University of New Mexico, 2015 (cit. on pp. [65](#), [157](#)).
- [194] F. Bloch and N. E. Bradbury. On the Mechanism of Unimolecular Electron Capture. *Phys. Rev.* 48 (8 Oct. 1935), pp. 689–695 (cit. on pp. [66](#), [128](#)).
- [195] H. Shimamori and Y. Hatano. Thermal electron attachment to O₂ in the presence of various compounds as studied by a microwave cavity technique combined with pulse radiolysis. *Chemical Physics* 21.2 (Apr. 1977), pp. 187–201 (cit. on pp. [66](#), [128](#)).
- [196] N. L. Aleksandrov. Three-body electron attachment to a molecule. *Usp. Fiz. Nauk* 154 (1988), pp. 177–206 (cit. on pp. [66](#), [128](#)).
- [197] H. Shimamori and Y. Hatano. Mechanism of thermal electron attachment in O₂N₂ mixtures. *Chemical Physics* 12.4 (1976), pp. 439–445 (cit. on pp. [66](#), [128](#)).
- [198] Y.-i. Kokaku et al. Mechanism of thermal electron attachment in O₂-C₂H₄, O₂-CO₂, and O₂-neopentane mixtures. *The Journal of Chemistry Physics* 71.12 (1979), pp. 4883–4887 (cit. on pp. [66](#), [128](#)).

REFERENCES

- [199] D. Snowden-Ifft. Discovery of multiple, ionization-created by CS₂ anions and new mode of operation for drift chambers. *Rev. of Sci. Instrum.* 85.013303 (Jan. 2014) (cit. on pp. [66](#), [137](#), [140](#)).
- [200] F. Sauli. *Principles of operation of multiwire proportional and drift chambers*. Tech. rep. 09. Geneva: CERN, 1977 (cit. on pp. [67](#), [73](#)).
- [201] G. Charpak and F. Sauli. Multiwire proportional chambers and drift chambers. *Nucl. Inst. Meth.* 162 (Mar. 1979), pp. 405–428 (cit. on pp. [67](#), [73](#)).
- [202] Cremat. *CR-111 charge sensitive preamplifier: application guide*. Technical Datasheet. 2014 (cit. on pp. [67](#), [90](#), [92](#)).
- [203] Cremat. *CR-200 Gaussian Shaping Amplifier*. Technical Datasheet. 2014 (cit. on pp. [67](#), [91](#)).
- [204] S. E. Vahsen et al. The directional dark matter detector (D³). *EAS Pub. Ser.* 43 (2012), pp. 43–50 (cit. on p. [70](#)).
- [205] E. Baracchini. NITEC: a Negative Ion Time Expansion Chamber for directional dark matter searches. *Talk presented during the 5th Workshop on Directional Detection of Dark Matter (CYGNUS2015), Los Angeles, USA*. 2015 (cit. on pp. [70](#), [71](#)).
- [206] G. Aad et al. ATLAS pixel detector electronics and sensors. *JINST* 3.07 (Sept. 2008), P07007 (cit. on p. [70](#)).
- [207] D. Nygren. Columnar recombination: a tool for nuclear recoil directional sensitivity in a xenon-based direct detection WIMP search. *Journal of Physics: Conference Series* 460 (2013), p. 012006 (cit. on p. [71](#)).
- [208] J. Li. Directional dark matter by polar angle direct detection and application of columnar recombination. *Phys. Rev. D* 92.10 (4 Aug. 2015), p. 043523 (cit. on p. [71](#)).

REFERENCES

- [209] G. Mohlabeng et al. Dark matter directionality revisited with a high pressure xenon gas detector. *J. of High Energy Phys.* 2015.7 (2015), pp. 1–20 (cit. on p. 71).
- [210] H. Cao et al. Measurement of scintillation and ionization yield and scintillation pulse shape from nuclear recoils in liquid argon. *Phys. Rev. D* 91 (6 May 2015), p. 092007 (cit. on p. 71).
- [211] M. Rescigno. *Recoil Directionality Studies in Two-Phase Liquid Argon TPC Detectors*. Talk presented at the 11th conference on Identification of Dark Matter (IDM2016). Sheffield, 2016 (cit. on p. 71).
- [212] T. Franarin and M. Fairbairn. Reducing the solar neutrino background in dark matter searches using polarized helium-3. *Phys. Rev. D* 94 (5 Sept. 2016), p. 053004 (cit. on p. 71).
- [213] T. Katsuragawa et al. Status and analysis system of directional dark matter search with nuclear emulsion. *CYGNUS 2013: 4th Workshop on Directional Detection of Dark Matter. Journal of Physics: Conference Series*. 469. 2013, p. 012004 (cit. on p. 71).
- [214] N. D’Ambrosio et al. Nuclear emulsions as a very high high resolution detector for directional dark matter search. *JINST* 9.C01043 (2014), pp. 173–194 (cit. on p. 71).
- [215] T. Asada et al. Detector developing for directional dark matter search with nuclear emulsion. *CYGNUS 2013: 4th Workshop on Directional Detection of Dark Matter. Journal of Physics: Conference Series*. 469. 2013, p. 012010 (cit. on p. 71).
- [216] L. Capparelli et al. Directional dark matter searches with carbon nanotubes. *Physics of the Dark Universe* 9-10.6 (Feb. 2015), pp. 24–30 (cit. on p. 72).
- [217] F. Cappella et al. On the potentiality of the ZnWO₄ anisotropic detectors to measure the directionality of Dark Matter. *The European Physical Journal C* 73.1 (Feb. 2013), pp. 1–13 (cit. on p. 72).

REFERENCES

- [218] V. Caracciolo et al. The ADAMO Project and developments. *Journal of Physics: Conference Series* 718.4 (July 2016), p. 042011 (cit. on p. 72).
- [219] H. Sekiya et al. *Studies on ZnWO₄ crystals for the direction-sensitive dark matter search*. Talk presented at the 11th conference on Identification of Dark Matter (IDM2016). Sheffield, 2016 (cit. on p. 72).
- [220] J. B. R. Battat et al. Readout technologies for directional WIMP Dark Matter detection. *Physics Reports* 662 (Nov. 2016), pp. 1–46 (cit. on p. 73).
- [221] N. Phan and E. Lee. *First studies of SF₆ gas in a TPC*. Talk presented during the 5th Workshop on Directional Detection of Dark Matter (CYGNUS2015), Los Angeles, USA. 2015 (cit. on p. 73).
- [222] N. S. Phan et al. The novel properties of SF₆ for directional dark matter experiments. *Preprint: arXiv1609.05249* (Dec. 2016) (cit. on p. 73).
- [223] P. Cushman et al. Working Group Report: WIMP Dark Matter Direct Detection. *Proceedings, 2013 Community Summer Study on the Future of U.S. Particle Physics: Snowmass on the Mississippi (CSS2013): Minneapolis, MN, USA, July 29-August 6, 2013*. 2013 (cit. on p. 75).
- [224] Instruments Inc., Texas. *LMH6574 4:1 High speed video multiplexer*. Technical Datasheet. Dec. 2014 (cit. on pp. 77, 111, 112, 114, 115).
- [225] EAGLE Team. *EAGLE: Easily Applicable Graphical Layout Editor*. USA, 2014 (cit. on p. 78).
- [226] A. Moreno-Baez et al. Processing Gerber files for manufacturing printed circuit boards. *Procedia Engineering* 35 (Apr. 2012). International Meeting of Electrical Engineering Research 2012, pp. 240–244 (cit. on p. 80).

REFERENCES

- [227] Y. Chiba and T. Taniguchi. A Simple Semi-Automatic Wire Winding Machine for MWPC. *Japanese Journal of Applied Physics* 19.6 (Apr. 1980), pp. 1191–1192 (cit. on p. 86).
- [228] M. Kuze et al. An Automatic Wire-Winding Machine for MWPC's. *Japanese Journal of Applied Physics* 26.8 (Mar. 1987), pp. 1348–1351 (cit. on p. 86).
- [229] D. P. Snowden-Ifft and J. L. Gauvreau. High precision measurements of carbon disulfide negative ion mobility and diffusion. *Rev. Sci. Instrum.* 84.5 (2013), p. 053304 (cit. on pp. 87, 128, 147, 159, 162).
- [230] R. Veenhof. *GARFIELD Software*. 1984 (cit. on p. 90).
- [231] I. Smirnov. *HEED Software*. 1997 (cit. on p. 90).
- [232] Cremat. *CR-150-R5 evaluation board: application guide*. Technical Datasheet. 2014 (cit. on p. 93).
- [233] J. F. Ziegler. *Stopping Range of Ions in Matter (SRIM) Software*. 1985 (cit. on p. 96).
- [234] J. F. Ziegler, M. Ziegler, and J. Biersack. SRIM-The stopping and range of ions in matter (2010). *Nucl. Inst. and Meth. in Phys. Res. Sect. B: Beam Interactions with Materials and Atoms* 268 (11—12 2010). 19th International Conference on Ion Beam Analysis, pp. 1818–1823 (cit. on pp. 96, 147).
- [235] T. Z. Kowalski and A. R. Stopczynski. The gas gain process in Ar/CO₂ filled proportional tubes. *Nucl. Inst. and Meth. in Phys. Res. Sect. A: Accel., Spectrometers, Detect. and Assoc. Equip.* 323.1 (1992), pp. 289–293 (cit. on p. 99).
- [236] T. Z. Kowalski. Gas gain limitation in low pressure proportional counters filled with TEG mixtures. *JINST* 9.12 (2014), p. C12007 (cit. on p. 99).

REFERENCES

- [237] G. F. Reinking, L. G. Christophorou, and S. R. Hunter. Studies of total ionization in gases/mixtures of interest to pulsed power applications. *Journal of Applied Physics* 60.2 (July 1986), pp. 499–508 (cit. on pp. [101](#), [134](#)).
- [238] A. Hitachi. Bragg-like curve for dark matter searches: binary gases. *Radiat. Phys. Chem.* 77.10–12 (Oct. 2008), pp. 1311–1317 (cit. on pp. [101](#), [102](#), [134](#), [135](#)).
- [239] J. Lindhard et al. Integral equations governing radiation effects (notes on atomic collisions, III). *Mat. Fys. Medd. Dan. Vid. Selsk.* 33.10 (1963), pp. 1–42 (cit. on pp. [101](#), [134](#)).
- [240] MKS. *ORTEC 926-M32-USB multichannel Analyzer*. Operation Manual. 2014 (cit. on p. [101](#)).
- [241] H. A. Bethe and J. Ashkin. Passage of Radiation Through Matter. *Exp. Nucl. Phys.* Ed. by E. Segré. New York: Wiley, 1953 (cit. on p. [102](#)).
- [242] G. F. Knoll. *Radiation detection and measurement*. Vol. 3. John Wiley & Sons, Inc., Jan. 2010, p. 796 (cit. on p. [102](#)).
- [243] W. Blum, W. Riegler, and L. Rolandi. *Particle Detection with Drift Chambers*. Ed. by A. Chao, Fabjan C. W., and F. Zimmermann. 2nd ed. Geneva: Springer Verlag, 2008 (cit. on pp. [102](#), [147](#)).
- [244] National Instruments. *Getting Started with LabVIEW*. 11500 North Mopac Expressway Austin, Texas 78759-3504 USA, June 2013 (cit. on p. [104](#)).
- [245] Halvorsen, Hans-Petter. *Introduction to LabVIEW*. Department of Electrical Engineering, Information Technology and Cybernetics, Telemark University College, Norway, 2014 (cit. on p. [104](#)).
- [246] National Instruments. *16-Channel, 50 MS/s, 14-Bit Digitizer Adapter Module for NI FlexRIO NI 5751*. Technical Datasheet. 11500 North Mopac Expressway Austin, Texas 78759-3504 USA, 2014 (cit. on p. [104](#)).

REFERENCES

- [247] National Instruments. *NI FlexRIO FPGA Modules*. Technical Datasheet. 11500 North Mopac Expressway Austin, Texas 78759-3504 USA, 2014 (cit. on pp. [104](#), [105](#)).
- [248] J. Va’vra et al. Measurement of electron drift parameters for helium and CF₄-based gases. *Nucl. Inst. and Meth. in Phys. Res. Sect. A: Accel., Spectrometers, Detect. and Assoc. Equip.* 324 (1993), pp. 113–126 (cit. on p. [109](#)).
- [249] P. Horowitz and W. Hill. *The art of electronics-3rd edition*. Cambridge university press, 2015, p. 1071 (cit. on p. [110](#)).
- [250] W. Stalling. *Data and computer communications*. 8th ed. United States of America: Pearson Prentice Hall, 2007 (cit. on p. [110](#)).
- [251] J. Battat, J. Phillips, and C. Holman. *A 16:1 analog multiplexer: some results and lessons learned*. Talk presented in the DRIFT collaboration meeting held Occidental College, Los Angeles, USA. 2015 (cit. on p. [115](#)).
- [252] N. J. C. Spooner. Techniques for Head-Tail directional recoil measurements in the DRIFT-II dark matter detector. *International workshop on identification of dark matter, 2008. Proceedings of Science*. Stockholm, Sweden, Aug. 2008 (cit. on p. [127](#)).
- [253] S. Burgos et al. First measurement of the head-tail directional nuclear recoil signature at energies relevant to WIMP dark matter searches. *Astroparticle Physics* 31.4 (Aug. 2009), pp. 261–266 (cit. on pp. [127](#), [129](#), [130](#), [141](#), [143](#), [146](#), [151–153](#), [159](#), [163](#), [171](#)).
- [254] S. Burgos et al. Measurement of the range component directional signature in a DRIFT-II detector using ²⁵²Cf neutrons. *Nucl. Inst. and Meth. in Phys. Res. Sect. A: Accel., Spectrometers, Detect. and Assoc. Equip.* 600.2 (Mar. 2009), pp. 417–423 (cit. on pp. [127](#), [153](#), [155](#), [157](#), [159](#), [160](#), [162–165](#), [171](#)).
- [255] D. N. Muna. Three Dimensional Analysis and Track Reconstruction in the DRIFT-II Dark Matter Detector. PhD thesis. University of Sheffield, 2008 (cit. on pp. [127](#), [153](#)).

REFERENCES

- [256] J. B. R. Battat et al. First measurement of nuclear recoil head-tail sense in a fiducialised WIMP dark matter detector. *JINST* 11.10 (Oct. 2016), P10019 (cit. on pp. [127](#), [159](#)).
- [257] N. J. C. Spooner et al. Simulations of the nuclear recoil head-tail signature in gases relevant to directional dark matter searches. *Astroparticle Physics* 34 (2010), pp. 284–292 (cit. on pp. [127](#), [143](#), [147](#)).
- [258] R. C. Martin, J. B. Knauer, and P. A. Balo. Production, Distribution, and Applications of Californium-252 Neutron Sources. *Proceedings of 4th Topical Meeting on Industrial Radiation and Radioisotope Measurement Applications*. 1999 (cit. on p. [127](#)).
- [259] K. Pushkin and D. Snowden-Ifft. Measurements of W-value, mobility and gas gain in electronegative gaseous CS₂ and CS₂ gas mixtures. *Nucl. Inst. and Meth. in Phys. Res. Sect. A: Accel., Spectrometers, Detect. and Assoc. Equip.* 606.3 (July 2009), pp. 569–577 (cit. on p. [135](#)).
- [260] J. Allison et al. Geant4 developments and applications. *IEEE Transactions on Nuclear Science* 53.1 (Feb. 2006), pp. 270–278 (cit. on pp. [139](#), [152](#)).
- [261] F. Fernandez-Alonso and D. L. Price. *Neutron Scattering-Fundamentals: Experimental Methods in the Physical Sciences*. Ed. by T. Lucatorto, A. C. Parr, and K. Baldwin. 44th ed. Academic Press of Elsevier, 2013 (cit. on p. [148](#)).
- [262] K. Lau and J. Pyrlík. Optimization of centroid-finding algorithms for cathode strip chambers. *Nucl. Inst. and Meth. in Phys. Res. A: Accel., Spectrometers, Detect. and Assoc. Equip.* 366 (Dec. 1995), pp. 298–309 (cit. on p. [155](#)).
- [263] M. Chemloul and V. Comparat. A new type of centroid finding method for position sensitive detectors. *Nuclear Inst. and Meth. in Phys. Res. Sect. A: Accel., Spectrometers, Detect. and Assoc. Equip.* 367 (1995), pp. 290–294 (cit. on p. [155](#)).

REFERENCES

- [264] I. Endo et al. Systematic shifts of evaluated charge centroid for the cathode read-out multiwire proportional chamber. *Nucl. Inst. and Meth. in Phys. Res.* 188.1 (Sept. 1981), pp. 51–58 (cit. on p. [155](#)).
- [265] S. R. Hunter and L. G. Christophorou. Basic Studies of Gases for Fast Switches. *Annual Summary Report, 1 Oct. 1985 - 30 Nov. 1986 Oak Ridge National Lab., TN. NASA STI/Recon Technical Report N.* Vol. 89. Oak Ridge National Laboratory for U.S. Department of Energy. Aug. 1988 (cit. on p. [157](#)).
- [266] S. Burgos et al. Studies of neutron detection and backgrounds with the DRIFT-IIa dark matter detector. *Astroparticle Physics* 28.4-5 (Sept. 2007), pp. 409–421 (cit. on pp. [171](#), [174](#), [182](#)).
- [267] E. Tziaferi et al. First measurement of low intensity fast neutron background from rock at the Boulby Underground Laboratory. *Astroparticle Physics* 27.5 (Dec. 2007), pp. 326–338 (cit. on p. [174](#)).
- [268] P. F. Smith et al. Simulation studies of neutron shielding, calibration and veto systems for gaseous dark matter detectors. *Astroparticle Physics* 22.5-6 (Oct. 2005), pp. 409–420 (cit. on p. [174](#)).
- [269] M. Carson et al. Simulations of neutron background in a time projection chamber relevant to dark matter searches. *Nucl. Inst. and Meth. in Phys. Res. Sect. A: Accel., Spectrometers, Detect. and Assoc. Equip.* 546.3 (July 2005), pp. 509–522 (cit. on p. [174](#)).
- [270] C. Ghag. Simulation , Calibration & Exploitation of the DRIFT-II Directional Dark Matter Detector. PhD thesis. University of Edinburgh, 2006 (cit. on p. [174](#)).
- [271] W. B. Wilson et al. *SOURCES 4C: a code for calculating (α,n), spontaneous fission, and delayed neutron sources and spectra.* Tech. rep. Los Alamos National Laboratory, 2002 (cit. on p. [175](#)).

REFERENCES

- [272] F. Mouton. GEANT4 Update: Shielded and unshielded background neutron simulations. *DRIFT Priv. Commun.* (2015) (cit. on pp. [181–183](#)).
- [273] G. Feldman and R. Cousins. Unified approach to the classical statistical analysis of small signals. *Phys. Rev. D* 57.7 (1998), p. 3873 (cit. on p. [183](#)).